

DOT/FAA/AR-05/39

Office of Aviation Research
Washington, D.C. 20591

Experimental Investigation of Ice Accretion Effects on a Swept Wing

August 2005

Final Report

This document is available to the U.S. public
through the National Technical Information
Service (NTIS), Springfield, Virginia 22161.



U.S. Department of Transportation
Federal Aviation Administration

NOTICE

This document is disseminated under the sponsorship of the U.S. Department of Transportation in the interest of information exchange. The United States Government assumes no liability for the contents or use thereof. The United States Government does not endorse products or manufacturers. Trade or manufacturer's names appear herein solely because they are considered essential to the objective of this report. This document does not constitute FAA certification policy. Consult your local FAA aircraft certification office as to its use.

This report is available at the Federal Aviation Administration William J. Hughes Technical Center's Full-Text Technical Reports page: actlibrary.tc.faa.gov in Adobe Acrobat portable document format (PDF).

1. Report No. DOT/FAA/AR-05/39	2. Government Accession No.	3. Recipient's Catalog No.	
4. Title and Subtitle EXPERIMENTAL INVESTIGATION OF ICE ACCRETION EFFECTS ON A SWEPT WING		5. Report Date August 2005	
		6. Performing Organization Code	
7. Author(s) Michael Papadakis¹, Hsiung-Wei Yeong¹, See-Cheuk Wong¹, Mario Vargas², and Mark Potapczuk²		8. Performing Organization Report No.	
9. Performing Organization Name and Address ¹Department of Aerospace Engineering Wichita State University Wichita, KS 67260 ²NASA John H. Glenn Research Center at Lewis Field Cleveland, OH 44135		10. Work Unit No. (TRAIS)	
		11. Contract or Grant No.	
12. Sponsoring Agency Name and Address U.S. Department of Transportation Federal Aviation Administration Office of Aviation Research Washington, DC 20591		13. Type of Report and Period Covered Final Report	
		14. Sponsoring Agency Code AIR-100	
15. Supplementary Notes The FAA William J. Hughes Technical Center Technical Monitor was James Riley.			
16. Abstract An experimental investigation was conducted to study the effects of 2-, 5-, 10-, and 22.5-min ice accretions on the aerodynamic performance of a swept finite wing. The ice shapes tested included castings of ice accretions obtained from icing tests at the NASA Glenn Icing Research Tunnel (IRT) and simulated ice shapes obtained with the LEWICE 2.0 ice accretion code. The conditions used for the icing tests were selected to provide five glaze ice shapes with complete and incomplete scallop features and a small rime ice shape. The LEWICE ice shapes were defined for the same conditions as those used in the icing tests. All aerodynamic performance tests were conducted in the 7- x 10-ft Low-Speed Wind Tunnel Facility at Wichita State University. Six component force and moment measurements, aileron hinge moments, and surface pressures were obtained for a Reynolds number of 1.8 million based on mean aerodynamic chord and aileron deflections in the range of -15° to 20°. Tests were performed with the clean wing, six IRT ice shape castings, seven smooth LEWICE ice shapes, and seven rough LEWICE ice shapes. Roughness for the LEWICE ice shapes was simulated with 36-size grit. The experiments conducted showed that the glaze ice castings reduced the maximum lift coefficient of the clean wing by 11.5% to 93.6%, while the 5-min rime ice casting increased maximum lift by 3.4%. Minimum iced wing drag was 133% to 3533% greater with respect to the clean case. The drag of the iced wing near the clean wing stall angle of attack was 17% to 104% higher than that of the clean case. In general, the aileron remained effective in changing the lift of the clean and iced wings for all angles of attack and aileron deflections tested. Aileron hinge moments for the iced wing cases remained within the maximum and minimum limits defined by the clean wing hinge moments. Tests conducted with the LEWICE ice shapes showed that in general the trends in aerodynamic performance degradation of the wing with the simulated ice shapes were similar to those obtained with the IRT ice shape castings. However, in most cases, the ice castings resulted in greater aerodynamic performance losses than those obtained with the LEWICE ice shapes. For the majority of the LEWICE ice shapes, the addition of 36-size grit roughness to the smooth ice shapes increased aerodynamic performance losses.			
17. Key Words Ice accretion, Three-dimensional, Finite swept wing, Experimental aerodynamic effects, Ice shape castings, glaze ice		18. Distribution Statement This document is available to the public through the National Technical Information Service (NTIS) Springfield, Virginia 22161.	
19. Security Classif. (of this report) Unclassified	20. Security Classif. (of this page) Unclassified	21. No. of Pages 207	22. Price

ACKNOWLEDGEMENTS

This work was supported by a grant from the Federal Aviation Administration (FAA). NASA Glenn Research Center provided extensive support for this program. The authors would like to thank Dr. James T. Riley, the grant technical monitor of the FAA William J. Hughes Technical Center, Mr. Eugene Hill, the FAA Icing National Resource Specialist and Tom Bond, the Chief of the Icing Branch at the NASA Glenn Research Center for their support. The authors acknowledge the extensive efforts of the following NASA personnel who helped with the icing tunnel tests and the fabrication of the ice shape castings: Dave Sheldon, Gene Addy, David Brinkman, the icing research tunnel crew, and Robert Reminder. Thanks are also due to the Raytheon Aircraft Company in Wichita, KS, for providing the wing body mount for the aerodynamic tests. Finally, the authors would like to acknowledge the extensive efforts of the following Wichita State University (WSU) personnel: Dennis Regnier, Norma Campos, Michael Boccia, and Joshua Fong for their assistance with the wind tunnel tests and with the analysis of the experimental data; Art Porter of the WSU Machine Shop for his efforts in fabricating the wind tunnel model and the simulated ice shapes; the wind tunnel crew for their support during the experimental investigation.

TABLE OF CONTENTS

	Page
EXECUTIVE SUMMARY	xxi
1. INTRODUCTION	1-1
2. EXPERIMENTAL FACILITIES AND PROCEDURES	2-1
2.1 Icing Tests at the NASA Glenn IRT	2-1
2.1.1 Test Facility	2-1
2.1.2 Test Model	2-2
2.1.3 Test Model Hardware for the Icing Tests	2-3
2.1.4 Icing Conditions and Test Matrix	2-5
2.1.5 Procedure to Obtain Ice Accretions	2-6
2.1.6 Casting Process	2-8
2.2 Aerodynamic Tests at the WSU 7- x 10-ft Tunnel	2-11
2.2.1 Test Facility	2-11
2.2.2 Test Model and Installation	2-11
2.2.3 Icing Research Tunnel Ice Castings and LEWICE Ice Shapes	2-14
2.2.4 Test Procedure	2-27
2.2.5 Test Measurements	2-31
3. RESULTS AND DISCUSSION	3-1
3.1 Icing Conditions and Ice Accretions (NASA IRT)	3-1
3.1.1 Icing Condition 1—Complete Scallop Condition ($\tau = 10$ min)	3-1
3.1.2 Icing Condition 2—Incomplete Scallop Condition ($\tau = 10$ min)	3-2
3.1.3 Icing Condition 3—Scaled Condition ($\tau = 5$ min)	3-2
3.1.4 Icing Condition 4—Complete Scallop Condition ($\tau = 2$ min)	3-5
3.1.5 Icing Condition 5—Complete Scallop Condition ($\tau = 22.5$ min)	3-6
3.1.6 Icing Condition 6—IPS Failure Condition ($\tau = 22.5$ min)	3-7
3.2 Aerodynamic Performance Studies	3-8
3.2.1 Data Quality and Repeatability	3-10
3.2.2 Compressibility Effects	3-17
3.2.3 Clean and Iced Wing Performance	3-18
3.2.4 Comparison of IRT and LEWICE Ice Shapes	3-43
3.2.5 Effect of Aileron Deflection	3-82
3.2.6 Effect of Large Scallop Features	3-91

3.2.7	Reynolds Number Effects	3-97
4.	CONCLUSIONS	4-1
4.1	Performance of Clean Wing	4-1
4.2	Effects of IRT Ice Shape Castings	4-1
4.3	Definition of LEWICE Ice Shapes	4-2
4.4	Effects of Smooth LEWICE Ice Shapes	4-2
4.5	Effects of Rough LEWICE Ice Shapes	4-2
4.6	Rough Versus Smooth LEWICE Ice Shapes	4-2
4.7	Icing Research Tunnel Versus Rough LEWICE Ice Shapes	4-3
4.8	Aileron Performance	4-3
4.9	Reynolds Number Effects	4-3
5.	REFERENCES	5-1

APPENDICES

A—Run Log for Icing Tests at NASA Glenn Icing Research Tunnel

B—Run Log for Aerodynamic Investigation at Wichita State University

C—Pressure Data From Icing Tests

D—Flow Angularity Studies

E—Simulated Frost Using Sandpaper

F—Effect of Aileron Deflection (Supplementary)

G—Computation of LEWICE Ice Shape Profiles

H—Comparison of Two- and Three-Dimensional Wing Ice Shape Traces and Lift Data

LIST OF FIGURES

Figure	Page
2-1 NASA Glenn Icing Research Tunnel Planview	2-1
2-2 Wing Planform	2-2
2-3 Airfoil Section and Wing Parameters	2-2
2-4 Wing in the Low Position Showing the RLEs	2-4
2-5 Specifications of the Top, Middle, and Bottom RLEs	2-4
2-6 Low, Normal, and High Positions of the Wing in the IRT	2-4
2-7 Wing in High Position	2-5
2-8 Wing in Low Position With the Top Leading-Edge Segment Removed	2-5
2-9 A Heated Copper Plate Was Used to Cut Ice Accretions for Tracing Purposes	2-8
2-10 Ice Accretion Pencil-Traced on Cardboard	2-8
2-11 A Sample of a Pencil Tracing of an Ice Accretion	2-8
2-12 Top RLE Segment With Ice Accretion Inside the Wooden Molding Box	2-9
2-13 Middle RLE With IRT-CS22 Ice Accretion Attached to the Inside of a Wooden Molding Box—Side View	2-9
2-14 Leading Edge With Ice Accretion Prepared for Making the Mold—Top View	2-9
2-15 The Mold and Leading Edge Were Placed Inside the Box to Make the Casting	2-10
2-16a Close-Up of Ice Shape Casting	2-10
2-16b Close-Up of the Actual Ice Accretion	2-10
2-17 Wichita State University 7- x10-ft Wind Tunnel Facility	2-11
2-18 Wing and Streamlined Body in WSU Test Section—Side View	2-12
2-19 Installation of Clean Wing in WSU Wind Tunnel—Front View	2-12
2-20 Installation of Clean Wing in WSU Wind Tunnel—Side View	2-12
2-21 Installation of Clean Wing on Tunnel Turntable—Rear View	2-13

2-22	Housing for Servomotor, Torque Cell, and LCDT	2-13
2-23	Close-Up of Wing Root and Dental Dam—Pressure Surface	2-14
2-24	Close-Up of Wing Root and Dental Dam—Suction Surface	2-14
2-25	Icing Research Tunnel CS10 Ice Shape Casting Installed on Wing—Side View	2-15
2-26	Close-Up of IRT-CS10 Ice Shape Casting at Wing Root	2-15
2-27	Close-Up of Installation of IRT-IS10 Ice Shape Casting on Wing Model	2-16
2-28	Close-Up of Installation of IRT-CS22 Ice Shape Casting on Wing Model	2-16
2-29	Installation of IRT-SC5 Ice Shape Casting on Wing Model—Side View	2-16
2-30	Icing Research Tunnel CS2 Ice Shape Casting on Test Model—Front View	2-16
2-31	GLC-305 Swept Wing With IRT-CS22 Ice Shape Casting—Front View	2-17
2-32	Front View of IRT-IPSF22 Ice Shape Casting at Wing Root	2-17
2-33	Polyurethane Castings of the Six Ice Shapes Obtained From Icing Tests at IRT	2-17
2-34	Smooth and Rough LEWICE Ice Shapes	2-20
2-35	Comparison of IRT and LEWICE Ice Shapes for Icing Condition 1 (CS10)	2-21
2-36	Comparison of IRT and LEWICE Ice Shapes for Icing Condition 2 (IS10)	2-21
2-37	Comparison of IRT and LEWICE Ice Shapes for Icing Condition 3 (SC5)	2-22
2-38	Comparison of IRT and LEWICE Ice Shapes for Icing Condition 4 (CS2)	2-22
2-39	Comparison of IRT and LEWICE Ice Shapes for Icing Condition 5 (CS22)	2-23
2-40	Comparison of IRT and LEWICE Ice Shapes for Icing Condition 6 (IPSF22)	2-23
2-41	Details of Ice Shapes Obtained From Icing Condition 2	2-24
2-42	Comparison of Profile of LR-CS22N and LR-CS22S Ice Shapes—Tip Section	2-24
2-43	Comparison of Profile of LR-CS22N and LR-CS22S Ice Shapes—Root Section	2-24
2-44	Installation of LR-CS10 Rough LEWICE Ice Shape on Wing Model	2-25
2-45	Close-Up of LR-IS10 Ice Shape at Tip of Wing Model	2-25
2-46	Installation of LR-SC5 Rough LEWICE Ice Shape on Wing Model	2-26

2-47	Installation of LR-CS2 Rough LEWICE Ice Shape on Wing Model	2-26
2-48	Installation of LS-CS22N Smooth LEWICE Ice Shape on Wing Model	2-26
2-49	Installation of LR-CS22N Rough LEWICE Ice Shape on Wing Model	2-26
2-50	Installation of LS-IPSF22 Ice Shape on Wing Model—Suction Side	2-27
2-51	Installation of LS-IPSF22 Ice Shape on Wing Model—Pressure Side	2-27
2-52	Installation of Seven-Hole Flow Probes on Wing Model—Front View	2-29
2-53	Installation of Seven-Hole Flow Probes on Wing Model—Side View	2-29
2-54	Close-Up of Seven-Hole Flow Probe Near to Wing Root (16% Semispan)	2-29
2-55	Close-Up of Seven-Hole Flow Probe Near to Wing Tip (80% Semispan)	2-29
2-56	Tufts Installation on Clean Wing and Streamlined Body—Pressure Surface	2-30
2-57	Installation of Yarn Tufts on Iced Wing and Streamlined Body—Suction Surface	2-30
2-58	Tufts Show That Flow Downstream of Ice Shape Was Separated Near Wing Tip	2-30
2-59	Tufts Show Complete Flow Separation at Wing Tip	2-30
3-1	Icing Condition 1, Front View of Ice Accretion on the Top RLE	3-1
3-2	Icing Condition 1, Side View of Ice Accretion on Pressure Side of the Top RLE	3-1
3-3	Icing Condition 1, Front View of the Complete Ice Accretion on the Top RLE	3-2
3-4	Icing Condition 1, Casting From the Ice Accretion on the Top RLE	3-2
3-5	Icing Condition 2, Front View of Ice Accretion on the Bottom RLE	3-3
3-6	Icing Condition 2, Side View of Ice Accretion on Suction Side of the Bottom RLE	3-3
3-7	Icing Condition 2, Front View of the Complete Ice Accretion on the Bottom RLE	3-3
3-8	Icing Condition 2, Casting From the Ice Accretion on the Bottom RLE	3-3
3-9	Icing Condition 3, Front View of Ice Accretion on the Bottom RLE	3-4
3-10	Icing Condition 3, Side View of Ice Accretion on Suction Side of the Bottom RLE	3-4
3-11	Icing Condition 3, Front View of the Complete Ice Accretion on the Bottom RLE	3-4
3-12	Icing Condition 3, Casting From the Ice Accretion on the Bottom RLE	3-4

3-13	Icing Condition 4, Front View of Ice Accretion on the Middle RLE	3-5
3-14	Icing Condition 4, Side View of Ice Accretion on Suction Side of the Middle RLE	3-5
3-15	Icing Condition 4, Front View of the Complete Ice Accretion on the Middle RLE	3-5
3-16	Icing Condition 4, Casting From the Ice Accretion on the Middle RLE	3-5
3-17	Icing Condition 5, Front View of Ice Accretion on the Middle RLE	3-6
3-18	Icing Condition 5, Side View of Ice Accretion on Suction Side of the Middle RLE	3-6
3-19	Icing Condition 5, Front View of the Complete Ice Accretion on the Middle RLE	3-6
3-20	Icing Condition 5, Casting From the Ice Accretion on the Middle RLE	3-6
3-21	Icing Condition 6, Front View of Ice Accretion on the Top RLE	3-7
3-22	Icing Condition 6, Side View of Ice Accretion on Pressure Side of the Top RLE	3-7
3-23	Icing Condition 6, Front View of the Complete Ice Accretion on the Top RLE	3-8
3-24	Icing Condition 6, Casting From the Ice Accretion on the Top RLE	3-8
3-25	Notation for Pitching Moment, Hinge Moment, and Aileron Deflection Angle	3-8
3-26	Regions A, B, and C for Hinge-Moment Curve of Clean and Iced Configurations	3-9
3-27	Repeatability of C_L , C_D , C_M , and C_H ; Clean Configuration; $Re = 1.8 \times 10^6$; $\delta_A = 0^\circ$	3-11
3-28	Repeatability of Pressure Distributions at 15% Semispan; Clean Configuration; $Re = 1.8 \times 10^6$; $\delta_A = 0^\circ$	3-12
3-29	Repeatability of Pressure Distributions at 50% Semispan; Clean Configuration; $Re = 1.8 \times 10^6$; $\delta_A = 0^\circ$	3-13
3-30	Repeatability of Pressure Distributions at 85% Semispan; Clean Configuration; $Re = 1.8 \times 10^6$; $\delta_A = 0^\circ$	3-14
3-31	Setup to Check External Balance	3-15
3-32	Setup to Check Hinge-Moment Load Cell	3-15
3-33	Data Sampling Studies of C_L , C_D , C_M , and C_H ; Clean Configuration; $Re = 1.8 \times 10^6$; $\delta_A = 0^\circ$	3-16

3-34	Effect of IRT Ice Shapes on C_L , C_D , C_M , and C_H ; IRT-CS10, IRT-IS10, IRT-SC5, IRT-CS2, IRT-CS22, and IRT-IPSF22 Configurations; $Re = 1.8 \times 10^6$; $\delta_A = 0^\circ$	3-19
3-35	Effect of IRT Ice Shapes on Pressure Distributions at 15% Semispan; IRT-CS10, IRT-IS10, IRT-SC5, IRT-CS2, IRT-CS22, and IRT-IPSF22 Configurations; $Re = 1.8 \times 10^6$; $\delta_A = 0^\circ$	3-20
3-36	Effect of IRT Ice Shapes on Pressure Distributions at 50% Semispan; IRT-CS10, IRT-IS10, IRT-SC5, IRT-CS2, IRT-CS22, and IRT-IPSF22 Configurations; $Re = 1.8 \times 10^6$; $\delta_A = 0^\circ$	3-21
3-37	Effect of IRT Ice Shapes on Pressure Distributions at 85% Semispan; IRT-CS10, IRT-IS10, IRT-SC5, IRT-CS2, IRT-CS22, and IRT-IPSF22 Configurations; $Re = 1.8 \times 10^6$; $\delta_A = 0^\circ$	3-22
3-38	Effect of Smooth LEWICE Ice Shapes on C_L , C_D , C_M , and C_H ; LS-CS10, LS-IS10, LS-SC5, LS-CS2, LS-CS22N, LS-CS22S, and LS-IPSF22 Configurations; $Re = 1.8 \times 10^6$; $\delta_A = 0^\circ$	3-23
3-39	Effect of Smooth LEWICE Ice Shapes on Pressure Distributions at 15% Semispan; LS-CS10, LS-IS10, LS-SC5, LS-CS2, LS-CS22N, LS-CS22S, and LS-IPSF22 Configurations; $Re = 1.8 \times 10^6$; $\delta_A = 0^\circ$	3-24
3-40	Effect of Smooth LEWICE Ice Shapes on Pressure Distributions at 50% Semispan; LS-CS10, LS-IS10, LS-SC5, LS-CS2, LS-CS22N, LS-CS22S, and LS-IPSF22 Configurations; $Re = 1.8 \times 10^6$; $\delta_A = 0^\circ$	3-25
3-41	Effect of Smooth LEWICE Ice Shapes on Pressure Distributions at 85% Semispan; LS-CS10, LS-IS10, LS-SC5, LS-CS2, LS-CS22N, LS-CS22S, and LS-IPSF22 Configurations; $Re = 1.8 \times 10^6$; $\delta_A = 0^\circ$	3-26
3-42	Effect of Rough LEWICE Ice Shapes on C_L , C_D , C_M , and C_H ; LR-CS10, LR-IS10, LR-SC5, LR-CS2, LR-CS22N, LR-CS22S, and LR-IPSF22 Configurations; $Re = 1.8 \times 10^6$; $\delta_A = 0^\circ$	3-27
3-43	Effect of Rough LEWICE Ice Shapes on Pressure Distributions at 15% Semispan; LR-CS10, LR-IS10, LR-SC5, LR-CS2, LR-CS22N, LR-CS22S, and LR-IPSF22 Configurations; $Re = 1.8 \times 10^6$; $\delta_A = 0^\circ$	3-28
3-44	Effect of Rough LEWICE Ice Shapes on Pressure Distributions at 50% Semispan; LR-CS10, LR-IS10, LR-SC5, LR-CS2, LR-CS22N, LR-CS22S, and LR-IPSF22 Configurations; $Re = 1.8 \times 10^6$; $\delta_A = 0^\circ$	3-29

3-45	Effect of Rough LEWICE Ice Shapes on Pressure Distributions at 85% Semispan; LR-CS10, LR-IS10, LR-SC5, LR-CS2, LR-CS22N, LR-CS22S, and LR-IPSF22 Configurations; $Re = 1.8 \times 10^6$; $\delta_A = 0^\circ$	3-30
3-46	Effect of IRT-CS10, LS-CS10, and LR-CS10 Ice Shapes (Icing Condition 1) on C_L , C_D , C_M , and C_H ; $Re = 1.8 \times 10^6$; $\delta_A = 0^\circ$	3-44
3-47	Effect of IRT-IS10, LS-IS10, and LR-IS10 Ice shapes (Icing Condition 2) on C_L , C_D , C_M , and C_H ; $Re = 1.8 \times 10^6$; $\delta_A = 0^\circ$	3-45
3-48	Effect of IRT-SC5, LS-SC5, and LR-SC5 Ice Shapes (Icing Condition 3) on C_L , C_D , C_M , and C_H ; $Re = 1.8 \times 10^6$; $\delta_A = 0^\circ$	3-46
3-49	Effect of IRT-CS2, LS-CS2, and LR-CS2 Ice Shapes (Icing Condition 4) on C_L , C_D , C_M , and C_H ; $Re = 1.8 \times 10^6$; $\delta_A = 0^\circ$	3-47
3-50	Effect of IRT-CS22, LS-CS22N, LS-CS22S, LR-CS22N, and LR-CS22S Ice Shapes (Icing Condition 5) on C_L , C_D , C_M , and C_H ; $Re = 1.8 \times 10^6$; $\delta_A = 0^\circ$	3-48
3-51	Effect of IRT-IPSF22, LS-IPSF22, and LR-IPSF22 Ice Shapes (Icing Condition 6) on C_L , C_D , C_M , and C_H ; $Re = 1.8 \times 10^6$; $\delta_A = 0^\circ$	3-49
3-52	Effect of IRT-CS10, LS-CS10, and LR-CS10 Ice Shapes (Icing Condition 1) on Pressure Distributions at 15% Semispan; $Re = 1.8 \times 10^6$; $\delta_A = 0^\circ$	3-50
3-53	Effect of IRT-CS10, LS-CS10, and LR-CS10 Ice Shapes (Icing Condition 1) on Pressure Distributions at 50% Semispan; $Re = 1.8 \times 10^6$; $\delta_A = 0^\circ$	3-51
3-54	Effect of IRT-CS10, LS-CS10, and LR-CS10 Ice Shapes (Icing Condition 1) on Pressure Distributions at 85% Semispan; $Re = 1.8 \times 10^6$; $\delta_A = 0^\circ$	3-52
3-55	Effect of IRT-IS10, LS-IS10, and LR-IS10 Ice Shapes (Icing Condition 2) on Pressure distributions at 15% Semispan; $Re = 1.8 \times 10^6$; $\delta_A = 0^\circ$	3-53
3-56	Effect of IRT-IS10, LS-IS10, and LR-IS10 Ice Shapes (Icing Condition 2) on Pressure Distributions at 50% Semispan; $Re = 1.8 \times 10^6$; $\delta_A = 0^\circ$	3-54
3-57	Effect of IRT-IS10, LS-IS10, and LR-IS10 Ice Shapes (Icing Condition 2) on Pressure Distributions at 85% Semispan; $Re = 1.8 \times 10^6$; $\delta_A = 0^\circ$	3-55
3-58	Effect of IRT-SC5, LS-SC5, and LR-SC5 Ice Shapes (Icing Condition 3) on Pressure Distributions at 15% Semispan; $Re = 1.8 \times 10^6$; $\delta_A = 0^\circ$	3-56
3-59	Effect of IRT-SC5, LS-SC5, and LR-SC5 Ice Shapes (Icing Condition 3) on Pressure Distributions at 50% Semispan; $Re = 1.8 \times 10^6$; $\delta_A = 0^\circ$	3-57

3-60	Effect of IRT-SC5, LS-SC5, and LR-SC5 Ice Shapes (Icing Condition 3) on Pressure Distributions at 85% Semispan; $Re = 1.8 \times 10^6$; $\delta_A = 0^\circ$	3-58
3-61	Effect of IRT-CS2, LS-CS2, and LR-CS2 Ice Shapes (Icing Condition 4) on Pressure Distributions at 15% Semispan; $Re = 1.8 \times 10^6$; $\delta_A = 0^\circ$	3-59
3-62	Effect of IRT-CS2, LS-CS2, and LR-CS2 Ice Shapes (Icing Condition 4) on Pressure Distributions at 50% Semispan; $Re = 1.8 \times 10^6$; $\delta_A = 0^\circ$	3-60
3-63	Effect of IRT-CS2, LS-CS2, and LR-CS2 Ice Shapes (Icing Condition 4) on Pressure Distributions at 85% Semispan; $Re = 1.8 \times 10^6$; $\delta_A = 0^\circ$	3-61
3-64	Effect of IRT-CS22, LS-CS22N, LS-CS22S, LR-CS22N, and LR-CS22S Ice Shapes (Icing Condition 5) on Pressure Distributions at 15% Semispan; $Re = 1.8 \times 10^6$; $\delta_A = 0^\circ$	3-62
3-65	Effect of IRT-CS22, LS-CS22N, LS-CS22S, LR-CS22N, and LR-CS22S Ice Shapes (Icing Condition 5) on Pressure Distributions at 50% Semispan; $Re = 1.8 \times 10^6$; $\delta_A = 0^\circ$	3-63
3-66	Effect of IRT-CS22, LS-CS22N, LS-CS22S, LR-CS22N, and LR-CS22S Ice Shapes (Icing Condition 5) on Pressure Distributions at 85% Semispan; $Re = 1.8 \times 10^6$; $\delta_A = 0^\circ$	3-64
3-67	Effect of IRT-IPSF22, LS-IPSF22, and LR-IPSF22 Ice Shapes (Icing Condition 6) on Pressure Distributions at 15% Semispan; $Re = 1.8 \times 10^6$; $\delta_A = 0^\circ$	3-65
3-68	Effect of IRT-IPSF22, LS-IPSF22, and LR-IPSF22 Ice Shapes (Icing Condition 6) on Pressure Distributions at 50% Semispan; $Re = 1.8 \times 10^6$; $\delta_A = 0^\circ$	3-66
3-69	Effect of IRT-IPSF22, LS-IPSF22, and LR-IPSF22 Ice Shapes (Icing Condition 6) on Pressure Distributions at 85% Semispan; $Re = 1.8 \times 10^6$; $\delta_A = 0^\circ$	3-67
3-70	Effect of Aileron Deflection on Lift and Aileron Hinge-Moment Coefficients; Clean Configuration; $Re = 1.8 \times 10^6$	3-83
3-71	Effect of Aileron Deflection on Lift and Aileron Hinge-Moment Coefficients; IRT-CS22 Ice Shape; $Re = 1.8 \times 10^6$	3-84
3-72	Effect of Aileron Deflection on Lift and Aileron Hinge-Moment Coefficients; IRT-IPSF22 Ice Shape; $Re = 1.8 \times 10^6$	3-85
3-73	Effect of Aileron Deflection on Lift and Aileron Hinge-Moment Coefficients; LR-IPSF22 Ice Shape; $Re = 1.8 \times 10^6$	3-86
3-74	Ice Accretion on a Swept Wing at Glaze Ice Conditions	3-93

3-75	Development of Roughness Elements and Ice Feathers During Ice Accretion on a Swept Wing	3-93
3-76	Icing Research Tunnel CS22 Ice Shape Filled With Modeling Compound	3-94
3-77	Effect of Scallop Features on Aerodynamic Performance; IRT-CS22 Ice Shape With and Without Modeling Compound; $Re = 1.8 \times 10^6$; $\delta_A = 0^\circ$	3-95
3-78	Reynolds Number Effect on C_L ; Clean and Iced Wing; $\delta_A = 0^\circ$	3-98

LIST OF TABLES

Table	Page
2-1 Icing Conditions for IRT Ice Shape Castings	2-6
2-2 Summary of Ice Shape Sections and Corresponding Icing Conditions	2-7
2-3 Icing Conditions for LEWICE Ice Shapes	2-15
2-4 Test Conditions for Aerodynamic Performance Data	2-28
3-1 Effect of IRT Ice Shapes on C_L and C_D ; $Re_{MAC} = 1.8 \times 10^6$; $\delta_A = 0^\circ$	3-31
3-2 Effect of IRT Ice Shapes on $C_{L,stall}$, α_{stall} , and $C_{D,min}$; $Re_{MAC} = 1.8 \times 10^6$; $\delta_A = 0^\circ$	3-31
3-3 Effect of IRT Ice Shapes on Hinge-Moment Coefficient Slope; $Re_{MAC} = 1.8 \times 10^6$; $\delta_A = 0^\circ$	3-32
3-4 Effect of Smooth LEWICE Ice Shapes on C_L and C_D ; $Re_{MAC} = 1.8 \times 10^6$; $\delta_A = 0^\circ$	3-32
3-5 Effect of Smooth LEWICE Ice Shapes on $C_{L,stall}$, α_{stall} , and $C_{D,min}$; $Re_{MAC} = 1.8 \times 10^6$; $\delta_A = 0^\circ$	3-33
3-6 Effect of Smooth LEWICE Ice Shapes on Hinge-Moment Coefficient Slope; $Re_{MAC} = 1.8 \times 10^6$; $\delta_A = 0^\circ$	3-33
3-7 Effect of Rough LEWICE Ice Shapes on C_L and C_D ; $Re_{MAC} = 1.8 \times 10^6$; $\delta_A = 0^\circ$	3-34
3-8 Effect of Rough LEWICE Ice Shapes on $C_{L,stall}$, α_{stall} , and $C_{D,min}$; $Re_{MAC} = 1.8 \times 10^6$; $\delta_A = 0^\circ$	3-34
3-9 Effect of Rough LEWICE Ice Shapes on Hinge-Moment Coefficient Slope; $Re_{MAC} = 1.8 \times 10^6$; $\delta_A = 0^\circ$	3-35
3-10 Cl_{stall} of all Configurations With Aileron Deflection; $Re_{MAC} = 1.8 \times 10^6$	3-87

LIST OF ACRONYMS AND SYMBOLS

2D	Two-dimensional
3D	Three-dimensional
Al	Aluminum
AOA	Angle of attack (in degrees)
CFD	Computational fluid dynamics
FAA	Federal Aviation Administration
FAR	Federal Aviation Regulation
IPS	Ice protection system
IPSF	Ice protection system failure condition, 22.5-min ice accretion time (icing condition 6)
IRT	Icing Research Tunnel
LE	Leading edge
LEB	Leading-edge bubble
LEWICE	NASA Glenn Ice Accretion Code (Version 2.0)
LS	Wing lower surface
LTPT	Low-Turbulence Pressure Tunnel
LVDT	Linear variable differential transducer
LWC	Liquid water content
MAC	Mean aerodynamic chord
MVD	Median volumetric diameter
NASA	National Aeronautics and Space Administration
PSI	Pressure Systems Incorporated

RLE	Removable leading edge
TE	Trailing edge
US	Wing upper surface
WSU	Wichita State University
a_0	2D lift curve slope (per radian)
AR	Aspect ratio
b	Wing span
C_a	Aileron mean chord length behind the hinge line
C_D	Drag coefficient
$C_{D,min}$	Minimum drag coefficient
ΔC_D	Percentage change in drag coefficient with respect to the clean wing
C_H	Hinge-moment coefficient
$C_{H,\alpha}$	$= dC_H/d\alpha$; Change in hinge-moment coefficient with respect to AOA; control floating parameter
$C_{H,\delta}$	$= dC_H/d\delta$; slope of C_H vs. δ_A curve; control heaviness parameter
C_L	Lift coefficient
$C_{L,max}$	Maximum lift coefficient
$C_{L,stall}$	Lift coefficient corresponding to the point on the lift curve where massive flow separation (stall) occurs
ΔC_L	Percentage change in lift coefficient with respect to the clean wing
$C_{L,\alpha}$	$= dC_L/d\alpha$; change in lift coefficient with respect to AOA
C_M	Pitching-moment coefficient
$C_{M,clean}$	Pitching-moment coefficient of the clean wing about the 25% MAC location

$C_{M,LEWICE}$	Pitching-moment coefficient of wing with LEWICE ice shape about the 25% MAC location
$C_{M,MAC/4}$	Pitching-moment coefficient about the 25% MAC location
$dC_M/d\alpha$	Change in pitching-moment coefficient with respect to the AOA
C_p	Pressure coefficient
C_{p_0}	Suction pressure coefficient for incompressible flow
$C_{p_{cr}}$	Critical pressure coefficient
d_{cr}	Critical distance
H_M	Hinge moment
M_∞	Free-stream Mach number
S	Wing planform area
S_a	Aileron planform area behind the hinge line
Re_{MAC}	Reynolds number based on MAC
T_{total}	Total temperature
V_∞	Free-stream velocity
x/c	Nondimensional chordwise distance
α	Geometric angle of attack (in degrees)
α_e	Effective angle of attack (in degrees)
α_{local}	Local geometric angle of attack (in degrees)
α_{stall}	Geometric angle of attack at which stall occurs (in degrees)
δ_A	Aileron deflection angle (in degrees)
γ	= 1.4; ratio of specific heats

Λ	Sweepback angle at leading edge
ρ	Free-stream density
τ	Ice accretion time (in minutes)

EXECUTIVE SUMMARY

Aircraft certification requires the evaluation of the effects of ice accretions on aircraft aerodynamic components such as wings, tails, and control surfaces. Ice accumulation on aerodynamic surfaces can have a significant impact on aircraft performance, handling qualities, and thus, aircraft safety. In general, ice accumulation on aerodynamic surfaces can cause flow separation whose extent over the aerodynamic surface is a function of ice shape and wing geometry. The term critical is often used to identify ice shapes responsible for large degradation in the aerodynamic performance of lifting surfaces.

A number of experimental studies have been conducted over the years in an effort to assess the effect of various forms of ice accretions on aircraft aerodynamic performance and handling qualities. Most of these studies, however, have been limited to two-dimensional airfoil sections due to tunnel and model cost constraints. Only a small number of investigations have addressed the impact of ice shapes on iced three-dimensional (3D) finite wings.

To address the lack of experimental data for iced 3D finite wing configurations, the Federal Aviation Administration (FAA), Wichita State University (WSU), the National Aeronautics and Space Administration (NASA), and general aviation aircraft manufacturers initiated a collaborative research program in the fall of 2000 for a systematic evaluation of ice accretion effects on finite wings. The main objective of this research program was the development of a 3D experimental database of ice accretion effects on a swept 3D finite wing. The database can be used for developing certification guidance material and for improving and validating simulation tools for aerodynamic analysis and design. A research grant was awarded to WSU to design and fabricate a wind tunnel model and to conduct icing and aerodynamic performance tests to develop the required database.

The specific goals of the research program were to (1) investigate wing sensitivity to various forms of ice accretions, (2) compare the effects of actual ice shapes from icing tunnel tests with equivalent simulated ice shapes, (3) assess the effects of glaze ice shape features such as horn angle, horn height and surface roughness on wing aerodynamic performance, and (4) develop an experimental database of ice shape effects on the aerodynamic performance of a swept finite span wing with an aileron control surface. The principal accomplishments of this research program, which was completed in the fall of 2002, are summarized below.

A number of meetings were conducted with the FAA, NASA, and general aviation manufacturers to select a wing model, ice shapes, and test conditions, and to define experimental methodologies and procedures. A 5-ft semispan swept finite wing reflection plane model equipped with an aileron control surface was designed, fabricated, and instrumented at WSU. Tests were conducted at the NASA Glenn Icing Research Tunnel (IRT) to generate five glaze ice shapes with complete and incomplete scallop features and one rime ice shape. Ice shape castings were produced by NASA personnel from the actual ice accretions for aerodynamic testing. Simulated 3D ice shapes were defined with the NASA Glenn LEWICE ice accretion code for the same icing conditions used in the IRT icing tests. The 3D ice shapes were fabricated out of wood or aluminum at WSU and were prepared for aerodynamic testing. Extensive experiments were conducted at the WSU 7- x 10-ft wind tunnel facility over a period of 10 weeks to generate

the required data for the clean and iced wing. Twenty ice shapes and eight roughness cases were tested along with the clean wing. The ice shapes included six IRT castings and seven smooth and seven rough LEWICE shapes. The roughness cases included 120- and 150-grit sandpaper to simulate the effect of frost on wing aerodynamic performance. Lift, drag, pitching moment, hinge moment, and pressure distributions were obtained for all configurations tested.

The experimental results obtained showed that the stall lift coefficients for the wing with the glaze ice shape castings were 11.5% to 93.6% less than the clean wing. For the 5-min rime ice shape, the stall lift coefficient was 3.4% higher than the clean wing. The IRT ice shape castings tested increased the minimum clean wing drag coefficient by 133% to 3533% and increased drag near stall by 17% to 104%. In general, the aileron remained effective in changing the lift of the clean and iced wings for all angles of attack and aileron deflections tested. Aileron hinge moments for the iced wing remained within the maximum and minimum limits defined by the clean wing hinge-moment data. In general, the trends in aerodynamic performance degradation of the wing with the simulated rough LEWICE ice shapes were similar to those obtained with the IRT ice shape castings. However, in most cases, the ice shape castings resulted in greater aerodynamic performance losses than that obtained with the rough LEWICE shapes. In most cases, the rough LEWICE ice shapes caused greater aerodynamic performance degradation than did their smooth counterparts.

1. INTRODUCTION.

Aircraft certification requires the evaluation of the effects of ice accretions on aircraft aerodynamic components such as wings, tails, and control surfaces. Ice accumulation on aerodynamic surfaces can have a significant impact on aircraft performance, handling qualities, and thus, aircraft safety. A wide range of ice accretions is possible, depending on aircraft configuration, icing, and flow conditions. Potential ice accretions include glaze ice, rime ice, runback, and beak ice, as well as small ice shapes which can have considerable degradation in aircraft performance. In general, ice accumulation on aerodynamic surfaces can cause flow separation whose extent over the aerodynamic surface is a function of ice shape and wing geometry. The term critical is often used to identify ice shapes responsible for large degradation in the aerodynamic performance of lifting surfaces.

A number of experimental studies have been conducted over the years (refer to reference 1 for a comprehensive review) in an effort to assess the effect of various forms of ice accretions on aircraft aerodynamic performance and handling qualities. Most of these studies have been limited to two-dimensional (2D) airfoil sections due to tunnel and model cost constraints. Only a small number of investigations have addressed the impact of ice shapes on finite wings.

To address the lack of experimental data for three-dimensional (3D) iced wing configurations, scientists and engineers from the Federal Aviation Administration (FAA), the National Aeronautics and Space Administration (NASA), the general aviation aircraft industry, and Wichita State University (WSU) conducted a meeting to plan a research program for a systematic evaluation of ice accretion effects on finite wings. The main objective of this research program was the development of a 3D experimental database of ice accretion effects on a swept finite wing. The database was needed for developing certification guidance material and for improving and validating simulation tools for aerodynamic analysis and design. A research grant was awarded to WSU to design and fabricate a wind tunnel model and to conduct icing and aerodynamic performance tests to develop the required database. The specific goals of the WSU research effort were to

- investigate wing sensitivity to various forms of ice accretions.
- compare the effects of actual ice shapes from icing tunnel tests with equivalent simulated ice shapes.
- assess the effects of glaze ice shape features such as horn angle, horn height, and surface roughness on wing aerodynamic performance.
- develop an experimental database of ice shape effects on aerodynamic performance of a swept finite wing with an aileron control surface.

To accomplish the above objectives, wind tunnel tests were planned with a wing representative of modern business jet and regional jet aircraft wing planforms. The wing selection was based on input from the FAA, NASA, and the aircraft industry. An important consideration in the selection of the airfoil section for the finite wing was the availability of 2D iced airfoil

aerodynamic performance data for comparison with the 3D iced wing aerodynamic performance results. The airfoil selected was a GLC-305 section, which is representative of a modern business jet wing section. NASA has conducted extensive 2D wind tunnel tests with this airfoil in recent years using a range of ice accretions.

The ice shapes selected for the experimental investigation included the following:

- Polyurethane castings of ice accretions obtained from icing tests at the NASA Glenn Icing Research Tunnel (IRT).
- Smooth LEWICE ice shapes obtained for the same icing conditions as the ones used in the generation of the ice shape castings.
- Rough LEWICE ice shapes obtained by adding grit roughness to the surface of the smooth LEWICE ice shapes.

This report describes the icing tests performed in the IRT and the aerodynamic tests conducted at WSU with the ice castings and the simulated LEWICE ice shapes. Experimental data presented includes lift, drag, pitching moment, aileron hinge moment, and surface pressure data.

2. EXPERIMENTAL FACILITIES AND PROCEDURES.

The experimental investigation consisted of ice accretion tests and aerodynamic performance wind tunnel tests. The icing tests were conducted over a time period of 5 days at the IRT facility to obtain six ice shape castings for aerodynamic testing. The aerodynamic performance investigation took place at the 7- x 10-ft Low-Speed Wind Tunnel facility at WSU. The clean wing and 20 ice shape configurations were tested at the WSU wind tunnel over a time period of 10 weeks. This section describes the test model and ice shapes tested, the experimental setup, test conditions, test measurements, and procedures used in the experimental investigations conducted.

2.1 ICING TESTS AT THE NASA GLENN IRT.

The first part of the experiment was conducted at the NASA Glenn 6- x 9-ft Icing Research Tunnel to obtain castings of ice accretions formed on a swept wing model. Details of the icing tests are provided in the following sections.

2.1.1 Test Facility.

The IRT is a closed-loop refrigerated wind tunnel. Its test section is 6 ft (1.8 m) high, 9 ft (2.7 m) wide, and 20 ft (6.0 m) long. In the test section, the total air temperature can be varied between -20°F (-30°C) and $+33^{\circ}\text{F}$ ($+1^{\circ}\text{C}$), within accuracy of $\pm 1^{\circ}\text{F}$ ($\pm 0.5^{\circ}\text{C}$), and a maximum velocity of 390 mph (160 m/s) can be attained. A spray system allows control of the liquid water content (LWC) between 0.2 to 3.0 g/m^3 and provides droplet median volumetric diameters (MVD) from 15 to $40 \text{ }\mu\text{m}$. Figure 2-1 shows the planview of the NASA Glenn Icing Research Tunnel.

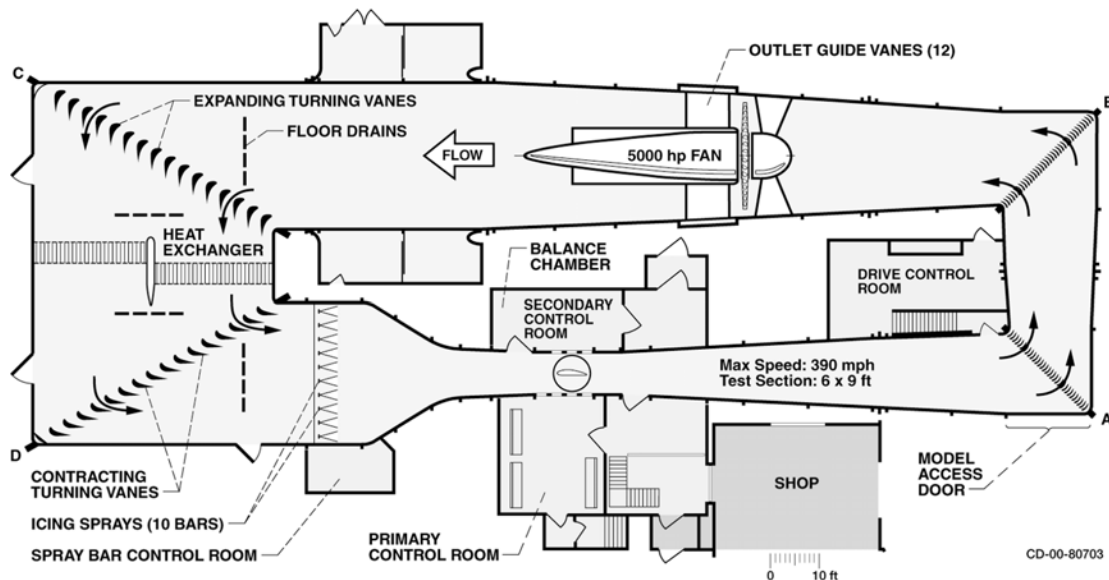


FIGURE 2-1. NASA GLENN ICING RESEARCH TUNNEL PLANVIEW

2.1.2 Test Model.

Aerodynamic considerations and facility size limitations determined the overall size of the wing model. Details of the swept wing model are provided in figures 2-2 and 2-3. The model was a swept finite wing with a GLC-305 airfoil section aligned in the streamwise direction. The airfoil section had a maximum thickness to chord ratio of 0.087 at approximately 38% local chord. The airfoil section remained constant from the wing root to the wing tip. The wing had a 28° leading edge (LE) sweep, a 15.6° trailing-edge (TE) sweep, a 60-in. semispan, a 7.35 ft^2 area (half wing), an aspect ratio (AR) of 6.80 (left and right wing), a taper ratio of 0.4, and a geometric twist of 0° at the root and -4° (washout) at the tip. The wing root and tip chords were 25.2 inches and 10.08 inches respectively. In addition, the wing mean aerodynamic chord (MAC) was 18.72 inches and was located 25.74 inches from the wing root. The model was instrumented with 203 pressure ports distributed chordwise at five spanwise locations corresponding to 15%, 30%, 50%, 68%, and 85% semispan.

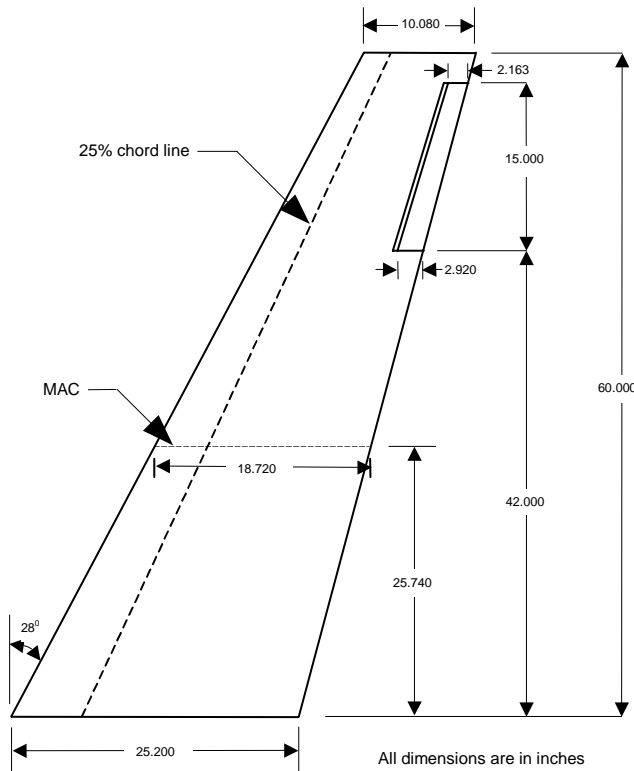
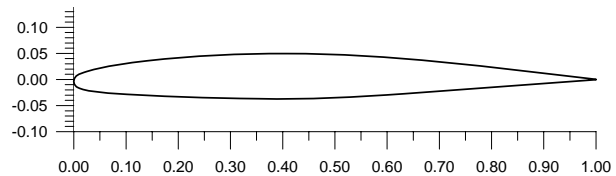


FIGURE 2-2. WING PLANFORM

AIRFOIL SECTION

1. GLC-305 section in streamwise direction ($t/c_{\max}=0.087$ at $x/c=0.38$). Airfoil section is constant from root to tip.
2. Trailing edge thickness = 0.04 in (constant spanwise)



WING PLANFORM

1. 5 ft semispan (72% of WSU tunnel height)
2. Root chord = 25.2 in, Tip chord = 10.08 in, MAC = 18.72 in
3. t/c varies linearly from root to tip
4. Planform Area (half wing, $S/2$) = 7.35 ft^2 ; wing area to test section area ratio = $7.35/(7 \times 10) = 0.105$
5. taper ratio = 0.4, trapezoidal planform, linear chord variation from root to tip
6. $AR = b^2/S = 10^2 / (2 \times 7.35) = 6.8027$
7. 25° quarter chord sweep, 28° leading edge sweep

WING GEOMETRIC TWIST AND DIHEDRAL

1. Geometric twist about 25% local chord (0° at root, -4° at tip)
2. Dihedral = 0°
3. AILERON CONTROL SURFACE
1. 25% local chord (from 70% to 95% semispan); $C_{\text{root}} = 3.66 \text{ in}$, $C_{\text{tip}} = 2.712 \text{ in}$
2. Elliptical leading edge (pivot at 80% local wing chord), Gap = 0.5% local chord
3. Deflection range: -20° to $+20^\circ$
4. Aileron area behind the hinge line, $S_a = 0.2647 \text{ ft}^2$
5. Aileron average chord behind the hinge line, $c_a = [(2.163 + 2.92)/2]/12 = 0.2118 \text{ ft}$

FIGURE 2-3. AIRFOIL SECTION AND WING PARAMETERS

2.1.3 Test Model Hardware for the Icing Tests.

The icing tests conducted for the purpose of generating ice castings for the swept finite wing required considerable planning to maximize the number of test runs during each day of testing. In general, once an icing test was completed, the ice casting process required approximately 1 day to provide a mold. Thus, the wing cannot be used until the mold was completed and removed from the wing. Another limitation of the ice casting process was the spanwise length of the casting cannot exceed 25 inches.

The goal of the icing tests conducted in the IRT facility with the 60-in. semispan finite wing was to produce six ice castings approximately 68 inches long (the length of wing measured along the swept LE) in 5 days of testing. Due to the limitations of the ice casting process, only five 25-in. segments could be produced in 5 days, unless significant modifications were made to the wing model to allow multiple ice castings during each test day. This was accomplished by designing and constructing four wing leading edges. The first leading edge was for aerodynamic measurements only and extended the full span of the wing. Leading edges two through four, however, were divided into three spanwise segments each, as shown in figures 2-4 and 2-5. Thus, a total of nine leading-edge segments were produced in addition to the full-span leading edge. The removable leading edges were labeled top, middle, and bottom. The bottom removable leading edge (RLE) was 25 inches long and extended from the wing root to 36.79% semispan. The middle segment was also 25 inches long and extended from 36.79% semispan to 73.78% semispan. The top RLE had a length of 17.95 inches and extended from 73.78% semispan to the wing tip. Note that the sum of the lengths of the three RLEs was 67.98 inches, which is the distance from the wing root to the wing tip measured along the swept leading edge. This distance is equal to the wing semispan divided by the cosine of the leading-edge sweep angle (i.e., $\frac{60}{\cos 28^\circ}$). The advantage of having 18 leading-edge segments was that every time an ice accretion test was completed, the leading-edge segment with the ice shape was removed for the ice molding process and a clean segment was placed on the wing. This permitted multiple icing runs to be conducted each test day.

Additional model hardware had to be designed and fabricated to support the icing tests at the NASA Glenn IRT. The additional hardware included brackets and a 1-ft wing extension to permit the placement in the wing from 5.5 inches below the IRT floor to 11.5 inches above the floor. This was required to place the wing inside the uniform LWC region of the icing cloud. By lowering the wing below the tunnel floor, LWC uniformity was maintained over the middle and top segments of the wing. With the wing in the high position, the middle and bottom segments of the wing leading edge were exposed to the uniform region of the icing cloud. For aerodynamic pressure measurement, it was necessary to install the wing with its root section placed on the tunnel floor. This required additional hardware to be fabricated. The three wing placements with respect to the IRT tunnel floor are shown in figures 2-6 to 2-8.



FIGURE 2-4. WING IN THE LOW POSITION SHOWING THE RLEs

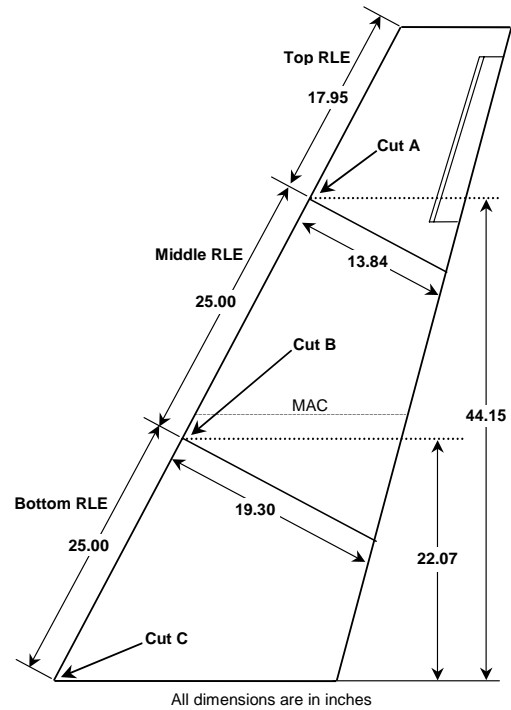


FIGURE 2-5. SPECIFICATIONS OF THE TOP, MIDDLE, AND BOTTOM RLEs

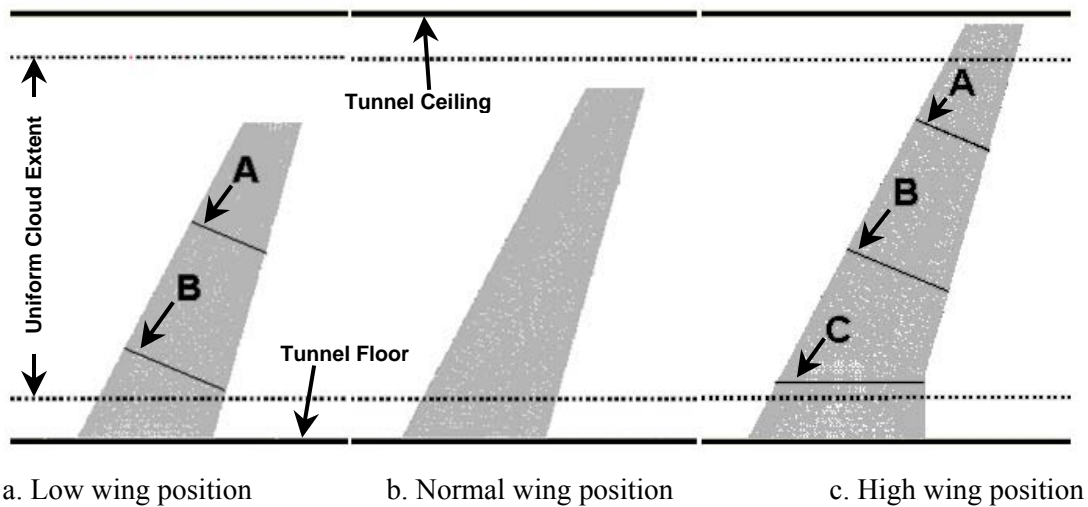


FIGURE 2-6. LOW, NORMAL, AND HIGH POSITIONS OF THE WING IN THE IRT (Cuts were made to remove ice accretion from wing at locations A, B, and C.)



FIGURE 2-7. WING IN HIGH POSITION



FIGURE 2-8. WING IN LOW POSITION
WITH THE TOP LEADING-EDGE
SEGMENT REMOVED

2.1.4 Icing Conditions and Test Matrix.

Table 2-1 lists the six icing conditions selected to obtain the ice accretions for the aerodynamic investigation. These icing conditions were selected to provide four glaze ice shapes with complete and incomplete scallop features, a 22.5-min glaze ice accretion representative of an ice protection system (IPS) failure case, and a 5-min rime ice shape. Glaze ice accretions with complete and incomplete scallop features are discussed in detail in references 2 to 4. The four ice shapes with scallop features were obtained using progressively longer ice accretion times to provide a range of horn sizes for aerodynamic testing. The rime ice shape was based on a scaled icing condition from icing tests conducted with a 2D 36-in. chord GLC-305 airfoil. Ice shape details are provided in table 2-2. Appendix A lists all of the runs done in the IRT to obtain ice accretions for the top, middle, and bottom RLEs at each of the six icing conditions.

TABLE 2-1. ICING CONDITIONS FOR IRT ICE SHAPE CASTINGS

Icing Condition	Description	*AOA (deg)	V (mph)	T _{total} (°F)	LWC (g/m ³)	MVD (μm)	τ (min)
1 (Glaze)	Complete Scallop Condition (ID: Ice1 or IRT-CS10)	4	250.0	25.0	0.68	20.0	10.0
2 (Glaze)	Incomplete Scallop Condition (ID: Ice2 or IRT-IS10)	4	150.0	25.0	0.65	20.0	10.0
3 (Rime)	Scaled Condition from 2D tests (ID: Ice3 or IRT-SC5)	6	201.3	11.7	0.51	14.5	5.0
4 (Glaze)	Complete Scallop Condition (ID: Ice4 or IRT-CS2)	4	250.0	25.0	0.68	20.0	2.0
5 (Glaze)	Complete Scallop Condition (ID: Ice5 or IRT-CS22)	4	250.0	25.0	0.68	20.0	22.5
6 (Glaze)	Failed Ice Protection (ID: Ice6 or IRT-IPSF22)	4	150.0	27.0	0.46	20.0	22.5

* AOA = angle of attack

2.1.5 Procedure to Obtain Ice Accretions.

Two icing runs at each icing condition were needed to obtain one complete ice accretion over the total length of the wing leading edge (i.e., 67.95 inches). The first run with the wing in the low position provided the ice accretion on the top RLE. In this position, the ice accretions on the middle and bottom RLEs were not used. A second run with the wing in the high position provided the ice accretion on the middle and bottom RLEs. In this position, the ice accretion of the leading edge near the tip was not used. From the two wing positions (at a given icing condition), three removable leading edges with ice accretions were obtained and were used to make a set of three molds, and later a set of three castings. Each icing condition resulted in a set of three castings, providing a full-span ice shape casting. Ultimately, six sets of castings were obtained during the test (one set for each of the six icing conditions) for a total of 18 castings.

At the start of each run, the tunnel was brought to the target velocity and total temperature before activating the tunnel spray system. During the run, the tunnel parameters were recorded using the NASA Glenn Escort data acquisition system. Once the target ice accretion time was reached, the spray system was shut off, and the tunnel was brought to idle. At this point, tunnel crew entered the test section and photographs were taken with a 35-mm camera following a predetermined sequence and locations. Cuts were then made on the ice accretion using a heated 1/8-in.-thick copper plate to prepare the leading edges for tracings and removal, as depicted in figure 2-9. When the wing was placed in the low position, only one cut (perpendicular to the LE) was needed at the location where the top and the middle leading edges joined. This cut was named cut A and is shown in figure 2-5. When the wing was placed in the high position, three cuts were made: one at the intersection where the top and middle RLEs joined (cut A), another at the location where the middle and bottom RLEs joined (cut B), and one at the lower part of the bottom RLE (cut C). Cuts A and B were made perpendicular to the LE, whereas cut C was

parallel to the flow direction (streamwise direction) because it was located at the exact root of the wing. At each cut, illustrated in figure 2-10, a pencil tracing of the ice shape was made on a cardboard template. Figure 2-11 shows an example of a pencil tracing. After the ice section tracings were completed, the leading edges were detached from the wing and moved to the cold room adjacent to the tunnel to begin the casting process.

TABLE 2-2. SUMMARY OF ICE SHAPE SECTIONS AND CORRESPONDING ICING CONDITIONS










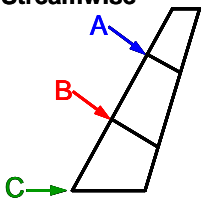
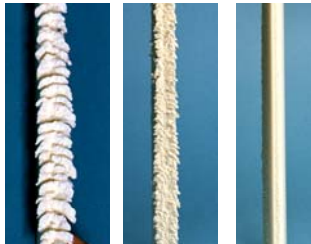










<p>Ice1 or IRT-CS10</p> <p>A </p> <p>B </p> <p>C </p> <p>Complete Scallops V = 250 mph AOA = 4° T_{total} = 25 °F LWC = 0.68 g/m³ MVD = 20 μm Time = 10 min</p>	<p>Ice2 or IRT-IS10</p> <p></p> <p></p> <p></p> <p>Incomplete Scallops V = 150 mph AOA = 4° T_{total} = 25 °F LWC = 0.65 g/m³ MVD = 20 μm Time = 10 min</p>	<p>Ice3 or IRT-SC5</p> <p></p> <p></p> <p></p> <p>No Scallops V = 201 mph AOA = 6° T_{total} = 11.7 °F LWC = 0.51 g/m³ MVD = 14.5 μm Time = 5 min</p>	<p>A: Normal to LE B: Normal to LE C: Streamwise</p>  <p>Ice1 Ice2 Ice3</p>  <p>Ice4 Ice5 Ice6</p> 
<p>Ice4 or IRT-CS2</p> <p>A </p> <p>B </p> <p>C </p> <p>Initial Formation V = 250 mph AOA = 4° T_{total} = 25 °F LWC = 0.68 g/m³ MVD = 20 μm Time = 2 min</p>	<p>Ice5 or IRT-CS22</p> <p></p> <p></p> <p></p> <p>Complete Scallops V = 250 mph AOA = 4° T_{total} = 25 °F LWC = 0.68 g/m³ MVD = 20 μm Time = 22.5 min</p>	<p>Ice6 or IRT-IPSF22</p> <p></p> <p></p> <p></p> <p>IPS Failure Case V = 150 mph AOA = 4° T_{total} = 27 °F LWC = 0.46 g/m³ MVD = 20 μm Time = 22.5 min</p>	



FIGURE 2-9. A HEATED COPPER PLATE WAS USED TO CUT ICE ACCRETIONS FOR TRACING PURPOSES (IRT-CS22 at tip of bottom RLE)



FIGURE 2-10. ICE ACCRETION PENCIL-TRACED ON CARDBOARD (IRT-CS22 at tip of bottom RLE)

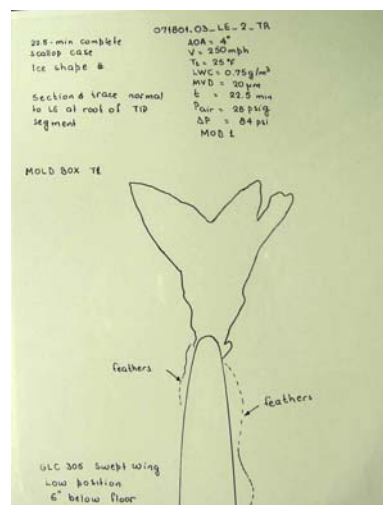


FIGURE 2-11. A SAMPLE OF A PENCIL TRACING OF AN ICE ACCRETION (IRT-CS22 at root of top RLE)

2.1.6 Casting Process.

The casting process involved two steps: making the mold and making the actual casting.

The process started when the LE was removed and taken to the cold room. The LE was placed inside a wooden box (figure 2-12) made specially for the molding process. The top of the box and one of its sides were removed to free up space for handling the delicate ice accretion. Once the RLE was attached to the inside of the box with bolts, the removed side of the box was reinstalled. The box was left open at the top for pouring in the mold material. Figures 2-13 and

2-14 show side and top views of the ice accretion on the RLE attached inside the wooden box. Styrofoam pieces were placed around the ice accretion, without touching it, to reduce the quantity of mold material needed.



FIGURE 2-12. TOP RLE SEGMENT WITH ICE ACCRETION INSIDE THE WOODEN MOLDING BOX



FIGURE 2-13. MIDDLE RLE WITH IRT-CS22 ICE ACCRETION ATTACHED TO THE INSIDE OF A WOODEN MOLDING BOX—SIDE VIEW



FIGURE 2-14. LEADING EDGE WITH ICE ACCRETION PREPARED FOR MAKING THE MOLD—TOP VIEW

Preparation of the Dow Corning 3110 room temperature vulcanized mold material started before the tunnel runs. Dow Corning 3110 was poured in containers and mixed with Dow Corning 200, 20 centistokes, at 10% of the Dow Corning 3110 by weight. Each container was degassed for 30 minutes or more in a bell jar and then placed in a freezer. When the leading edge was ready inside the box, a container with Dow Corning 3110 was removed from the freezer and Dow Corning no. 4 catalyst was added, at a 1-to-125 ratio of the Dow Corning 3110 by weight. After mixing, it was degassed in the bell jar for 5 minutes, moved to the cold room, and poured into the box containing the leading edge with the ice accretion. The mold was left to cure overnight. In the morning, the mold was separated from the leading edge.

Once the molds were finished, they were moved to the model shop of the NASA Glenn Research Center, where the castings were made. To make a casting, a mold was placed inside the same box used to make it. The wing RLE that was used to make the mold was placed in the same position as when the mold was made. This is illustrated in figure 2-15. A separation distance was left between the LE and the mold to create a thin wall for the casting. A polyurethane elastomer, Ciba-Geigy RP 6430, was poured in and left to cure. After curing, the LE was separated from the casting, and the mold material was removed from around the casting.



FIGURE 2-15. THE MOLD AND LEADING EDGE WERE PLACED INSIDE THE BOX TO MAKE THE CASTING

Figure 2-16a shows a close-up of the casting obtained from the ice accretion, and figure 2-16b shows a close-up of the actual ice accretion. Comparison of the two figures illustrates the detail captured with the casting process.



FIGURE 2-16a. CLOSE-UP OF ICE SHAPE CASTING



FIGURE 2-16b. CLOSE-UP OF THE ACTUAL ICE ACCRETION

2.2 AERODYNAMIC TESTS AT THE WSU 7- x 10-ft TUNNEL.

All aerodynamic performance tests were conducted in the WSU 7- x 10-ft Beech Memorial Low-Speed Wind Tunnel. Details of the wind tunnel investigation are provided below.

2.2.1 Test Facility.

The WSU wind tunnel is a single-return, closed circuit facility with a maximum speed of 160 mph (235 ft/s), corresponding to a Reynolds number of 1.46 million per foot. The test section is 7 ft high by 10 ft wide by 12 ft long. Four screens located in the plenum chamber upstream of the test section are used for flow conditioning. The contraction ratio between the plenum and test sections is 6 to 1. The tunnel is equipped with a four-bladed, 11-ft diameter, variable pitch propeller, which is driven by a 1000 horsepower electric motor. Figure 2-17 shows the planview of the facility.

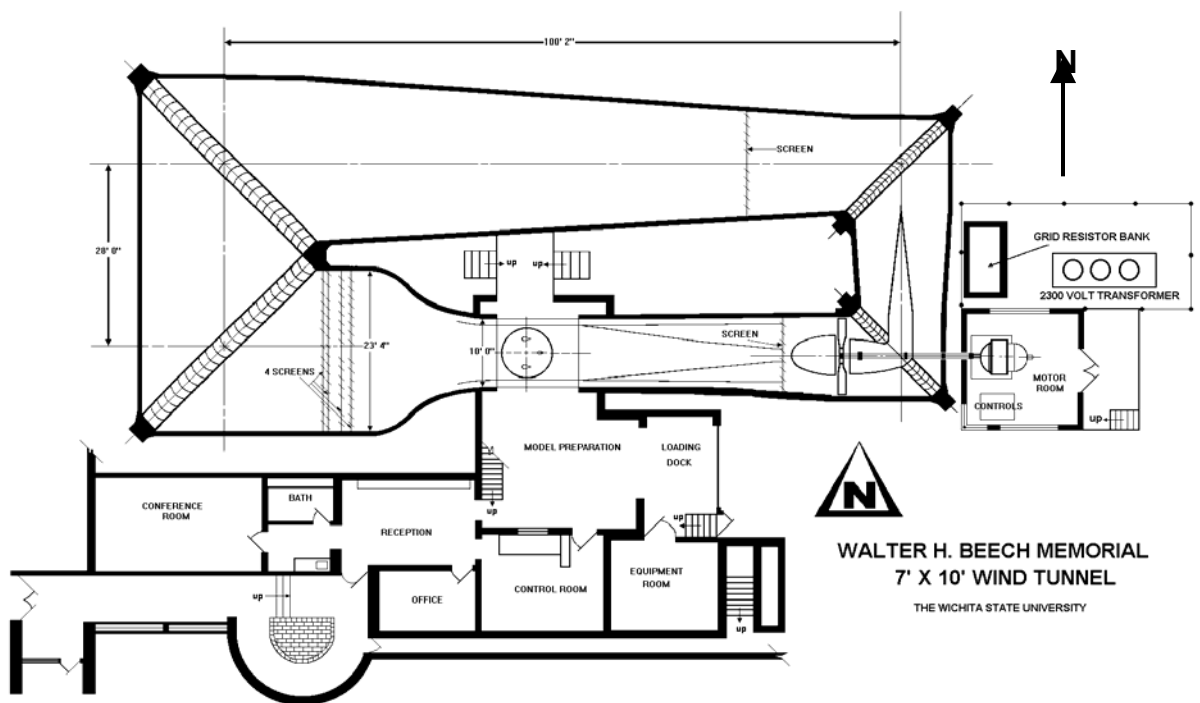


FIGURE 2-17. WICHITA STATE UNIVERSITY 7- x 10-ft WIND TUNNEL FACILITY

2.2.2 Test Model and Installation.

Details of the finite swept wing model used in the aerodynamic performance tests were shown in figures 2-2 and 2-3. An aileron control surface was added to the wing model for investigating the effect of ice accretions on the behavior of control surface effectiveness and hinge moments. The aileron had a 15-in. span starting at 42 inches from the wing root, and its leading edge sweep was 18.93° . The leading edge and hinge line were at 75% and 80% of the wing local chord respectively. Note that, due to the wing taper, the local wing chord varied linearly with spanwise distance. The aileron surface behind the hinge line had a geometric mean chord of 0.2118 ft and a planform area of 0.2647 ft^2 .

The wing model was installed as a reflection plane model, as shown in figures 2-18 to 2-20. It was instrumented with 203 pressure ports distributed chordwise at five spanwise locations, corresponding to 15%, 30%, 50%, 68%, and 85% semispan, as shown in figure 2-20. The number of chordwise pressure ports for each spanwise station was 52 ports at 15% semispan (near the wing root), 49 ports at 30% semispan, 41 ports at 50% semispan (mid-semispan), 32 ports at 68% semispan, and 29 ports at 85% semispan (near the wing tip).

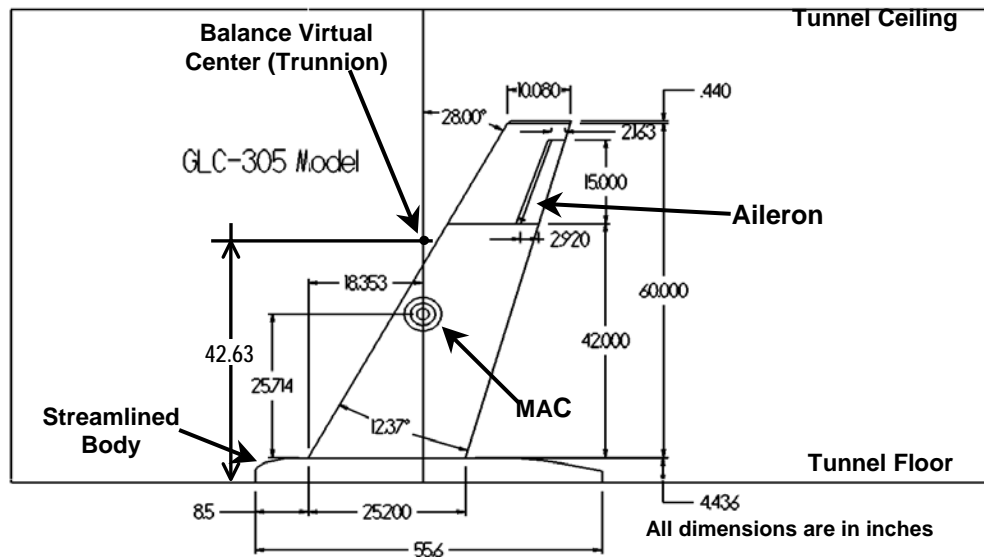


FIGURE 2-18. WING AND STREAMLINED BODY IN WSU TEST SECTION—SIDE VIEW



FIGURE 2-19. INSTALLATION OF CLEAN WING IN WSU WIND TUNNEL—FRONT VIEW

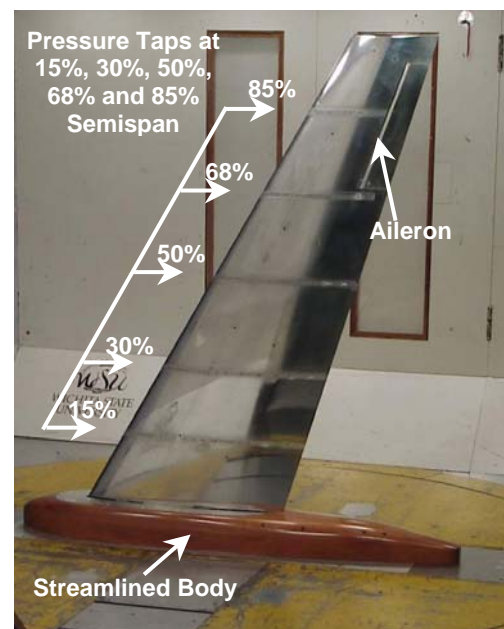


FIGURE 2-20. INSTALLATION OF CLEAN WING IN WSU WIND TUNNEL—SIDE VIEW

A direct current servomotor was used for deflecting the aileron and a torque cell for measuring aileron hinge moments. The deflection of the aileron was measured with a linear variable differential transducer (LVDT). The servomotor, torque cell, and LVDT were housed inside the wing mount, which connected the wing to the external balance, as shown in figures 2-21 and 2-22.

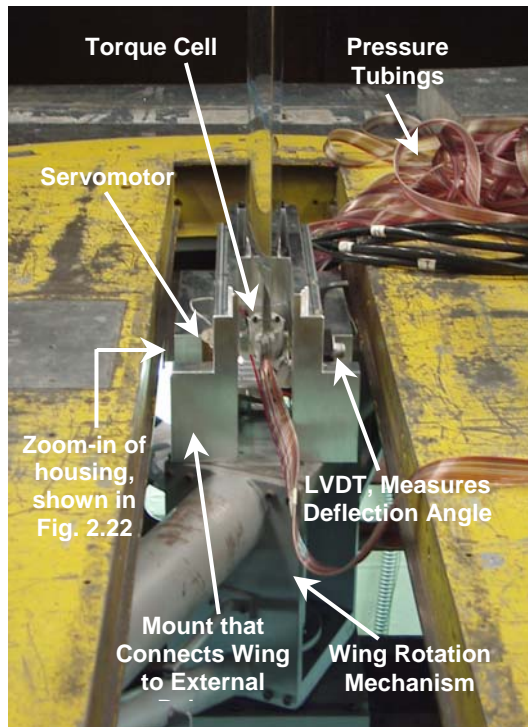


FIGURE 2-21. INSTALLATION OF CLEAN WING ON TUNNEL TURNTABLE—REAR VIEW

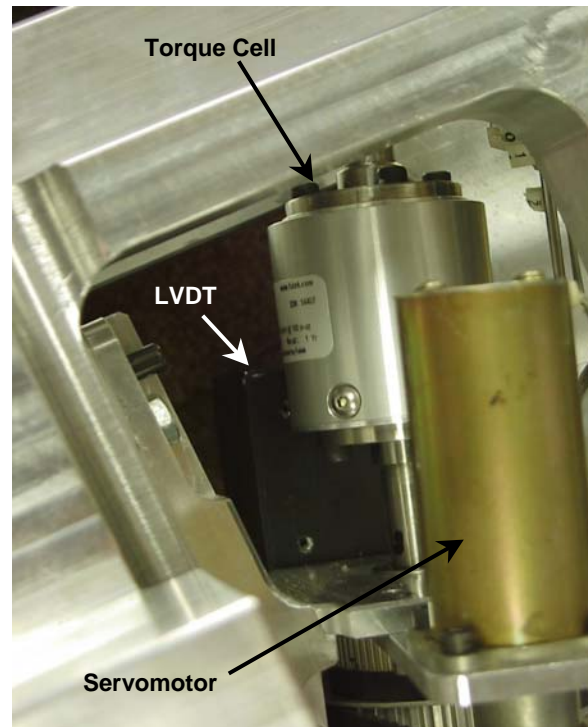


FIGURE 2-22. HOUSING FOR SERVOMOTOR, TORQUE CELL, AND LVDT (Photographed under the wing, near the trailing edge.)

Two large aluminum (Al) brackets were designed to connect the wing to the tunnel external balance and to raise the wing model 4.4 inches above the tunnel floor. Raising the model above the tunnel floor was necessary to keep the wing root section above the floor boundary layer, which was approximately 1.5 inches high. Since the Al brackets were exposed to the flow, the wing aerodynamic measurements would have been affected by the aerodynamic loads on the brackets. To eliminate this problem, a wooden fuselage-like body was used to shield the wing support brackets from the airflow. The streamlined body was 4.436 inches high and 55.6 inches long. Aerodynamic forces on the body did not affect the wing force and moment measurements since it was not connected to the tunnel balance. Extensive computational flow dynamics (CFD) studies were performed prior to the experimental investigation to ensure that the streamlined body did not modify the wing flow field and that the flow over the body remained attached even at high angles of attack (beyond wing stall). A small 0.25-in. gap was allowed between the wing root section and the streamlined body to prevent contact between the wing and the body. The 0.25-in. gap was sealed with a latex strip called dental dam, as shown in figures 2-23 and 2-24, to prevent flow leakage through the gap that could have modified the flow near the wing root.

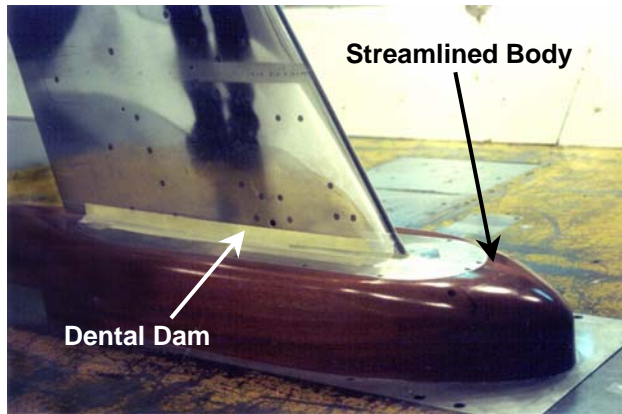


FIGURE 2-23. CLOSE-UP OF WING
ROOT AND DENTAL
DAM—PRESSURE SURFACE

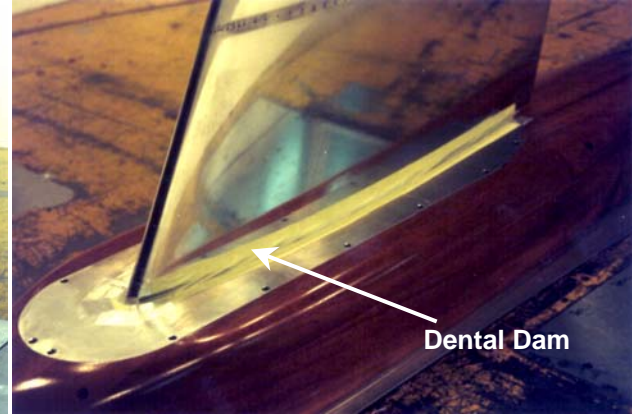


FIGURE 2-24. CLOSE-UP OF WING
ROOT AND DENTAL
DAM—SUCTION SURFACE

2.2.3 Icing Research Tunnel Ice Castings and LEWICE Ice Shapes.

The ice shapes selected for the aerodynamic experiments included six polyurethane castings of actual ice accretions and seven simulated ice shapes defined with the NASA Glenn LEWICE 2.0 ice accretion code. Icing conditions and ice shape notations are provided in tables 2-1 to 2-3. To assess the effects of ice roughness on aerodynamic performance, the LEWICE ice shapes were tested with and without simulated roughness. A total of 20 ice shapes were investigated during the experimental study.

2.2.3.1 IRT Ice Shape Castings.

The ice shapes tested were polyurethane castings of actual ice accretions obtained at the NASA Glenn IRT facility with the GLC-305 wing model, as summarized in tables 2-1 and 2-2. For each icing condition, a set of three castings were made from the top, middle, and bottom RLEs, and these castings were glued together using epoxy to make a full span IRT ice shape casting. A total of six IRT ice castings were produced: IRT-CS10, IRT-IS10, IRT-SC5, IRT-CS2, IRT-CS22, and IRT-IPSF22, corresponding to icing conditions 1 through 6, respectively. Figures 2-25 to 2-32 show the installation of various IRT ice shape castings on the wing model. Also, figure 2-33 presents close-up views of all six IRT ice shape castings.

TABLE 2-3. ICING CONDITIONS FOR LEWICE ICE SHAPES

Icing Condition	Description	AOA** (deg)	V (mph)	T _{total} (°F)	LWC (g/m ³)	MVD (μm)	τ (min)
1 (Glaze)*	Complete Scallop Condition (ID: LS-CS10 and LR-CS10)	4	250.0	25.0	0.68	20.0	10.0
2 (Glaze)*	Incomplete Scallop Condition (ID: LS-IS10 and LR-IS10)	4	150.0	25.0	0.65	20.0	10.0
3 (Rime)*	Scaled Condition from 2D tests (ID: LS-SC5 and LR-SC5)	6	201.3	11.7	0.51	14.5	5.0
4 (Glaze)*	Complete Scallop Condition (ID: LS-CS2 and LR-CS2)	4	250.0	25.0	0.68	20.0	2.0
5 (Glaze)*	Complete Scallop Condition (ID: LS-CS22N and LR-CS22N)	4	250.0	25.0	0.68	20.0	22.5
5 (Glaze) ⁺	Complete Scallop Condition (ID: LS-CS22S and LR-CS22S)	4	250.0	25.0	0.68	20.0	22.5
6 (Glaze)*	Failed Ice Protection (ID: LS-IPSF22 and LR-IPSF22)	4	150.0	27.0	0.46	20.0	22.5

The methodology used to define the LEWICE ice shapes is discussed in section 2.2.3.

Roughness was simulated with 36-size loose grit (average roughness height is approximately 0.0211 inch or 0.5356 mm).

*Computed using airfoil sections and the component of velocity normal to the wing leading edge (see section 2.2.3).

⁺Computed using streamwise velocity and airfoil sections (see section 2.2.3).

**AOA = Angle of attack.

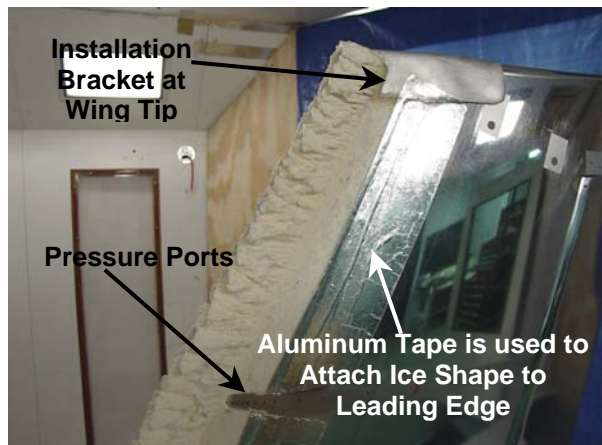


FIGURE 2-25. ICING RESEARCH TUNNEL CS10 ICE SHAPE CASTING INSTALLED ON WING—SIDE VIEW

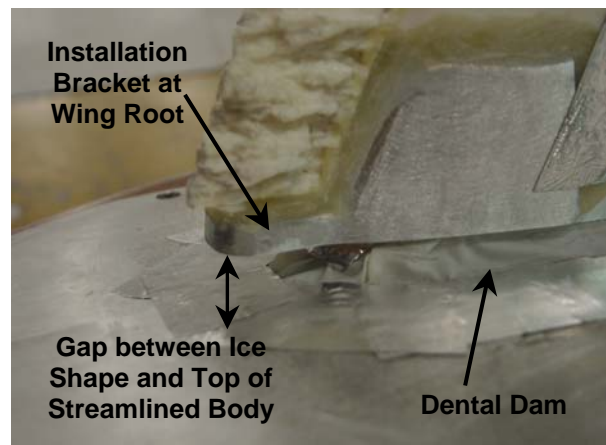


FIGURE 2-26. CLOSE-UP OF IRT-CS10 ICE SHAPE CASTING AT WING ROOT

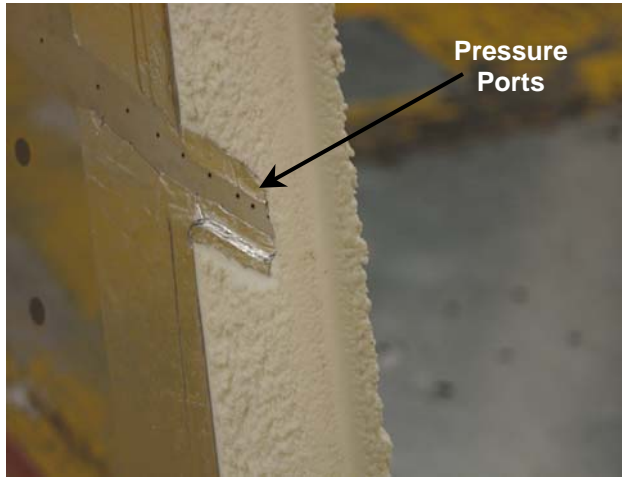


FIGURE 2-27. CLOSE-UP OF INSTALLATION OF IRT-IS10 ICE SHAPE CASTING ON WING MODEL

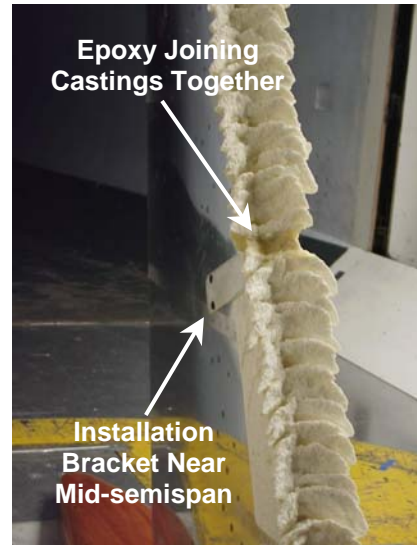


FIGURE 2-28. CLOSE-UP OF INSTALLATION OF IRT-CS22 ICE SHAPE CASTING ON WING MODEL



FIGURE 2-29. INSTALLATION OF IRT-SC5 ICE SHAPE CASTING ON WING MODEL—SIDE VIEW

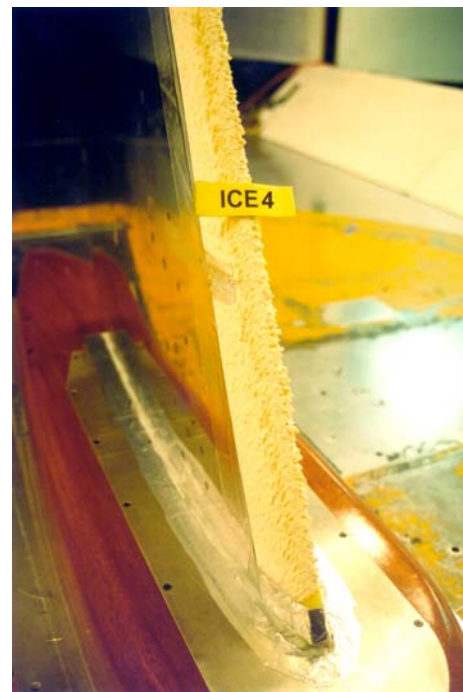


FIGURE 2-30. ICING RESEARCH TUNNEL CS2 ICE SHAPE CASTING ON TEST MODEL—FRONT VIEW



FIGURE 2-31. GLC-305 SWEPT WING WITH IRT-CS22 ICE SHAPE CASTING—FRONT VIEW



FIGURE 2-32. FRONT VIEW OF IRT-IPSF22 ICE SHAPE CASTING AT WING ROOT



(a) View of IRT ice shapes near wing tip – Tip segments



(b) View of IRT ice shapes near wing root – Root segments

FIGURE 2-33. POLYURETHANE CASTINGS OF THE SIX ICE SHAPES OBTAINED FROM ICING TESTS AT IRT

For ease of installation during testing, ice shape castings were made with cuffs that wrapped around the wing LE. The small ice shape castings were mounted to the wing using aluminum tape. The larger castings, IRT-CS10, IRT-CS22, and IRT-IPSF22, had aluminum brackets at selected spanwise locations that allowed these castings to be attached securely to the wing. This was necessary due to the considerable aerodynamic loads experienced by these large ice shapes. The leading-edge cuffs and the brackets on the IRT castings provided the additional benefit of consistent ice shape attachment to the wing during repeated installations.

2.2.3.2 Smooth LEWICE Ice Shapes.

The simulated shapes were 3D ice shapes that were defined from a series of 2D ice sections obtained with the LEWICE ice accretion code [5]. Table 2-3 summarizes all icing conditions for LEWICE analyses. The procedure used to define the 3D LEWICE ice shapes is detailed in reference 6 and is summarized below:

1. Streamwise wing sections at 0% (wing root), 15%, 50%, 85%, and 100% (wing tip) semispan were selected for the development of the LEWICE ice shapes.
2. Next, four additional wing sections were defined by taking the intersection of the wing with planes normal to the wing LE at 15%, 50%, 85%, and 100% semispan. The LE of the normal sections was at the same spanwise location as the streamwise sections defined in step 1.
3. 3D Navier-Stokes computations were performed at WSU with the clean wing. In the computations, the IRT walls were included to simulate the tunnel wall effects on the wing flow field. The geometric angles of attack (α) used in the analysis were 4° and 6° to match the angles of attack in the icing tests. Analysis pressures for streamwise sections at 15%, 50%, and 85% semispan were compared with experimental pressure distributions obtained in the IRT facility. Good correlation between experiment and analysis was demonstrated. From the computed flow fields, pressure distributions were obtained for the four wing sections normal to the wing LE defined in step 2 and for the streamwise section at the wing root.
4. 2D ice accretion analyses were conducted with the LEWICE 2.0 computer code. The computations were performed using five sections of the GLC-305 swept finite wing. These included the streamwise section at the wing root and the four sections normal to the wing LE at 15%, 50%, 85%, and 100% semispan (see step 2 above). The icing conditions for the LEWICE analysis were identical to those used in the IRT icing tests (see tables 2-1 and 2-3). However, the LEWICE angle of attack for each wing section was adjusted to match the pressure distributions from the Navier-Stokes analysis described in step 3. The velocity for the ice accretion computations conducted with the four sections defined normal to the wing leading edge was set to equal the component of the free-stream normal to the wing LE.
5. For each icing condition in table 2-3, five LEWICE ice shape sections (one streamwise and four normal to the wing leading edge) were obtained. The five ice shape sections

along with the wing geometry were imported into a computer-aided design software package and were used to define 3D LEWICE ice shapes. The 2D ice shape sections at the five spanwise locations were connected with spline surfaces and with plane surfaces. A comparison of the 3D ice shapes obtained using spline interpolation with corresponding ice shapes obtained with linear interpolation showed very small differences. Since the spline interpolation method provided a smooth transition in the spanwise direction between the five 2D sections, it was used to define the 3D LEWICE ice shapes, corresponding to icing conditions 1 to 4 (ice shapes LS-CS10, LS-IS10, LS-SC5, and LS-CS2). Straight-line interpolation was used for the remaining two ice shapes (LS-CS22N and LS-IPSF22), which were the large 22.5-min glaze ice accretions. The reason for using straight-line interpolation for LS-CS22N and LS-IPSF22 was to match the method used by some aircraft manufacturers in defining 3D LEWICE ice shapes from 2D sections.

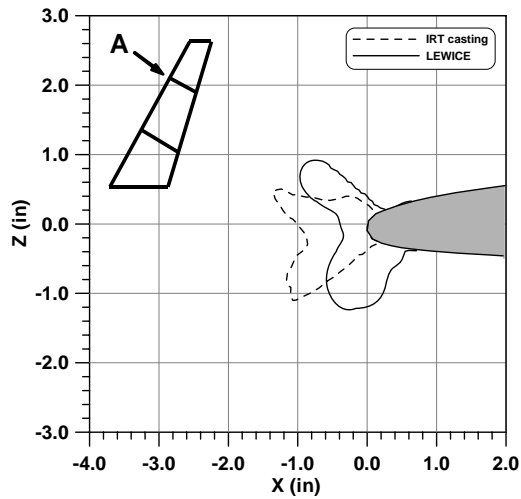
The use of airfoil sections normal to the wing LE along with the normal component of the velocity vector for the LEWICE analysis was based on input from NASA. However, some airframers prefer to use streamwise airfoil sections and the streamwise velocity in defining 3D ice shapes with the LEWICE computer code. Typically, streamwise ice accretion analyses produce ice shapes with larger horns (for glaze ice shapes) due to the higher water load resulting from the higher speed (streamwise velocity is greater than the velocity component normal to the LE). To compare the aerodynamic effects of LEWICE ice shapes based on normal and streamwise wing sections and flow velocities, one more (seventh) LEWICE ice shape was defined. This shape was obtained using the procedure discussed in steps 3 to 5 above. However, for this ice shape, streamwise wing sections at 0%, 15%, 50%, 85%, and 100% semispan were used along with the streamwise free-stream speed to define five 2D LEWICE ice shapes. The icing condition used for the seventh LEWICE ice shape (LS-CS22S) was icing condition 5 in table 2-1, which in the IRT icing tests produced a 22.5-min scalloped ice shape with large horns.

Close-up views of all LEWICE ice shapes are shown in figure 2-34. The smooth LEWICE sections and corresponding IRT ice shape tracings are compared in figures 2-35 to 2-40. Section comparisons were made at spanwise locations labeled cut A, cut B, and cut C in figure 2-5. The sections at stations A and B were taken normal to the wing leading edge. The section at station C was in the streamwise direction. Section C was at the wing root, section B was 25 inches from the root (measured along the wing leading edge), and section A was at 50 inches from the root (measured along the wing leading edge). Note that the distance from the wing root to the wing tip measured along the wing leading edge was 67.95 inches. Figures 2-35 to 2-40 demonstrate that the ice accretions had a notable twist from the tip of the wing towards the root. This was due to the geometric twist of the wing. For all ice shapes obtained at α of 4° , the wing tip section was at α_{local} of 0° , while the wing root was at $+4^\circ$. Thus, the ice on the root accreted towards the lower surface of the wing; while at the wing tip, it was almost equally distributed on both surfaces. In comparing the LEWICE sections with the tracings of the IRT ice shapes, it is important to realize that the traces do not reflect the complex 3D features of the IRT ice shapes. A comparison between the 3D LEWICE and IRT ice casting shapes for icing condition 2 is provided in figure 2-41. Figures 2-42 and 2-43 compare the profiles of LEWICE ice shapes obtained for icing condition 5 using streamwise and normal sections to the wing LE as discussed above.

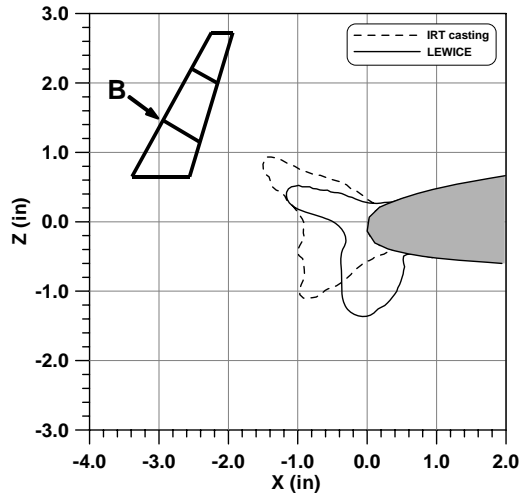
The LS-CS10, LS-IS10, LS-SC5, LS-CS2, and LS-IPSF22 ice shapes were made of aluminum, whereas the LS-CS22N and LS-CS22S ice shapes were fabricated of wood. All LEWICE ice shapes were manufactured with LE cuffs to secure and ensure proper installation onto the wing. The large ice shapes LS-CS10, LS-CS22N, LS-CS22S, and LS-IPSF22 had aluminum brackets to provide additional support and consistency during repeated installations.



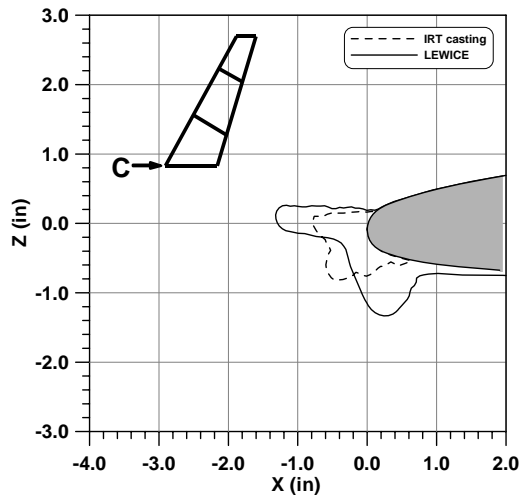
FIGURE 2-34. SMOOTH AND ROUGH LEWICE ICE SHAPES



(a) Profiles at station A (50 inches from root)

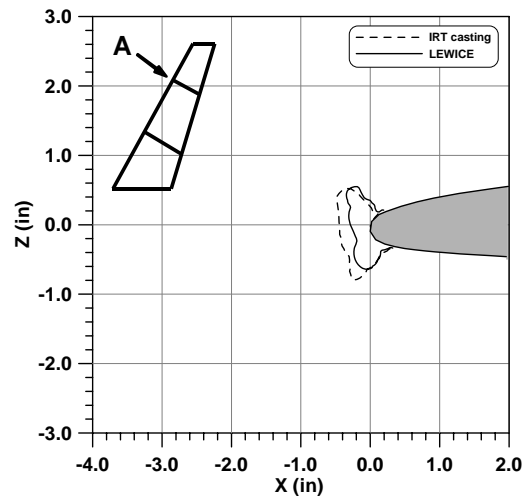


(b) Profiles at station B (25 inches from root)

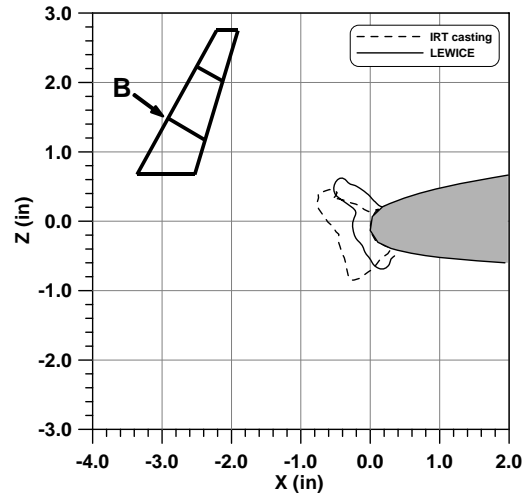


(c) Profiles at station C (wing root)

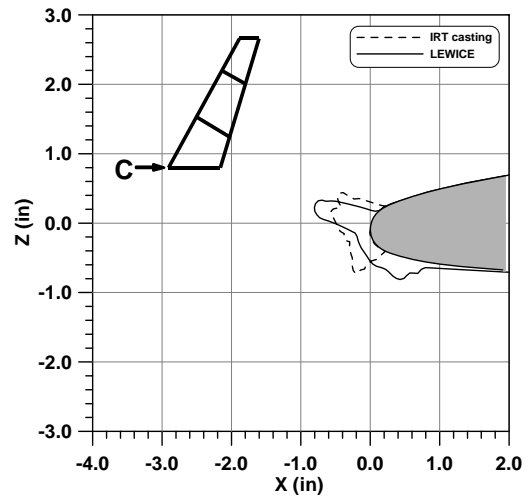
FIGURE 2-35. COMPARISON OF IRT AND LEWICE ICE SHAPES FOR ICING CONDITION 1 (CS10)



(a) Profiles at station A (50 inches from root)

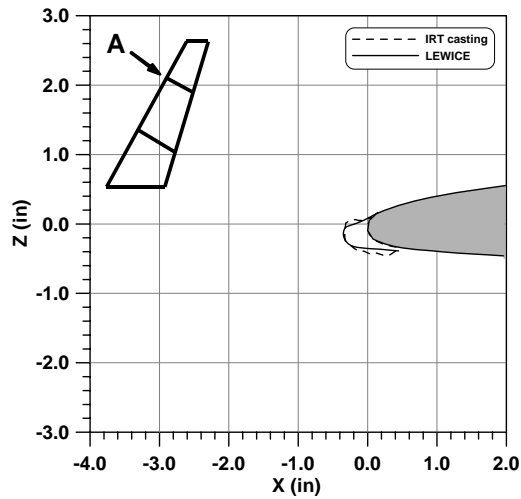


(b) Profiles at station B (25 inches from root)

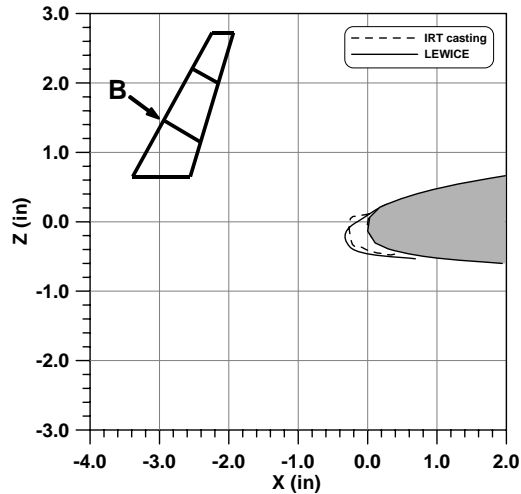


(c) Profiles at station C (wing root)

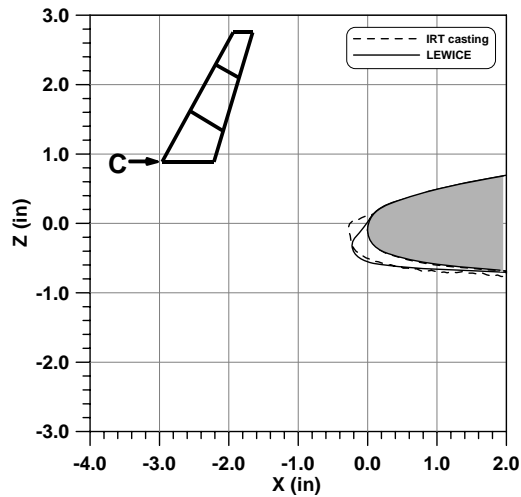
FIGURE 2-36. COMPARISON OF IRT AND LEWICE ICE SHAPES FOR ICING CONDITION 2 (IS10)



(a) Profiles at station A (50 inches from root)

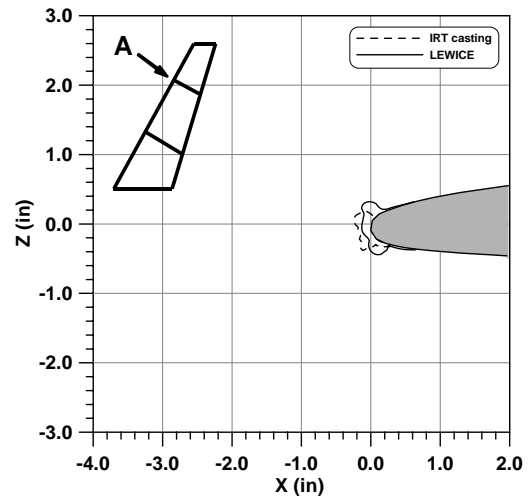


(b) Profiles at station B (25 inches from root)

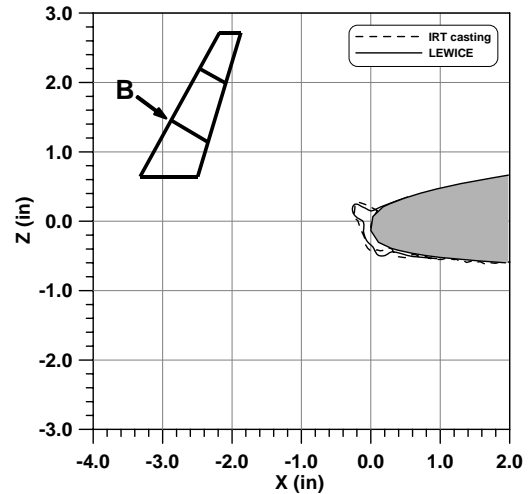


(c) Profiles at station C (wing root)

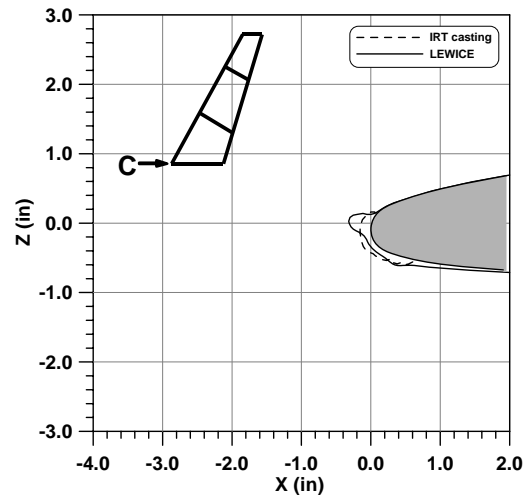
FIGURE 2-37. COMPARISON OF IRT AND LEWICE ICE SHAPES FOR ICING CONDITION 3 (SC5)



(a) Profiles at station A (50 inches from root)

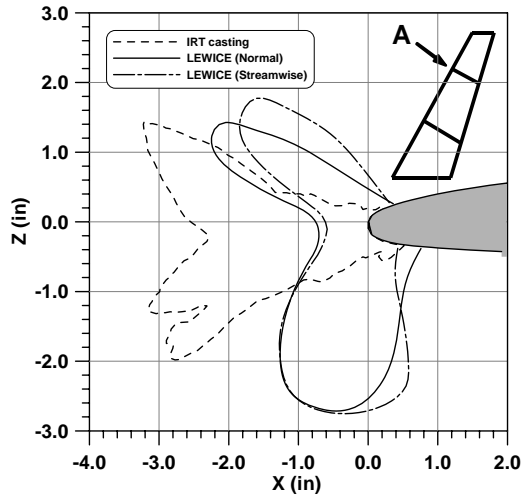


(b) Profiles at station B (25 inches from root)

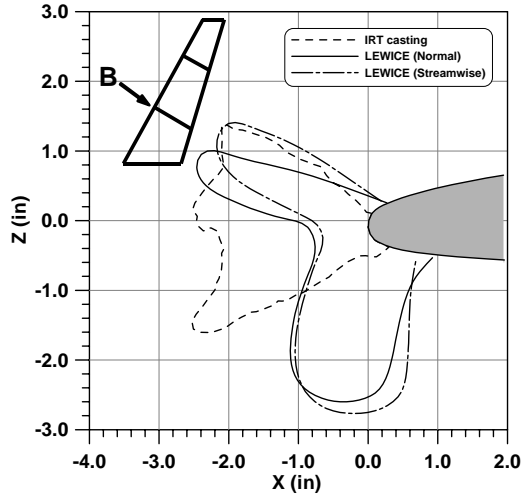


(c) Profiles at station C (wing root)

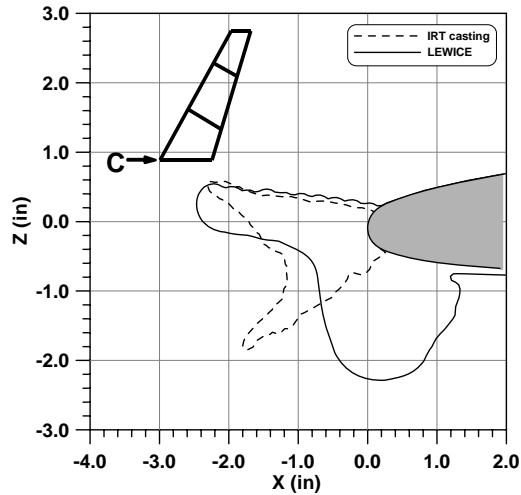
FIGURE 2-38. COMPARISON OF IRT AND LEWICE ICE SHAPES FOR ICING CONDITION 4 (CS2)



(a) Profiles at station A (50 inches from root)

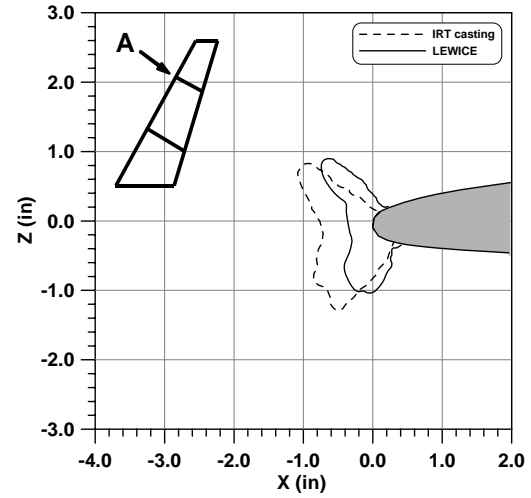


(b) Profiles at station B (25 inches from root)

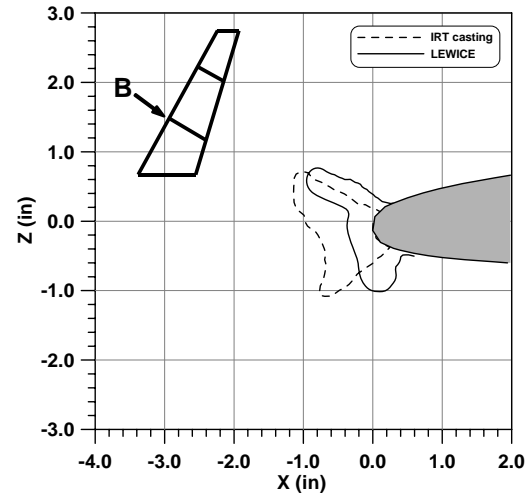


(c) Profiles at station C (wing root)

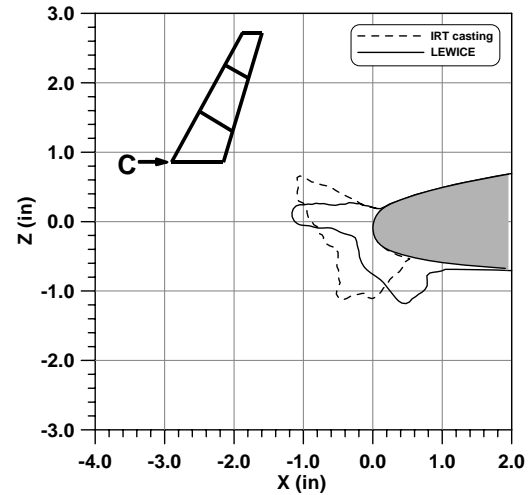
FIGURE 2-39. COMPARISON OF IRT AND LEWICE ICE SHAPES FOR ICING CONDITION 5 (CS22)



(a) Profiles at station A (50 inches from root)



(b) Profiles at station B (25 inches from root)



(c) Profiles at station C (wing root)

FIGURE 2-40. COMPARISON OF IRT AND LEWICE ICE SHAPES FOR ICING CONDITION 6 (IPSF22)

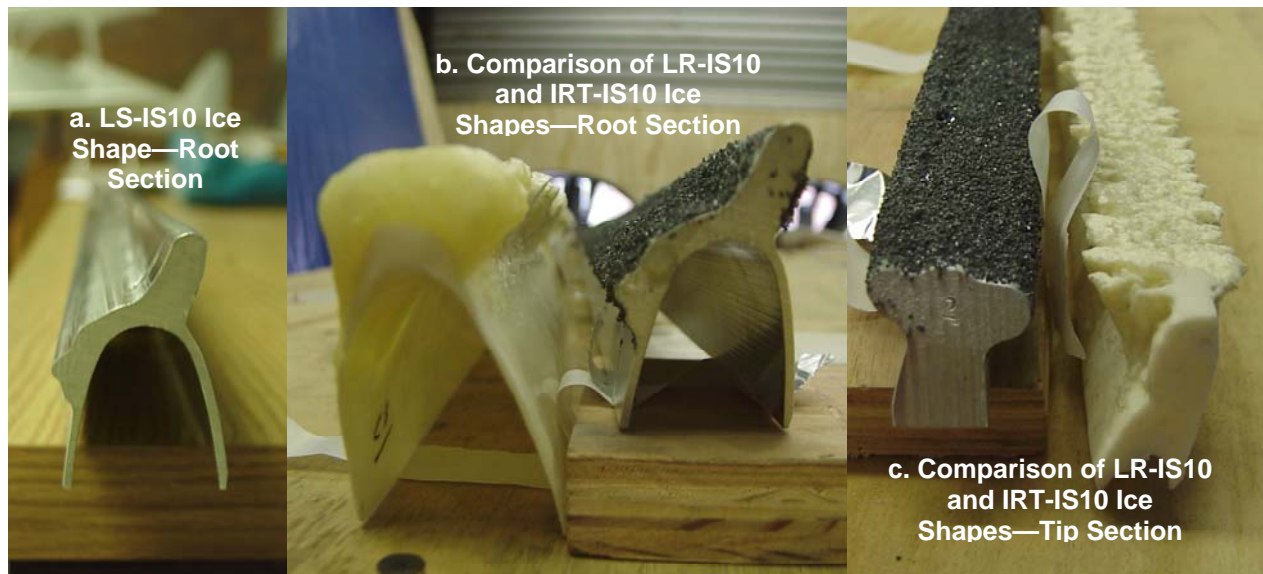


FIGURE 2-41. DETAILS OF ICE SHAPES OBTAINED FROM ICING CONDITION 2

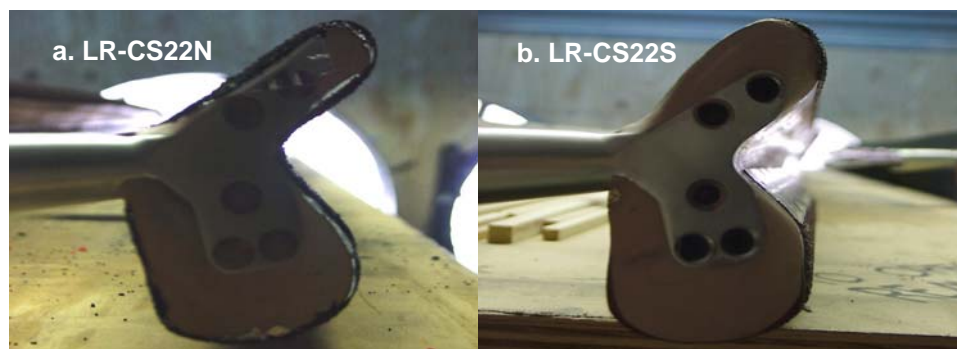


FIGURE 2-42. COMPARISON OF PROFILE OF LR-CS22N AND LR-CS22S ICE SHAPES—TIP SECTION

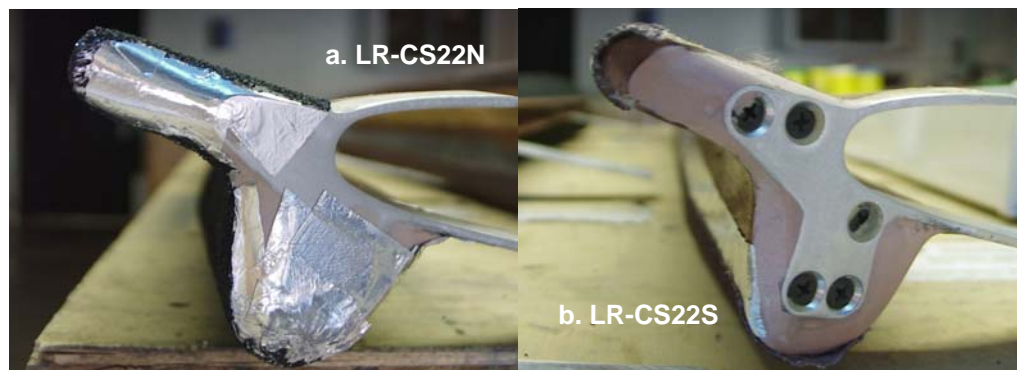


FIGURE 2-43. COMPARISON OF PROFILE OF LR-CS22N AND LR-CS22S ICE SHAPES—ROOT SECTION

2.2.3.3 Rough LEWICE Ice Shapes.

The effect of ice shape roughness was simulated by adding 36-size (average roughness height is approximately 0.0211 inches or 0.5356 mm) loose grit to the smooth LEWICE ice shapes. The roughened LEWICE (LR) ice shapes were named LR-CS10, LR-IS10, LR-SC5, LR-CS2, LR-CS22N, LR-CS22S, and LR-IPSF22. Figures 2-44 to 2-51 show the installation of LEWICE ice shapes on the wing model.



FIGURE 2-44. INSTALLATION OF LR-CS10 ROUGH LEWICE ICE SHAPE ON WING MODEL

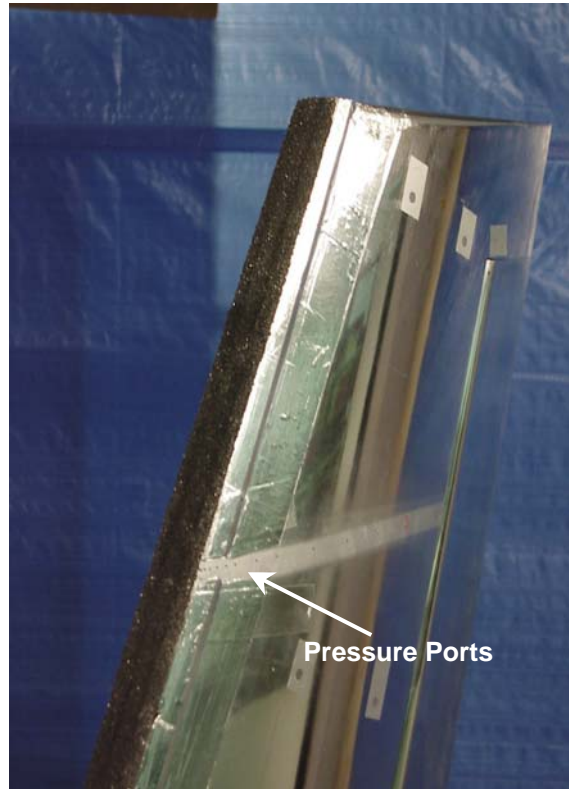


FIGURE 2-45. CLOSE-UP OF LR-IS10 ICE SHAPE AT TIP OF WING MODEL



FIGURE 2-46. INSTALLATION OF LR-CS5 ROUGH LEWICE ICE SHAPE ON WING MODEL



FIGURE 2-47. INSTALLATION OF LR-CS2 ROUGH LEWICE ICE SHAPE ON WING MODEL



FIGURE 2-48. INSTALLATION OF LS-CS22N SMOOTH LEWICE ICE SHAPE ON WING MODEL



FIGURE 2-49. INSTALLATION OF LR-CS22N ROUGH LEWICE ICE SHAPE ON WING MODEL



FIGURE 2-50. INSTALLATION OF LS-IPSF22 ICE SHAPE ON WING MODEL—SUCTION SIDE



FIGURE 2-51. INSTALLATION OF LS-IPSF22 ICE SHAPE ON WING MODEL—PRESSURE SIDE

2.2.4 Test Procedure.

The wind tunnel investigation was divided into four parts that included model installation and verification of all instrumentation, preliminary, production, and flow visualization tests.

A significant effort was directed at the start of the experimental investigation to ensure that all necessary hardware and software for the aerodynamic experiments were in proper working order. Part of this effort included a complete external balance calibration, testing of the pressure instrumentation, and calibration of the aileron torque cell and LVDT. Next, a number of preliminary wind tunnel tests were conducted with the clean wing to evaluate test repeatability, assess tunnel flow angularity, and establish data-sampling rates and sampling period. Moreover, tests were performed to check force, moment, hinge moment, and pressure instrumentation, and to evaluate the method for mounting the ice shapes onto the wing LE. During the preliminary tests, the software for acquiring and reducing experimental data were tested for accuracy using known static loads that were applied to the wing and the aileron.

The third segment of the investigation was the production runs. The first set of production runs were conducted with the clean wing using fixed and free transition. Next, tests were performed with all 20 ice shape configurations, which included six IRT ice shape castings, seven smooth LEWICE ice shapes, and seven rough LEWICE ice shapes. Conditions for the experimental investigation included AOA sweeps for ten aileron deflections, as shown in table 2-4. The Reynolds number (Re) for all the tests was fixed at 1.8 million, and it was computed using the wing MAC. For all runs, the complete set (6 components) of forces and moments for the wing were obtained. Aileron hinge moments and wing surface pressures were also recorded. A

limited Reynolds number study was also conducted with the clean and selected iced wing configurations for Re_{MAC} of 0.5, 1.0, 1.5, and 1.8 million. A complete run log for all the production runs is listed in appendix B.

TABLE 2-4. TEST CONDITIONS FOR AERODYNAMIC PERFORMANCE DATA

Reynolds number based on wing MAC (million)	1.8
Dynamic pressure, Q (psf)	50
Free-stream Mach number, M_∞	0.185
Free-stream velocity (V_∞)	225.3 ft/s, 68.7 m/s, 153.7 mph, 133.5 kts
Mach number normal to wing LE	0.16
Wing geometric α -range (deg.)	-8 to +20 by 1°
Aileron deflection, δ_A (deg.)	-15, -10, -5, -2.5, 0, 2.5, 5, 10, 15, 20

Static tares were obtained for the clean wing and for all ice shapes investigated. There was no need to obtain dynamic tares for the wing model since the model mount was not exposed to the flow, and the streamline body fairing was not connected to the external balance.

Flow angularity and wing downwash were measured for a portion of the runs. This was accomplished with two, seven-hole flow angularity probes, designed and calibrated by AEROPROBE. The seven-hole probes were installed on the clean wing at two stations corresponding to approximately 16% and 80% semispan. Seven-hole probes were selected because they can measure the three components of velocity, the total pressure, and the static pressure at a point in the flow. The seven-hole flow probes provided results with high accuracy for flow angles as high as 75° [7]. The data from the seven-hole probes were used to estimate local α near the inboard and outboard sections of the wing. The tests with the flow probes included α -sweeps for three aileron deflections (0°, -15°, and +20°). The Reynolds number in all cases was 1.8 million, based on wing MAC. Installation of the seven-hole flow probes is depicted in figures 2-52 to 2-55.

At the end of production runs, flow visualization tests were performed for selected configurations, which included all IRT castings, two smooth LEWICE ice shapes (LS-CS22S and LS-IPSF22), and all rough LEWICE ice shapes. Visualization of the clean and iced wing flow fields was accomplished using white yarn tufts attached to both surfaces of the wing model and the wing fairing. Each flow visualization run was performed at a Reynolds number of 1.5 million based on wing MAC and consisted of an α -sweep (-8° to +16°, increment of 1°) with the aileron in the neutral position. Figures 2-56 and 2-57 show example installations of yarn tufts on the clean and iced wing. Three video cameras were used to monitor the flow pattern on both surfaces of the model. One of the cameras, which was positioned outside the south wall of the tunnel, was used to capture the flow pattern on the suction (upper) surface of the wing. The other two cameras were located above the window at the tunnel ceiling and outside the tunnel's north wall. These cameras recorded the flow pattern on the pressure side of the wing. Separated flow patterns near the wing tip of an iced wing configuration are illustrated in figures 2-58 and 2-59.

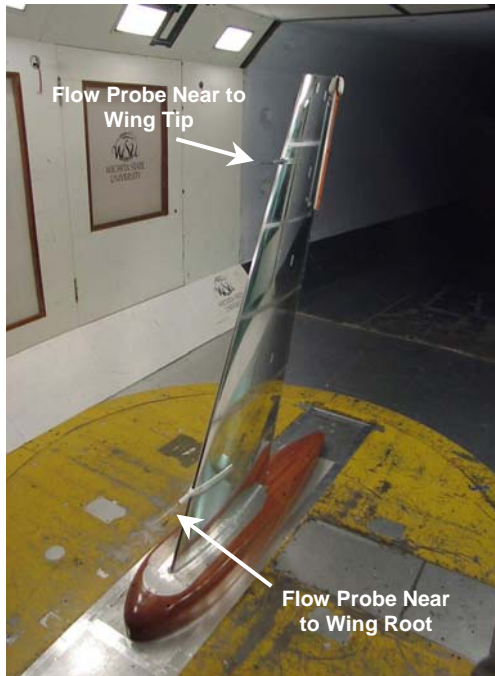


FIGURE 2-52. INSTALLATION OF SEVEN-HOLE FLOW PROBES ON WING MODEL—FRONT VIEW

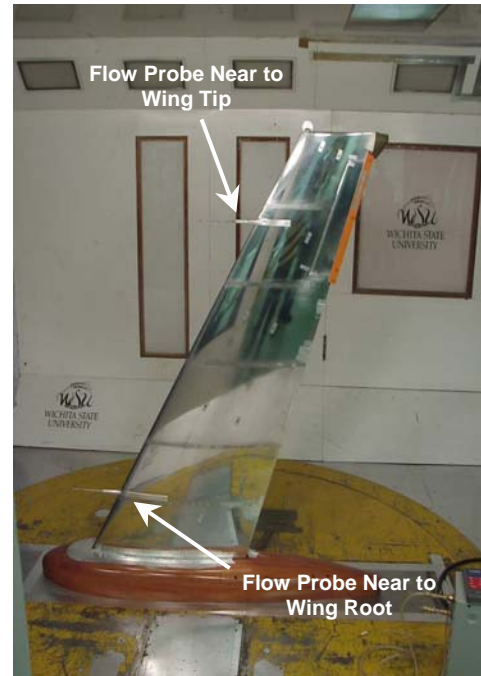


FIGURE 2-53. INSTALLATION OF SEVEN-HOLE FLOW PROBES ON WING MODEL—SIDE VIEW

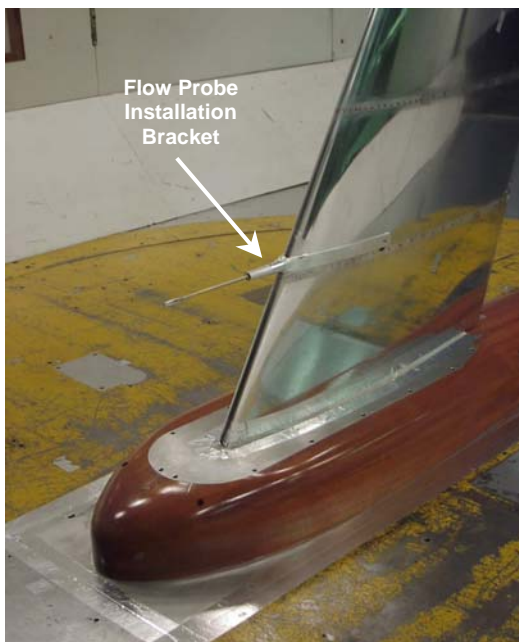


FIGURE 2-54. CLOSE-UP OF SEVEN-HOLE FLOW PROBE NEAR TO WING ROOT (16% SEMISPAN)

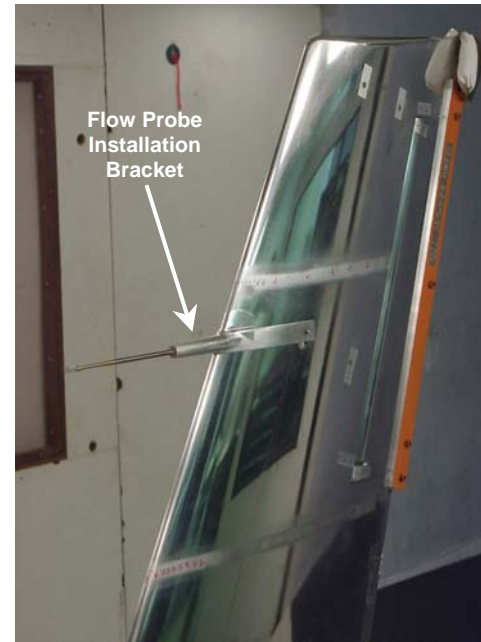


FIGURE 2-55. CLOSE-UP OF SEVEN-HOLE FLOW PROBE NEAR TO WING TIP (80% SEMISPAN)

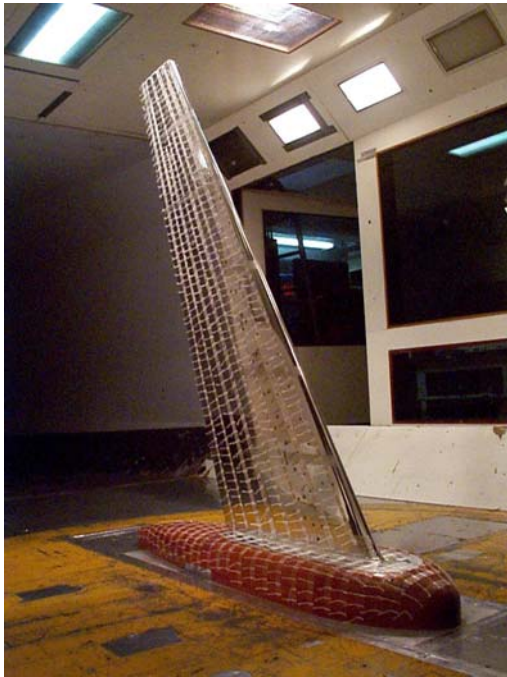


FIGURE 2-56. TUFTS INSTALLATION ON CLEAN WING AND STREAMLINED BODY—PRESSURE SURFACE

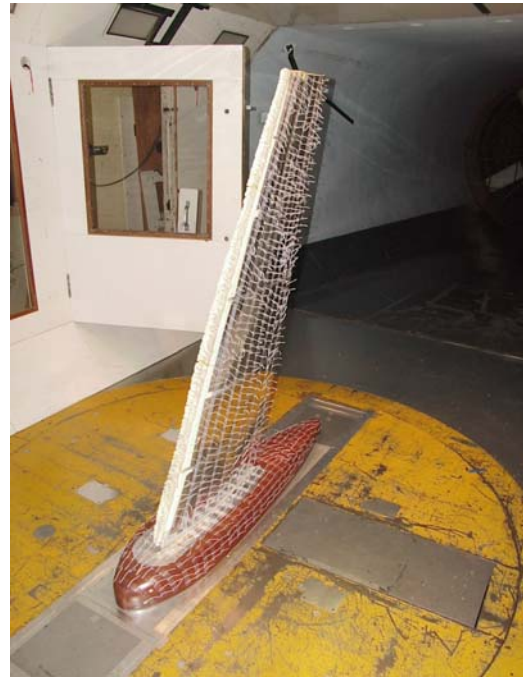


FIGURE 2-57. INSTALLATION OF YARN TUFTS ON ICED WING AND STREAMLINED BODY—SUCTION SURFACE



FIGURE 2-58. TUFTS SHOW THAT FLOW DOWNSTREAM OF ICE SHAPE WAS SEPARATED NEAR WING TIP

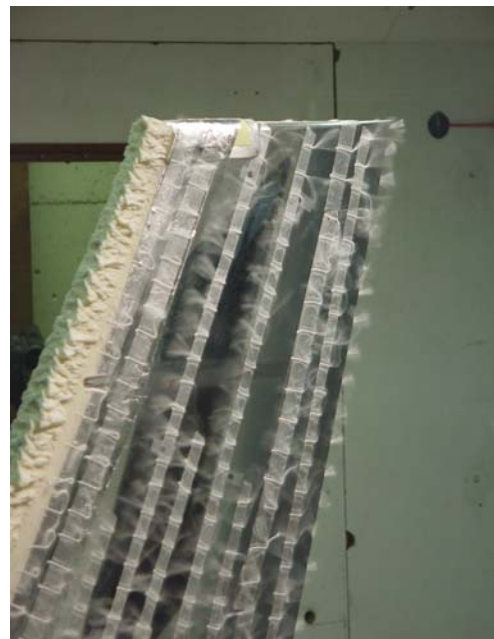


FIGURE 2-59. TUFTS SHOW COMPLETE FLOW SEPARATION AT WING TIP

2.2.5 Test Measurements.

Aerodynamic forces and moments were measured with a six-component truncated pyramid-type external balance. Aileron hinge moments were measured with a 10-in-lb temperature compensated torque sensor. The resolution of the hinge-moment torque cell was 0.005 in-lb. Force balance measurements were resolved as follows: ± 0.75 lb for lift, ± 0.3 lb for drag, and ± 0.2 ft-lb for pitching moment. The resolution of the aerodynamic coefficients obtained at a tunnel dynamic pressure of 50 psf was 0.002 for lift coefficient (C_L), 0.0008 for drag coefficient (C_D), 0.0003 for pitching-moment coefficient (C_M), and 0.0001 for hinge-moment coefficient (C_H).

Pressure measurements were obtained with a Pressure Systems Inc. 8400 Industrial System processor. Pressures were resolved to ± 0.0025 psi corresponding to a pressure coefficient (C_p) of 0.0072 for a test dynamic pressure of 50 psf.

Aerodynamic coefficients for each α were computed by taking the average of two sets of measurements. Each set consisted of 1024 data points (per channel) obtained over a time interval of 4 seconds. Thus, the value of each of the force and moment coefficients was computed by taking the average of 2048 data points per α .

3. RESULTS AND DISCUSSION.

This section discusses the characteristics of the six ice accretions obtained from the icing tests at the NASA IRT facility and selected experimental data from aerodynamic experiments conducted at the WSU wind tunnel facility. Additional information regarding the icing tests is given in reference 8.

3.1 Icing Conditions and Ice Accretions (NASA IRT).

Conditions for the IRT icing tests are summarized in table 2-1 and include five glaze conditions with ice accretion times (τ) of 2, 10, and 22.5 minutes and a 5-min rime ice case. Ice accretion characteristics for each icing condition are discussed below.

3.1.1 Icing Condition 1—Complete Scallop Condition ($\tau = 10$ min).

At this glaze icing condition, the ice accretion on the top RLE segment (figure 3-1) shows well-defined scallop tips beginning at the attachment lines. The space between the scallop tips shows some accumulation of ice. The scallop tips are covered with roughness elements. The side view of the ice accretion on the pressure side of the wing (lower surface), shown in figure 3-2, demonstrates the feather formation of the scallop tips. Figure 3-3 provides an overall view of the ice accretion obtained at the top RLE. The casting photograph in figure 3-4 shows how the ice accretion increases in size away from the tip of the wing. The ice accretions on the middle and bottom RLEs exhibited the same characteristics as the ones observed with the ice on the top RLE.



FIGURE 3-1. ICING CONDITION 1, FRONT VIEW OF ICE ACCRETION ON THE TOP RLE



FIGURE 3-2. ICING CONDITION 1, SIDE VIEW OF ICE ACCRETION ON PRESSURE SIDE OF THE TOP RLE



FIGURE 3-3. ICING CONDITION 1, FRONT VIEW OF THE COMPLETE ICE ACCRETION ON THE TOP RLE

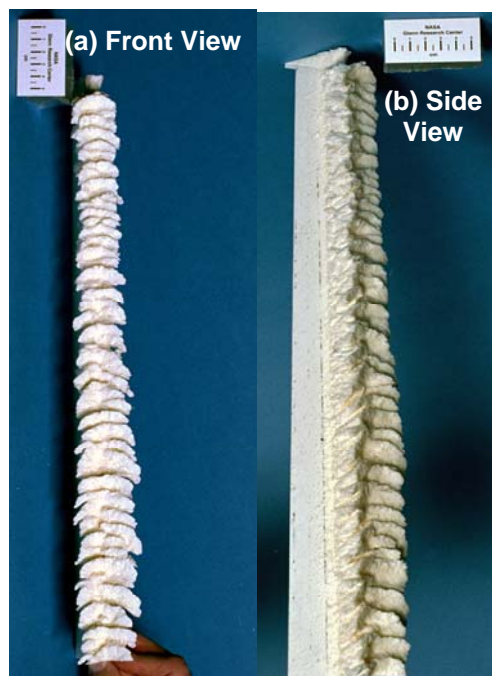


FIGURE 3-4. ICING CONDITION 1, CASTING FROM THE ICE ACCRETION ON THE TOP RLE

3.1.2 Icing Condition 2—Incomplete Scallop Condition ($\tau = 10$ min).

For this glaze icing condition, which is typical of an incomplete scallop case, the ice shape on the bottom RLE, shown in figure 3-5, exhibits scallop tips beginning at some distance from the attachment line. The side view of the ice accretion on the suction side of the bottom RLE segment is presented in figure 3-6 and shows the scallop tips and their feather structure. The ice accretions on the top and middle leading-edge segments exhibited the same characteristics. Figure 3-7 presents an overall view of the ice accretion on the bottom RLE, while figure 3-8 shows front and side views of the ice casting for this wing segment. The side view in figure 3-8 demonstrates the ice shape characteristics on the pressure side of the bottom RLE segment of the wing.

3.1.3 Icing Condition 3—Scaled Condition ($\tau = 5$ min).

This condition was obtained by scaling a reference icing condition [9] tested with a 2D 36-in. chord GLC-305 wing model. The icing condition for the 2D wing was $\alpha = 6^\circ$, $V_\infty = 201.3$ mph, $T_{\text{total}} = 11.7^\circ\text{F}$, $\text{LWC} = 0.40 \text{ g/m}^3$, $\text{MVD} = 20 \text{ }\mu\text{m}$, and $\tau = 16.7$ minutes. Aerodynamic tests with the 2D airfoil and the ice shape obtained with the reference icing condition were conducted in the Low-Turbulence Pressure Tunnel (LTPT) at NASA Langley Research Center [10]. Comparison of the aerodynamic performance data from the LTPT tests with corresponding results from the WSU finite wing tests using the scaled ice shape will help evaluate differences between 2D and 3D iced wing aerodynamics.



FIGURE 3-5. ICING CONDITION 2, FRONT VIEW OF ICE ACCRETION ON THE BOTTOM RLE

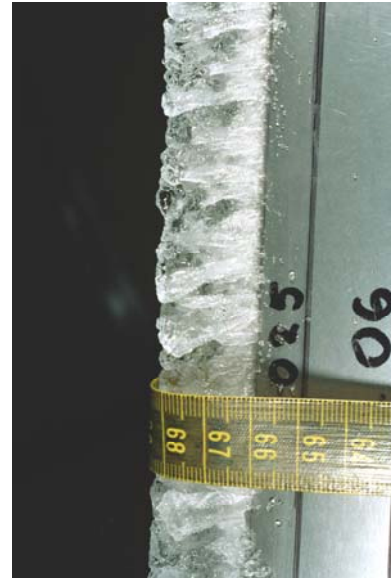


FIGURE 3-6. ICING CONDITION 2, SIDE VIEW OF ICE ACCRETION ON SUCTION SIDE OF THE BOTTOM RLE

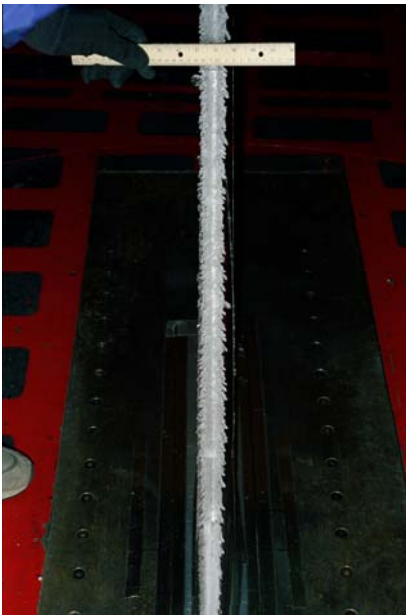


FIGURE 3-7. ICING CONDITION 2, FRONT VIEW OF THE COMPLETE ICE ACCRETION ON THE BOTTOM RLE

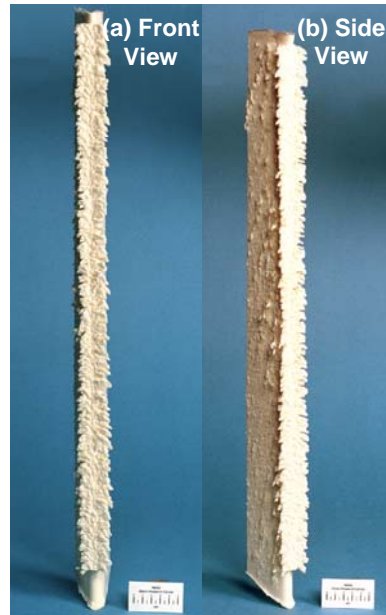


FIGURE 3-8. ICING CONDITION 2, CASTING FROM THE ICE ACCRETION ON THE BOTTOM RLE

The ice accretion presented in figure 3-9 is a no-scallop case. The side view of the ice accretion on the pressure side of the wing, depicted in figure 3-10, shows a feather structure. The ice around the attachment line is smooth with a pointed shape and a whitish color. This indicates that the ice accretion is of the rime type. Figure 3-11 shows an overall view of the ice accretion

obtained on the bottom RLE. Figure 3-12 shows a front and side view of the casting from the ice accretion on the bottom RLE. The side view corresponds to the suction side of the wing. The ice on the top, middle, and bottom RLEs show the same characteristics.

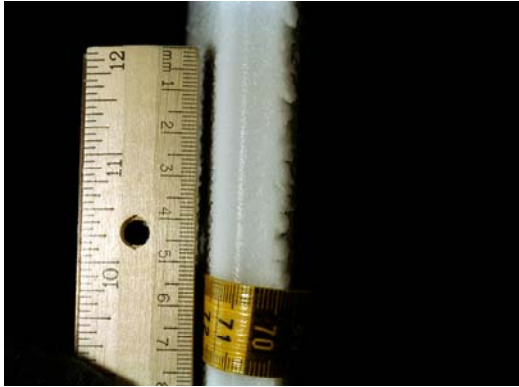


FIGURE 3-9. ICING CONDITION 3, FRONT VIEW OF ICE ACCRETION ON THE BOTTOM RLE



FIGURE 3-10. ICING CONDITION 3, SIDE VIEW OF ICE ACCRETION ON SUCTION SIDE OF THE BOTTOM RLE



FIGURE 3-11. ICING CONDITION 3, FRONT VIEW OF THE COMPLETE ICE ACCRETION ON THE BOTTOM RLE

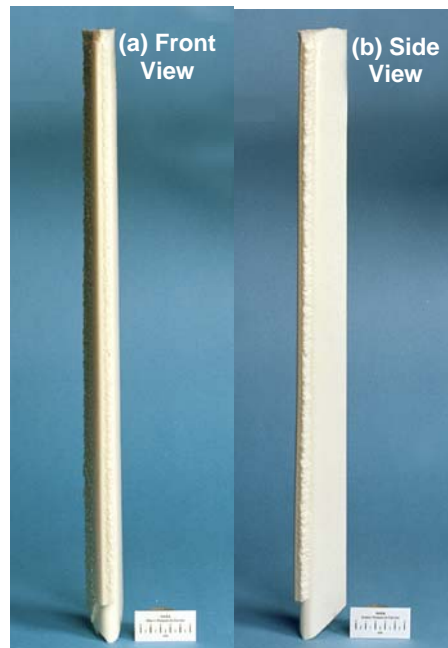


FIGURE 3-12. ICING CONDITION 3, CASTING FROM THE ICE ACCRETION ON THE BOTTOM RLE

3.1.4 Icing Condition 4—Complete Scallop Condition ($\tau = 2$ min).

This icing condition was chosen to obtain an ice shape for a complete scallop case at a short ice accretion time. The only difference between this condition and icing conditions 1 and 5 was the duration of the ice accretion time: 2 minutes versus 10 and 22.5 minutes, respectively. The ice accretion in figure 3-13 shows the presence of scallop tip. The scallop tips on the suction side of the wing were more developed than on the pressure side. Figure 3-14 shows the ice accretion scallop tips and their feather formation on the suction side of the wing. Figure 3-15 provides an overall view of the ice accretion obtained over the middle RLE. Figure 3-16 shows the front and side views of the ice casting from the ice accretion on the middle RLE. The side view of the ice casting corresponds to the suction side of the wing.



FIGURE 3-13. ICING CONDITION 4, FRONT VIEW OF ICE ACCRETION ON THE MIDDLE RLE



FIGURE 3-14. ICING CONDITION 4, SIDE VIEW OF ICE ACCRETION ON SUCTION SIDE OF THE MIDDLE RLE



FIGURE 3-15. ICING CONDITION 4, FRONT VIEW OF THE COMPLETE ICE ACCRETION ON THE MIDDLE RLE

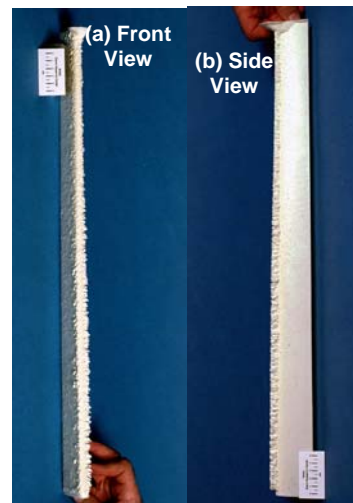


FIGURE 3-16. ICING CONDITION 4, CASTING FROM THE ICE ACCRETION ON THE MIDDLE RLE

3.1.5 Icing Condition 5—Complete Scallop Condition ($\tau = 22.5$ min).

This icing case was selected to obtain a complete scallop ice shape for a long ice accretion time. In general, the ice shape in figure 3-17 had similar characteristics as icing condition 1 but its size was considerably larger. Figure 3-18 shows a side view of the ice accretion on the suction side of the wing that demonstrates the ice shape scallop tips and their feather structure. Figure 3-19 shows an overall view of the ice accretion obtained over the middle RLE. Figure 3-20 provides front and side views of the casting from the ice accretion on the middle RLE. The side view is of the wing pressure side.

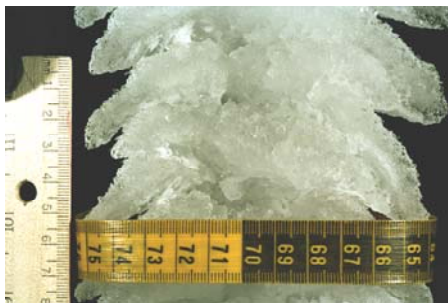


FIGURE 3-17. ICING CONDITION 5, FRONT VIEW OF ICE ACCRETION ON THE MIDDLE RLE



FIGURE 3-18. ICING CONDITION 5, SIDE VIEW OF ICE ACCRETION ON SUCTION SIDE OF THE MIDDLE RLE



FIGURE 3-19. ICING CONDITION 5, FRONT VIEW OF THE COMPLETE ICE ACCRETION ON THE MIDDLE RLE



FIGURE 3-20. ICING CONDITION 5, CASTING FROM THE ICE ACCRETION ON THE MIDDLE RLE

When this icing condition was run with the wing model in the high position, a piece of the ice accretion was consistently shed off the wing. For this reason, the velocity for icing condition 5 was reduced to 225 mph with the wing in the high position. To maintain the same water mass flux as in the case at 250 mph, the LWC was increased to 0.89 g/m^3 . Photographic data from the ice accretion at 250 mph and the one obtained at 225 mph indicated that the two ice accretions were very close in overall characteristics. The ice castings made from the ice accretion obtained at 225 mph and 0.89 g/m^3 were the middle and bottom RLEs. The ice casting for the top RLE segment was obtained from the ice accretion tests conducted at a speed of 250 mph and LWC of 0.68 g/m^3 .

Icing conditions 1, 4, and 5 were selected to investigate the stages in the evolution of complete scallop ice shapes obtained with progressively longer time and the aerodynamic performance effects of these ice shapes.

3.1.6 Icing Condition 6—IPS Failure Condition ($\tau = 22.5 \text{ min}$).

This condition was chosen to be within the FAA Title 14 Code of Federal Regulation Part 25 Appendix C envelopes [11] to provide an ice shape that was representative of an ice protection system failure case. The ice accretion depicted in figure 3-21 exhibited scallop tips, which were not well defined. The scallop formation appears to have started away from the attachment line, although this is not certain because glaze ice covered the area around the attachment line. In addition, the ice was not transparent enough to allow determination of the presence of feathers around the attachment line area. A side view of the ice accretion (figure 3-22) shows the scallop tips formed by the glaze ice feathers. Figure 3-23 provides an overall view of the ice accretion obtained on the top RLE. A significant accumulation of ice on the wing tip was observed, and in general, the ice accretion was not uniform, as shown in figure 2-33. Over the leading edges of the bottom and middle removable segments, the glaze ice accretion exhibited indistinct scallop tips, and glaze ice covered the attachment line area. Figure 3-24 shows front and side views of the casting obtained from the ice accretion on the top RLE. The side view corresponds to the wing suction side (upper surface).



FIGURE 3-21. ICING CONDITION 6,
FRONT VIEW OF ICE ACCRETION ON
THE TOP RLE



FIGURE 3-22. ICING CONDITION 6,
SIDE VIEW OF ICE ACCRETION ON
PRESSURE SIDE OF THE TOP RLE



FIGURE 3-23. ICING CONDITION 6, FRONT VIEW OF THE COMPLETE ICE ACCRETION ON THE TOP RLE



FIGURE 3-24. ICING CONDITION 6, CASTING FROM THE ICE ACCRETION ON THE TOP RLE

3.2 AERODYNAMIC PERFORMANCE STUDIES.

Experimental lift, drag, pitching-moment, hinge-moment, and surface pressure coefficients for the clean and iced wing of selected test cases are presented in this section. All aerodynamic coefficients have been corrected for tunnel wall effects using the procedure discussed in reference 12. Pressure coefficients were computed using the corrected tunnel dynamic pressure. No other corrections were applied to the pressure data. Note that in all cases, the angles of attack in the figures are the geometric angles of attack and have not been corrected for upwash or downwash effects.

Pitching-moment measurements were resolved to the quarter-chord location of the mean aerodynamic chord. By convention, nose-up pitching moment is considered positive, as illustrated in figure 3-25.

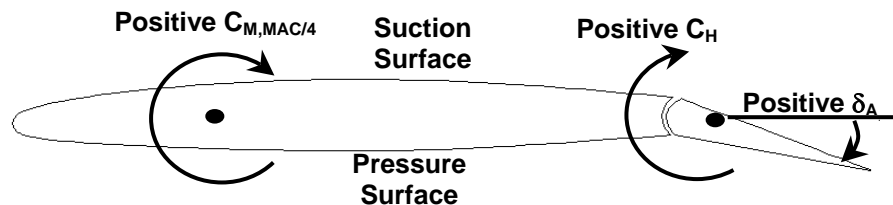


FIGURE 3-25. NOTATION FOR PITCHING MOMENT, HINGE MOMENT, AND AILERON DEFLECTION ANGLE

Aileron hinge-moment coefficients were obtained from the following formula:

$$C_H = \frac{Hm}{0.5 \cdot \rho \cdot V_\infty^2 \cdot S_a \cdot c_a} \quad (3-1)$$

where Hm is the hinge-moment and S_a and c_a are the aileron planform area and the aileron mean chord behind the hinge line respectively. (The values for S_a and c_a are provided in figure 2-3.) The sign convention for C_H is positive for hinge moments causing the aileron trailing edge to move down. Aileron deflections corresponding to trailing edge down are also considered positive. Figure 3-25 depicts the sign convention for C_H and δ_A .

In the following discussion, the hinge-moment curve is divided into three regions (A, B, and C), corresponding to the linear, near-stall, and poststall ranges of the lift curve, as shown in figure 3-26. Typically, in region A, the decrease of C_H was linear, small and gradual, while in region B, the growth was much greater due to increasing flow separation over the control surface. Note the anomaly or break from region A to region B with increase C_L and the differences between the clean and iced configurations. In region C, the hinge moment remained nearly constant, since beyond stall the pressure distribution over the aileron upper surface did not vary significantly for positive α .

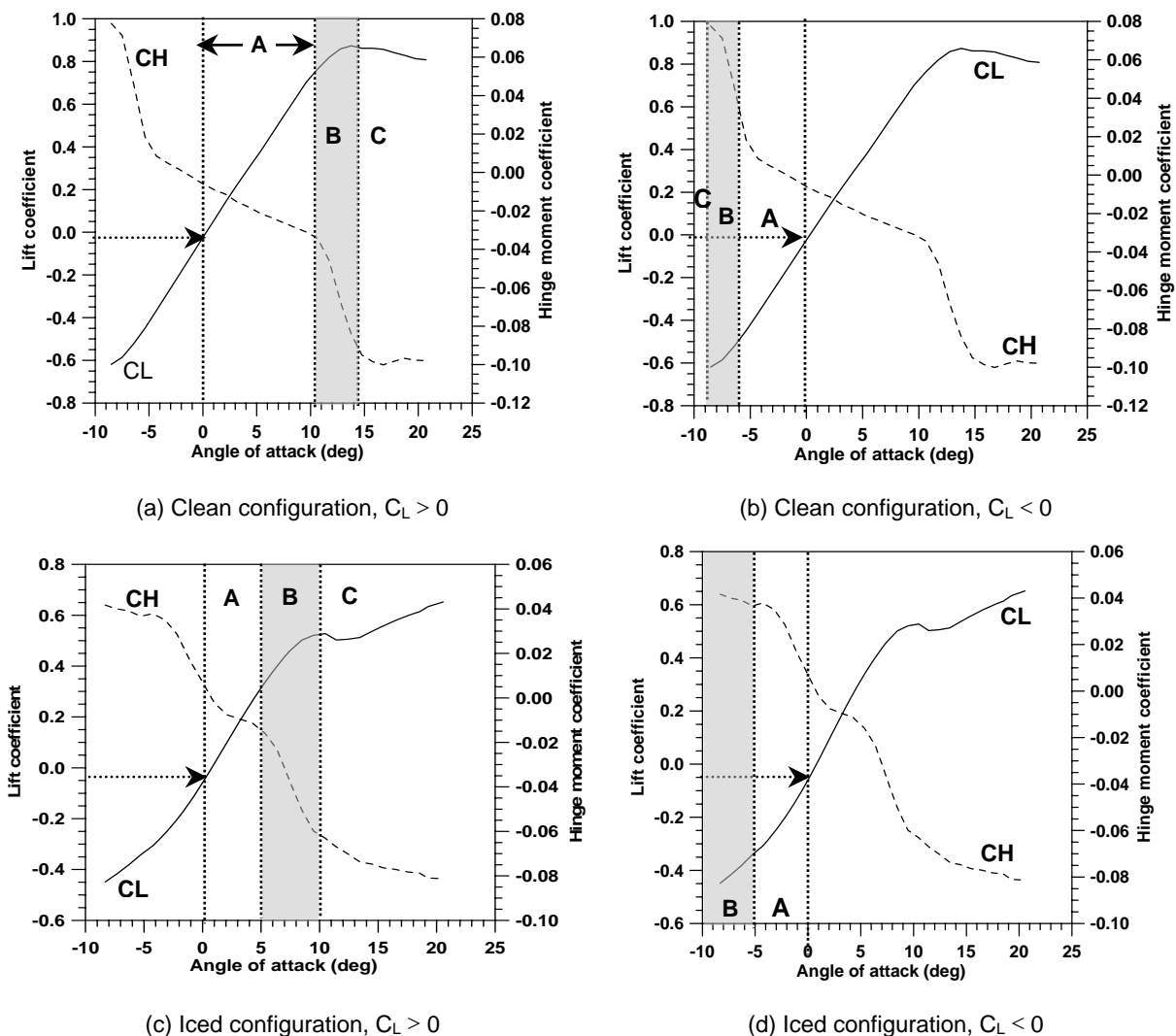


FIGURE 3-26. REGIONS A, B, AND C FOR HINGE-MOMENT CURVE OF CLEAN AND ICED CONFIGURATIONS

All pressure data are presented in the form of C_p versus chordwise distance (x/c). In all cases, negative C_p coefficients corresponding to the suction side (upper surface) of the wing are plotted upward.

3.2.1 Data Quality and Repeatability.

The WSU wind tunnel facility has been used for commercial and research testing over the years. Facility personnel have considerable expertise in wind tunnel testing, instrumentation, data acquisition, and data processing. To obtain quality data, careful planning and well thought out test were implemented during the aerodynamic investigation as discussed below.

- An analysis was performed to determine instrumentation sensitivity needed to provide the required resolution of force, moment, and pressure coefficients for the primary test condition, which was α -sweeps at Reynolds number based on MAC of 1.8 million.
- Prior to WSU wind tunnel entry, a complete external balance calibration was performed. Instrumentation such as pressure transducers, torque tubes, load cells, flow probes, and model hardware were checked to ensure proper operation and accuracy.
- The repeatability of the experimental data is a function of instrumentation, data-sampling rates, flow quality, flow unsteadiness, and model setup procedures. To verify the repeatability of the experimental setup, tests with the baseline configuration were repeated, and the results were compared. Repeatability of lift, drag, pitching-moment, and hinge-moment coefficients are provided in figure 3-27. Also, figures 3-28 to 3-30 show pressure distributions of 15%, 50%, and 85% semispan locations at α of -4° , 0° , 4° , 8° , 12° , and 16° . The maximum average percentage difference of aerodynamic coefficients from individual test runs from the average of all test repeats was 1% for C_L , 2% for C_D , 1% for C_H , and 3% for C_p . Most of the variation occurring near wing stall was due to flow field unsteadiness and small amplitude model vibration.
- At regular intervals during the wind tunnel tests, the balance, the hinge-moment system, and the pressure transducers were tested with known inputs to verify that they were working properly. For the balance tests, known forces were applied to the model, and force and moment data were obtained for a complete α -sweep at zero airspeed. Figures 3-31 and 3-32 show the setup for balance and hinge-moment system checking.
- To ensure repeatability in the installation of the ice shape tested, all ice shapes were attached to cuffs designed to fit the wing LE. For the large ice shapes, brackets were also installed at selected spanwise locations to provide additional support and minimize deflections due to the aerodynamic loads.
- Preliminary tests were conducted with all models prior to the start of the production runs to verify tunnel and model instrumentation and data acquisition hardware and software. Static tares were obtained for all ice shapes to account for the weight effects of each ice shape on the aerodynamic measurements.

- A limited number of tests were conducted prior to the production runs to investigate data-sampling periods, as shown in figure 3-33. All the force and moment coefficients obtained from wind tunnel tests are average values based on multiple measurements over a period of time. Sampling rate and sampling time depend on tunnel facility, test model, and airspeed, and are usually established experimentally for each tunnel facility. For the WSU tests, 1024 readings were taken per α for each force and moment coefficient. The sampling time was 4 seconds. For a dynamic pressure of 50 psf, the airspeed in the WSU wind tunnel was approximately 222 ft/s. Given that the MAC of the wing is 1.56 ft, 1 second of data acquisition was equivalent to averaging the flow over the model 142 times. In 1 second, the air had traversed a distance equal to 142 chord lengths.
- All tests were conducted at constant Reynolds number, i.e., the speed of the tunnel was adjusted to maintain constant Re_{MAC} .

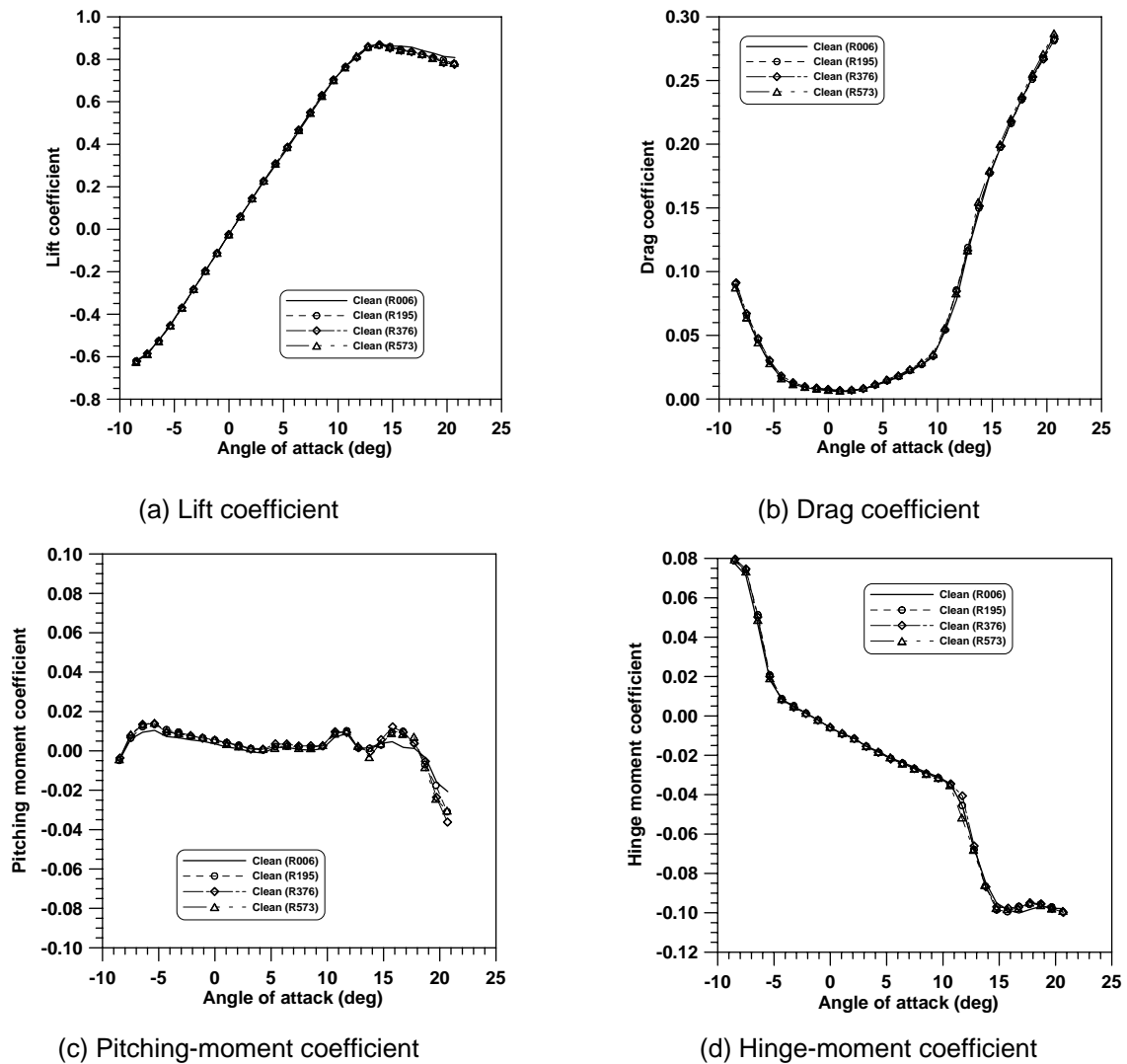
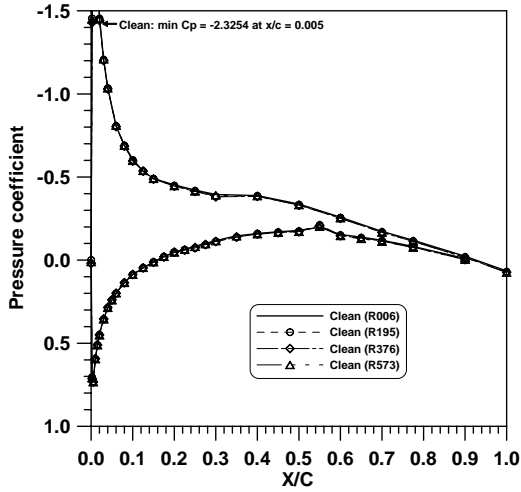
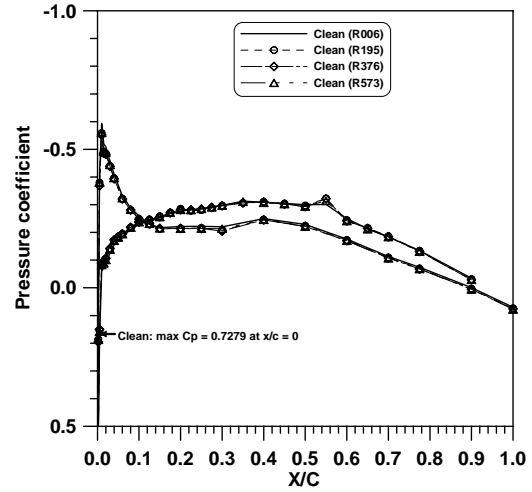


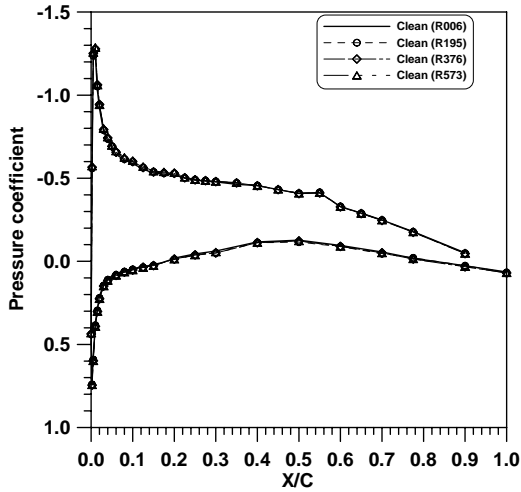
FIGURE 3-27. REPEATABILITY OF C_L , C_D , C_M , AND C_H ; CLEAN CONFIGURATION;
 $Re = 1.8 \times 10^6$; $\delta_A = 0^\circ$



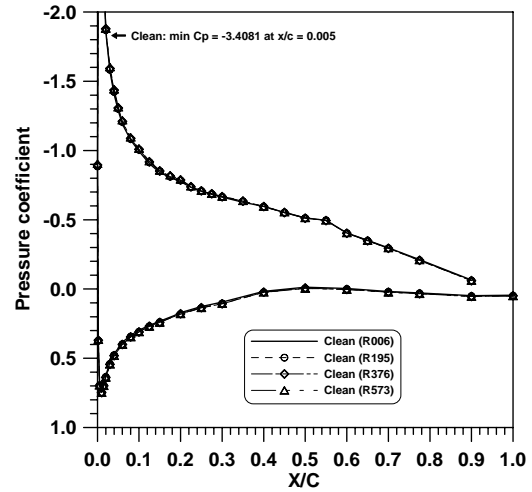
(a) C_p vs x/c ($\alpha = -4^\circ$)



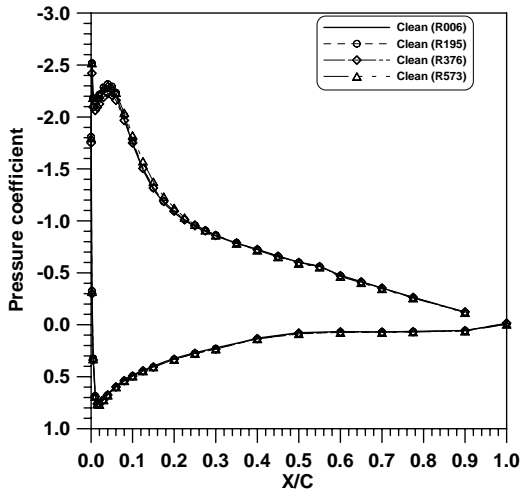
(b) C_p vs x/c ($\alpha = 0^\circ$)



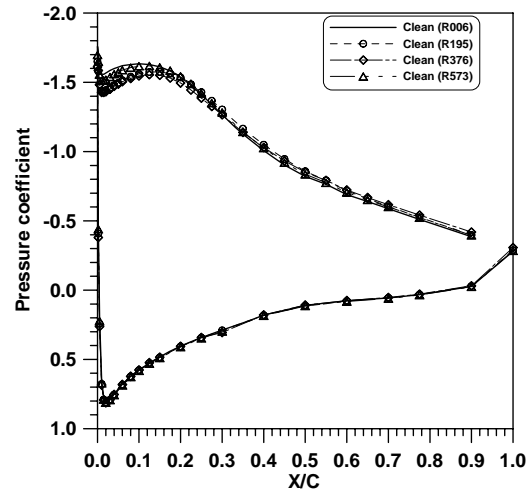
(c) C_p vs x/c ($\alpha = 4^\circ$)



(d) C_p vs x/c ($\alpha = 8^\circ$)

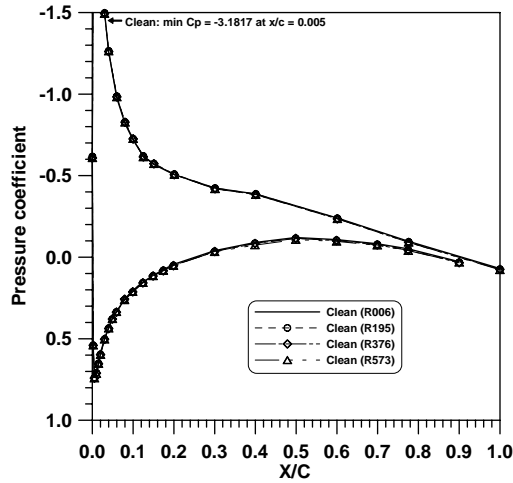


(e) C_p vs x/c ($\alpha = 12^\circ$)

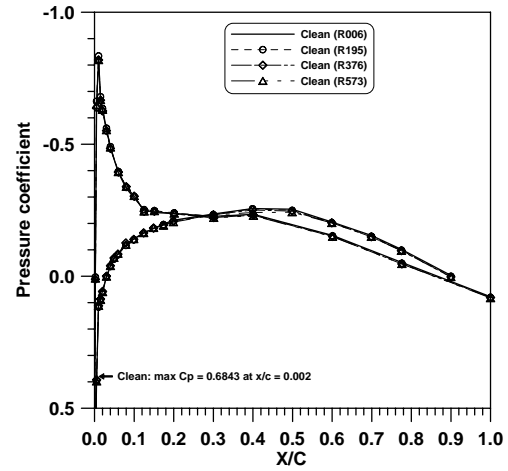


(f) C_p vs x/c ($\alpha = 16^\circ$)

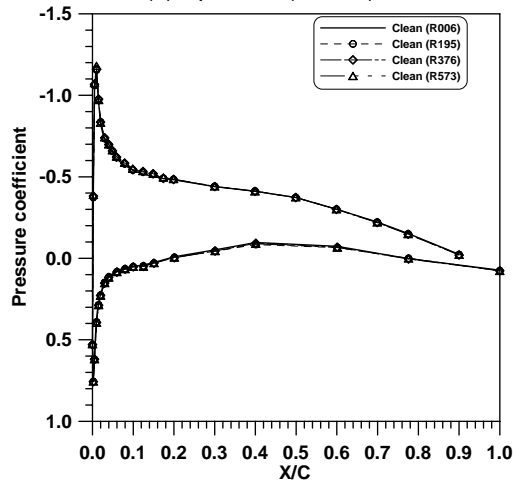
FIGURE 3-28. REPEATABILITY OF PRESSURE DISTRIBUTIONS AT 15% SEMISPAN; CLEAN CONFIGURATION; $Re = 1.8 \times 10^6$; $\delta_A = 0^\circ$



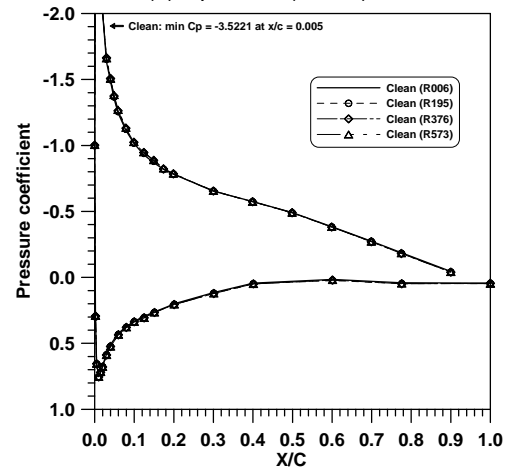
(a) C_p vs x/c ($\alpha = -4^\circ$)



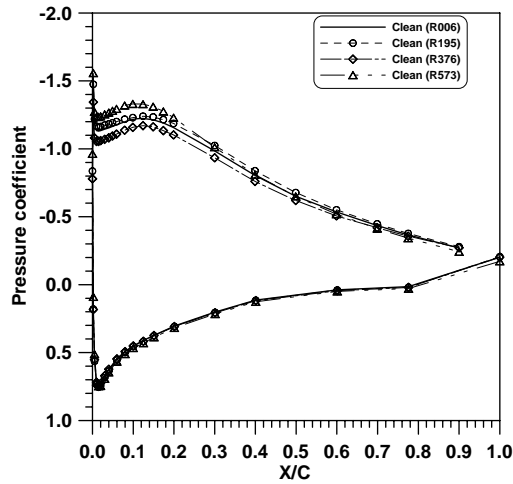
(b) C_p vs x/c ($\alpha = 0^\circ$)



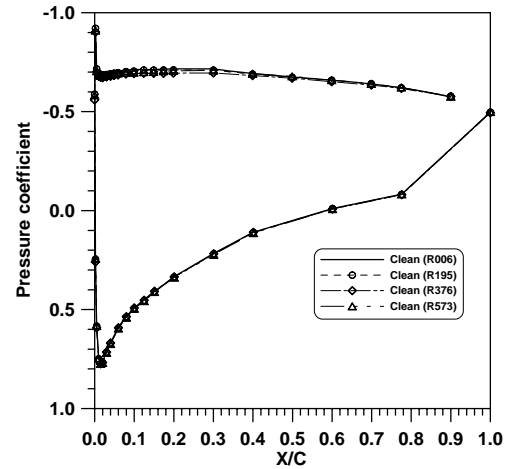
(c) C_p vs x/c ($\alpha = 4^\circ$)



(d) C_p vs x/c ($\alpha = 8^\circ$)

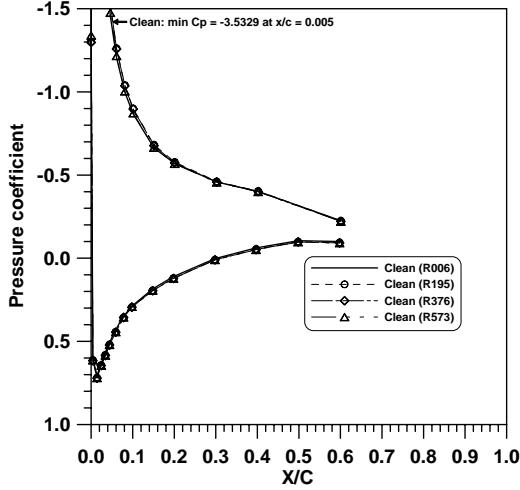


(e) C_p vs x/c ($\alpha = 12^\circ$)

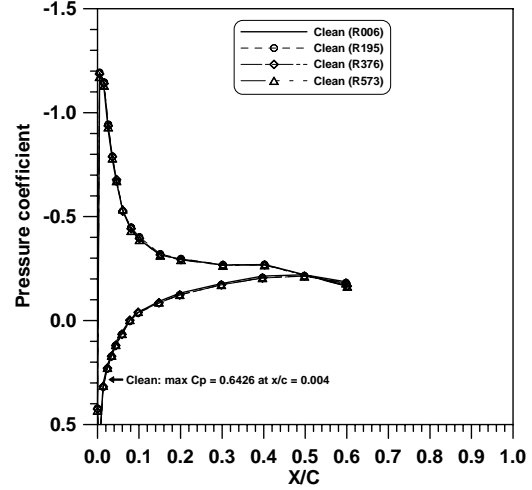


(f) C_p vs x/c ($\alpha = 16^\circ$)

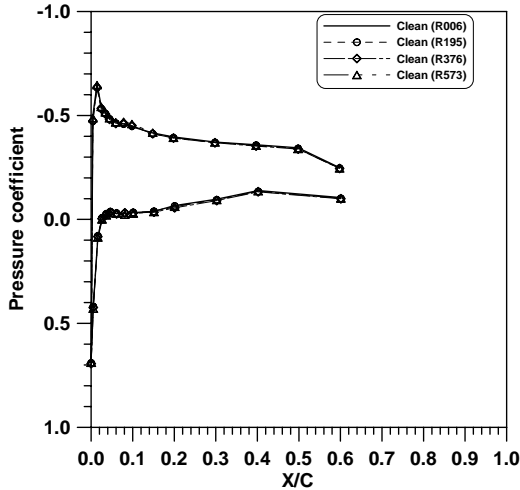
FIGURE 3-29. REPEATABILITY OF PRESSURE DISTRIBUTIONS AT 50% SEMISPAN; CLEAN CONFIGURATION; $Re = 1.8 \times 10^6$; $\delta_A = 0^\circ$



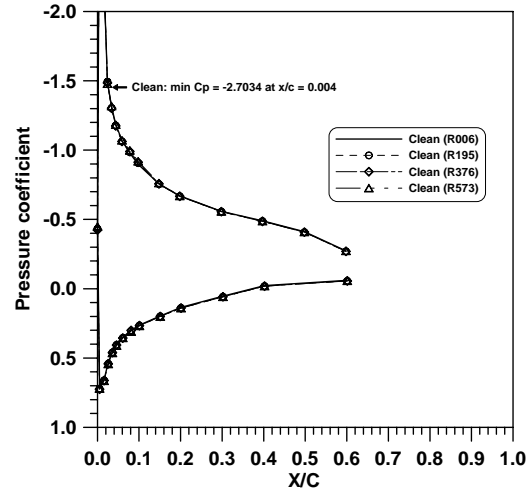
(a) C_p vs x/c ($\alpha = -4^\circ$)



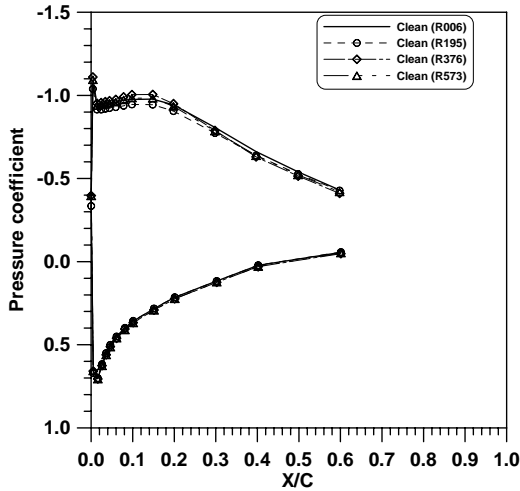
(b) C_p vs x/c ($\alpha = 0^\circ$)



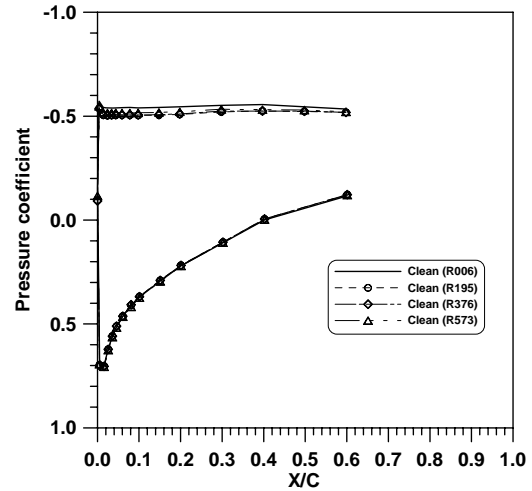
(c) C_p vs x/c ($\alpha = 4^\circ$)



(d) C_p vs x/c ($\alpha = 8^\circ$)

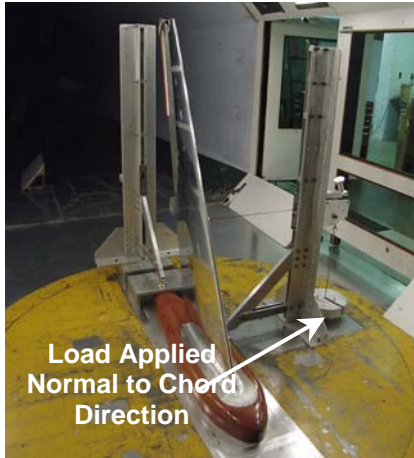


(e) C_p vs x/c ($\alpha = 12^\circ$)



(f) C_p vs x/c ($\alpha = 16^\circ$)

FIGURE 3-30. REPEATABILITY OF PRESSURE DISTRIBUTIONS AT 85% SEMISPAN;
CLEAN CONFIGURATION; $Re = 1.8 \times 10^6$; $\delta_A = 0^\circ$



(a) Front view of balance check setup



(a) Rear view of hinge-moment load cell check setup



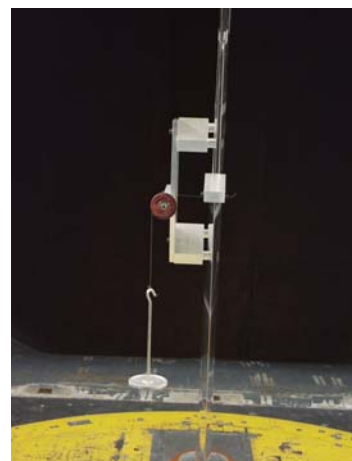
(b) Rear view of balance check setup



(b) Side view of hinge-moment load cell check setup



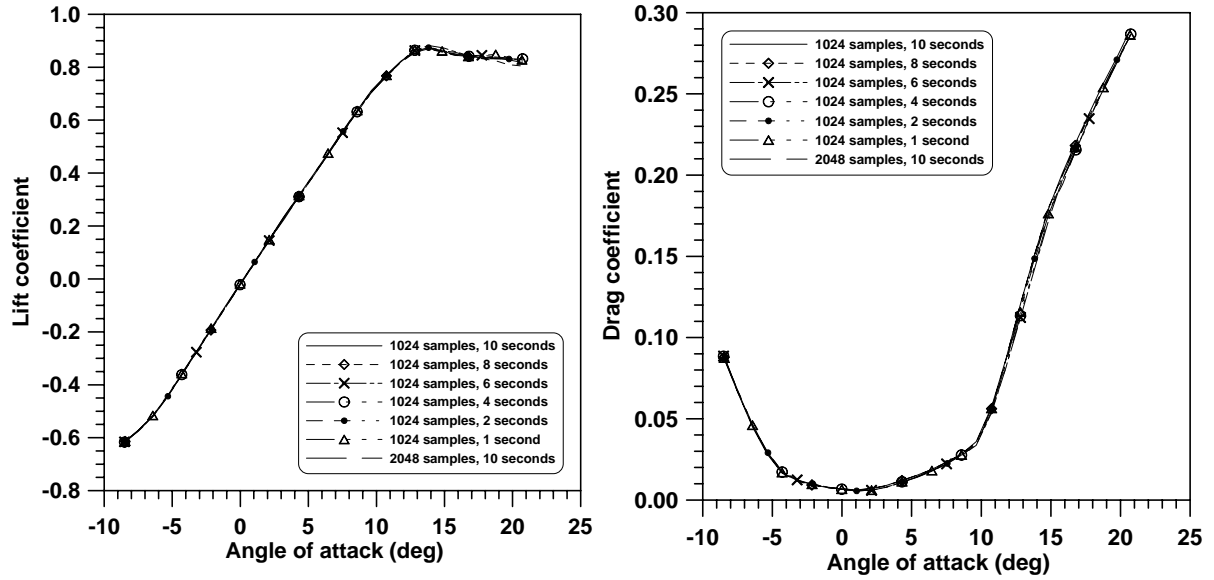
(c) Close-up of weight (load) applied in normal to chord direction



(c) Close-up of weight (load) applied in negative Hinge-moment direction (looking upstream)

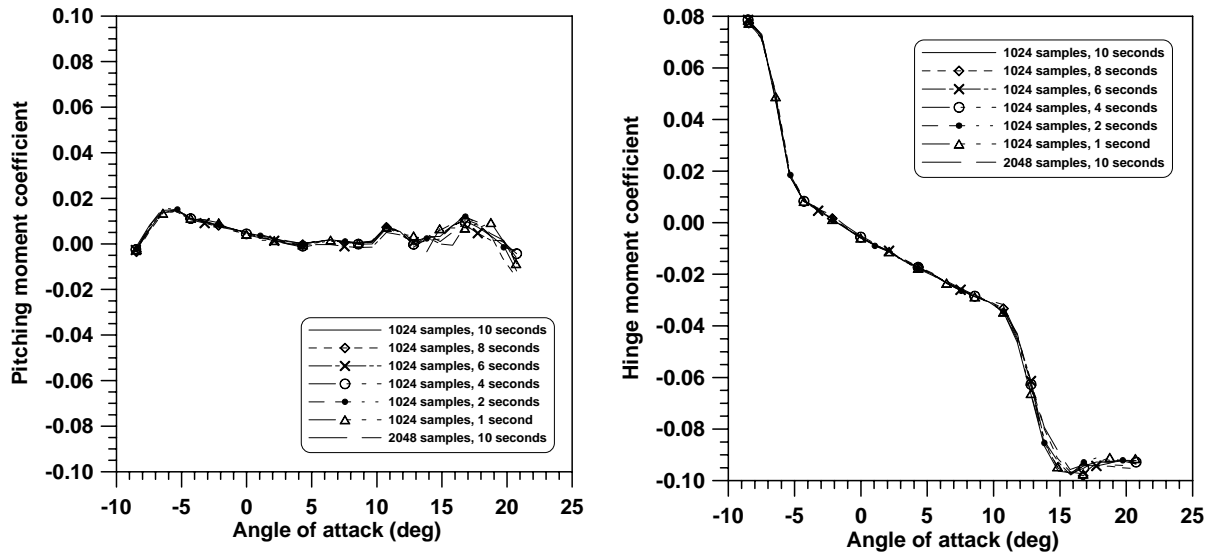
FIGURE 3-31. SETUP TO CHECK EXTERNAL BALANCE

FIGURE 3-32. SETUP TO CHECK HINGE-MOMENT LOAD CELL



(a) Lift coefficient

(b) Drag coefficient



(c) Pitching moment coefficient

(d) Hinge-moment coefficient

FIGURE 3-33. DATA SAMPLING STUDIES OF C_L , C_D , C_M , AND C_H ; CLEAN CONFIGURATION; $Re = 1.8 \times 10^6$; $\delta_A = 0^\circ$

In most wind tunnel studies, aerodynamic performance measurements rely on standard wind tunnel instrumentation, which typically include external or internal balances and, in some cases, pressure instrumentation. Near stall, extensive flow separation and vortex shedding increase model vibration and cause large wake unsteadiness, which can affect the accuracy of the

measured aerodynamic coefficients. Considering the lift coefficient, the objective in most wind tunnel tests is to determine lift curve slope, near-stall and poststall behavior, and $C_{L,max}$ for engineering purposes. In determining the degree of measurement accuracy needed, an analysis should be performed based on the acceptable level of accuracy with respect to the aircraft performance. For example, assuming an error in C_L of 0.01 for the wing used in this study, the corresponding error in lift at a speed of 131 kts (151 mph, $Q = 50$ psf) was approximately 3.7 lb. Given a $C_{L,max}$ of 0.87, the total lift generated by the wing at the same flow condition was 319.7 lb. For engineering purposes, an error of 3.7 lb in lift out of a total lift of 319.7 lb should be considered to determine if better accuracy is needed in measuring $C_{L,max}$.

Precise measurement of aerodynamic properties near stall is a very difficult task, which is beyond the scope of the study described in this report. The experimental difficulties stem from a number of factors such as the ones listed below:

- The exact dynamic responses of the balance with the model installed (e.g., response versus frequency) should be known and appropriate data-sampling rates and sampling periods should be established from experiments. The sampling periods should be long enough to account for both model and tunnel flow unsteadiness.
- Model deflections and variations in α due to model vibration and flow pulsing are difficult to accurately measure or monitor in real time.
- Tunnel blockage effects under stall conditions can be very significant, depending on model and tunnel size, and their impact on tunnel dynamic and static pressures are difficult to determine and correct.

Generally, experimental data for unsteady conditions require special tunnel facilities and are usually obtained with simple geometries such as airfoil sections. In most cases, the best way to obtain such data is through the use of extensive surface pressure time histories, which can then be integrated to provide the required coefficients.

In summary, the experimental data provided in this report have been obtained under carefully controlled conditions. Data near stall should be used with the understanding that it may be subject to some uncertainty.

3.2.2 Compressibility Effects.

For the clean GLC-305 airfoil section, the critical free-stream Mach number for 2D flow was determined to be 0.22. This value was obtained from the intersection of the two curves defined by equations 3-2 and 3-3 [13 and 14].

$$Cp_{cr} = \frac{2}{\gamma \cdot M_\infty^2} \left[\left(\frac{2 + (\gamma - 1) \cdot M_\infty^2}{\gamma + 1} \right)^{\frac{\gamma}{\gamma - 1}} - 1 \right] \quad (3-2)$$

$$C_p = \frac{C_{p_0}}{\sqrt{1-M_\infty^2} + \frac{M_\infty^2 \left(1 + \frac{\gamma-1}{2} \cdot M_\infty^2 \right)}{2\sqrt{1-M_\infty^2}}} C_{p_0} \quad (3-3)$$

In the equations above, $C_{p_{cr}}$ is the critical pressure coefficient for which the local Mach number is 1, C_{p_0} is the maximum suction pressure coefficient for incompressible flow, and C_p is the compressible pressure coefficient obtained using C_{p_0} and Laitone's compressibility correction given by equation 3-3. The value of C_{p_0} for the GLC-305 section was -10.1 and corresponded to α of 13.5° . This value was obtained from a 2D incompressible viscous flow analysis using the XFOIL [15] computer code.

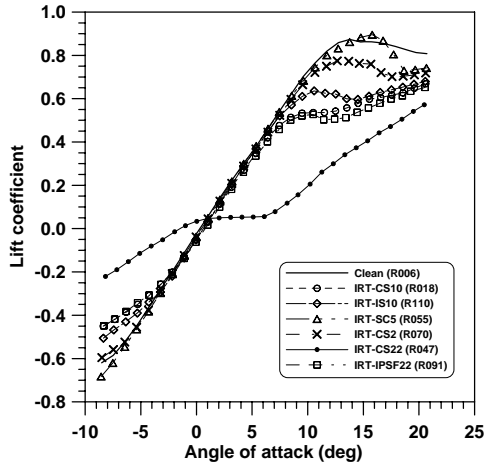
Note that the critical Mach number of 0.22 obtained from the 2D analysis and equations 3-2 and 3-3 is a conservative estimate. Typically, in 3D flow, the value of the free-stream Mach number (M_∞) required to achieve sonic flow over the wing for fixed α will be higher due to wing sweep and 3D flow relief effects. For the swept wing tested, the critical Mach number for 3D flow was $0.249 \left(\frac{0.22}{\cos 28^\circ} \right)$. Since all tests at the WSU wind tunnel facility were conducted at M_∞ of 0.185, the effect of compressibility on aerodynamic coefficients was not significant.

3.2.3 Clean and Iced Wing Performance.

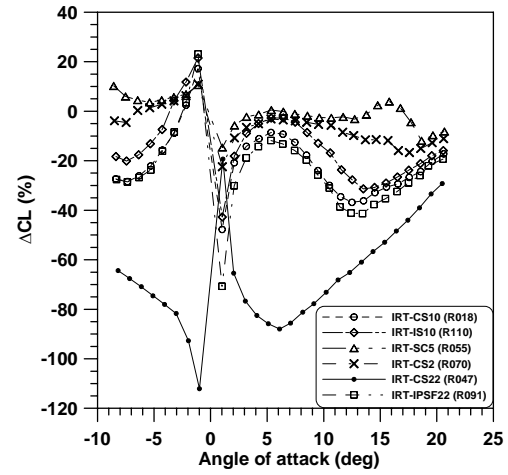
Aerodynamic performance for the clean and iced wing is presented in figures 3-34 to 3-45 and in tables 3-1 to 3-9 for δ_A of 0° . The data presented demonstrates the effects of all the ice shapes (six IRT ice shapes, seven smooth LEWICE ice shapes, and seven rough LEWICE ice shapes) investigated on lift, drag, pitching moments, hinge moments, and on the surface pressure distributions. For the purpose of discussion, the percentages in tables 3-1, 3-2, 3-4, 3-5, 3-7, and 3-8 have been calculated using the following formula:

$$\text{Change in property } X (\%) = \Delta X = \frac{X_{iced} - X_{clean}}{X_{clean}} \times 100 \quad (3-4)$$

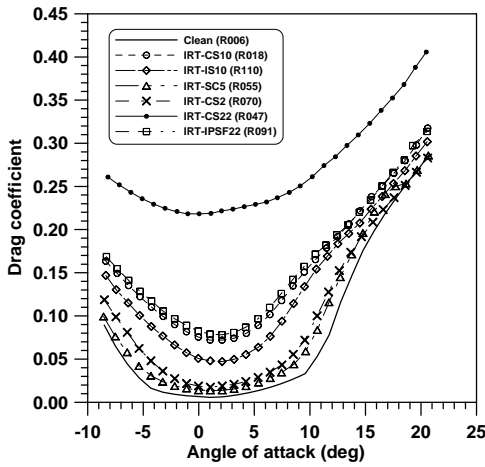
and, increase in X means that a negative X becomes more negative and a positive X becomes more positive.



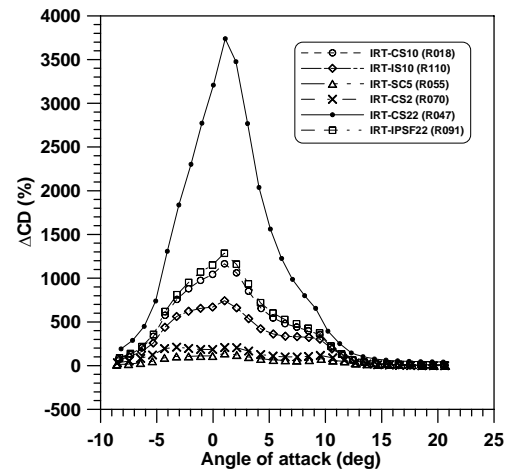
(a) Lift coefficient



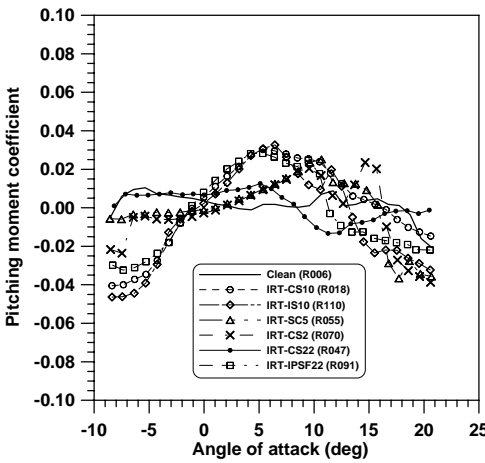
(b) ΔC_L vs α



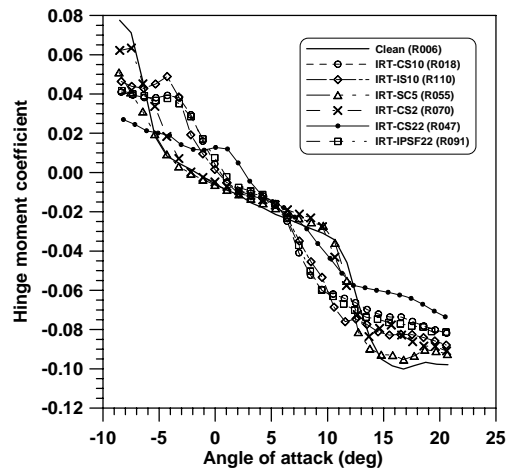
(c) Drag coefficient



(d) ΔC_D vs α

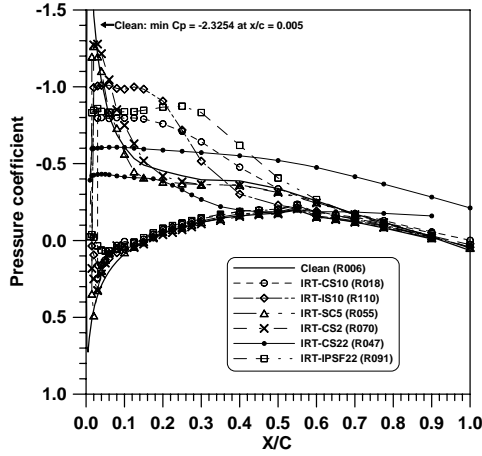


(e) Pitching-moment coefficient

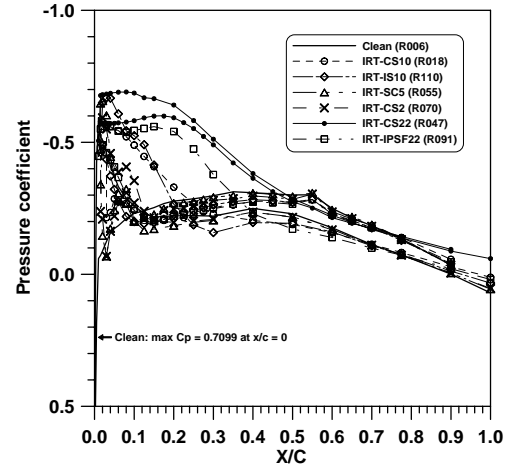


(f) Hinge-moment coefficient

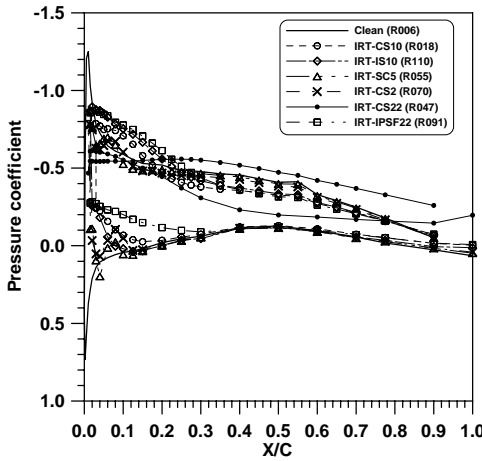
FIGURE 3-34. EFFECT OF IRT ICE SHAPES ON C_L , C_D , C_M , AND C_H ; IRT-CS10, IRT-IS10, IRT-SC5, IRT-CS2, IRT-CS22, AND IRT-IPSF22 CONFIGURATIONS; $Re = 1.8 \times 10^6$; $\delta_A = 0^\circ$



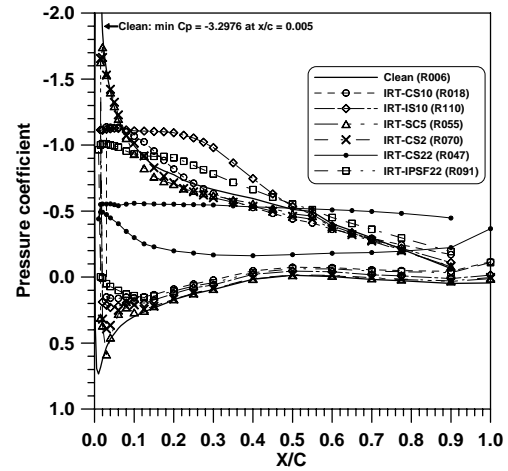
(a) C_p vs x/c ($\alpha = -4^\circ$)



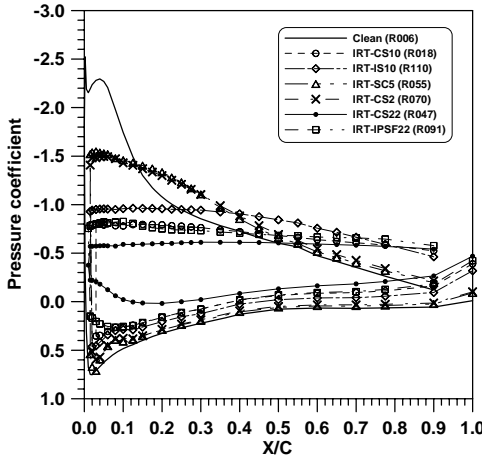
(b) C_p vs x/c ($\alpha = 0^\circ$)



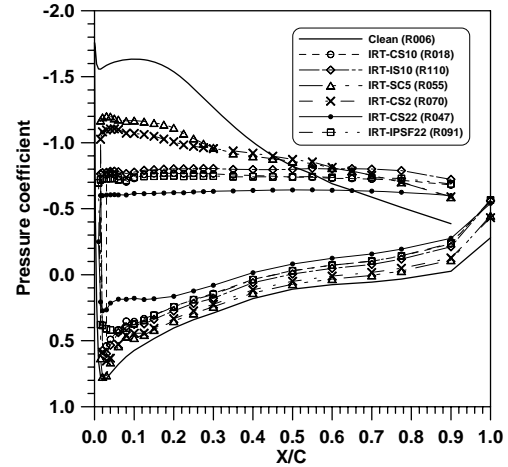
(c) C_p vs x/c ($\alpha = 4^\circ$)



(d) C_p vs x/c ($\alpha = 8^\circ$)

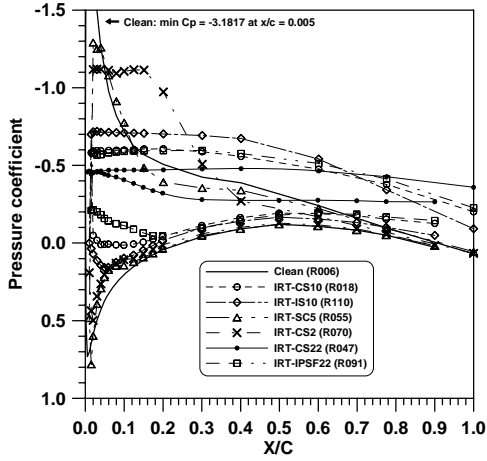


(e) C_p vs x/c ($\alpha = 12^\circ$)

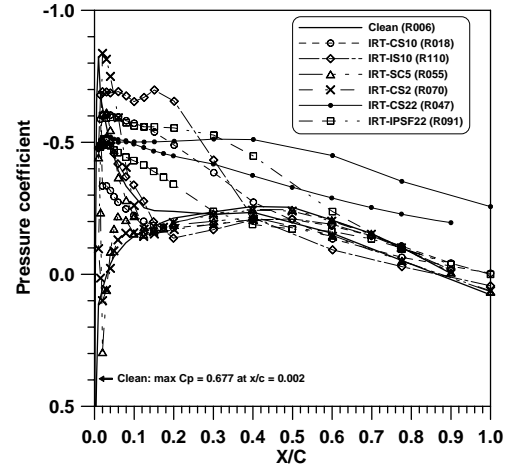


(f) C_p vs x/c ($\alpha = 16^\circ$)

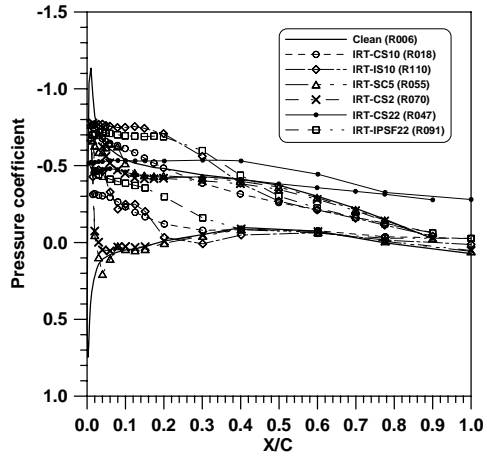
FIGURE 3-35. EFFECT OF IRT ICE SHAPES ON PRESSURE DISTRIBUTIONS AT 15% SEMISPAN; IRT-CS10, IRT-IS10, IRT-SC5, IRT-CS2, IRT-CS22, AND IRT-IPSF22 CONFIGURATIONS; $Re = 1.8 \times 10^6$; $\delta_A = 0^\circ$



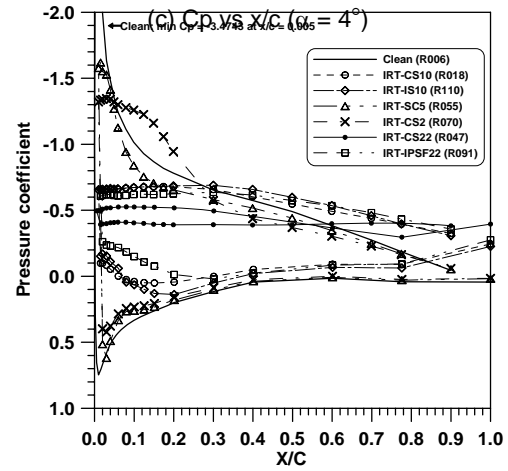
(a) C_p vs x/c ($\alpha = -4^\circ$)



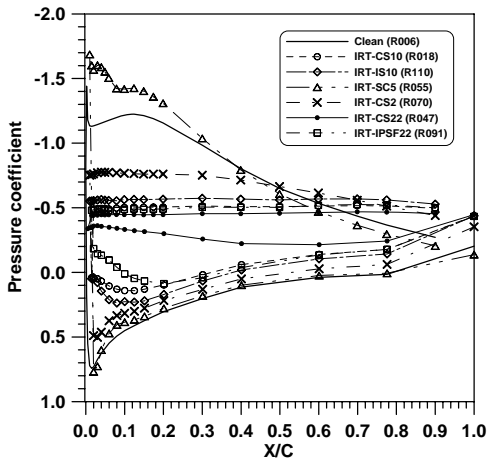
(b) C_p vs x/c ($\alpha = 0^\circ$)



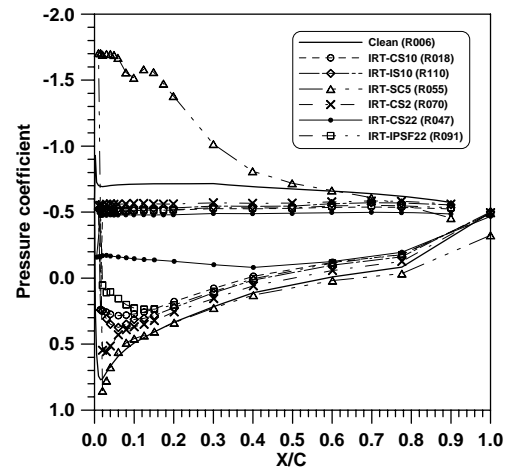
(c) C_p vs x/c ($\alpha = 4^\circ$)



(d) C_p vs x/c ($\alpha = 8^\circ$)

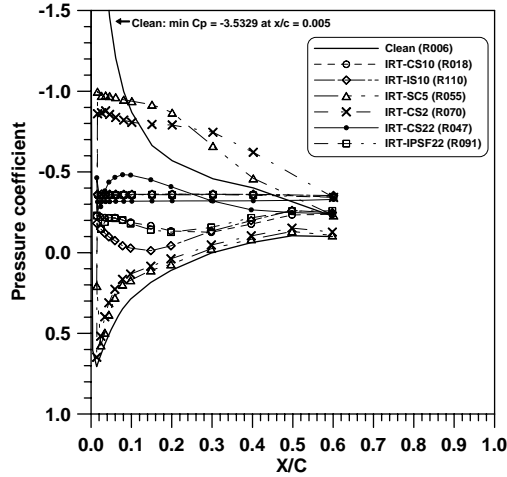


(e) C_p vs x/c ($\alpha = 12^\circ$)

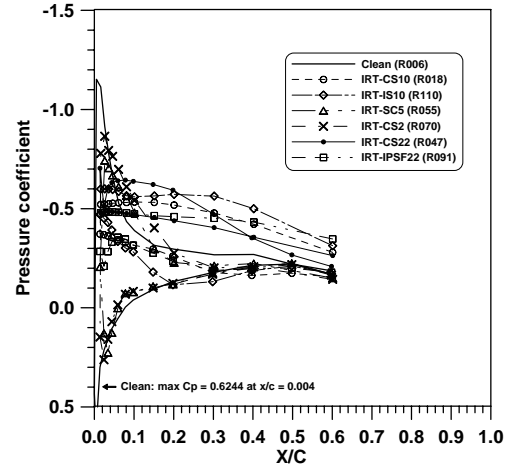


(f) C_p vs x/c ($\alpha = 16^\circ$)

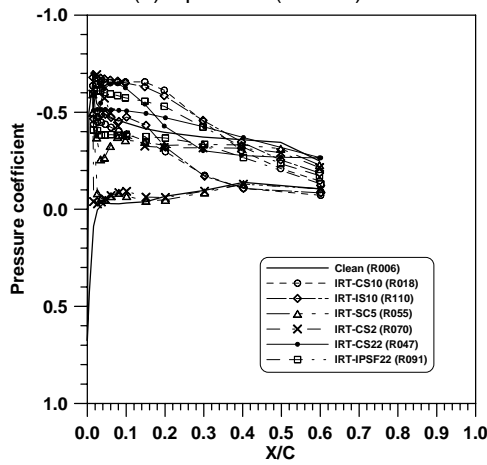
FIGURE 3-36. EFFECT OF IRT ICE SHAPES ON PRESSURE DISTRIBUTIONS AT 50% SEMISPAN; IRT-CS10, IRT-IS10, IRT-SC5, IRT-CS2, IRT-CS22, AND IRT-IPSF22 CONFIGURATIONS; $Re = 1.8 \times 10^6$; $\delta_A = 0^\circ$



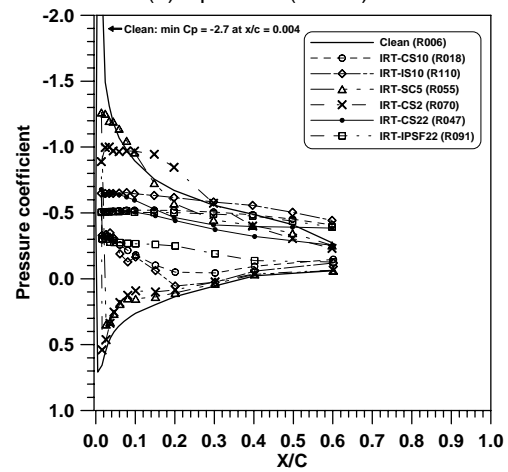
(a) C_p vs x/c ($\alpha = -4^\circ$)



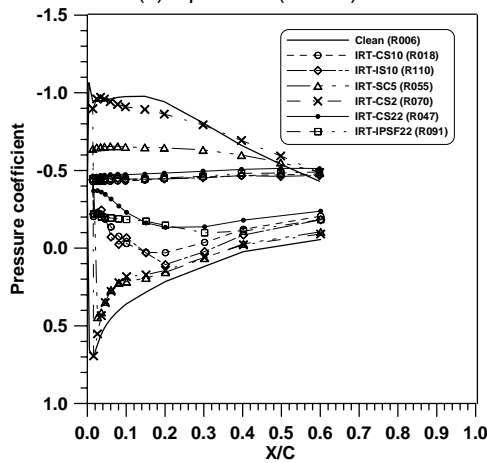
(b) C_p vs x/c ($\alpha = 0^\circ$)



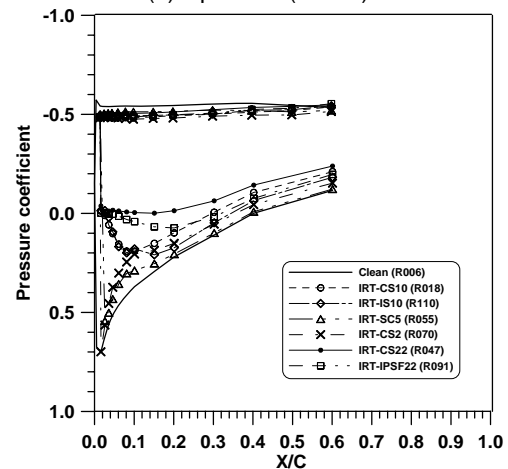
(c) C_p vs x/c ($\alpha = 4^\circ$)



(d) C_p vs x/c ($\alpha = 8^\circ$)

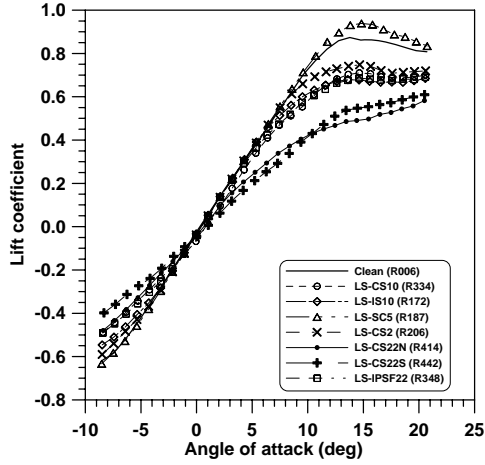


(e) C_p vs x/c ($\alpha = 12^\circ$)

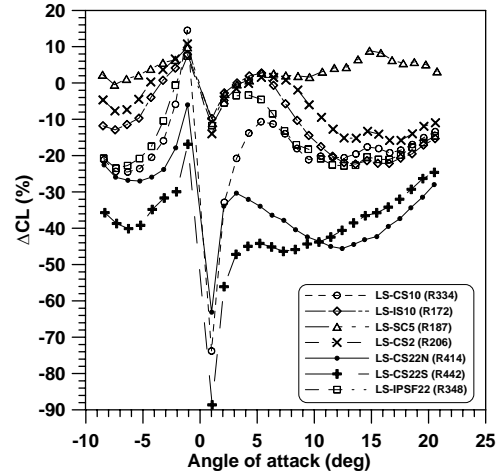


(f) C_p vs x/c ($\alpha = 16^\circ$)

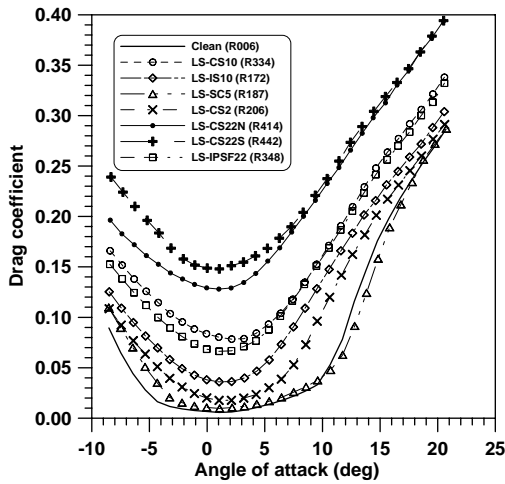
FIGURE 3-37. EFFECT OF IRT ICE SHAPES ON PRESSURE DISTRIBUTIONS AT 85% SEMISPAN; IRT-CS10, IRT-IS10, IRT-SC5, IRT-CS2, IRT-CS22, AND IRT-IPSF22 CONFIGURATIONS; $Re = 1.8 \times 10^6$; $\delta_A = 0^\circ$



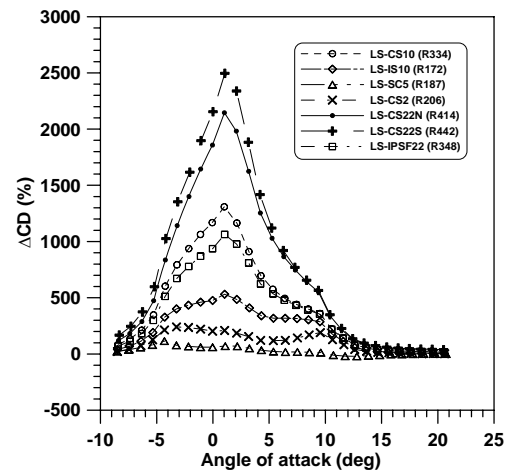
(a) Lift coefficient



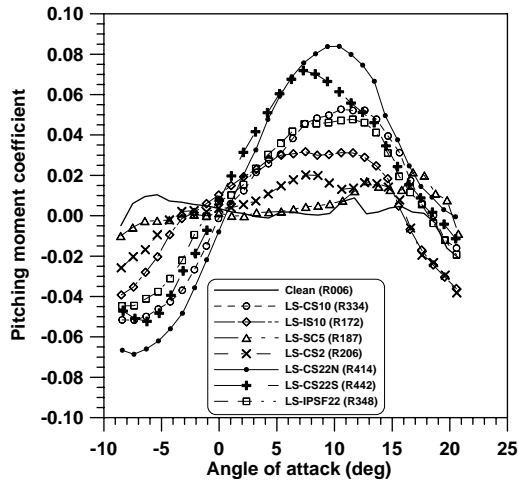
(b) ΔC_L vs α



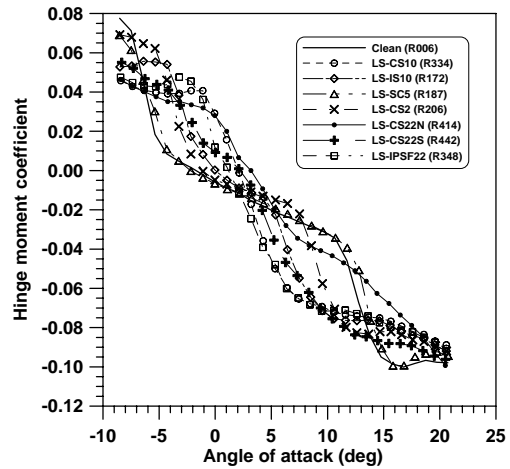
(c) Drag coefficient



(d) ΔC_D vs α

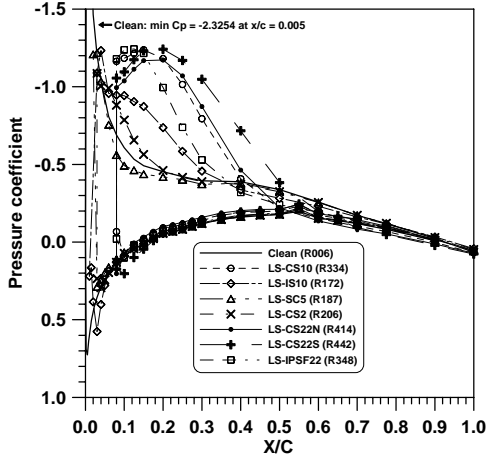


(e) Pitching-moment coefficient

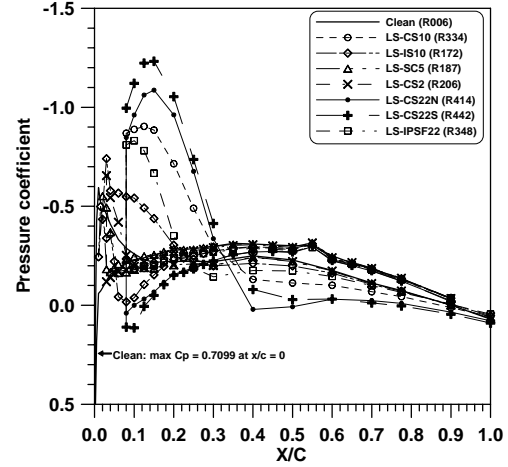


(f) Hinge-moment coefficient

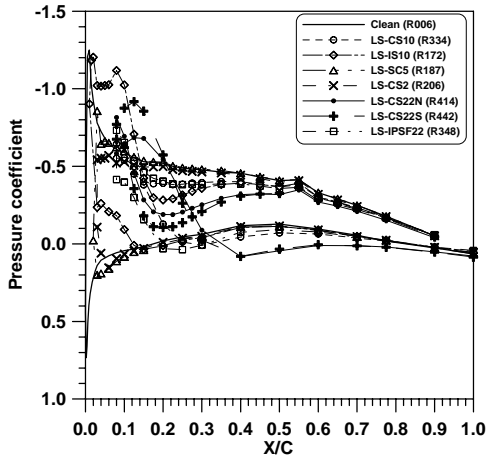
FIGURE 3-38. EFFECT OF SMOOTH LEWICE ICE SHAPES ON C_L , C_D , C_M , AND C_H ; LS-CS10, LS-IS10, LS-SC5, LS-CS2, LS-CS22N, LS-CS22S, AND LS-IPSF22 CONFIGURATIONS; $Re = 1.8 \times 10^6$; $\delta_A = 0^\circ$



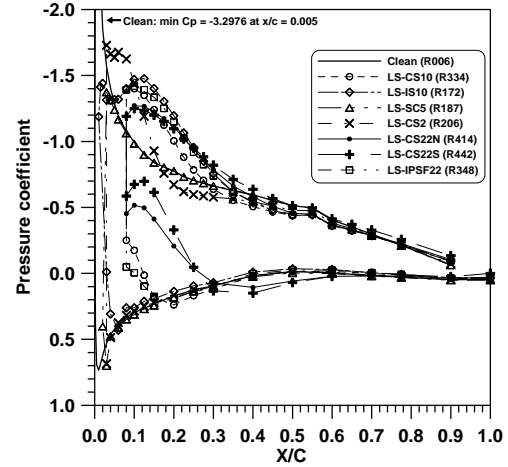
(a) C_p vs x/c ($\alpha = -4^\circ$)



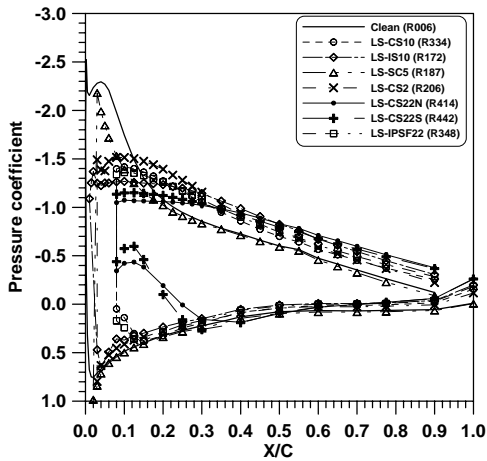
(b) C_p vs x/c ($\alpha = 0^\circ$)



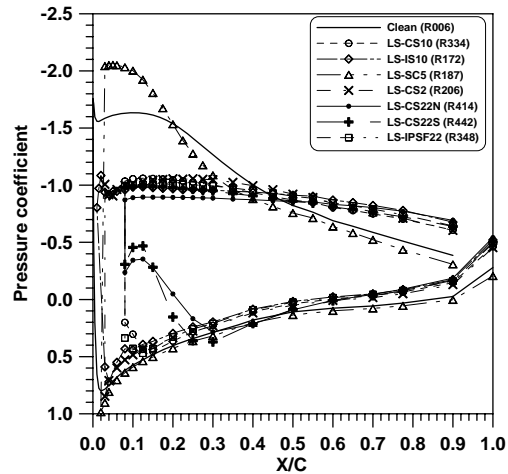
(c) C_p vs x/c ($\alpha = 4^\circ$)



(d) C_p vs x/c ($\alpha = 8^\circ$)

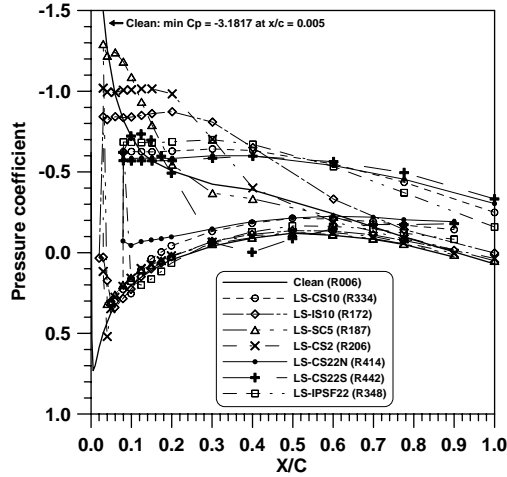


(e) C_p vs x/c ($\alpha = 12^\circ$)

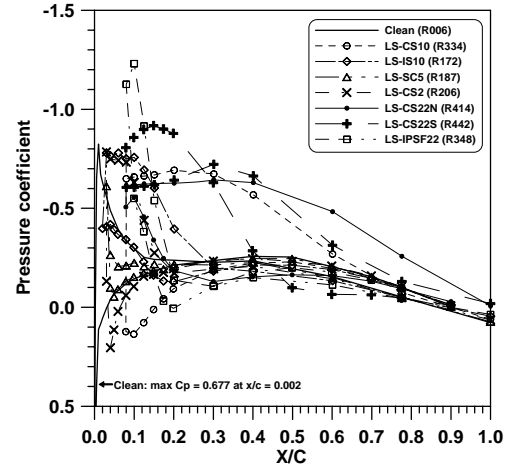


(f) C_p vs x/c ($\alpha = 16^\circ$)

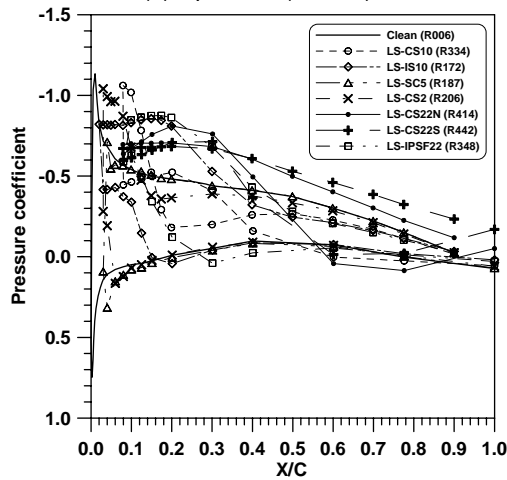
FIGURE 3-39. EFFECT OF SMOOTH LEWICE ICE SHAPES ON PRESSURE DISTRIBUTIONS AT 15% SEMISPAN; LS-CS10, LS-IS10, LS-SC5, LS-CS2, LS-CS22N, LS-CS22S, AND LS-IPSF22 CONFIGURATIONS; $RE = 1.8 \times 10^6$; $\delta_A = 0^\circ$



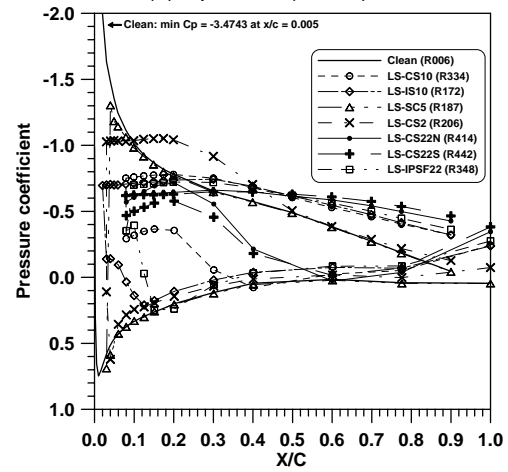
(a) C_p vs x/c ($\alpha = -4^\circ$)



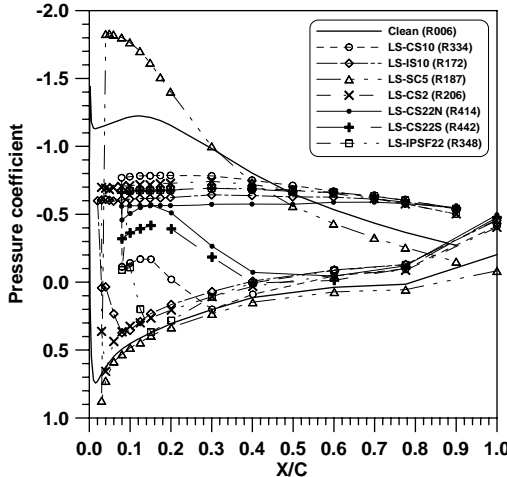
(b) C_p vs x/c ($\alpha = 0^\circ$)



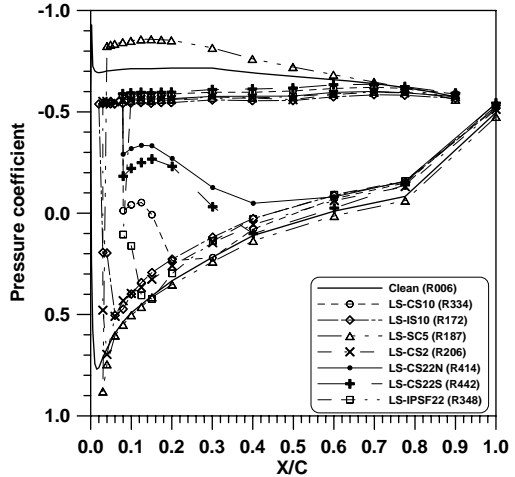
(c) C_p vs x/c ($\alpha = 4^\circ$)



(d) C_p vs x/c ($\alpha = 8^\circ$)

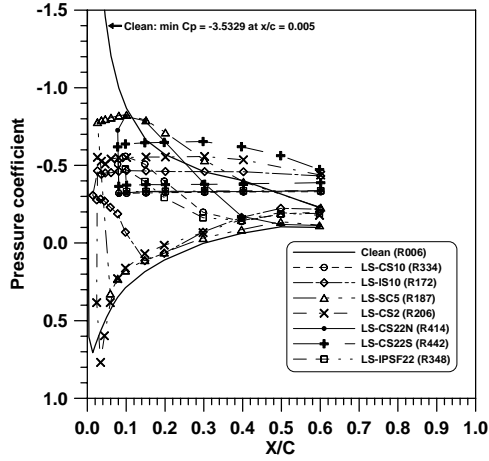


(e) C_p vs x/c ($\alpha = 12^\circ$)

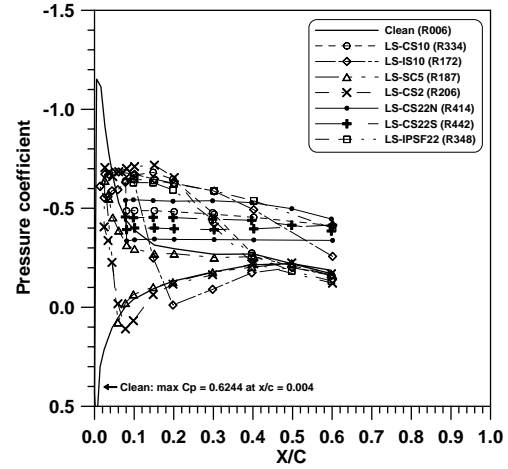


(f) C_p vs x/c ($\alpha = 16^\circ$)

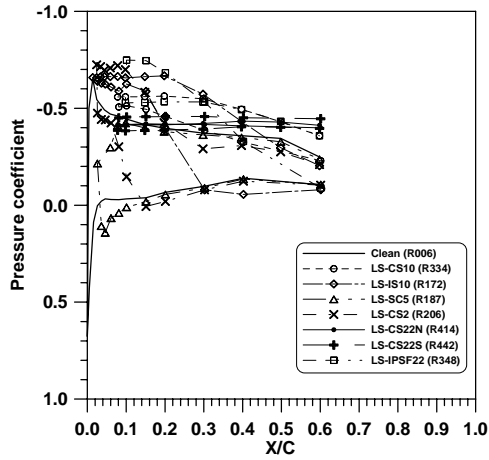
FIGURE 3-40. EFFECT OF SMOOTH LEWICE ICE SHAPES ON PRESSURE DISTRIBUTIONS AT 50% SEMISPAN; LS-CS10, LS-IS10, LS-SC5, LS-CS2, LS-CS22N, LS-CS22S, AND LS-IPSF22 CONFIGURATIONS; $Re = 1.8 \times 10^6$; $\delta_A = 0^\circ$



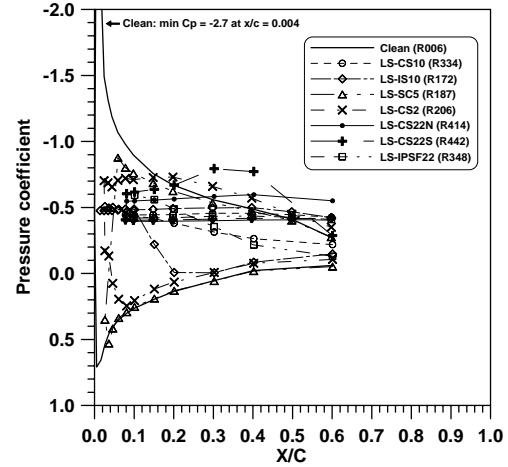
(a) C_p vs x/c ($\alpha = -4^\circ$)



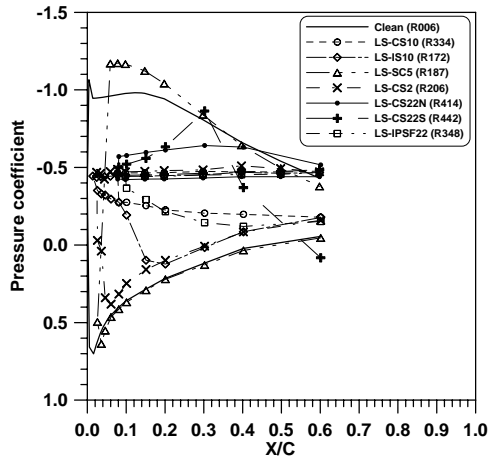
(b) C_p vs x/c ($\alpha = 0^\circ$)



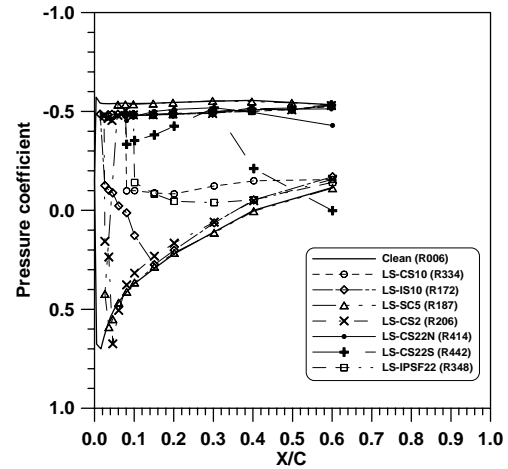
(c) C_p vs x/c ($\alpha = 4^\circ$)



(d) C_p vs x/c ($\alpha = 8^\circ$)

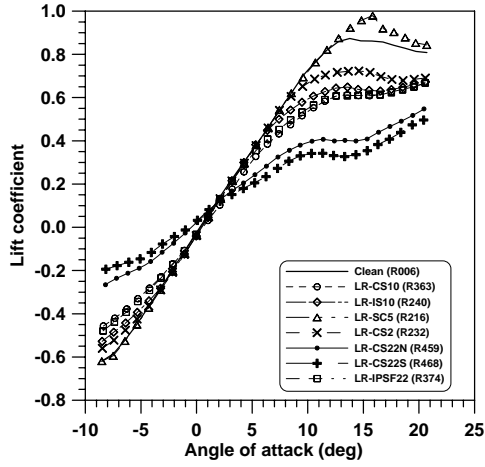


(e) C_p vs x/c ($\alpha = 12^\circ$)

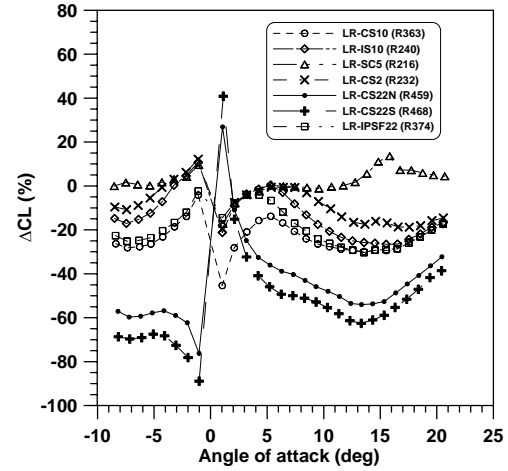


(f) C_p vs x/c ($\alpha = 16^\circ$)

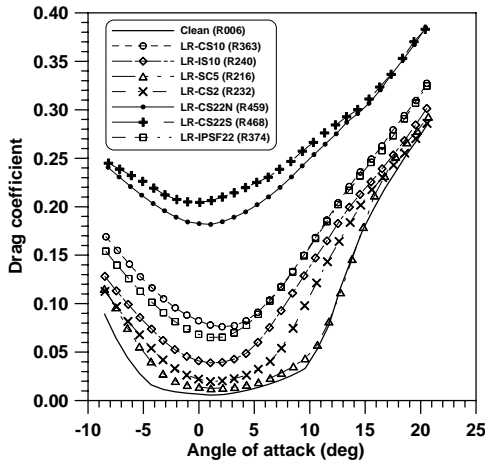
FIGURE 3-41. EFFECT OF SMOOTH LEWICE ICE SHAPES ON PRESSURE DISTRIBUTIONS AT 85% SEMISPAN; LS-CS10, LS-IS10, LS-SC5, LS-CS2, LS-CS22N, LS-CS22S, AND LS-IPSF22 CONFIGURATIONS; $Re = 1.8 \times 10^6$; $\delta_A = 0^\circ$



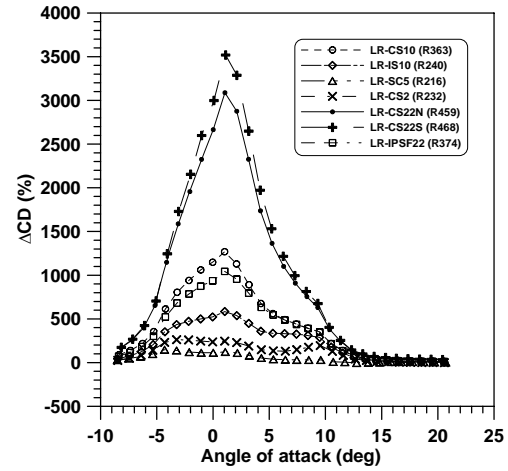
(a) Lift coefficient



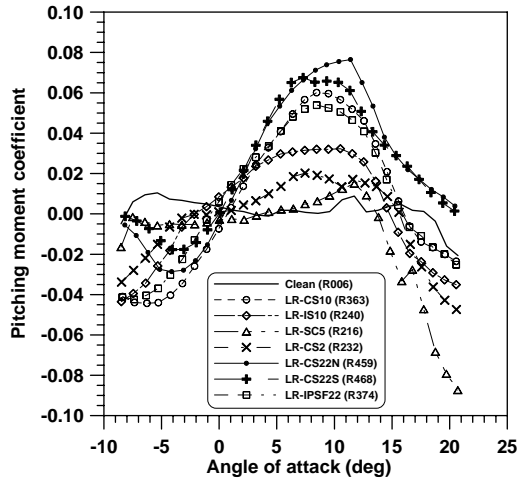
(b) ΔC_L vs α



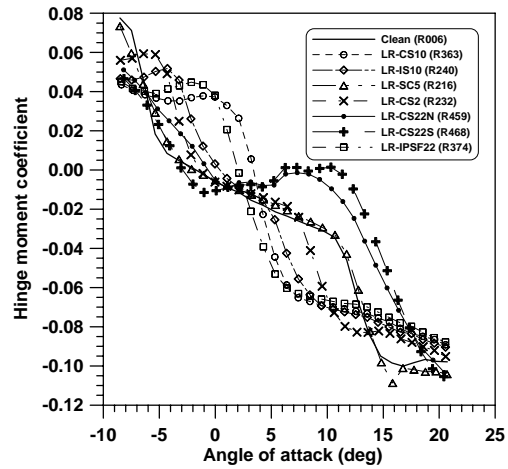
(c) Drag coefficient



(d) ΔC_D vs α

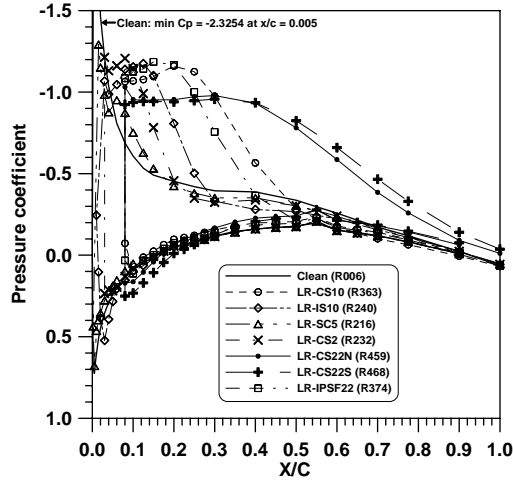


(e) Pitching moment coefficient

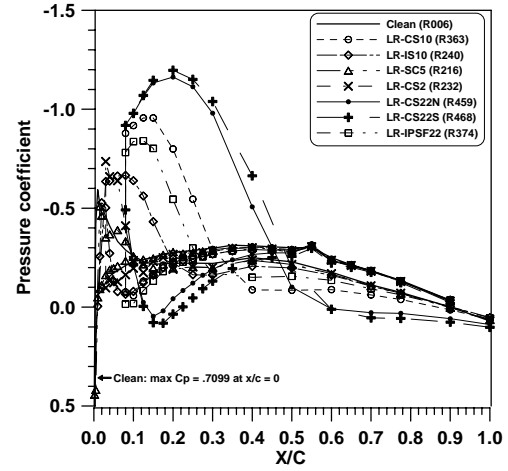


(f) Hinge-moment coefficient

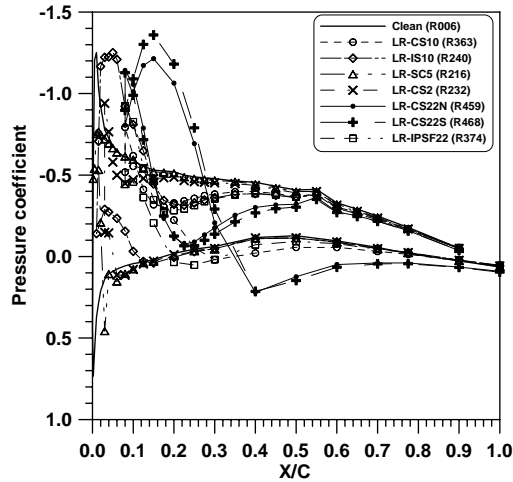
FIGURE 3-42. EFFECT OF ROUGH LEWICE ICE SHAPES ON C_L , C_D , C_M , AND C_H ; LR-CS10, LR-IS10, LR-SC5, LR-CS2, LR-CS22N, LR-CS22S, AND LR-IPSF22 CONFIGURATIONS; $Re = 1.8 \times 10^6$; $\delta_A = 0^\circ$



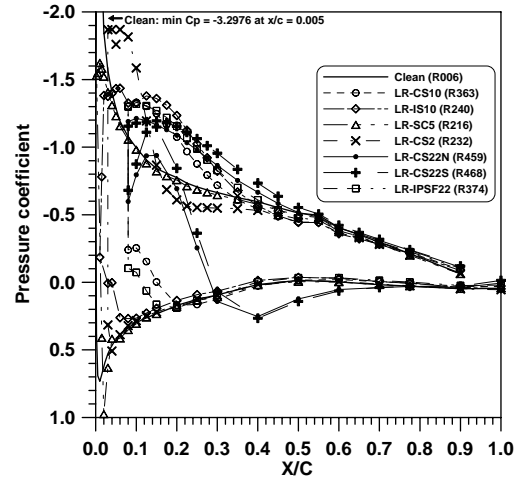
(a) C_p vs x/c ($\alpha = -4^\circ$)



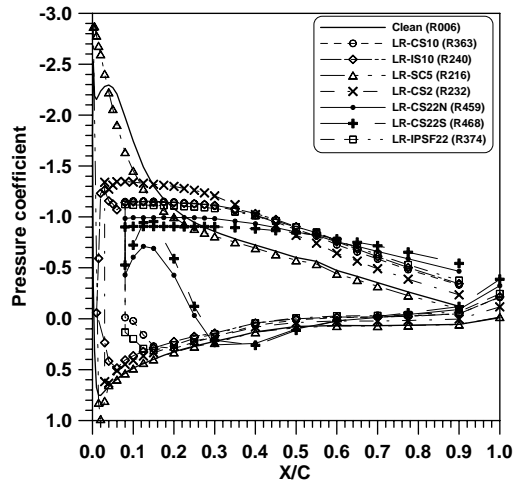
(b) C_p vs x/c ($\alpha = 0^\circ$)



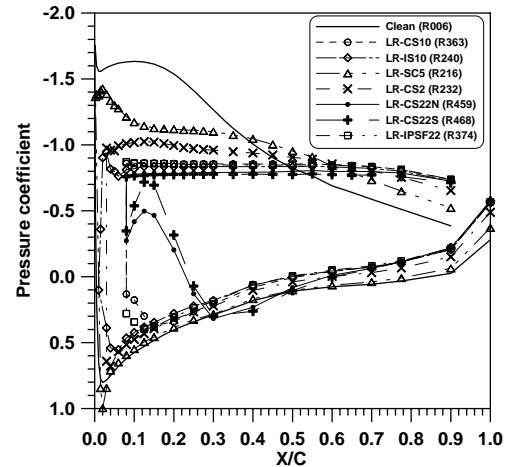
(c) C_p vs x/c ($\alpha = 4^\circ$)



(d) C_p vs x/c ($\alpha = 8^\circ$)

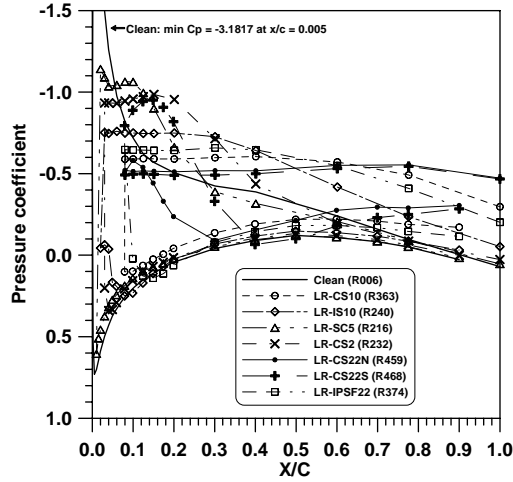


(e) C_p vs x/c ($\alpha = 12^\circ$)

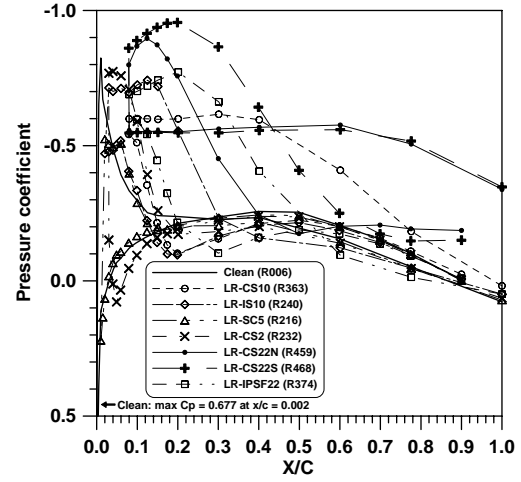


(f) C_p vs x/c ($\alpha = 16^\circ$)

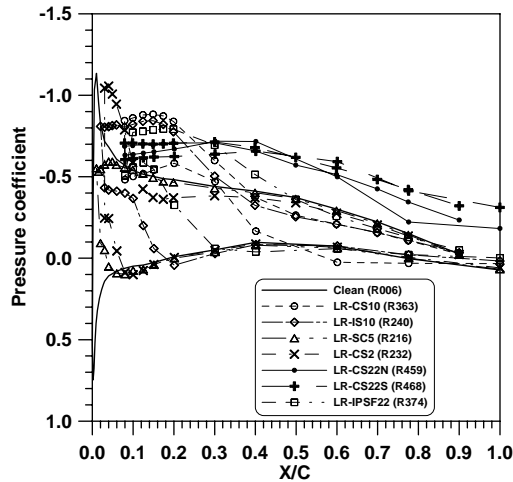
FIGURE 3-43. EFFECT OF ROUGH LEWICE ICE SHAPES ON PRESSURE DISTRIBUTIONS AT 15% SEMISPAN; LR-CS10, LR-IS10, LR-SC5, LR-CS2, LR-CS22N, LR-CS22S, AND LR-IPSF22 CONFIGURATIONS; $Re = 1.8 \times 10^6$; $\delta_A = 0^\circ$



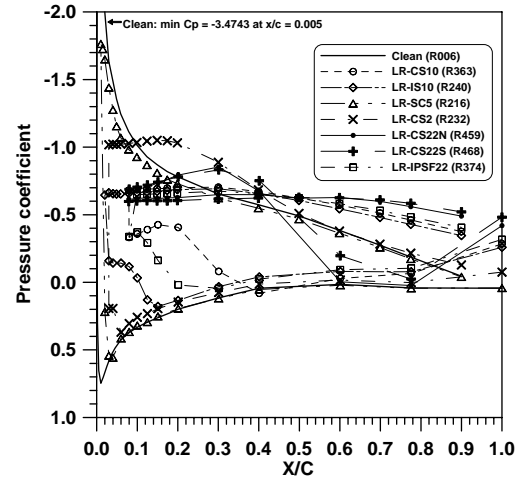
(a) C_p vs x/c ($\alpha = -4^\circ$)



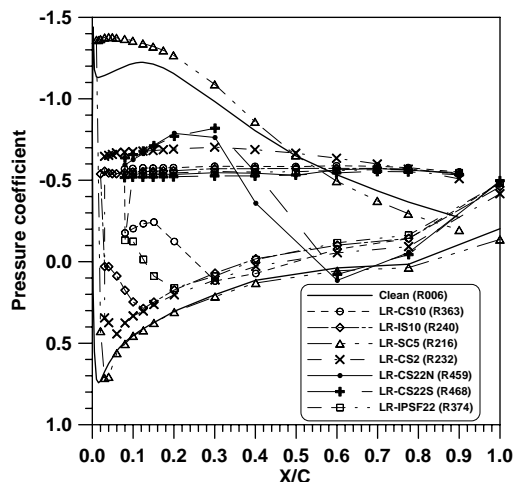
(b) C_p vs x/c ($\alpha = 0^\circ$)



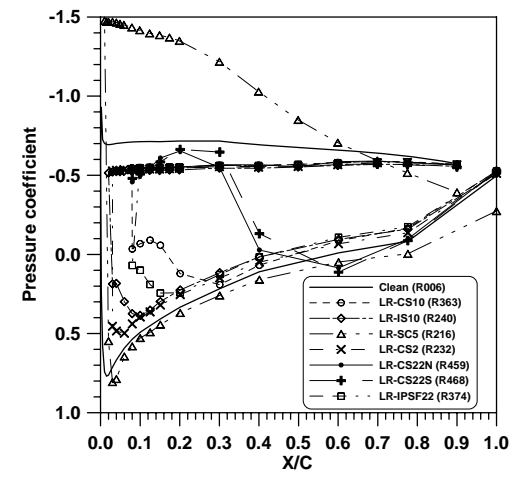
(c) C_p vs x/c ($\alpha = 4^\circ$)



(d) C_p vs x/c ($\alpha = 8^\circ$)

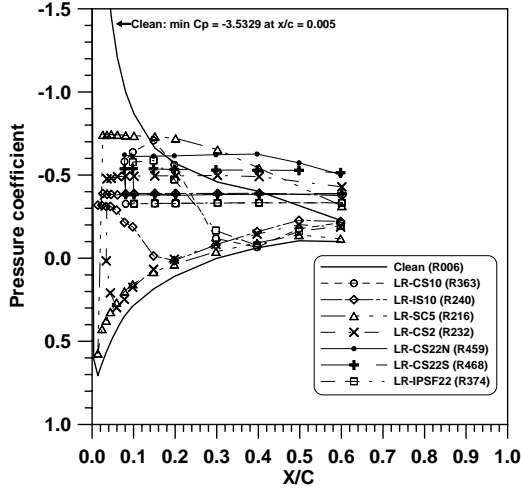


(e) C_p vs x/c ($\alpha = 12^\circ$)

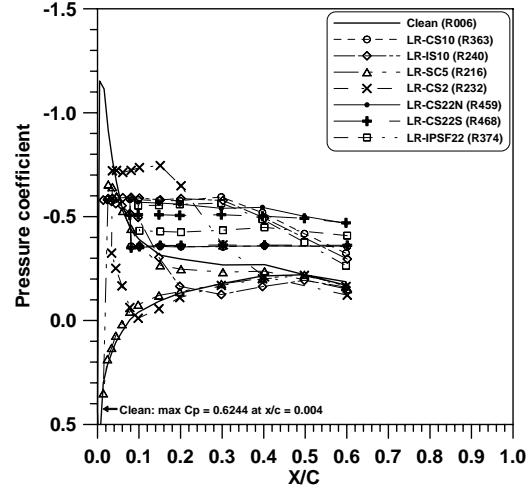


(f) C_p vs x/c ($\alpha = 16^\circ$)

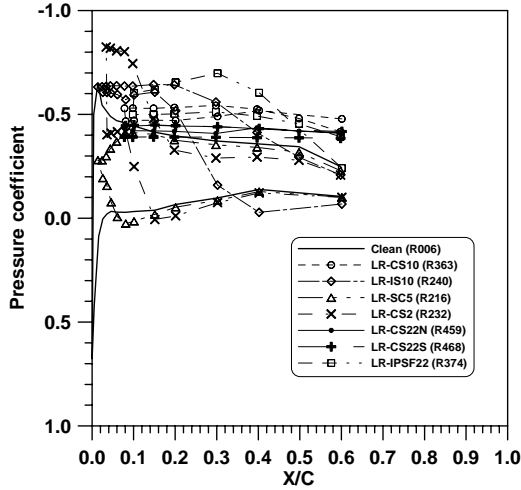
FIGURE 3-44. EFFECT OF ROUGH LEWICE ICE SHAPES ON PRESSURE DISTRIBUTIONS AT 50% SEMISPAN; LR-CS10, LR-IS10, LR-SC5, LR-CS2, LR-CS22N, LR-CS22S, AND LR-IPSF22 CONFIGURATIONS; $Re = 1.8 \times 10^6$; $\delta_A = 0^\circ$



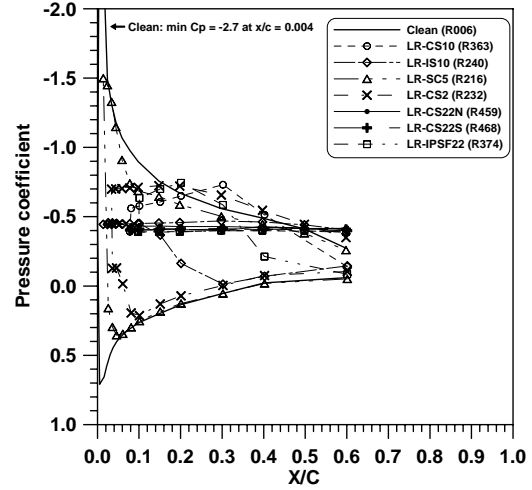
(a) C_p vs x/c ($\alpha = -4^\circ$)



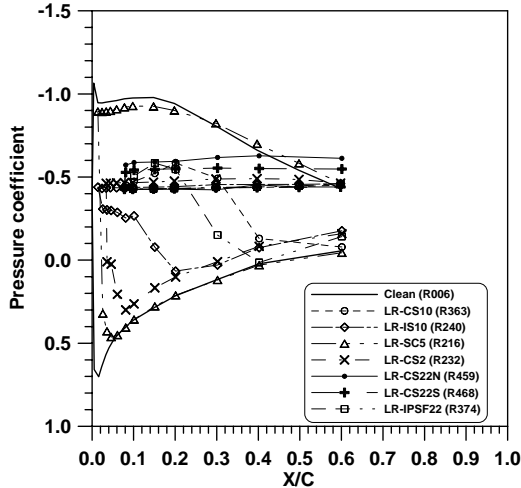
(b) C_p vs x/c ($\alpha = 0^\circ$)



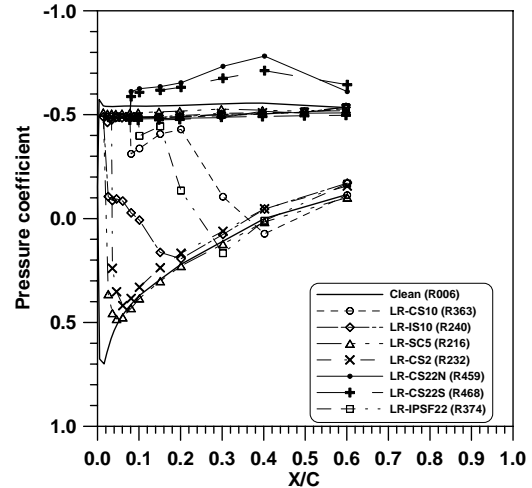
(c) C_p vs x/c ($\alpha = 4^\circ$)



(d) C_p vs x/c ($\alpha = 8^\circ$)



(e) C_p vs x/c ($\alpha = 12^\circ$)



(f) C_p vs x/c ($\alpha = 16^\circ$)

FIGURE 3-45. EFFECT OF ROUGH LEWICE ICE SHAPES ON PRESSURE DISTRIBUTIONS AT 85% SEMISPAN; LR-CS10, LR-IS10, LR-SC5, LR-CS2, LR-CS22N, LR-CS22S, AND LR-IPSF22 CONFIGURATIONS; $Re = 1.8 \times 10^6$; $\delta_A = 0^\circ$

TABLE 3-1. EFFECT OF IRT ICE SHAPES ON C_L AND C_D ; $Re_{MAC} = 1.8 \times 10^6$; $\delta_A = 0^\circ$

α (deg)	Configuration	C_L	ΔC_L	C_D	ΔC_D
3	CLEAN	0.22	0.0%	0.008	0.0%
	IRT-CS10	0.19	-13.6%	0.074	825.0%
	IRT-IS10	0.20	-9.1%	0.050	525.0%
	IRT-SC5	0.22	0.0%	0.016	100.0%
	IRT-CS2	0.21	-4.5%	0.021	162.5%
	IRT-CS22	0.05	-77.3%	0.224	2700.0%
	IRT-IPSF22	0.18	-18.2%	0.081	912.5%
5	CLEAN	0.38	0.0%	0.014	0.0%
	IRT-CS10	0.35	-7.9%	0.089	535.7%
	IRT-IS10	0.37	-2.6%	0.064	357.1%
	IRT-SC5	0.38	0.0%	0.023	64.3%
	IRT-CS2	0.37	-2.6%	0.029	107.1%
	IRT-CS22	0.05	-86.8%	0.229	1535.7%
	IRT-IPSF22	0.34	-10.5%	0.097	592.9%
10	CLEAN	0.76	0.0%	0.053	0.0%
	IRT-CS10	0.54	-28.9%	0.165	211.3%
	IRT-IS10	0.64	-15.8%	0.154	190.6%
	IRT-SC5	0.74	-2.6%	0.084	58.5%
	IRT-CS2	0.72	-5.3%	0.100	88.7%
	IRT-CS22	0.21	-72.4%	0.261	392.5%
	IRT-IPSF22	0.53	-30.3%	0.172	224.5%
15	CLEAN	0.86	0.0%	0.198	0.0%
	IRT-CS10	0.60	-30.2%	0.238	20.2%
	IRT-IS10	0.61	-29.1%	0.224	13.1%
	IRT-SC5	0.90	4.7%	0.221	11.6%
	IRT-CS2	0.76	-11.6%	0.209	5.6%
	IRT-CS22	0.41	-52.3%	0.323	63.1%
	IRT-IPSF22	0.56	-34.9%	0.234	18.3%

TABLE 3-2. EFFECT OF IRT ICE SHAPES ON $C_{L,stall}$, α_{stall} , AND $C_{D,min}$; $Re_{MAC} = 1.8 \times 10^6$; $\delta_A = 0^\circ$

Configuration	$C_{L,stall}$	$\Delta C_{L,stall}$	α_{stall}	$\Delta \alpha_{stall}$	C_L at $\alpha = 13.8^\circ$	ΔC_L at $\alpha = 13.8^\circ$	$C_{D,min}$	$\Delta C_{D,min}$	C_D at $\alpha = 13.8^\circ$	ΔC_D at $\alpha = 13.8^\circ$
Clean	0.87	0.0%	13.8°	0.0°	0.87	0.0%	0.006	0.0%	0.147	0.0%
IRT-CS10	0.54	-37.9%	10.5°	-3.3°	0.56	-35.6%	0.072	1100.0%	0.209	42.2%
IRT-IS10	0.64	-26.4%	10.6°	-3.2°	0.59	-32.2%	0.047	683.3%	0.198	34.7%
IRT-SC5	0.90	3.4%	15.8°	2.0°	0.86	-1.1%	0.014	133.3%	0.172	17.0%
IRT-CS2	0.77	-11.5%	12.7°	-1.1°	0.76	-12.6%	0.018	200.0%	0.174	18.4%
IRT-CS22	0.06	-93.6%	6.0°	-7.8°	0.36	-58.6%	0.218	3533.3%	0.300	104.1%
IRT-IPSF22	0.53	-39.1%	10.5°	-3.3°	0.53	-39.1%	0.078	1200.0%	0.210	42.9%

TABLE 3-3. EFFECT OF IRT ICE SHAPES ON HINGE-MOMENT COEFFICIENT SLOPE;
 $Re_{MAC} = 1.8 \times 10^6$; $\delta_A = 0^\circ$

Ice shape	Region A		Region B		Region C	
	dCH/d α (per deg)	α -range (deg)	dCH/d α (per deg)	α -range (deg)	dCH/d α (per deg)	α -range (deg)
Clean	-0.0026	0 to 10	-0.0155	10 to 14	-0.0001	14 to 20
IRT-CS10	-0.0038	0 to 6	-0.0091	6 to 10	-0.0019	10 to 20
IRT-IS10	-0.0032	0 to 6	-0.0106	6 to 10	-0.0016	10 to 20
IRT-SC5	-0.0022	0 to 9	-0.0143	9 to 15	0.0004	15 to 20
IRT-CS2	-0.0023	0 to 9	-0.0137	9 to 13	-0.0016	13 to 20
IRT-CS22	-0.0057	0 to 6	-0.0065	6 to 11	-0.0021	11 to 20
IRT-IPSF22	-0.0041	0 to 6	-0.0100	6 to 10	-0.0017	10 to 20

TABLE 3-4. EFFECT OF SMOOTH LEWICE ICE SHAPES ON C_L AND C_D ;
 $Re_{MAC} = 1.8 \times 10^6$; $\delta_A = 0^\circ$

α (deg)	Configuration	C_L	ΔC_L	C_D	ΔC_D
3	CLEAN	0.22	0.0%	0.008	0.0%
	LS-CS10	0.18	-18.2%	0.079	887.5%
	LS-IS10	0.22	0.0%	0.040	400.0%
	LS-SC5	0.22	0.0%	0.012	50.0%
	LS-CS2	0.22	0.0%	0.020	150.0%
	LS-CS22N	0.16	-27.3%	0.135	1587.5%
	LS-CS22S	0.12	-45.5%	0.155	1837.5%
	LS-IPSF22	0.22	0.0%	0.071	787.5%
5	CLEAN	0.38	0.0%	0.014	0.0%
	LS-CS10	0.34	-10.5%	0.093	564.3%
	LS-IS10	0.39	2.6%	0.058	314.3%
	LS-SC5	0.39	2.6%	0.017	21.4%
	LS-CS2	0.39	2.6%	0.030	114.3%
	LS-CS22N	0.25	-34.2%	0.156	1014.3%
	LS-CS22S	0.21	-44.7%	0.168	1100.0%
	LS-IPSF22	0.36	-5.3%	0.088	528.6%
10	CLEAN	0.76	0.0%	0.053	0.0%
	LS-CS10	0.61	-19.7%	0.171	222.6%
	LS-IS10	0.63	-17.1%	0.148	179.2%
	LS-SC5	0.79	3.9%	0.048	-9.4%
	LS-CS2	0.69	-9.2%	0.120	126.4%
	LS-CS22N	0.43	-43.4%	0.233	339.6%
	LS-CS22S	0.43	-43.4%	0.238	349.1%
	LS-IPSF22	0.61	-19.7%	0.169	218.9%
15	CLEAN	0.86	0.0%	0.198	0.0%
	LS-CS10	0.71	-17.4%	0.264	33.3%
	LS-IS10	0.67	-22.1%	0.231	16.7%
	LS-SC5	0.93	8.1%	0.189	-4.5%
	LS-CS2	0.74	-14.0%	0.217	9.6%
	LS-CS22N	0.50	-41.9%	0.313	58.1%
	LS-CS22S	0.55	-36.0%	0.319	61.1%
	LS-IPSF22	0.68	-20.9%	0.256	29.3%

TABLE 3-5. EFFECT OF SMOOTH LEWICE ICE SHAPES ON $C_{L, \text{stall}}$, α_{stall} , AND $C_{D \text{min}}$;
 $Re_{MAC} = 1.8 \times 10^6$; $\delta_A = 0^\circ$

Configuration	$C_{L, \text{stall}}$	$\Delta C_{L, \text{stall}}$	α_{stall}	$\Delta \alpha_{\text{stall}}$	C_L at $\alpha = 13.8^\circ$	ΔC_L at $\alpha = 13.8^\circ$	$C_{D, \text{min}}$	$\Delta C_{D, \text{min}}$	C_D at $\alpha = 13.8^\circ$	ΔC_D at $\alpha = 13.8^\circ$
Clean	0.87	0.0%	13.8°	0.0%	0.87	0.0%	0.006	0.0%	0.147	0.0%
LS-CS10	0.71	-18.4%	14.6°	5.8%	0.70	-19.5%	0.078	1200.0%	0.229	55.8%
LS-IS10	0.68	-21.8%	13.6°	-1.4%	0.68	-21.8%	0.036	500.0%	0.202	37.4%
LS-SC5	0.94	8.0%	14.8°	7.2%	0.93	6.9%	0.010	66.7%	0.124	-15.6%
LS-CS2	0.75	-13.8%	14.7°	6.5%	0.74	-14.9%	0.017	183.3%	0.182	23.8%
LS-CS22N	0.49	-43.7%	13.5°	-2.2%	0.49	-43.7%	0.128	2033.3%	0.289	96.6%
LS-CS22S	0.54	-37.9%	13.4°	-2.9%	0.54	-37.9%	0.148	2366.7%	0.294	100.0%
LS-IPSF22	0.69	-20.7%	14.6°	5.8%	0.68	-21.8%	0.066	1000.0%	0.225	53.1%

TABLE 3-6. EFFECT OF SMOOTH LEWICE ICE SHAPES ON HINGE-MOMENT
COEFFICIENT SLOPE; $Re_{MAC} = 1.8 \times 10^6$; $\delta_A = 0^\circ$

Ice Shape	Region A		Region B		Region C	
	$dC_H/d\alpha$ (per deg)	α -range (deg)	$dC_H/d\alpha$ (per deg)	α -range (deg)	$dC_H/d\alpha$ (per deg)	α -range (deg)
Clean	-0.0026	0 to 10	-0.0155	10 to 14	-0.0001	14 to 20
LS-CS10	-0.0134	0 to 7	-0.0014	7 to 15	-0.0024	14 to 20
LS-IS10	-0.0067	0 to 7	-0.0033	7 to 13	-0.0023	13 to 20
LS-SC5	-0.0027	0 to 11	-0.0175	11 to 14	0.0003	14 to 20
LS-CS2	-0.0031	0 to 8	-0.0068	8 to 14	-0.0017	14 to 20
LS-CS22N	-0.0089	0 to 6	-0.0039	6 to 14	-0.0060	14 to 20
LS-CS22S	-0.0095	0 to 7	-0.0045	7 to 13	-0.0016	13 to 20
LS-IPSF22	-0.0109	0 to 7	-0.0014	7 to 14	-0.0021	14 to 20

TABLE 3-7. EFFECT OF ROUGH LEWICE ICE SHAPES ON C_L AND C_D ;
 $Re_{MAC} = 1.8 \times 10^6$; $\delta_A = 0^\circ$

α (deg)	Configuration	C_L	ΔC_L	C_D	ΔC_D
3	CLEAN	0.22	0.0%	0.008	0.0%
	LR-CS10	0.18	-18.2%	0.077	862.5%
	LR-IS10	0.22	0.0%	0.043	437.5%
	LR-SC5	0.21	-4.5%	0.014	75.0%
	LR-CS2	0.21	-4.5%	0.023	187.5%
	LR-CS22N	0.17	-22.7%	0.189	2262.5%
	LR-CS22S	0.15	-31.8%	0.214	2575.0%
5	LR-IPSF22	0.21	-4.5%	0.070	775.0%
	CLEAN	0.38	0.0%	0.014	0.0%
	LR-CS10	0.33	-13.2%	0.091	550.0%
	LR-IS10	0.38	0.0%	0.060	328.6%
	LR-SC5	0.38	0.0%	0.019	35.7%
	LR-CS2	0.38	0.0%	0.032	128.6%
	LR-CS22N	0.24	-36.8%	0.202	1342.9%
10	LR-CS22S	0.21	-44.7%	0.225	1507.1%
	LR-IPSF22	0.36	-5.3%	0.089	535.7%
	CLEAN	0.76	0.0%	0.053	0.0%
	LR-CS10	0.55	-27.6%	0.168	217.0%
	LR-IS10	0.61	-19.7%	0.147	177.4%
	LR-SC5	0.76	0.0%	0.058	9.4%
	LR-CS2	0.69	-9.2%	0.121	128.3%
15	LR-CS22N	0.40	-47.4%	0.254	379.2%
	LR-CS22S	0.34	-55.3%	0.266	401.9%
	LR-IPSF22	0.57	-25.0%	0.167	215.1%
	CLEAN	0.86	0.0%	0.198	0.0%
	LR-CS10	0.61	-29.1%	0.249	25.8%
	LR-IS10	0.63	-26.7%	0.226	14.1%
	LR-SC5	0.98	14.0%	0.212	7.1%
	LR-CS2	0.72	-16.3%	0.218	10.1%
	LR-CS22N	0.41	-52.3%	0.307	55.1%
	LR-CS22S	0.35	-59.3%	0.311	57.1%
	LR-IPSF22	0.61	-29.1%	0.246	24.2%

TABLE 3-8. EFFECT OF ROUGH LEWICE ICE SHAPES ON $C_{L,stall}$,
 α_{stall} , AND $C_{D,min}$; $Re_{MAC} = 1.8 \times 10^6$, $\delta_A = 0^\circ$

Configuration	$C_{L,stall}$	$\Delta C_{L,stall}$	α_{stall}	$\Delta \alpha_{stall}$	C_L at $\alpha = 13.8^\circ$	ΔC_L at $\alpha = 13.8^\circ$	$C_{D,min}$	$\Delta C_{D,min}$	C_D at $\alpha = 13.8^\circ$	ΔC_D at $\alpha = 13.8^\circ$
Clean	0.87	0.0%	13.8°	0.0°	0.87	0.0%	0.006	0.0%	0.147	0.0%
LR-CS10	0.61	-29.9%	13.6°	-0.2°	0.61	-29.9%	0.076	1166.7%	0.221	50.3%
LR-IS10	0.65	-25.3%	13.6°	-0.2°	0.64	-26.4%	0.039	550.0%	0.200	36.1%
LR-SC5	0.98	12.6%	15.8°	2.0°	0.92	5.7%	0.013	116.7%	0.146	-0.7%
LR-CS2	0.72	-17.2%	13.7°	-0.1°	0.72	-17.2%	0.020	233.3%	0.184	25.2%
LR-CS22N	0.41	-52.9%	11.4°	-2.4°	0.40	-54.0%	0.182	2933.3%	0.291	98.0%
LR-CS22S	0.34	-60.9%	10.3°	-3.5°	0.33	-62.1%	0.205	3316.7%	0.295	100.7%
LR-IPSF22	0.61	-29.9%	12.6°	-1.2°	0.61	-29.9%	0.065	983.3%	0.218	48.3%

TABLE 3-9. EFFECT OF ROUGH LEWICE ICE SHAPES ON HINGE-MOMENT
COEFFICIENT SLOPE; $Re_{MAC} = 1.8 \times 10^6$, $\delta_A = 0^\circ$

Ice Shape	Region A		Region B		Region C	
	$dC_H/d\alpha$ (per deg)	α -range (deg)	$dC_H/d\alpha$ (per deg)	α -range (deg)	$dC_H/d\alpha$ (per deg)	α -range (deg)
Clean	-0.0026	0 to 10	-0.0155	10 to 14	-0.0001	14 to 20
LR-CS10	-0.0164	0 to 6	-0.0017	6 to 13	-0.0023	13 to 20
LR-IS10	-0.0062	0 to 6	-0.0040	6 to 13	-0.0021	13 to 20
LR-SC5	-0.0026	0 to 11	-0.0157	11 to 15	0.0005	15 to 20
LR-CS2	-0.0032	0 to 8	-0.0101	8 to 12	-0.0016	12 to 20
LR-CS22N	0.0007	0 to 7	-0.0036	7 to 11	-0.0100	11 to 20
LR-CS22S	0.0007	0 to 5	0.0009	5 to 10	-0.0120	10 to 20
LR-IPSF22	-0.0160	0 to 6	-0.0013	6 to 12	-0.0025	12 to 20

3.2.3.1 Clean Wing.

Maximum lift coefficient for the clean wing was 0.87 and occurred at an α of 13.8° , as shown in figure 3-34(a) and in table 3-2. The lift dropped gradually after stall and was reduced to about 0.81 at α of 20° . The slope of the linear portion of the lift curve was 4.41 per radian or 0.077 per degree. This slope correlates well with the slope of 0.064 obtained from equation 3-5 [16].

$$C_{L\alpha} = \frac{a_0 \cdot AR}{\left(\frac{a_0}{\pi}\right) + \sqrt{\left(\frac{AR}{\cos\Lambda_{1/2}}\right)^2 + \left(\frac{a_0}{\pi}\right)^2} - (AR \cdot M_\infty)^2} \quad (3-5)$$

where a_0 is the 2D lift slope of the GLC-305 airfoil and is equal to 0.084 per degree based on the data of reference 17, $\Lambda_{1/2}$ is the wing sweep angle at 50% chord and is equal to 22° , AR is the wing aspect ratio (6.8) given in figure 2-3 and M_∞ is the free-stream Mach number, which for the WSU wind tunnel tests was 0.185, as shown in table 2-4.

From examination of the pressure distributions and the flow visualization data obtained, flow separation was initiated at the wing LE and was combined with a leading-edge vortex. Flow separation was first observed for α of 9° near the 30% semispan station. The region of flow separation was very small in both the spanwise and chordwise directions (2% chord and about 3% semispan). As α was increased to 10° , a large trapezoidal region of rough and separated flow was observed between the 30% and 85% semispan stations and between 12% and 60% of wing chord. At α of 11° , considerable TE separation occurred near the wing trailing edge over a chord length of about 20%. Trailing edge separation extended from about 55% semispan to the wing tip. At α of 12° , flow separation was observed over the wing tip (outboard 15% of semispan) and near the TE of the inboard (5% to 30% semispan) portion of the wing. Finally, at α between 13° and 14° , complete flow separation occurred over most of the wing upper surface which led to wing stall.

Drag performance for the clean wing is presented in figure 3-34(c) and in tables 3-1 and 3-2. The minimum drag coefficient was 0.006 at α of 1° . The drag increased to a maximum value at

about 0.28 at α of 20° . The maximum lift to drag ratio for the swept wing was 27.5 at α of 3.2° . Pitching moment about the 25% MAC location was nearly flat, as shown in figure 3-34(e), until about stall where a considerable increase in negative pitching moment (leading edge down) was observed as the load center moved downstream of the quarter-chord point due to flow separation. Pitching-moment coefficient ranged from -0.187 to 0.15. The pitching moment is slightly stable and there is a tendency for pitch up at α of 10° to 12° . The pitching moment then breaks with positive stability, airplane nose down, following stall and α in the range 15° to 17° .

Hinge-moment coefficients are presented in figure 3-34(f) and in table 3-3. The maximum slope of the hinge-moment coefficient occurred in region B and was -0.0155 per degree. This corresponds to a change in hinge moment of 0.52 in-lb per degree for the wing model tested. For a control deflection of 0° , the hinge-moment coefficient was negative (i.e., leading edge down) for positive C as expected. The graph of hinge moment coefficient versus α is linear in the region corresponding to the linear part of the lift curve and breaks as maximum lift is approached and the hinge moment slightly reverses at α larger than 15° .

3.2.3.2 Icing Research Tunnel Ice Shape Castings.

3.2.3.2.1 Lift Coefficient.

Ice shapes caused significant changes in the wing lift characteristics, as shown in figures 3-34(a) and 3-34(b). With the exception of the IRT-SC5 ice shape, which increased $C_{L, \text{stall}}$ and α_{stall} with respect to the clean wing, all ice shapes reduced lift throughout the α -range. In addition, the iced wing α_{stall} and the linear lift slope were reduced with respect to the clean configuration. Table 3-1 provides lift performance for the clean and iced wing cases for angles of attack corresponding to the linear and nonlinear portions of the lift curve. Table 3-2 compares $C_{L, \text{stall}}$ and α_{stall} for all six ice shapes tested. The $C_{L, \text{stall}}$ reduction was in the range of 11.5% to 93.6% and the corresponding reduction in α_{stall} ranged from 8% to 56%. The largest degradation in lift performance was obtained with the IRT-CS22 ice shape. For this ice shape, the large upper and lower horns near the wing leading edge caused extensive flow separation, even at low α . The improved lift performance observed with the IRT-SC5 ice shape was mainly due to the small leading-edge droop (LE flap effect) caused by the ice shape. The pressure distributions at the 50% semispan station presented in figure 3-36 demonstrate that for α of 8° , the suction peak for the IRT-SC5 case was lower than the clean wing, indicating a lower effective α . In addition, figure 3-36(f) shows that at α of 16° , the baseline experienced extensive flow separation, while flow separation for the wing with the IRT-SC5 ice shape was considerably reduced.

The aerodynamic performance data for the IRT-CS2, IRT-CS10, and IRT-CS22 complete scallop glaze ice shapes indicate that the ice shapes with the larger horn size resulted in greater penalties in lift characteristics, as shown in figures 3-34(a) and 3-34(b). The iced wing performance in terms of α_{stall} and $C_{L, \text{stall}}$ was progressively reduced in the following ice shape sequence: IRT-CS2, IRT-CS10, and IRT-CS22.

3.2.3.2.2 Drag Coefficient.

The increase in the drag coefficient due to the ice shapes tested is demonstrated in figures 3-34(c) and 3-34(d) and in tables 3-1 and 3-2. In general, the increase in minimum drag due to the ice accretions ranged from 1.3 to 35 times that of the clean wing. The smallest drag rise was caused by the IRT-SC5 ice shape, while the largest drag increment was due to the IRT-CS22 wing. Near the α_{stall} of the clean wing, the drag due to the ice shapes was 17% to 104% greater than the clean wing. Furthermore, as the ice shape horn size increased (from IRT-CS2 to IRT-CS22 ice shapes), the drag increment of the iced wing increased, due to increased flow separation downstream of the ice shape.

3.2.3.2.3 Pitching-Moment Coefficient.

All pitching moment data presented in figure 3-34(e) are about the 25% MAC point. The addition of the ice shapes caused considerable changes in $C_{M, \text{MAC}/4}$ due to the shift in the load distribution caused by the separated flow downstream of the ice shapes. In general, for positive α , the ice shapes caused more positive pitching moment prior to stall compared to the clean wing case. Thus, the lift vector for the iced wing was upstream of the 25% MAC location. The ice shape causes unstable behavior, with a break at α of 6° . Stability increases for α greater than 6° . Note that a 0.01 change in the value of the pitching-moment coefficient corresponds to a change of 5.7 ft-lb in pitching moment about the MAC/4 point.

3.2.3.2.4 Hinge-Moment Coefficient.

The differences observed between the clean and iced wing cases in figure 3-34(f) were mainly due to the increased separation over the aileron upper surface caused by the ice shapes. In general, the ice shapes moved the start of region B to the left (lower α) and increased the hinge-moment coefficients over region B (C_H became more negative). In all cases, the maximum hinge moment for the iced wing in region C was bounded by the maximum C_H of the clean wing, as shown in figure 3-34(f). Note a shift in the entire C_H versus α plot. A control force reversal (i.e., change in C_H from positive to negative) was observed between α of 0° and 3° for the 10- and 22.5-min ice shapes. This was caused by increased flow separation over the lower surface of the wing that resulted in greater suction over the control lower surface. Thus, the aileron had the tendency to move trailing edge down for α between 0° and 3° .

The effect of horn height on aileron hinge moments can be assessed by reviewing the results obtained with the 2-min (IRT-CS2), 10-min (IRT-CS10), and 22.5-min (IRT-CS22) complete scallop glaze ice shapes. As demonstrated in table 3-3, the slope of the C_H curve in region B decreased as the ice horn height was decreased. However, in regions A and C, the C_H slope increased as the ice shape horn height was increased.

3.2.3.2.5 Pressure Distributions.

Pressure distributions corresponding to wing sections at the 15%, 50%, and 85% semispan locations are presented in figures 3-35, 3-36, and 3-37, respectively. The pressures are for α of -4° , 0° , 4° , 8° , 12° , and 16° , which cover the linear and nonlinear lift range. The results indicate

that, in most cases, the addition of ice shapes resulted in a dramatic change in the clean wing pressure distribution. Near the wing LE, surface pressures for the iced wing featured a region of separated flow, which was characterized by a flat pressure distribution followed by pressure recovery. The region under the flat curve in the pressure data indicates the presence of a separated flow bubble. The extent of bubble was a function of ice shape and α . In many cases, particularly near the 50% and 85% spanwise stations, massive flow separation was observed as α was increased. Massive flow separation was associated with flat pressure distributions that extended to the wing TE. At high positive α , separated flow was observed over the wing upper surface. For ice shape with the large horns, extensive flow separation occurred over both wing surfaces at low α . Flow separation caused considerable changes in the load distribution over the wing and the control surface, which was the main reason for the observed changes in aerodynamic performance and aileron hinge moment with respect to the clean wing. Pressure trends for the iced configurations and for each α presented in figures 3-35, 3-36, and 3-37 are summarized below:

- $\alpha = -4^\circ$: In general, suction was observed over the lower surface of the wing and was associated with a leading-edge bubble. For all ice shapes, the bubble extent increased towards the outboard sections of the wing. In most cases, the highest suction occurred near the inboard sections of the wing (i.e., 0% to 30% of semispan). The IRT-CS22 ice shape caused massive flow separation at practically all spanwise stations.
- $\alpha = 0^\circ$: Suction remained higher over the lower surface for practically all ice shapes. Once again, LE bubbles were evident at all three spanwise locations for most of the ice shapes tested. The bubble extent was a function of horn size. Large horns resulted in longer bubbles. For the IRT-CS10, IRT-IS10, IRT-CS22, and IRT-IPSF22 ice shapes, the maximum suction occurred at spanwise stations located between 15% and 50% semispan. For the small ice accretions, namely IRT-SC5 and IRT-CS2, the maximum suction took place over the outboard part of the wing. Note that at α of 0° , the wing tip was at a geometric α of -4° due to the wing twist.
- $\alpha = 4^\circ$: For this angle of attack, suction for most of the ice shape cases was increased over the wing upper surface. The C_p on the lower surface varied from negative near the LE, indicating the presence of separation bubbles, to low negative and, in some cases, positive near the TE. The extent of the upper surface bubbles varied with spanwise distance from root to tip due to the negative wing twist, which resulted in a lower α_{local} over the outboard sections. For the 10- and 22.5-min ice shapes, the extent of the separation bubbles was, in most cases, greater over the middle and outboard sections of the wing. For these ice shapes, maximum suction did not vary significantly with spanwise location.
- $\alpha = 8^\circ$: Upper surface suction and bubble extent was increased at this α at all spanwise stations for ice shapes IRT-CS10, IRT-IS10, IRT-CS2, IRT-CS22, and IRT-IPSF22. For the 10- and 22.5-min ice shapes, extensive flow separation was observed at the 85% semispan station. The 5-min rime ice shape, IRT-SC5, did not exhibit bubble formation over the two inboard stations. However, at the outboard station (85% semispan), a small bubble extending to about 20% chord was observed. Maximum upper surface suction

took place over the wing near 15% semispan. The only exception was the IRT-CS22 case for which the maximum suction occurred at the 85% semispan station. With the exception of the IRT-CS22 ice shape, all other ice shapes had positive or low negative pressure coefficients over the lower surface of the wing.

- $\alpha = 12^\circ$: Large bubbles were observed at the 15% semispan station and complete flow separation was evident over the wing upper surface at the 50% and 85% semispan locations with the 10- and 22.5-min ice shapes tested. The flow over the IRT-SC5 and IRT-CS2 ice shapes exhibited smaller bubbles compared to the larger ice shapes. The bubbles for these two ice accretions extended from about 20% to about 75% chord length, depending on ice shape and spanwise station. For all ice shapes, maximum suction was observed at the inboard station located at 15% semispan.
- $\alpha = 16^\circ$: At this angle of attack, massive flow separation was evident over the wing upper surface at all spanwise stations for all 10- and 22.5-min ice shapes. In all cases, maximum suction took place at the 15% semispan station. The 2- and 5-min ice accretions exhibited long bubbles over the inboard stations. However, at the outboard stations, the flow for these two ice shapes was completely separated over the wing upper surface.

The impact of the horn size on aerodynamic performance can be explained by reviewing the pressure distributions. Specifically for ice shapes with large horn heights, LE separation bubbles were observed at low α . These bubbles became progressively longer in the chordwise direction and eventually burst to form a region of massive flow separation. Ice shapes of smaller horn size formed bubbles with smaller chordwise extent. These bubbles did not appear until α was higher with respect to where the bubbles were observed with the larger horn ice shapes. With the IRT-CS22 configuration, extensive flow separation occurred over the wing suction surface even at low α . Although the flow over the upper surface of wing with the IRT-CS22 ice shape remained separated throughout the positive α -range, the lift increased as α was increased beyond about 6° . This was due to the increase in the pressure on the lower surface of the wing where the flow remained mostly attached. Pressure on the upper surface did not vary significantly with α once the wing had stalled.

3.2.3.3 Smooth LEWICE Ice Shapes.

The effects of the smooth LEWICE ice shapes on wing performance are demonstrated in figures 3-38 to 3-41 and in tables 3-4 to 3-6.

3.2.3.3.1 Lift Coefficient.

With the exception of the LS-SC5 ice shape, which increased $C_{L,stall}$ and α_{stall} , all ice shapes reduced lift performance with respect to the clean wing, as demonstrated in figures 3-38(a) and 3-38(b) and in tables 3-4 and 3-5. In assessing these reductions note that they could be larger if clean wing data were available for higher Reynolds numbers. The iced wing lift curves exhibited reduced lift coefficient and lower lift slope with respect to that of the clean wing. The reduction of $C_{L,stall}$ ranged from 18.4% to 43.7%. The largest loss in lift was obtained with the LS-CS22N ice shape. As shown in table 3-5, smooth LEWICE ice shapes LS-CS10, LS-SC5, LS-CS2, and

LS-IPSF22 increased α_{stall} by 5.8% to 7.2%, while LS-IS10, LS-CS22N, and LS-CS22S ice shapes reduced α_{stall} by 1.4% to 2.9%. The 5-min rime ice shape LS-SC5 increased $C_{L,\text{stall}}$ by 7% and increased α_{stall} by 1°. The observed performance increment in the iced wing lift was due to the leading-edge droop (i.e., leading-edge flap effect) caused by the 5-min rime ice shape.

The effect of horn height on the lift performance can be observed by comparing the iced wing lift performance with the LS-CS2, LS-CS10, LS-CS22N, and LS-CS22S ice shapes. The $C_{L,\text{stall}}$ reduction with respect to the clean wing was -13.8%, -18.4%, -43.7%, and -38% for the LS-CS2, LS-CS10, LS-CS22N, and LS-CS22S ice shapes respectively. The corresponding change in α_{stall} was 6.5%, 5.8%, -2.2%, and -2.9% for the same sequence of ice shapes.

3.2.3.3.2 Drag Coefficient.

In general, all smooth LEWICE ice shapes increased wing drag considerably, as demonstrated in figures 3-38(c) and 3-38(d) and in tables 3-4 and 3-5. The results presented show that the increase in $C_{D,\text{min}}$ due to the ice shapes ranged from 66.7% for ice shape LS-SC5 to 2366.7% for ice shape LS-CS22S with respect to the clean wing. For α near the clean wing α_{stall} , drag rise for the iced wing was in the range of -15.6% for the LS-SC5 to 100% for LS-CS22S with respect to the clean case. The effects of the LEWICE ice shape horn height on C_D was similar to that obtained with the IRT ice shapes, i.e., ice shapes with larger horn heights produced greater drag increments. Moreover, the larger horns of the LS-CS22S ice shape produced a larger drag increment with respect to the clean wing at lower α in comparison to the LS-CS22N ice shape. As α was increased, the difference in drag performance between these two 22.5-min ice shapes diminished.

3.2.3.3.3 Pitching-Moment Coefficient.

From figure 3-38(e), it is observed that the pitching moments about the 25% MAC point of the iced wing were considerably more positive or more negative than the clean wing, depending on α . This was the result of a shift in the center of the aerodynamic load due to flow separation. In general, flow separation downstream of the iced shape resulted in a front-loaded pressure distribution caused by the leading-edge separation bubbles. Another contributing factor to the observed increase in iced wing pitching moment was the aerodynamic load on the ice shape, which increased as α was increased. The largest increment in C_M was obtained with the LS-CS22N ice shape.

Pitching moment for the LS-SC5 configuration was comparable to the clean wing, particularly for α in the range of -4° to approximately 12°. As α was increased above 12°, however, the LS-SC5 ice shape produced more positive or more negative C_M than the clean case. The similarities and differences in the C_M curves of the clean and LS-SC5 cases can be explained by reviewing the C_p distributions shown in figures 3-39 to 3-41. For α of 4° and 8°, LS-SC5 produced a lower suction peak than the baseline at all three spanwise stations. However, pressure recovery downstream of the suction peak and the C_p distributions over the lower surface were similar to the clean case. As a result, iced wing C_M at 4° and 8° α was comparable to the clean wing. On the other hand, as α was increased to 12°, the iced configuration (LS-SC5) had a greater suction peak than the clean case at 50% semispan and over the outboard wing stations. As α was further

increased to 16° , while both configurations (clean and LS-SC5) experienced extensive flow separation near the wing tip, the LS-SC5 ice shape resulted in a separation bubble on the wing suction surface and produced higher leading-edge suction than the clean case, as shown in figures 3-39(f) and 3-40(f). Consequently, the LS-SC5 case resulted in higher C_M for α greater than 12° .

3.2.3.3.4 Hinge-Moment Coefficient.

Hinge-moment coefficients for all smooth LEWICE ice shapes tested are presented in figure 3-38(f). Hinge-moment coefficient slope ($C_{H\alpha}$) for the clean and iced wing are compared in table 3-6. In general, hinge moments for the iced wing were more positive or more negative with respect to the clean case, particularly in regions A and B of the hinge-moment curve. The observed increase or decrease in hinge moment was the result of flow separation over the aileron due to the ice shapes. In most cases, the start of region B in the iced wing C_H curve was at a lower α , and the slope of C_H was less than the clean wing. Note that the maximum and minimum hinge moments for all ice shape cases were bounded by the maximum and minimum C_H of the clean wing.

3.2.3.3.5 Pressure Distributions.

C_p distributions are presented in figures 3-39 to 3-41 for the 15%, 50%, and 85% semispan stations. Near the wing tip, extensive flow separation was observed over the wing suction surface for most iced configurations, as shown in figure 3-41. Considering the wing pressure distributions with the glaze ice shapes LS-CS2, LS-CS10, LS-CS22N, and LS-CS22S, ice shapes with larger horns produced longer bubbles, as was the case with their IRT ice shape counterparts. In general, the LS-CS22N and LS-CS22S cases had comparable C_p distributions at all stations. However, for 12° and 16° α , the LS-CS22S had higher pressure over the wing lower surface and hence generated higher lift.

3.2.3.4 Rough LEWICE Ice Shapes.

The effects of the rough LEWICE ice shapes on wing performance are demonstrated in figures 3-42 to 3-45 and in tables 3-7 to 3-9. The results showed that, in most cases, the rough LEWICE ice shapes resulted in greater reductions in $C_{L, \text{stall}}$ and α_{stall} and larger drag increments compared to the smooth LEWICE ice shapes. Roughness has a significant impact on the location of flow separation, particularly for large glaze ice shapes where the flow at high Reynolds numbers usually separates near the horn tip. The size of the separated region downstream of the ice shape is a function of the location of the separation point. Rough and smooth ice shapes can result in considerably different aerodynamic effects, particularly when the radius of the horn tips is large. For small ice shapes that do not exhibit horn features such as rime ice shapes, roughness may actually increase aerodynamic performance, depending on the Reynolds number. In this case, the location of flow separation is affected by the state of the boundary layer. At low Reynolds numbers, roughness can increase the energy levels in the boundary layer and delay flow separation, resulting in improved aerodynamic performance such as higher $C_{L, \text{stall}}$ and α_{stall} .

3.2.3.4.1 Lift Coefficient.

Note that effects of higher Reynolds numbers representative of flight on the clean wing are not known. In most cases, the rough LEWICE ice shapes decreased C_L throughout the α -range, as demonstrated in figures 3-42(a) and 3-42(b). One exception to this observation was the 5-min rime ice shape LR-SC5 that resulted in improved lift performance with respect to the clean wing. Tables 3-7 and 3-8 provide lift coefficients for selected angles of attack for the clean and iced wing cases. The reduction in $C_{L, \text{stall}}$ was 30%, 25%, -12.6% (increase), 17%, 53%, 61%, and 30% for the LR-CS10, LR-IS10, LR-SC5, LR-CS2, LR-CS22N, LR-CS22S, and LR-IPSF22, respectively. The reduction in α_{stall} for the glaze-iced configurations ranged from 0.1° to 3.5° , depending on ice shape. The 5-min rime ice shape increased the clean wing α_{stall} by 2° . With the exception of the 5-min rime and 2-min glaze ice shapes, all other rough LEWICE ice shapes reduced the linear lift slope of the clean wing.

Observe that ice shapes with the larger horn size resulted in greater penalties in lift performance, i.e., LR-CS2 ice shape had higher α_{stall} and $C_{L, \text{stall}}$ than LR-CS10, LR-CS22N, and LR-CS22S cases. Effects of horn height on C_L were similar to the trend of IRT ice shapes.

3.2.3.4.2 Drag Coefficient.

Table 3-7 lists C_D of clean and iced configurations at angles of attack of 3° , 5° , 10° , and 15° , while table 3-8 shows the effect of rough LEWICE ice shapes on $C_{D, \text{min}}$. Graphically, the C_D and ΔC_D curves are illustrated in figures 3-42(c) and 3-42(d), respectively. All roughened LEWICE ice shapes increased C_D throughout the α -range. The increase in $C_{D, \text{min}}$ with respect to the clean case ranged from 116.7% for LR-SC5 to 3316.7% for LR-CS22S. In terms of the horn height effects on C_D , the trends were similar to that obtained with the IRT ice shapes, i.e., ice shapes with larger horn heights produced greater drag increments. Moreover, the larger horns of LR-CS22S ice shape produced greater drag at lower α in comparison to the LR-CS22N ice shape. But, as α increased, the difference in drag performance diminished.

3.2.3.4.3 Pitching-Moment Coefficient.

The trends in C_M for the rough LEWICE ice shapes were similar to that obtained with the smooth LEWICE ice shapes, as demonstrated in figure 3-42(e). For positive α less than about 15° , flow separation downstream of the ice shapes caused the lift center to move upstream of the 25% MAC location, which led to more positive (leading edge up) pitching moment than the clean wing. However, for greater α , most of the iced wing cases experienced a large change, from positive to negative, in pitching moment. This was attributed to the flat pressure distribution associated with massive flow separation over the suction surface of the wing. For the glaze ice shapes LR-CS22N and LR-CS22S, the pitching moment remained positive throughout the positive α -range. For these two large ice shapes, extensive flow separation was present over both upper and lower wing surfaces for practically all positive α and the lift center did not move upstream of the 25% MAC location.

3.2.3.4.4 Hinge-Moment Coefficient.

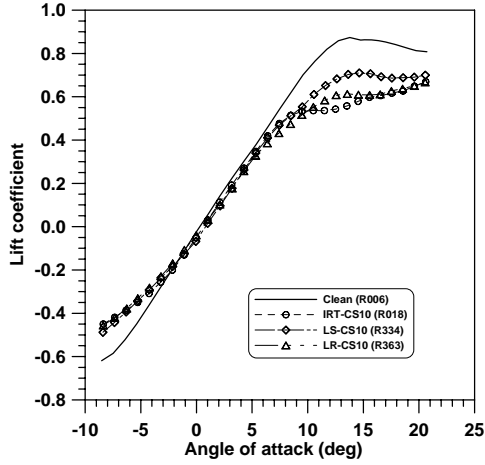
Aileron hinge moments for the iced wing configurations are depicted in figure 3-42(f). Table 3-9 provides the slopes and α -range for regions A, B, and C of the C_H curves. The results show that the LR-SC5 ice shape had a C_H curve similar to the clean case for practically the complete range of angles of attack. The ice shapes LR-CS22N and LR-CS22S resulted in large changes from the clean wing aileron hinge moments. In fact, for α in the range of 6° to 8° for the LR-CS22N case and 6° to 11° for the LR-CS22S ice shape, the aileron hinge moment was nearly zero, indicating zero stick force and possibly aileron float. Force reversal was the result of nearly equal pressure distributions over the suction and pressure sides of the aileron surfaces. The other four rough LEWICE ice shapes (LR-CS10, LR-IS10, LR-CS2, and LR-IPSF22) cause more positive or more negative hinge moments with respect to the clean wing over regions A and B of the C_H curve. Once again, the iced wing hinge moments were bounded by the clean wing C_H limits. One exception was the 5-min rime ice shape that resulted in slightly higher hinge moments with respect to the clean wing in region C of the C_H curve for positive α .

3.2.3.4.5 Pressure Distributions.

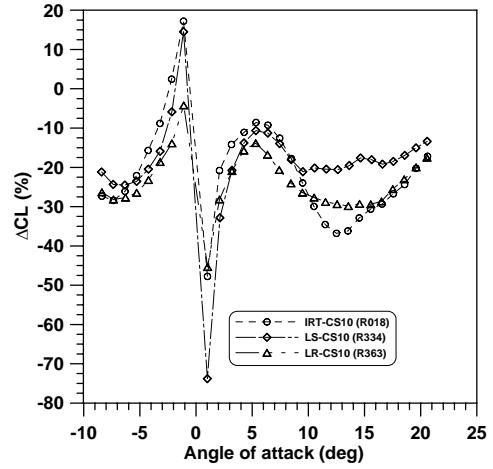
Effects of rough LEWICE ice shapes on pressure distributions are presented in figures 3-43 to 3-45 for the 15%, 50%, and 85% semispan stations. All glaze ice shapes produced separation bubbles downstream of the ice horns, which reduced the suction peak near the leading edge of the clean wing. Among all glaze ice cases, LR-CS2 caused the least penalties on aerodynamic performance due to the fact that its ice horns were smaller. Consequently, for positive α , the separation bubble on the suction wing surface had shorter extent. Pressure distributions aft of the bubble and on the pressure surface were comparable to the clean wing. As the ice shape horn height increased (such as LR-CS10, LR-CS22N, and LR-CS22S configurations), the size of the separation bubble was increased.

3.2.4 Comparison of IRT and LEWICE Ice Shapes.

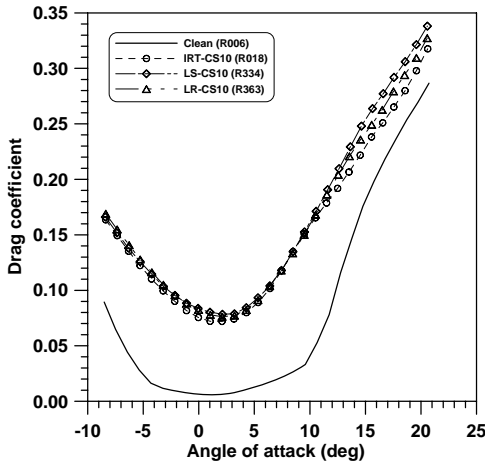
Figures 2-33 to 2-38 demonstrate that the differences in the geometric features of the LEWICE and IRT ice shape sections were considerable for the CS10, IS10, CS22, and IPSF22 cases. These differences included overall shape of ice section, height of the upper and lower ice horns, horn angle with respect to the horizontal and location of horn tip, and root with respect to the leading edge of the wing. For example, at stations A and B, the upper and lower horn tips of IRT-CS10 were further upstream of the LEWICE ice shape (LS-CS10) horn tips, as demonstrated in figure 2-33. In addition, at these two stations, the horn angles with respect to the horizontal were, in most cases, greater for the LEWICE ice shape. Note, however, that the upper and lower horn heights of the LEWICE and the IRT ice shape sections were similar for both spanwise stations. At station C, the LEWICE ice shape upper and lower horns extended further upstream and downstream with respect to the horns of the IRT casting. In addition, the height (distance of horn tip from airfoil LE) of the LEWICE horns was greater. Other significant differences between the simulated and the IRT ice shapes included the intricate roughness and feather-like features seen on the surface of the IRT ice shape castings presented in figure 2-33. To assess the effect of these geometric differences in the actual and simulated ice shapes on aerodynamic performance, experimental data obtained with the castings and the corresponding smooth and rough LEWICE ice shapes are compared in figures 3-46 to 3-69.



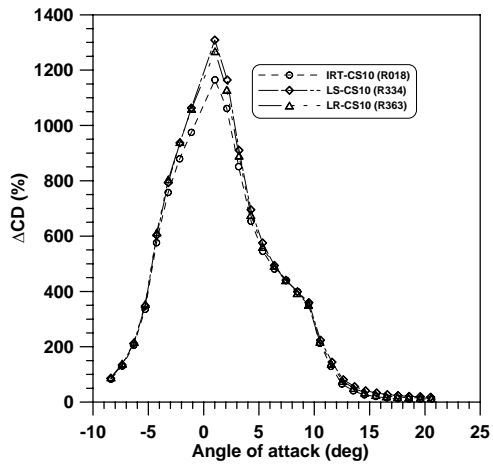
(a) Lift coefficient



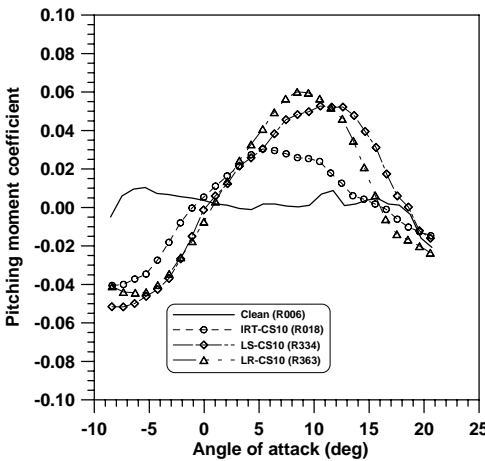
(b) ΔC_L vs α



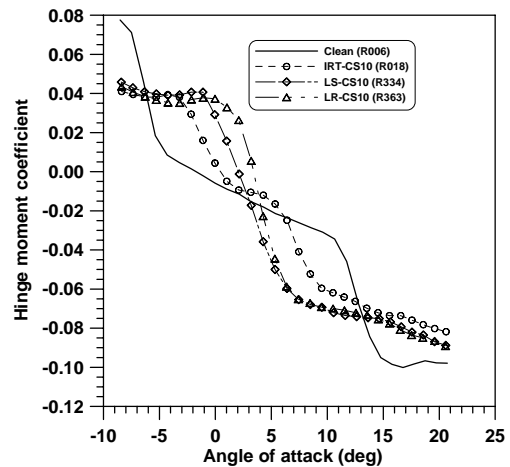
(c) Drag coefficient



(d) ΔC_D vs α

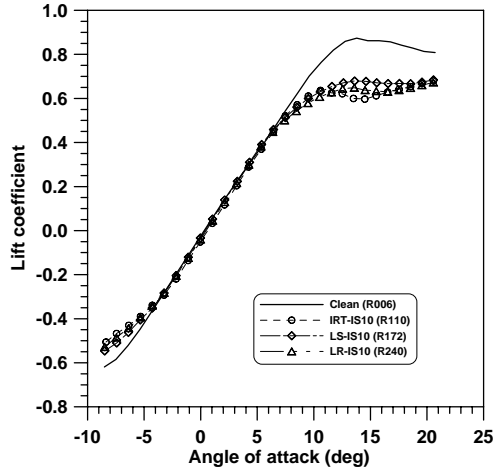


(e) Pitching-moment coefficient

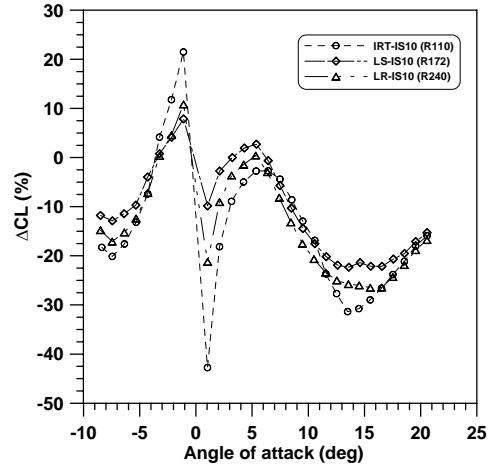


(f) Hinge-moment coefficient

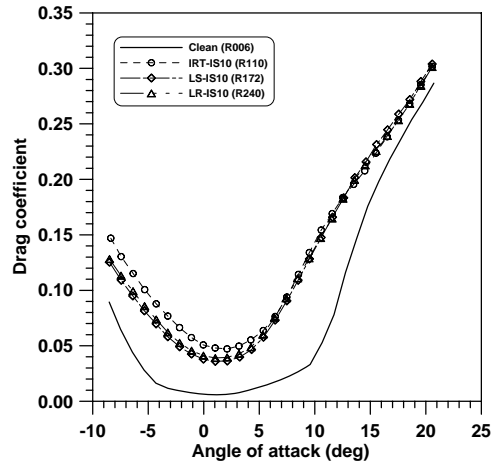
FIGURE 3-46. EFFECT OF IRT-CS10, LS-CS10, AND LR-CS10 ICE SHAPES (ICING CONDITION 1) ON C_L , C_D , C_M , AND C_H ; $Re = 1.8 \times 10^6$; $\delta_A = 0^\circ$



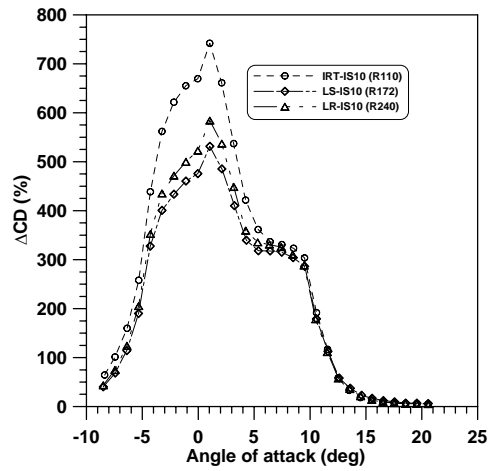
(a) Lift coefficient



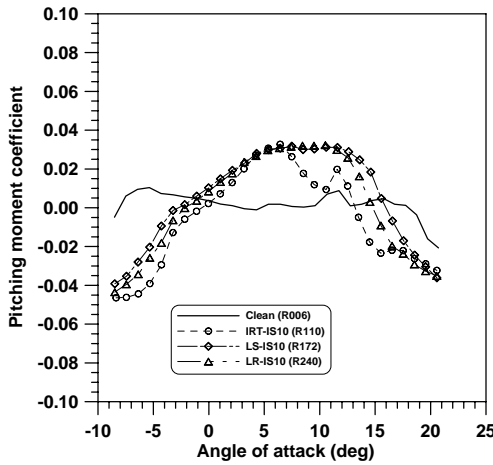
(b) ΔC_L vs α



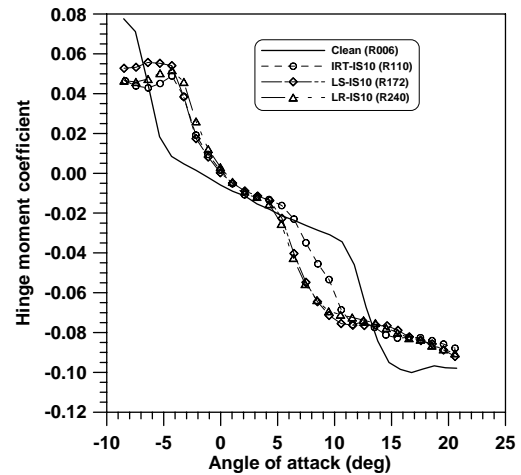
(c) Drag coefficient



(d) ΔC_D vs α

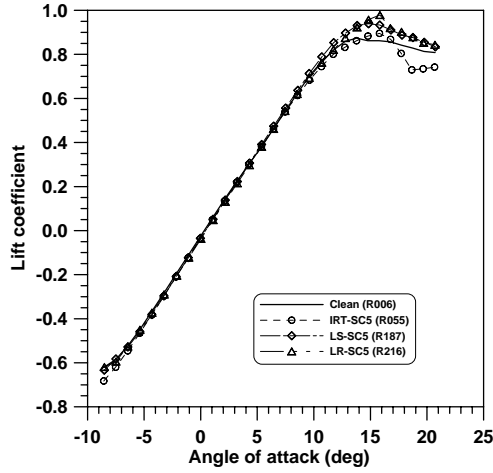


(e) Pitching-moment coefficient

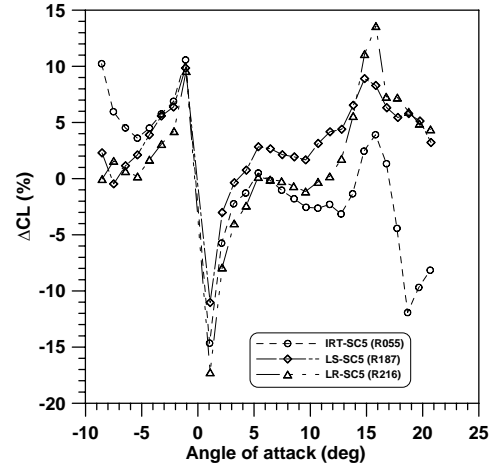


(f) Hinge-moment coefficient

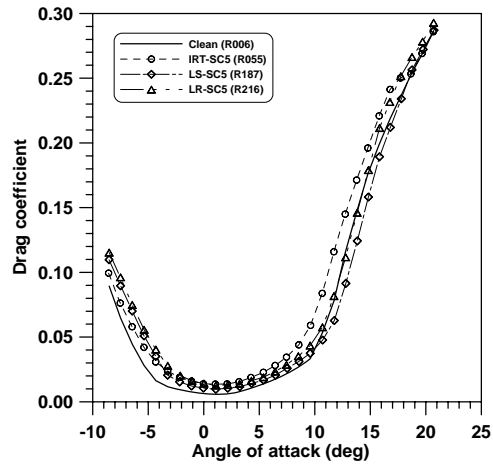
FIGURE 3-47. EFFECT OF IRT-IS10, LS-IS10, AND LR-IS10 ICE SHAPES (ICING CONDITION 2) ON C_L , C_D , C_M , AND C_H ; $Re = 1.8 \times 10^6$; $\delta_A = 0^\circ$



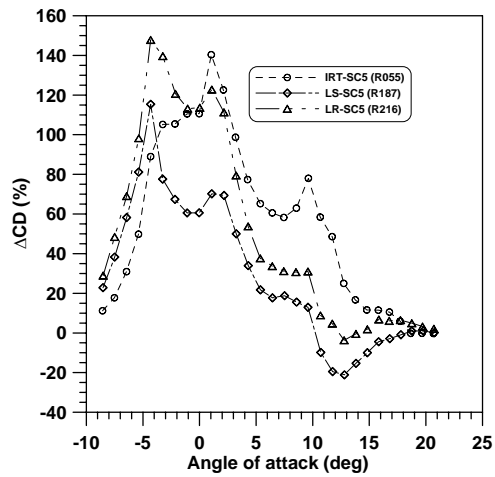
(a) Lift coefficient



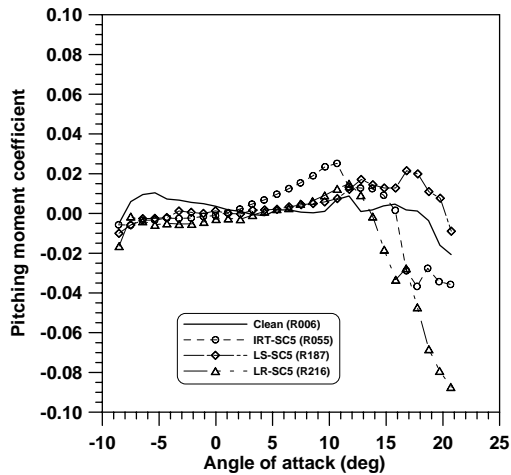
(b) ΔC_L vs α



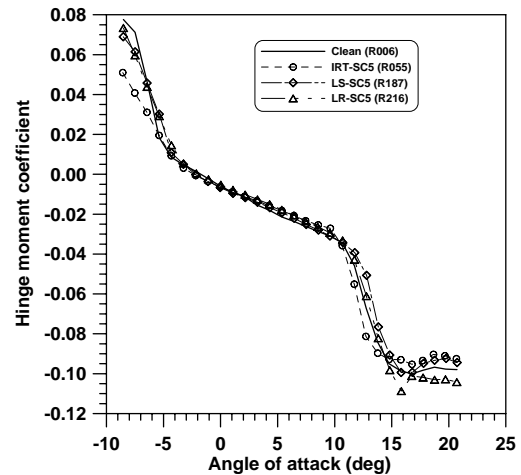
(c) Drag coefficient



(d) ΔC_D vs α

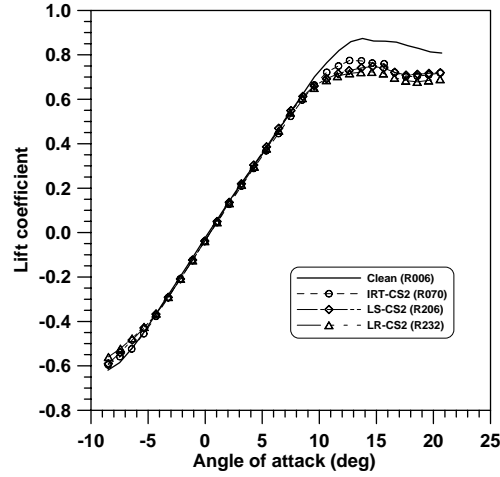


(e) Pitching-moment coefficient

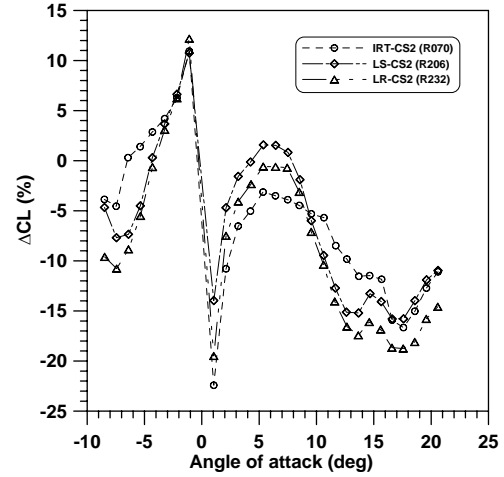


(f) Hinge-moment coefficient

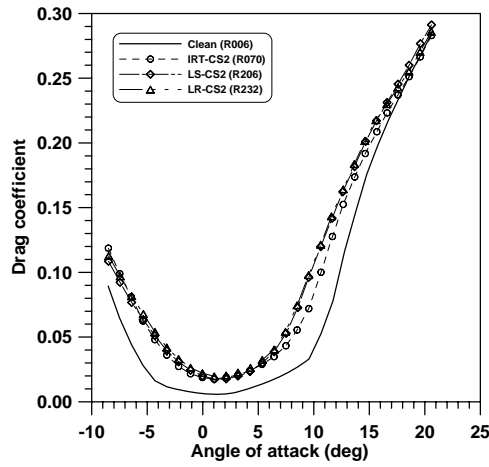
FIGURE 3-48. EFFECT OF IRT-SC5, LS-SC5, AND LR-SC5 ICE SHAPES (ICING CONDITION 3) ON C_L , C_D , C_M , AND C_H ; $Re = 1.8 \times 10^6$; $\delta_A = 0^\circ$



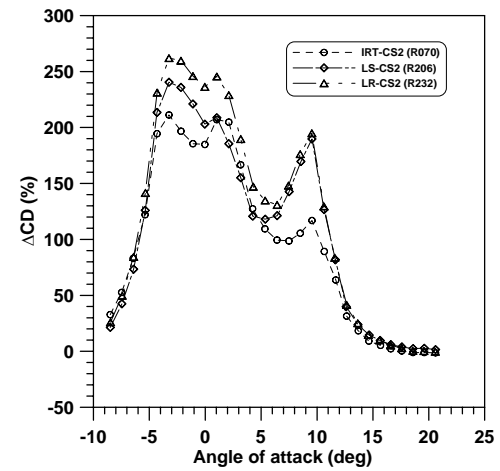
(a) Lift coefficient



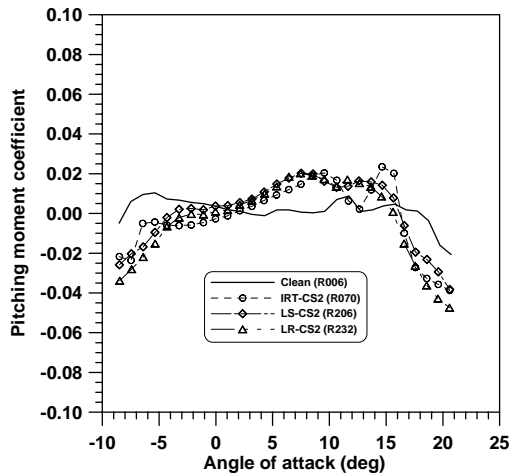
(b) ΔC_L vs α



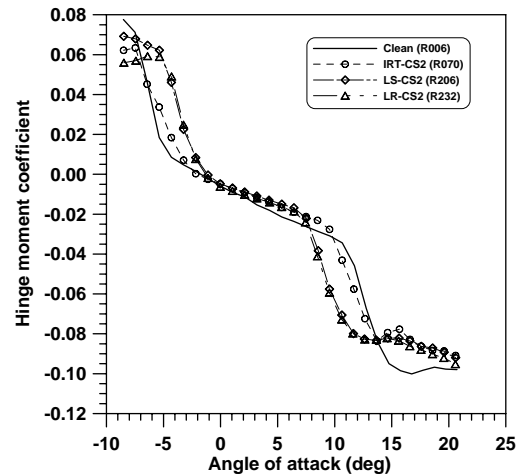
(c) Drag coefficient



(d) ΔC_D vs α

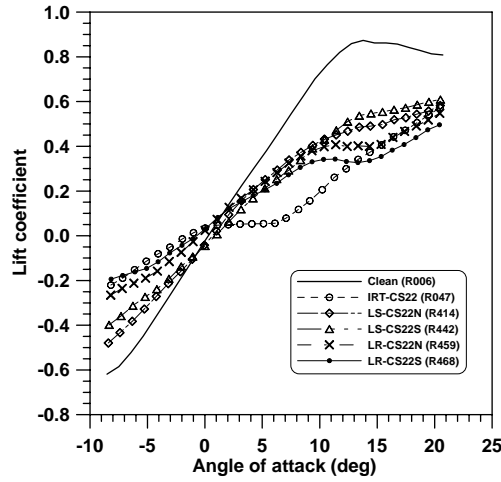


(e) Pitching-moment coefficient

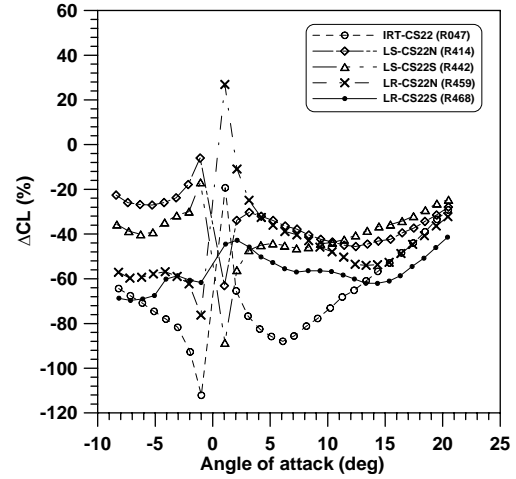


(f) Hinge-moment coefficient

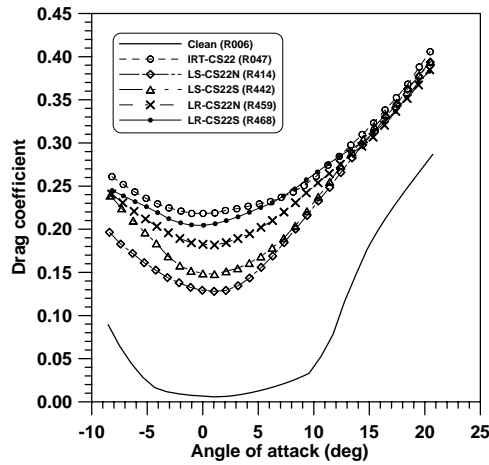
FIGURE 3-49. EFFECT OF IRT-CS2, LS-CS2, AND LR-CS2 ICE SHAPES (ICING CONDITION 4) ON C_L , C_D , C_M , AND C_H ; $Re = 1.8 \times 10^6$; $\delta_A = 0^\circ$



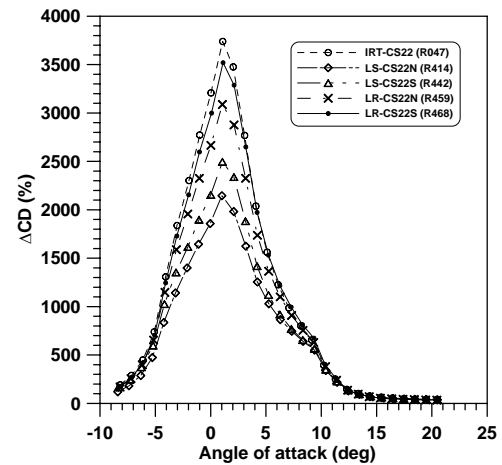
(a) Lift coefficient



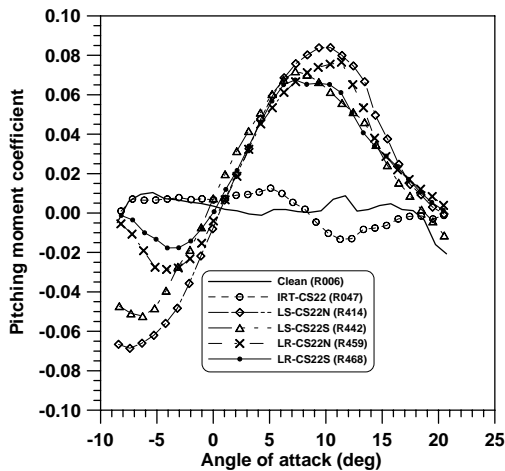
(b) ΔC_L vs α



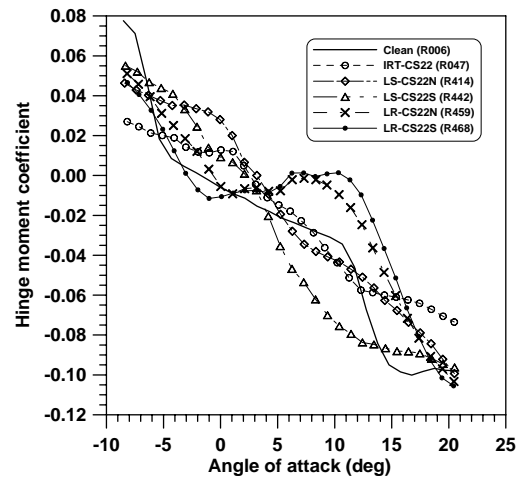
(c) Drag coefficient



(d) ΔC_D vs α

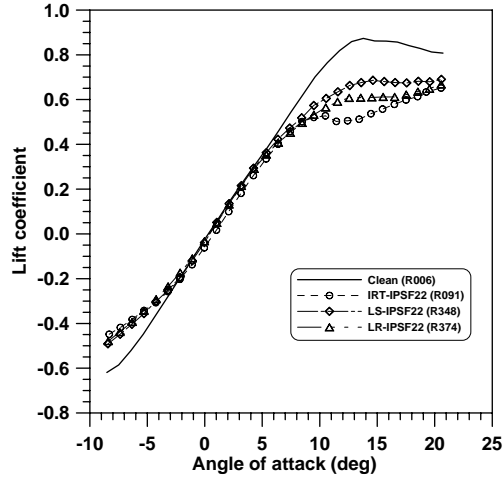


(e) Pitching-moment coefficient

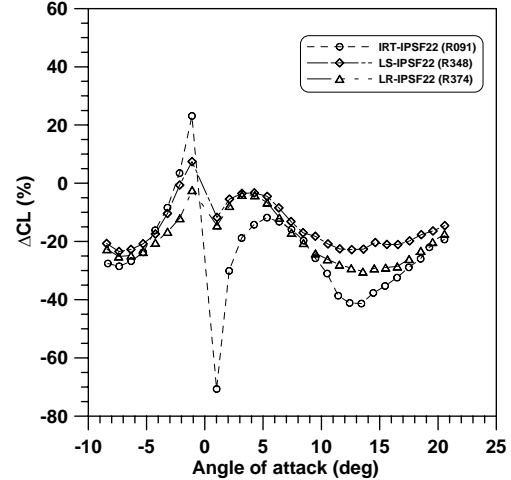


(f) Hinge-moment coefficient

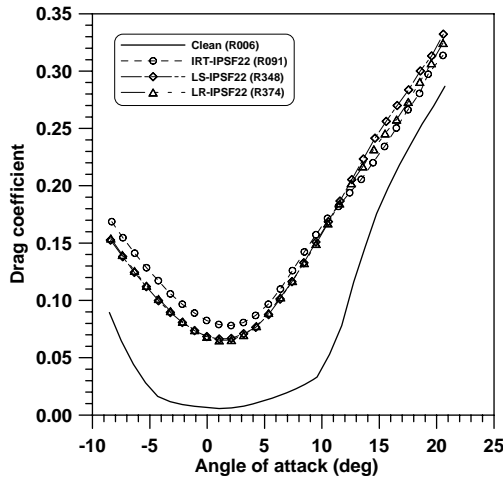
FIGURE 3-50. EFFECT OF IRT-CS22, LS-CS22N, LS-CS22S, LR-CS22N, AND LR-CS22S ICE SHAPES (ICING CONDITION 5) ON C_L , C_D , C_M , AND C_H ; $Re = 1.8 \times 10^6$; $\delta_A = 0^\circ$



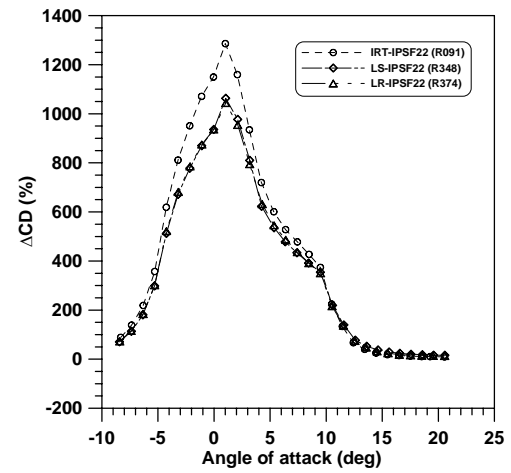
(a) Lift coefficient



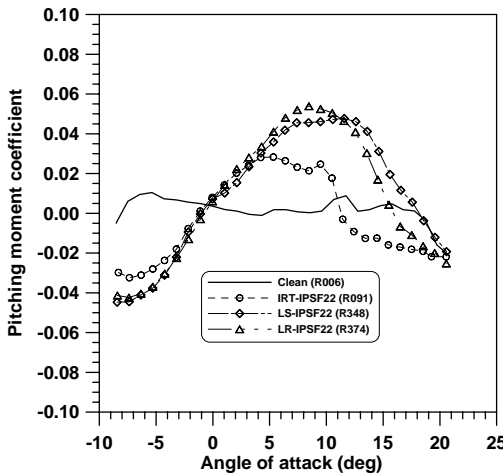
(b) ΔC_L vs α



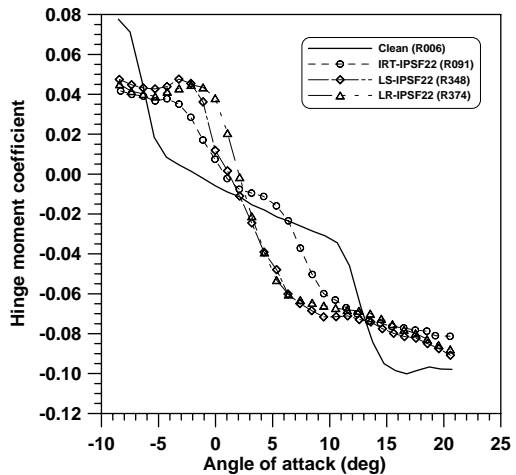
(c) Drag coefficient



(d) ΔC_D vs α

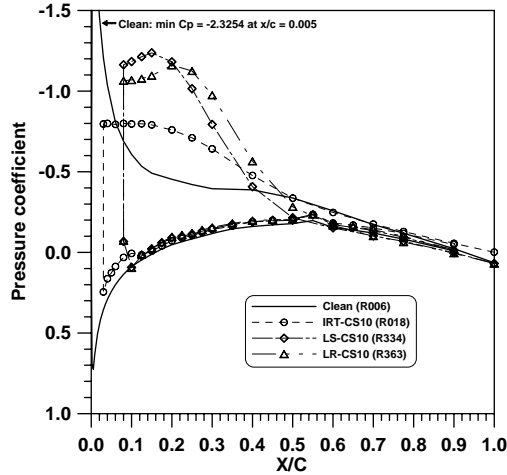


(e) Pitching-moment coefficient

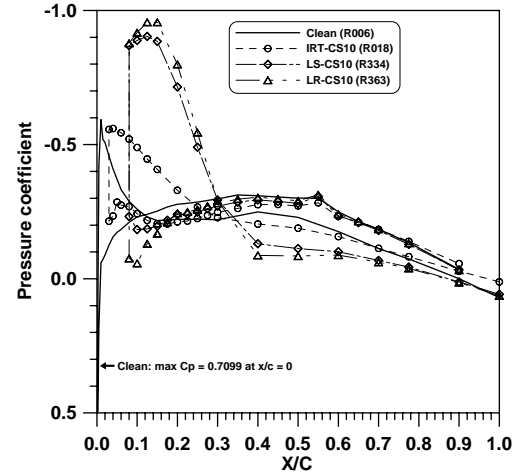


(f) Hinge-moment coefficient

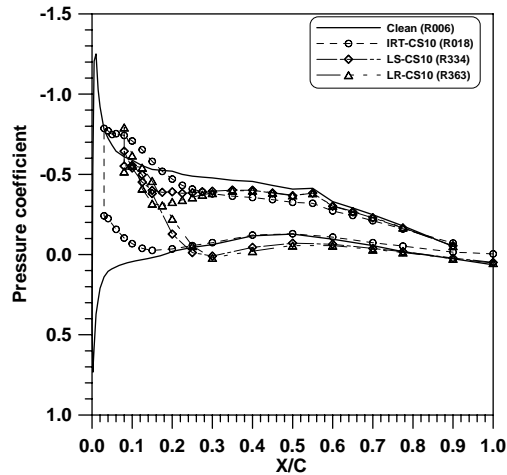
FIGURE 3-51. EFFECT OF IRT-IPSF22, LS-IPSF22, AND LR-IPSF22 ICE SHAPES (ICING CONDITION 6) ON C_L , C_D , C_M , AND C_H ; $Re = 1.8 \times 10^6$; $\delta_A = 0^\circ$



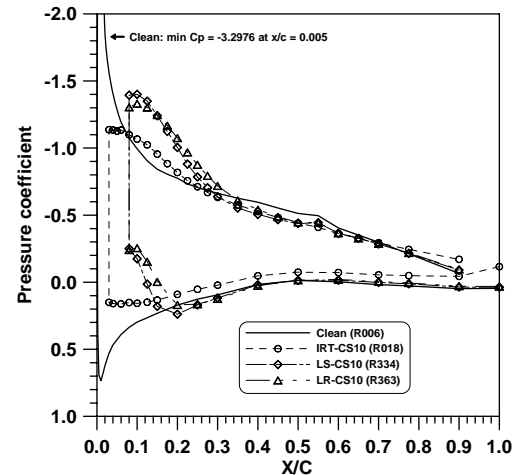
(a) C_p vs x/c ($\alpha = -4^\circ$)



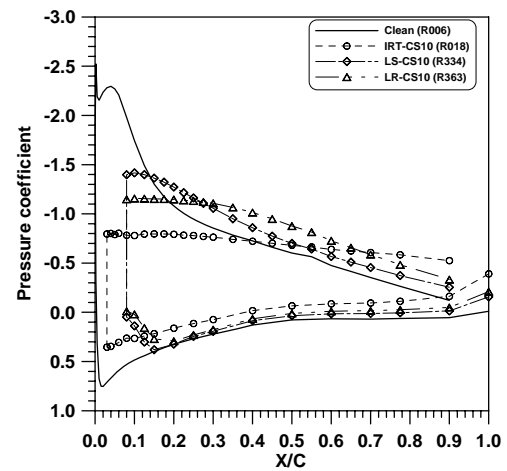
(b) C_p vs x/c ($\alpha = 0^\circ$)



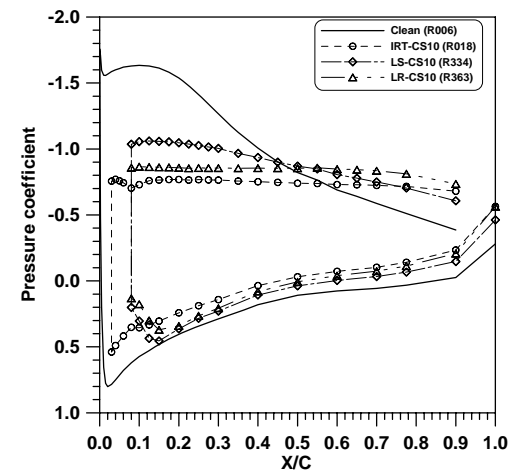
(c) C_p vs x/c ($\alpha = 4^\circ$)



(d) C_p vs x/c ($\alpha = 8^\circ$)



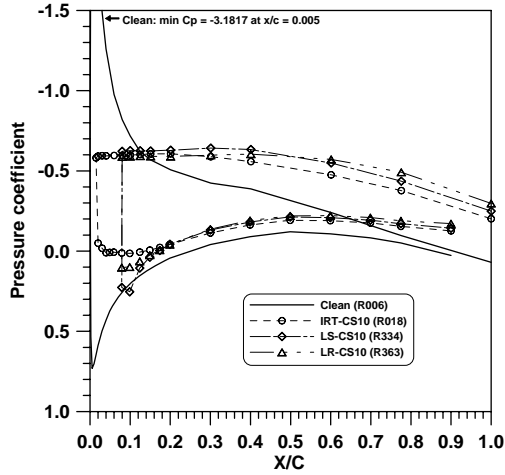
(e) C_p vs x/c ($\alpha = 12^\circ$)



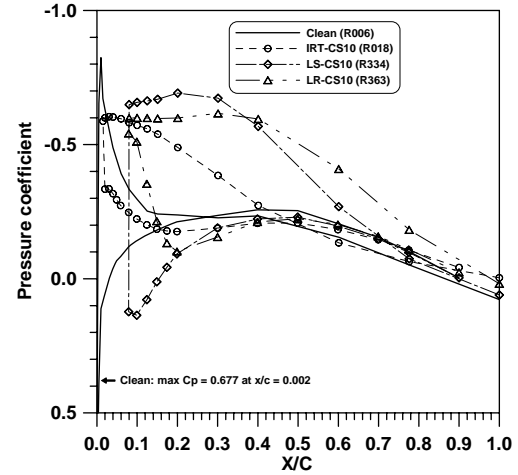
(f) C_p vs x/c ($\alpha = 16^\circ$)

FIGURE 3-52. EFFECT OF IRT-CS10, LS-CS10, AND LR-CS10 ICE SHAPES (ICING CONDITION 1) ON PRESSURE DISTRIBUTIONS AT 15% SEMISPAN;

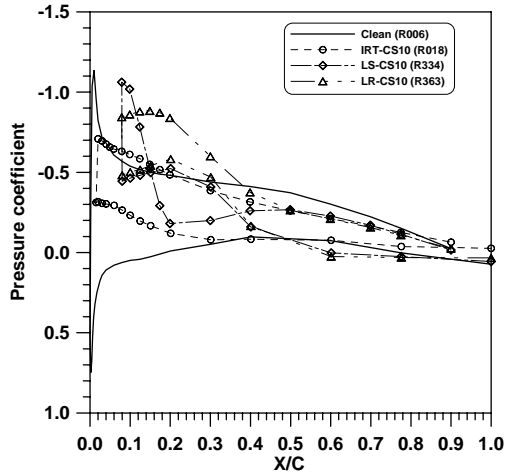
$$Re = 1.8 \times 10^6; \delta_A = 0^\circ$$



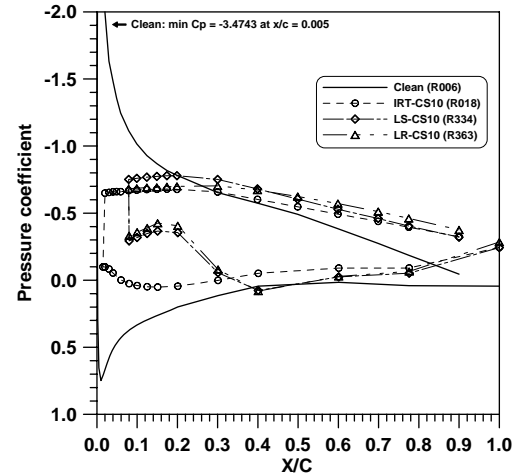
(a) C_p vs x/c ($\alpha = -4^\circ$)



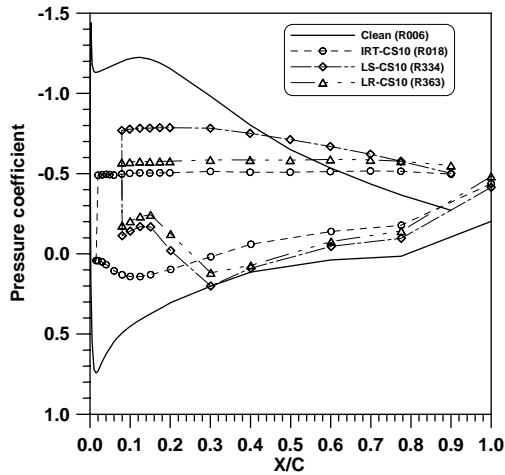
(b) C_p vs x/c ($\alpha = 0^\circ$)



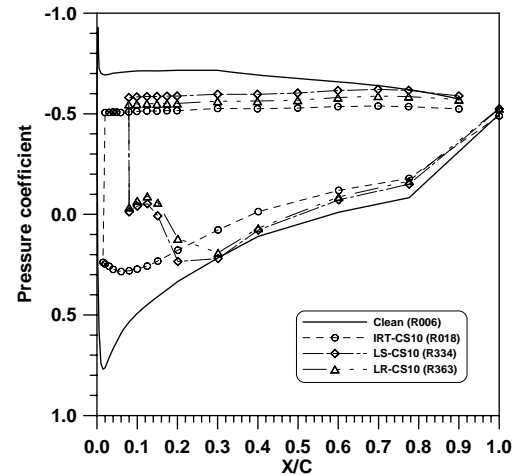
(c) C_p vs x/c ($\alpha = 4^\circ$)



(d) C_p vs x/c ($\alpha = 8^\circ$)



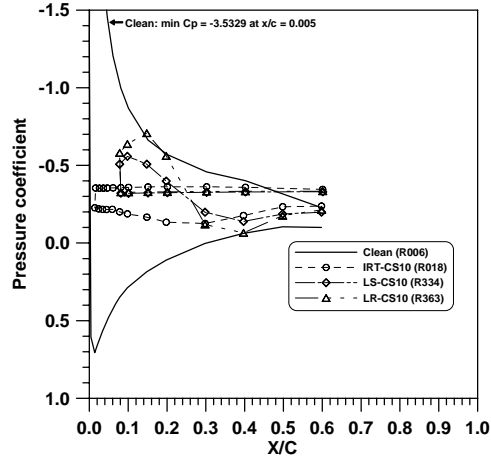
(e) C_p vs x/c ($\alpha = 12^\circ$)



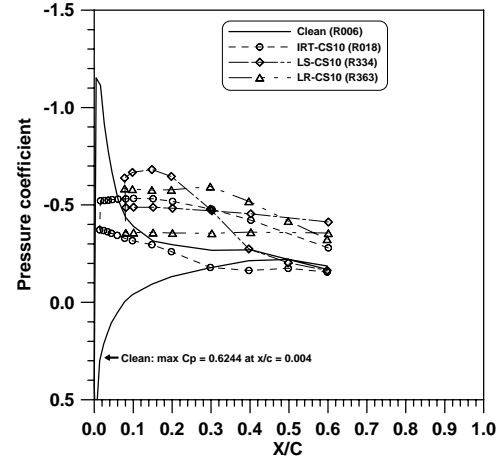
(f) C_p vs x/c ($\alpha = 16^\circ$)

FIGURE 3-53. EFFECT OF IRT-CS10, LS-CS10, AND LR-CS10 ICE SHAPES (ICING CONDITION 1) ON PRESSURE DISTRIBUTIONS AT 50% SEMISPAN;

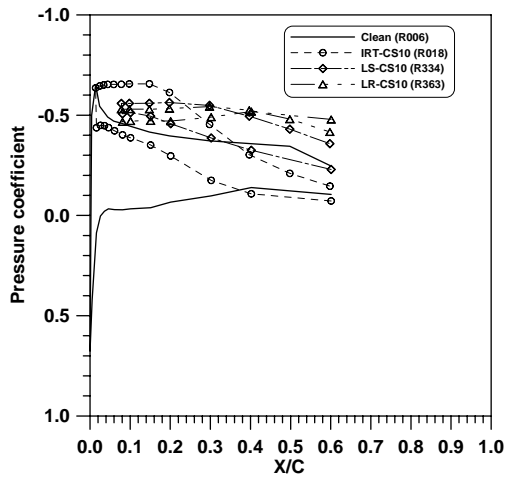
$$Re = 1.8 \times 10^6; \delta_A = 0^\circ$$



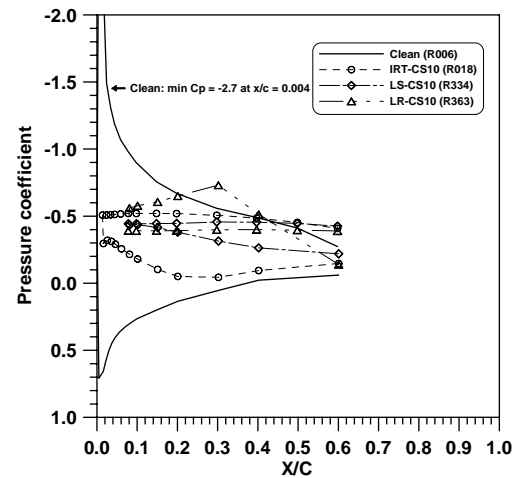
(a) C_p vs x/c ($\alpha = -4^\circ$)



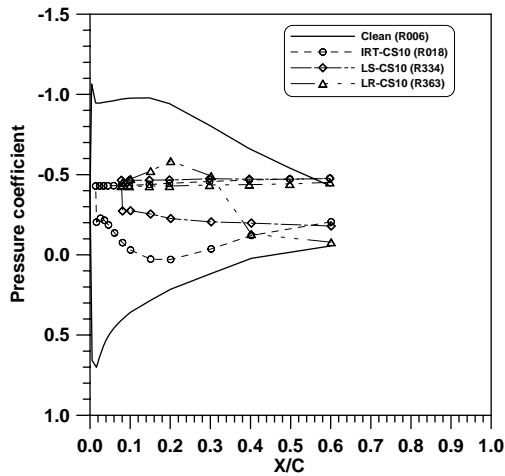
(b) C_p vs x/c ($\alpha = 0^\circ$)



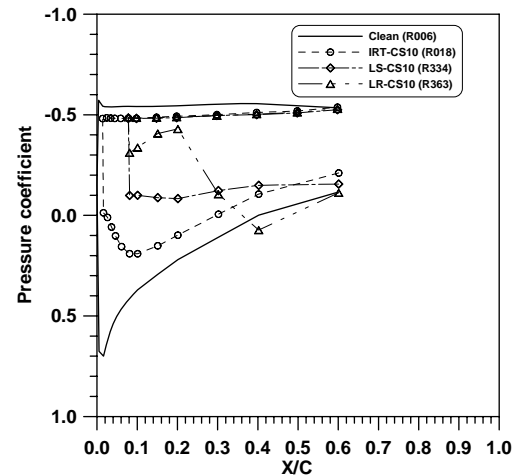
(c) C_p vs x/c ($\alpha = 4^\circ$)



(d) C_p vs x/c ($\alpha = 8^\circ$)



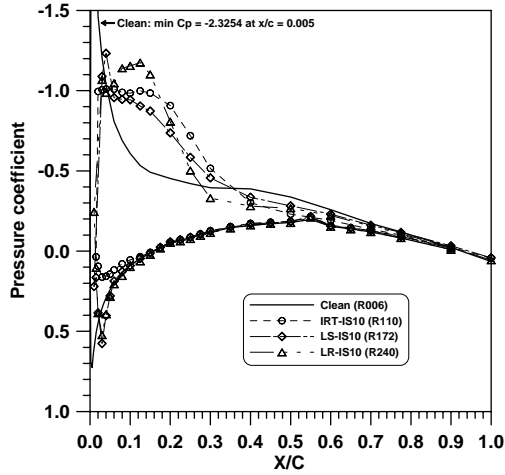
(e) C_p vs x/c ($\alpha = 12^\circ$)



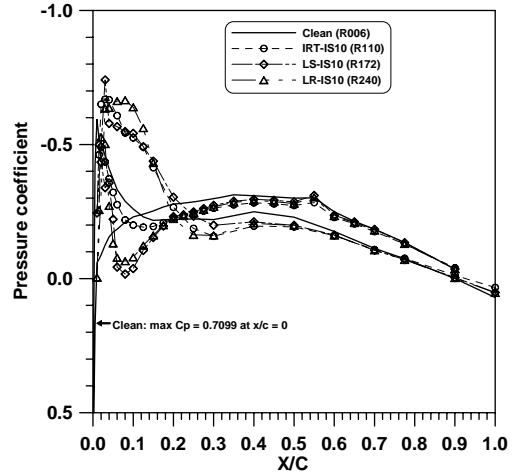
(f) C_p vs x/c ($\alpha = 16^\circ$)

FIGURE 3-54. EFFECT OF IRT-CS10, LS-CS10, AND LR-CS10 ICE SHAPES (ICING CONDITION 1) ON PRESSURE DISTRIBUTIONS AT 85% SEMISPAN;

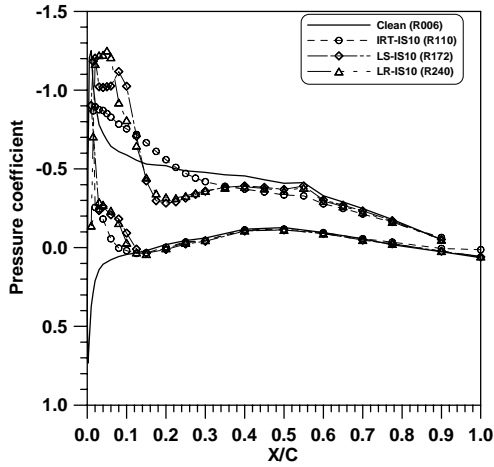
$$Re = 1.8 \times 10^6; \delta_A = 0^\circ$$



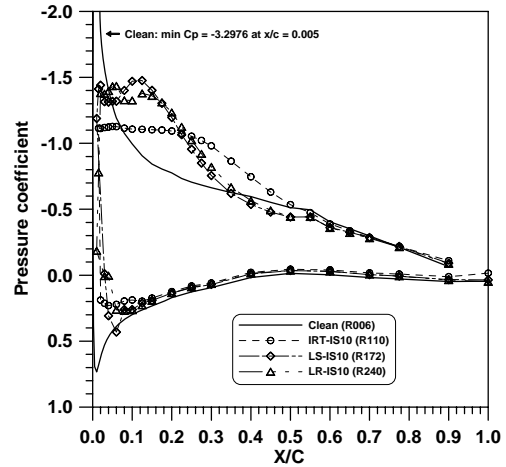
(a) C_p vs x/c ($\alpha = -4^\circ$)



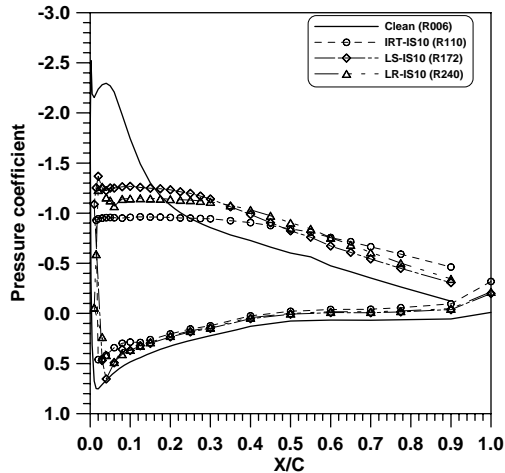
(b) C_p vs x/c ($\alpha = 0^\circ$)



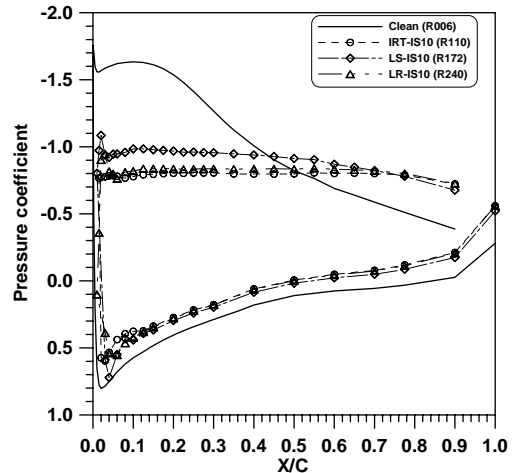
(c) C_p vs x/c ($\alpha = 4^\circ$)



(d) C_p vs x/c ($\alpha = 8^\circ$)



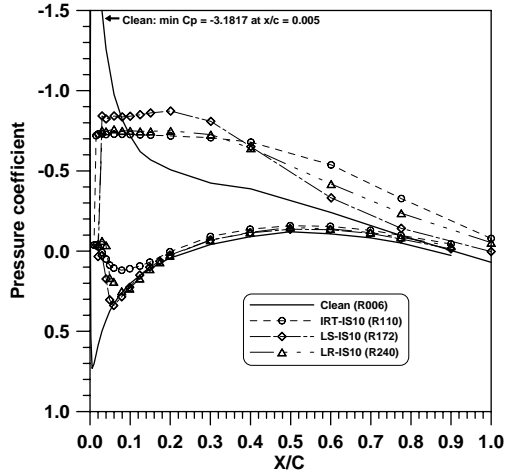
(e) C_p vs x/c ($\alpha = 12^\circ$)



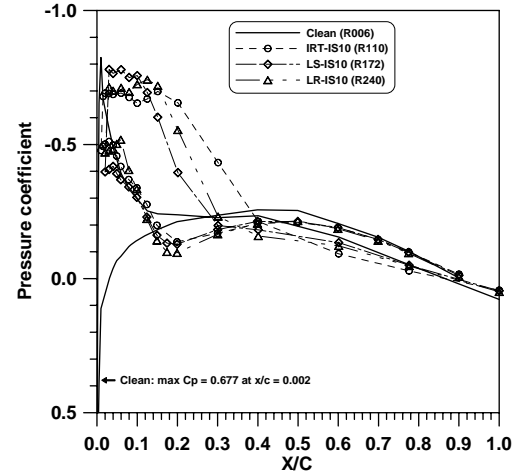
(f) C_p vs x/c ($\alpha = 16^\circ$)

FIGURE 3-55. EFFECT OF IRT-IS10, LS-IS10, AND LR-IS10 ICE SHAPES (ICING CONDITION 2) ON PRESSURE DISTRIBUTIONS AT 15% SEMISPAN;

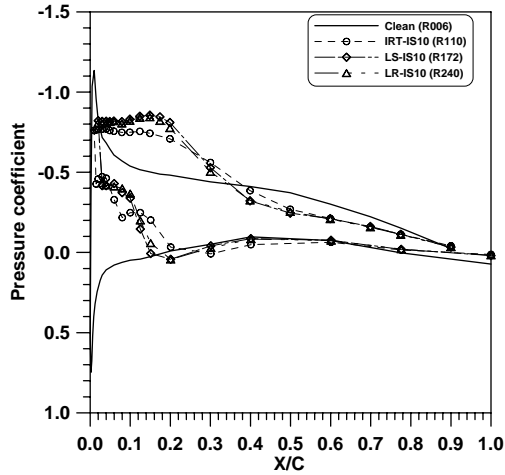
$$Re = 1.8 \times 10^6; \delta_A = 0^\circ$$



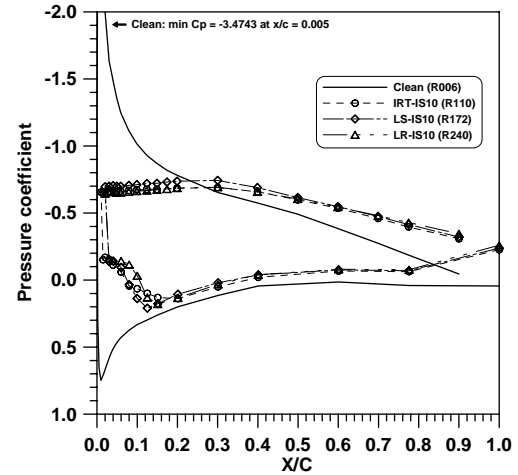
(a) C_p vs x/c ($\alpha = -4^\circ$)



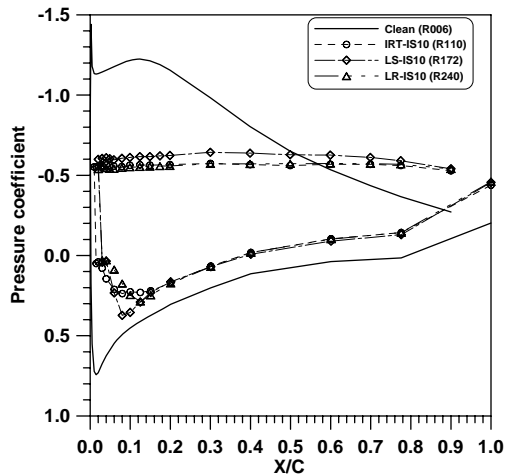
(b) C_p vs x/c ($\alpha = 0^\circ$)



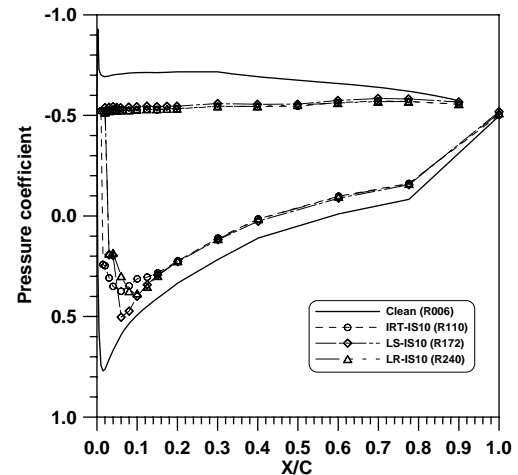
(c) C_p vs x/c ($\alpha = 4^\circ$)



(d) C_p vs x/c ($\alpha = 8^\circ$)



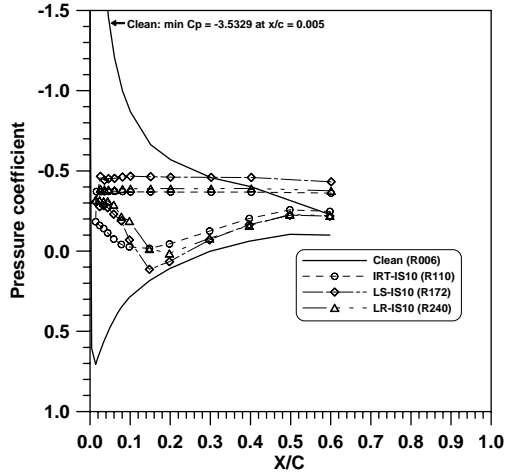
(e) C_p vs x/c ($\alpha = 12^\circ$)



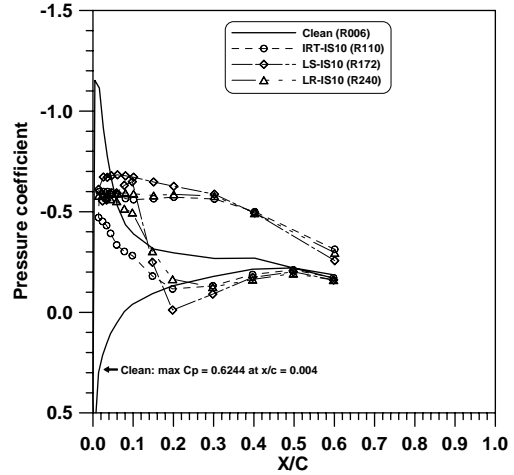
(f) C_p vs x/c ($\alpha = 16^\circ$)

FIGURE 3-56. EFFECT OF IRT-IS10, LS-IS10, AND LR-IS10 ICE SHAPES (ICING CONDITION 2) ON PRESSURE DISTRIBUTIONS AT 50% SEMISPAN;

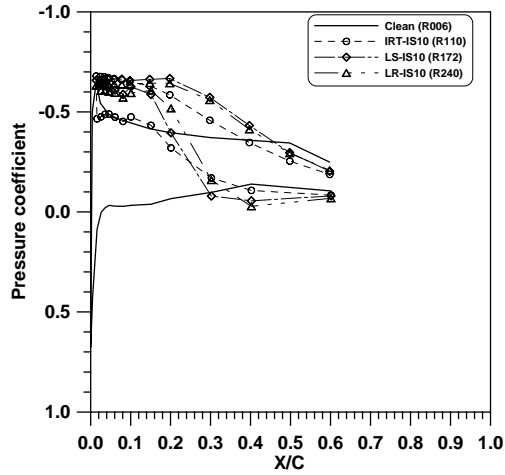
$$Re = 1.8 \times 10^6; \delta_A = 0^\circ$$



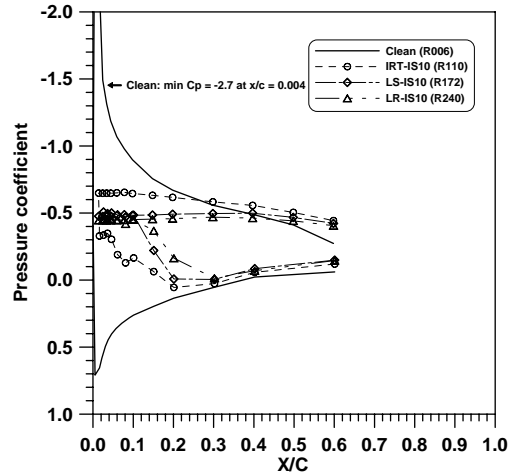
(a) C_p vs x/c ($\alpha = -4^\circ$)



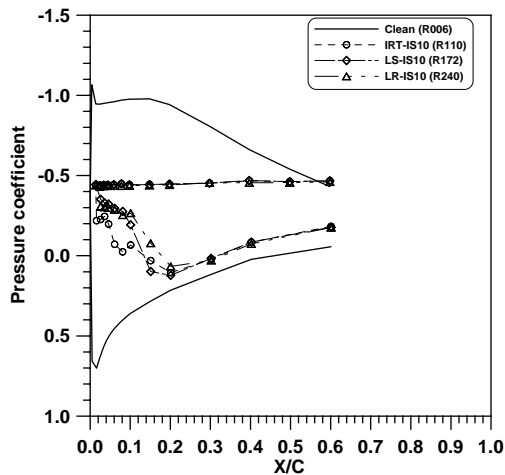
(b) C_p vs x/c ($\alpha = 0^\circ$)



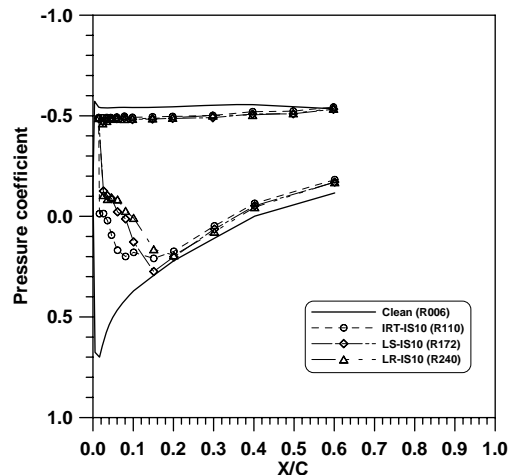
(c) C_p vs x/c ($\alpha = 4^\circ$)



(d) C_p vs x/c ($\alpha = 8^\circ$)



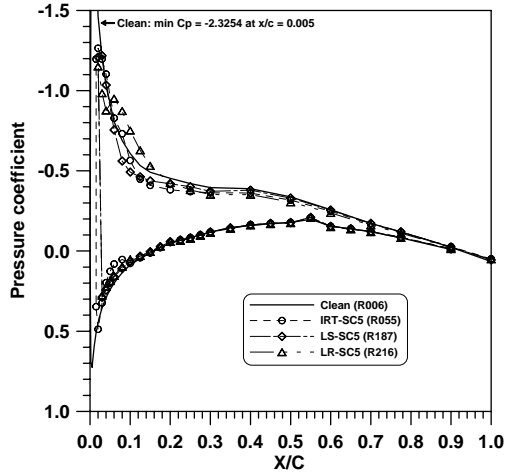
(e) C_p vs x/c ($\alpha = 12^\circ$)



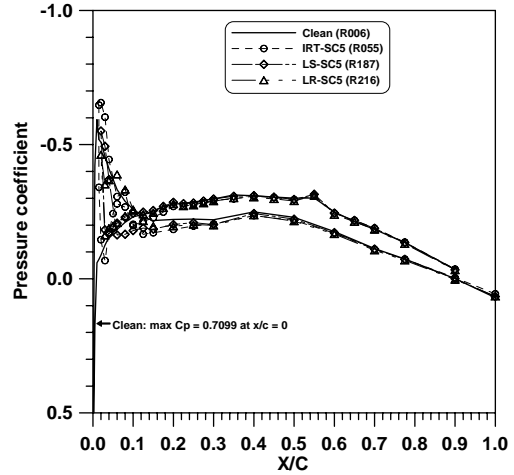
(f) C_p vs x/c ($\alpha = 16^\circ$)

FIGURE 3-57. EFFECT OF IRT-IS10, LS-IS10, AND LR-IS10 ICE SHAPES (ICING CONDITION 2) ON PRESSURE DISTRIBUTIONS AT 85% SEMISPAN;

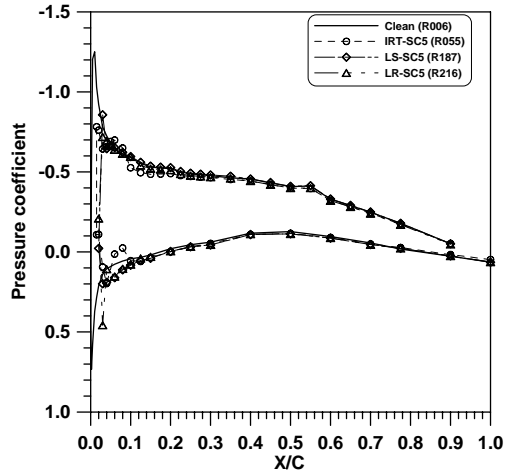
$$Re = 1.8 \times 10^6; \delta_A = 0^\circ$$



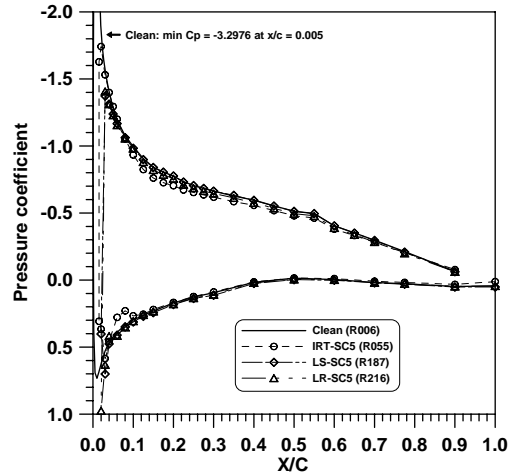
(a) C_p vs x/c ($\alpha = -4^\circ$)



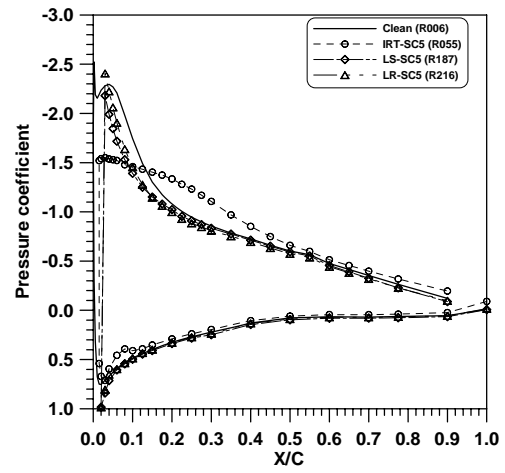
(b) C_p vs x/c ($\alpha = 0^\circ$)



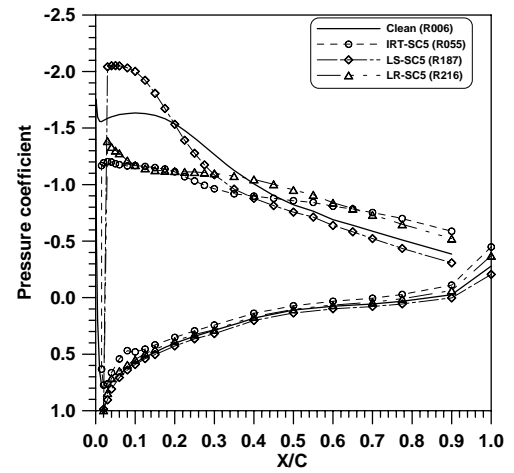
(c) C_p vs x/c ($\alpha = 4^\circ$)



(d) C_p vs x/c ($\alpha = 8^\circ$)



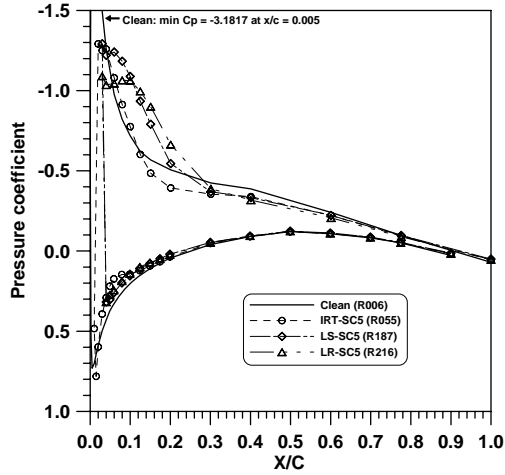
(e) C_p vs x/c ($\alpha = 12^\circ$)



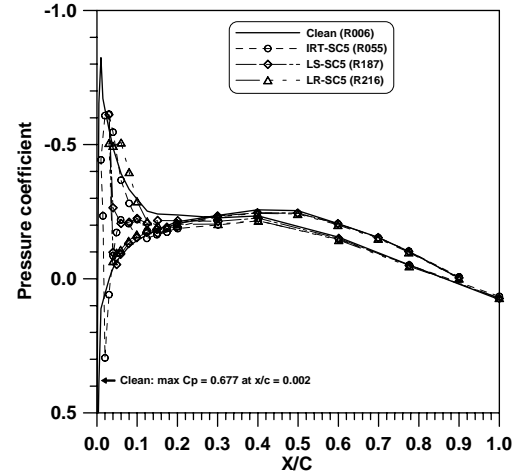
(f) C_p vs x/c ($\alpha = 16^\circ$)

FIGURE 3-58. EFFECT OF IRT-SC5, LS-SC5, AND LR-SC5 ICE SHAPES (ICING CONDITION 3) ON PRESSURE DISTRIBUTIONS AT 15% SEMISPAN;

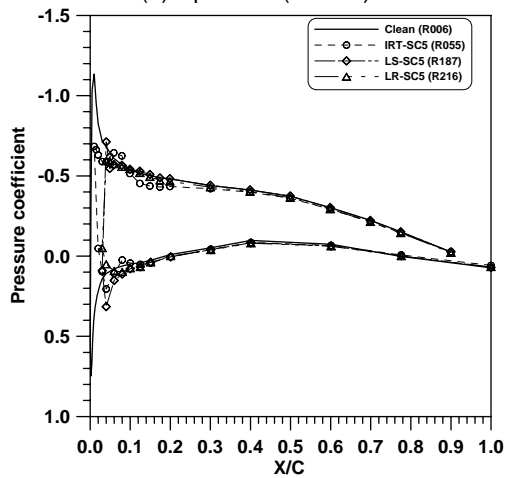
$$Re = 1.8 \times 10^6; \delta_A = 0^\circ$$



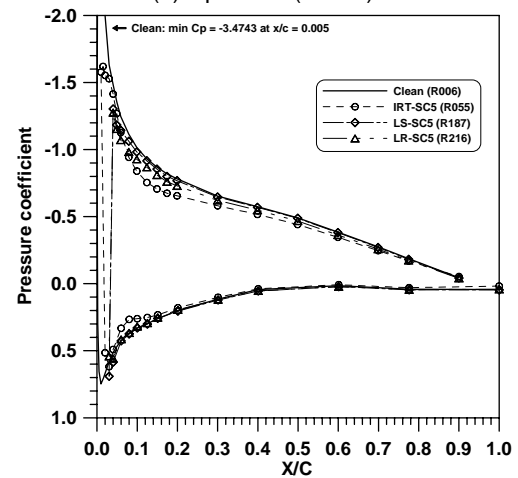
(a) C_p vs x/c ($\alpha = -4^\circ$)



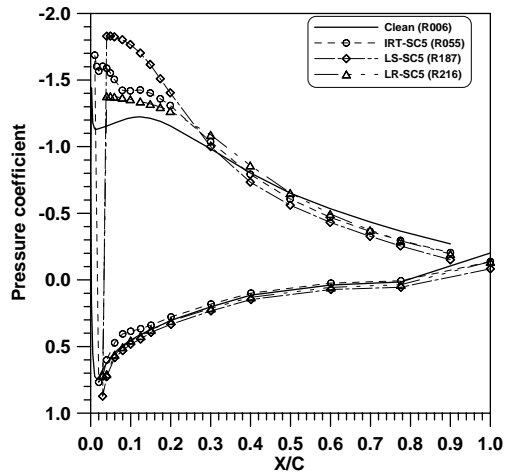
(b) C_p vs x/c ($\alpha = 0^\circ$)



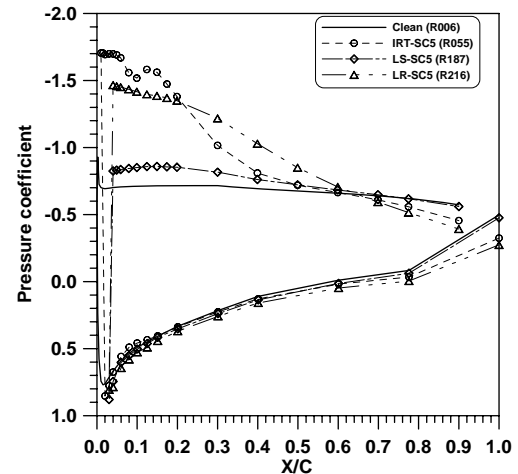
(c) C_p vs x/c ($\alpha = 4^\circ$)



(d) C_p vs x/c ($\alpha = 8^\circ$)



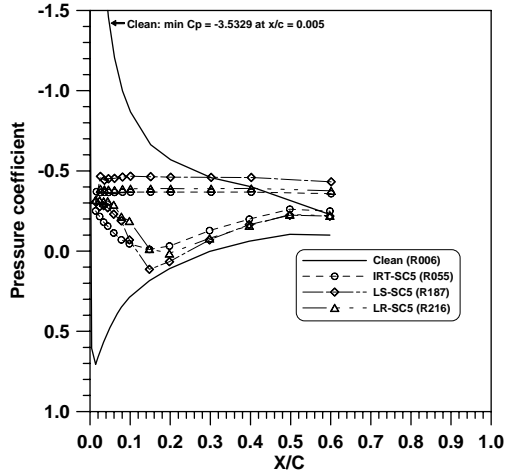
(e) C_p vs x/c ($\alpha = 12^\circ$)



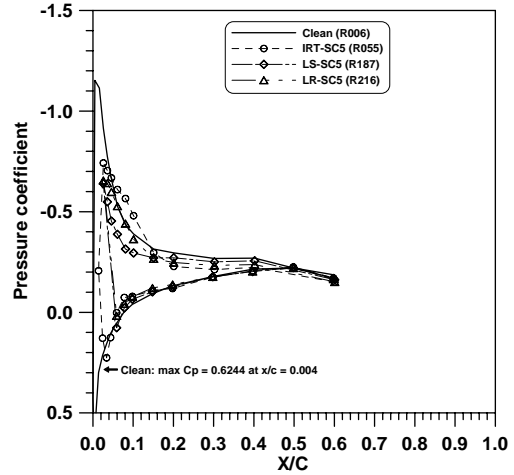
(f) C_p vs x/c ($\alpha = 16^\circ$)

FIGURE 3-59. EFFECT OF IRT-SC5, LS-SC5, AND LR-SC5 ICE SHAPES (ICING CONDITION 3) ON PRESSURE DISTRIBUTIONS AT 50% SEMISPAN;

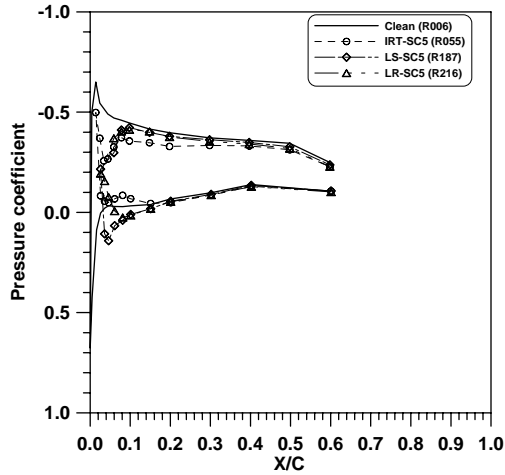
$$Re = 1.8 \times 10^6; \delta_A = 0^\circ$$



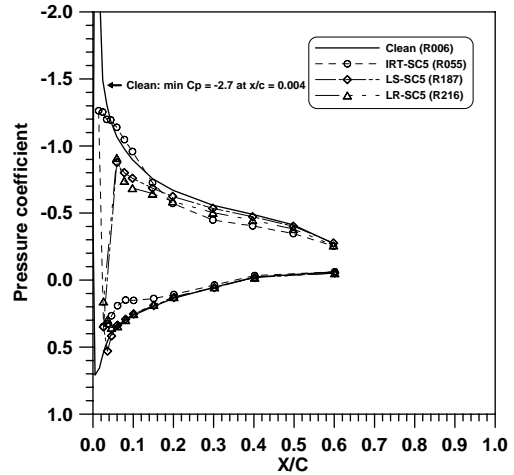
(a) C_p vs x/c ($\alpha = -4^\circ$)



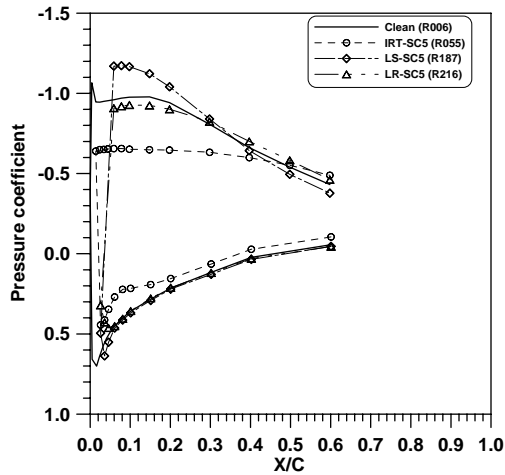
(b) C_p vs x/c ($\alpha = 0^\circ$)



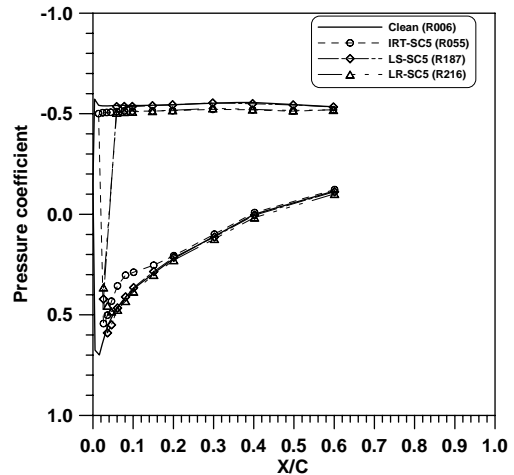
(c) C_p vs x/c ($\alpha = 4^\circ$)



(d) C_p vs x/c ($\alpha = 8^\circ$)



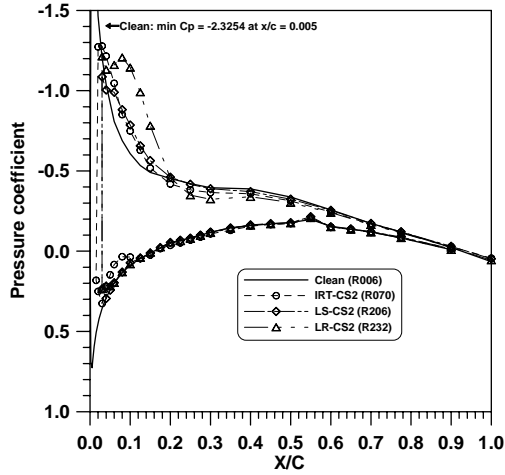
(e) C_p vs x/c ($\alpha = 12^\circ$)



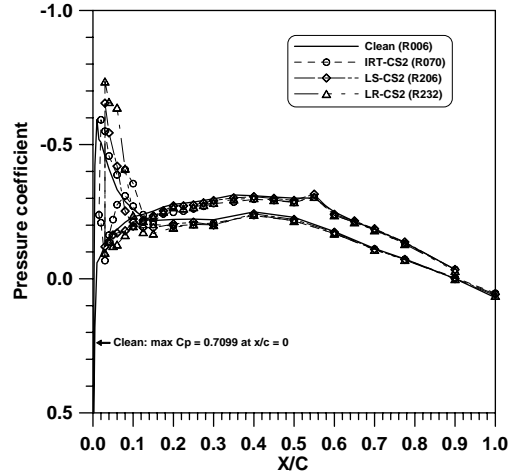
(f) C_p vs x/c ($\alpha = 16^\circ$)

FIGURE 3-60. EFFECT OF IRT-SC5, LS-SC5, AND LR-SC5 ICE SHAPES (ICING CONDITION 3) ON PRESSURE DISTRIBUTIONS AT 85% SEMISPAN;

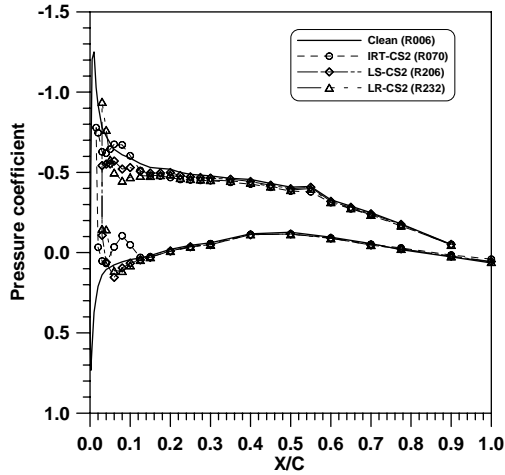
$$Re = 1.8 \times 10^6; \delta_A = 0^\circ$$



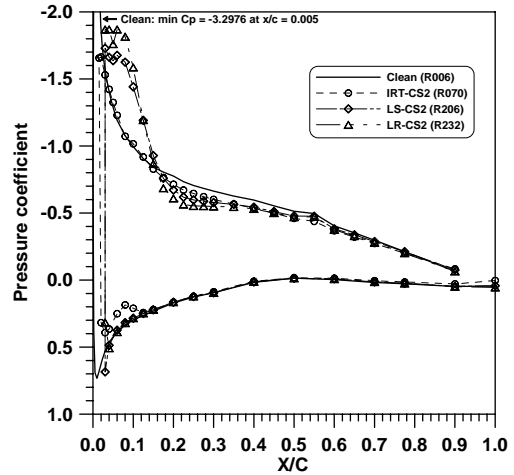
(a) C_p vs x/c ($\alpha = -4^\circ$)



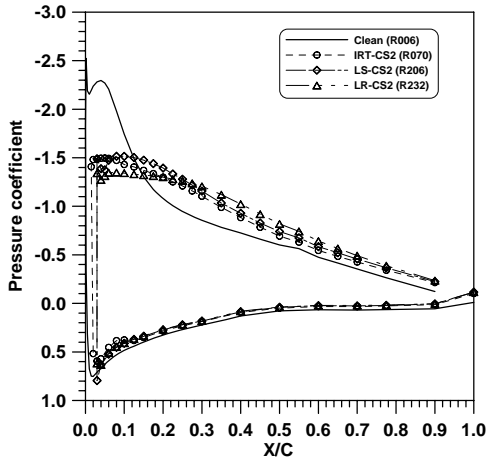
(b) C_p vs x/c ($\alpha = 0^\circ$)



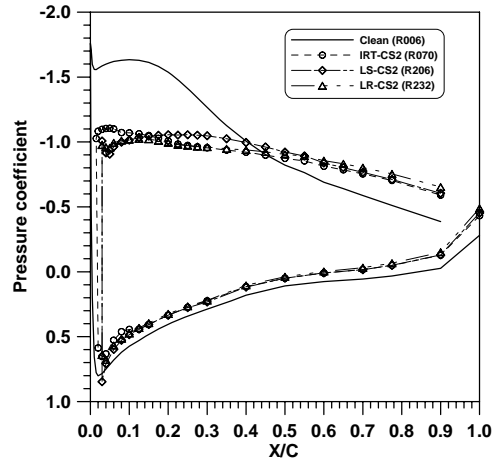
(c) C_p vs x/c ($\alpha = 4^\circ$)



(d) C_p vs x/c ($\alpha = 8^\circ$)



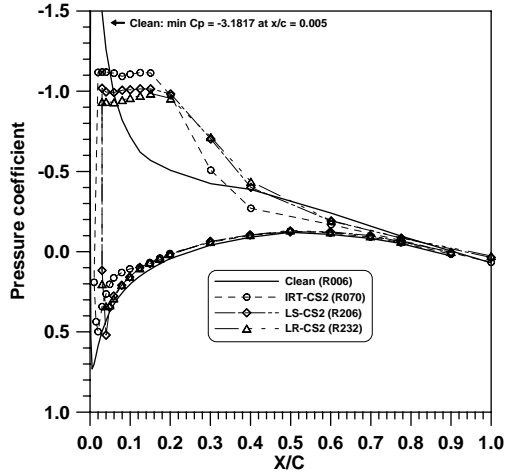
(e) C_p vs x/c ($\alpha = 12^\circ$)



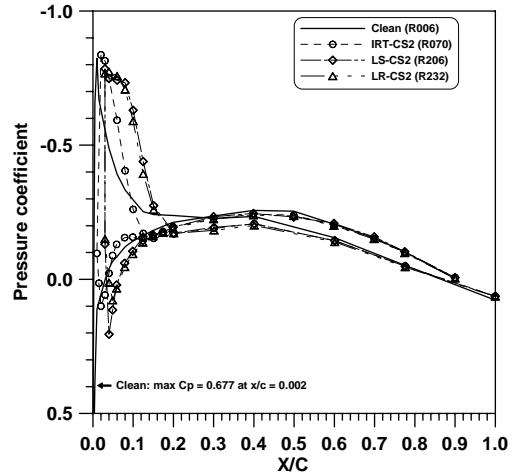
(f) C_p vs x/c ($\alpha = 16^\circ$)

FIGURE 3-61. EFFECT OF IRT-CS2, LS-CS2, AND LR-CS2 ICE SHAPES (ICING CONDITION 4) ON PRESSURE DISTRIBUTIONS AT 15% SEMISPAN;

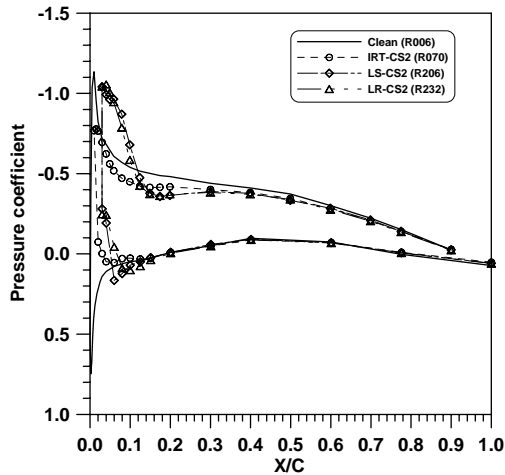
$$Re = 1.8 \times 10^6; \delta_A = 0^\circ$$



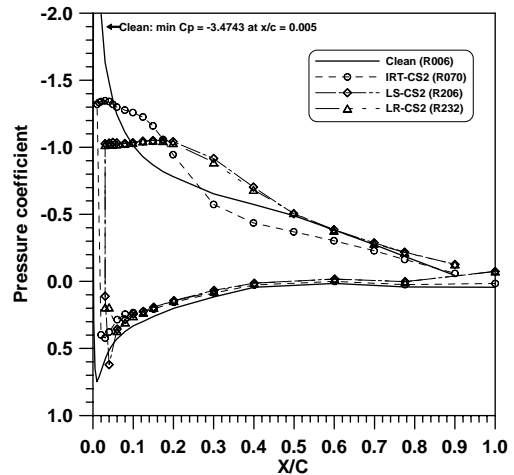
(a) C_p vs x/c ($\alpha = -4^\circ$)



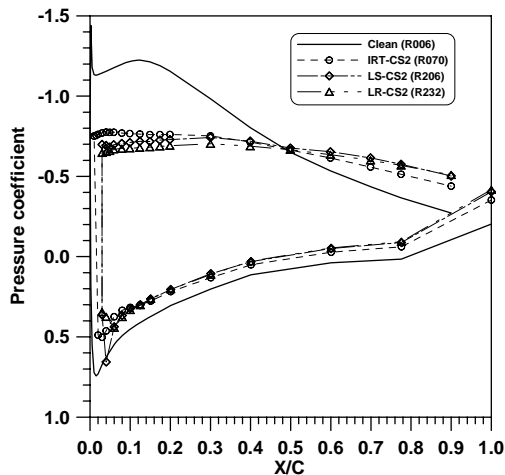
(b) C_p vs x/c ($\alpha = 0^\circ$)



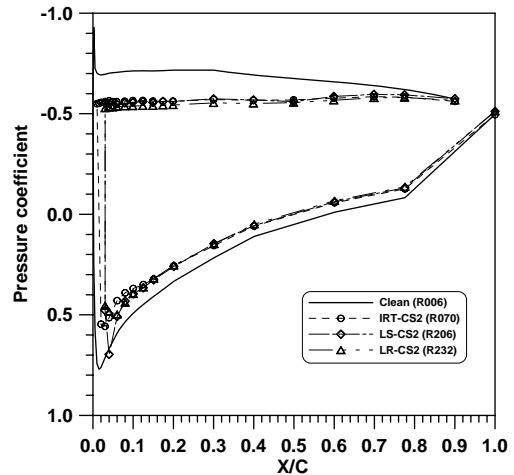
(c) C_p vs x/c ($\alpha = 4^\circ$)



(d) C_p vs x/c ($\alpha = 8^\circ$)



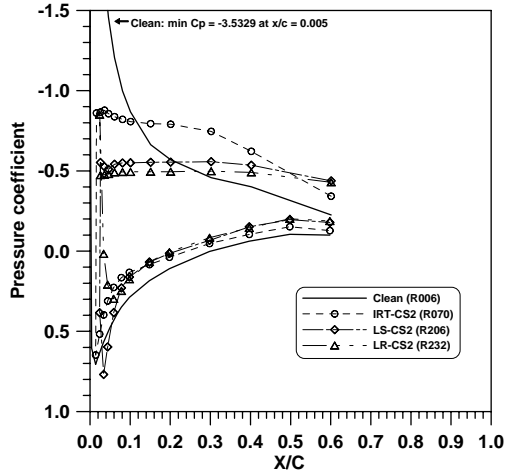
(e) C_p vs x/c ($\alpha = 12^\circ$)



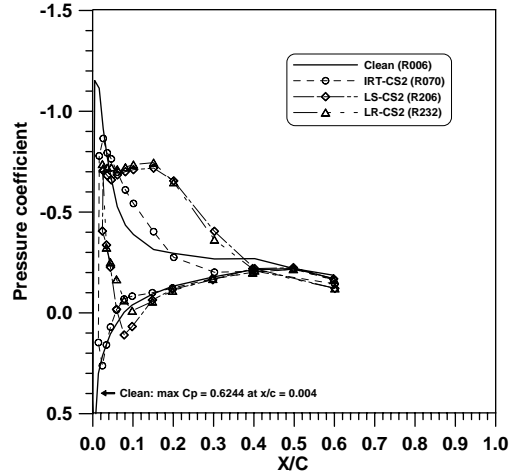
(f) C_p vs x/c ($\alpha = 16^\circ$)

FIGURE 3-62. EFFECT OF IRT-CS2, LS-CS2, AND LR-CS2 ICE SHAPES (ICING CONDITION 4) ON PRESSURE DISTRIBUTIONS AT 50% SEMISPAN;

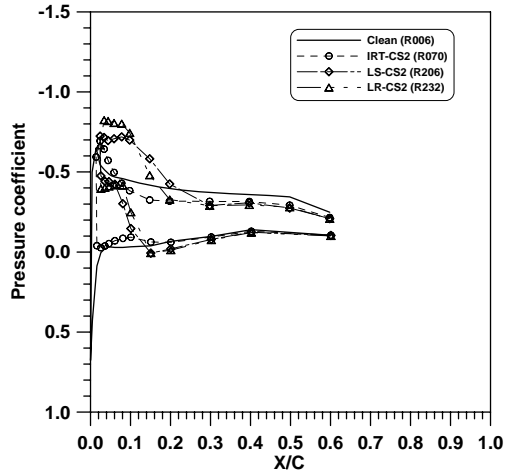
$$Re = 1.8 \times 10^6; \delta_A = 0^\circ$$



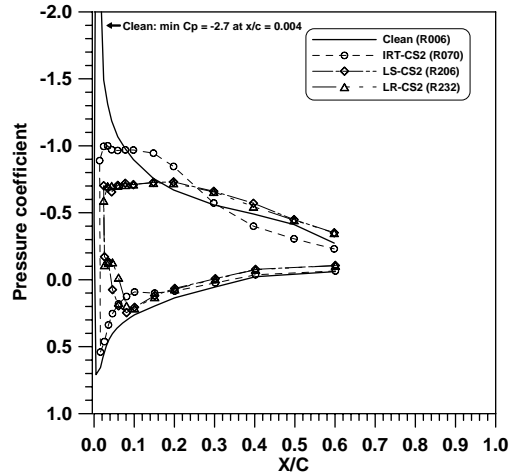
(a) C_p vs x/c ($\alpha = -4^\circ$)



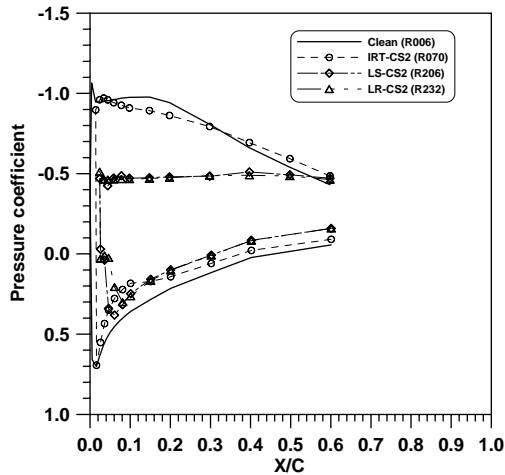
(b) C_p vs x/c ($\alpha = 0^\circ$)



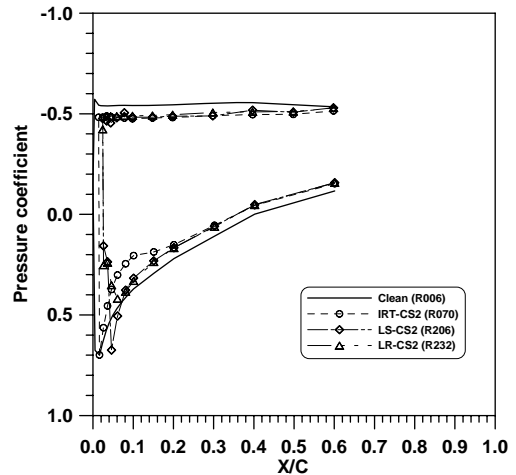
(c) C_p vs x/c ($\alpha = 4^\circ$)



(d) C_p vs x/c ($\alpha = 8^\circ$)



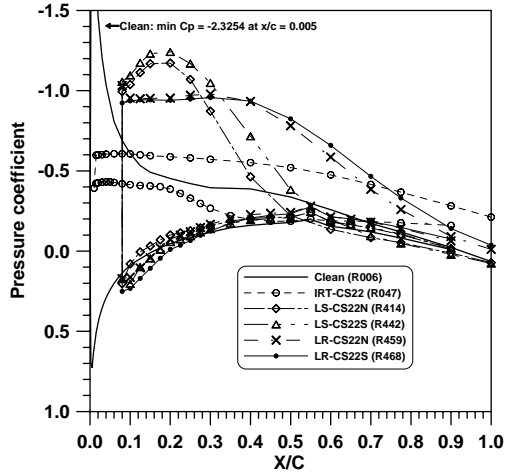
(e) C_p vs x/c ($\alpha = 12^\circ$)



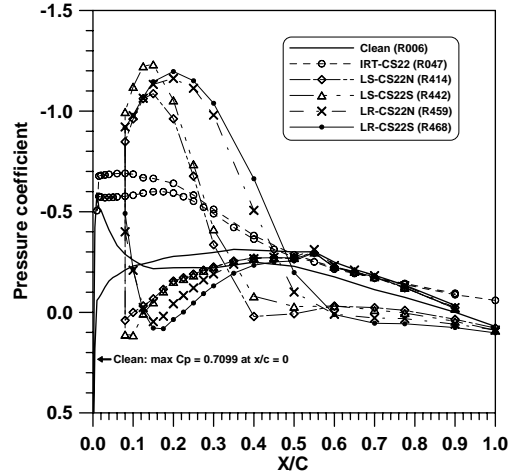
(f) C_p vs x/c ($\alpha = 16^\circ$)

FIGURE 3-63. EFFECT OF IRT-CS2, LS-CS2, AND LR-CS2 ICE SHAPES (ICING CONDITION 4) ON PRESSURE DISTRIBUTIONS AT 85% SEMISPAN;

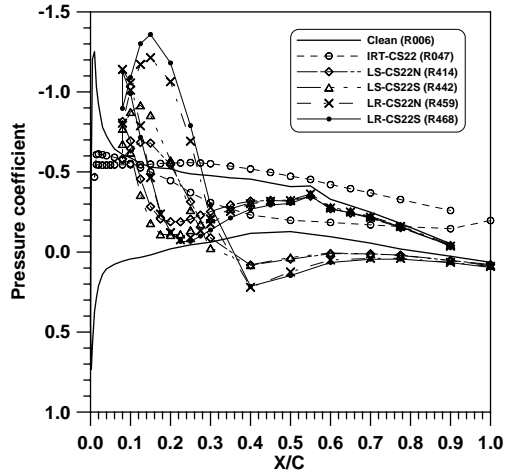
$$Re = 1.8 \times 10^6; \delta_A = 0^\circ$$



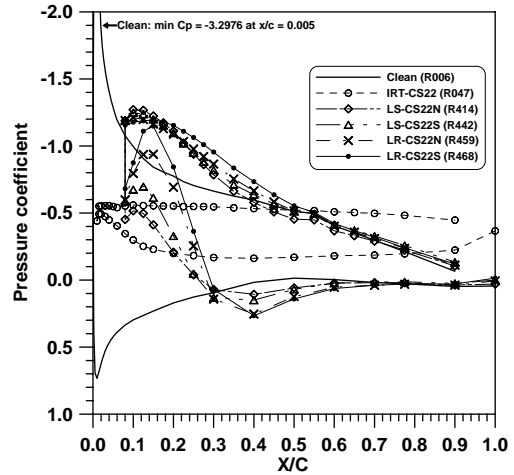
(a) C_p vs x/c ($\alpha = -4^\circ$)



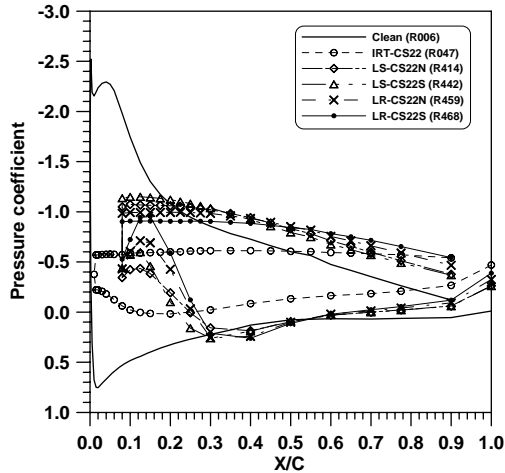
(b) C_p vs x/c ($\alpha = 0^\circ$)



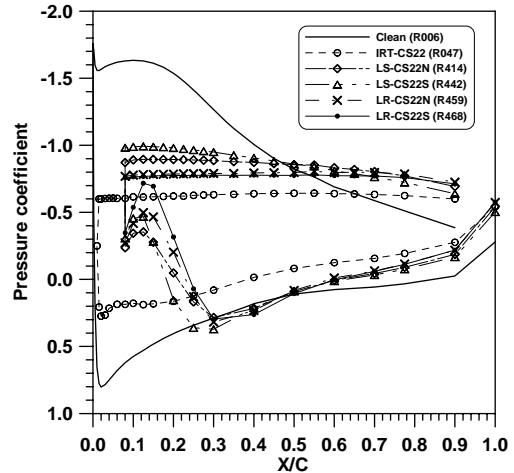
(c) C_p vs x/c ($\alpha = 4^\circ$)



(d) C_p vs x/c ($\alpha = 8^\circ$)

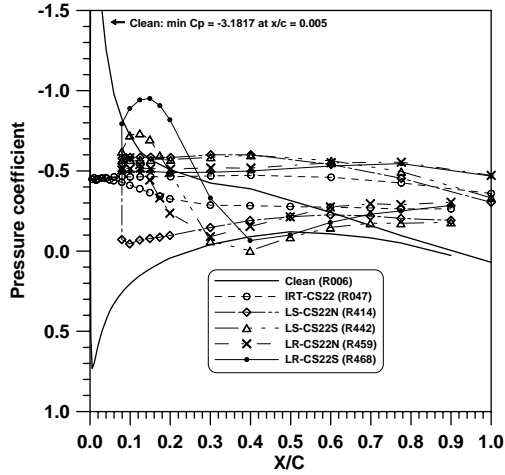


(e) C_p vs x/c ($\alpha = 12^\circ$)

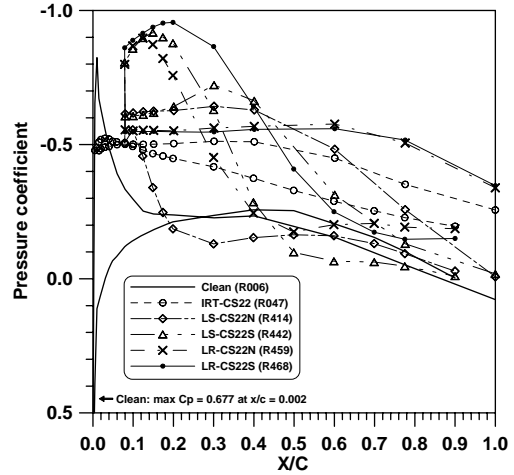


(f) C_p vs x/c ($\alpha = 16^\circ$)

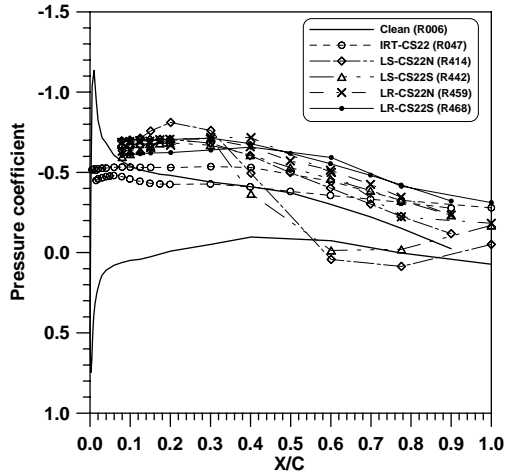
FIGURE 3-64. EFFECT OF IRT-CS22, LS-CS22N, LS-CS22S, LR-CS22N, AND LR-CS22S ICE SHAPES (ICING CONDITION 5) ON PRESSURE DISTRIBUTIONS AT 15% SEMISPAN; $Re = 1.8 \times 10^6$; $\delta_A = 0^\circ$



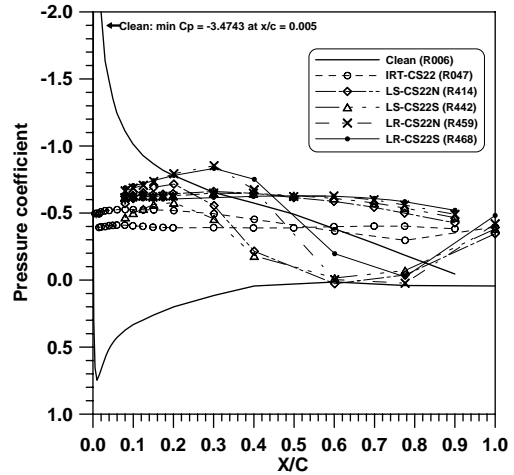
(a) C_p vs x/c ($\alpha = -4^\circ$)



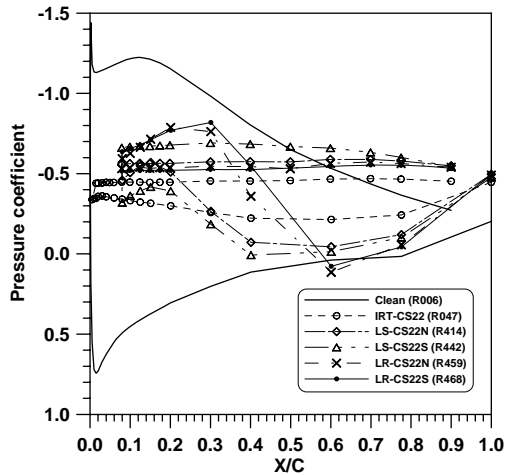
(b) C_p vs x/c ($\alpha = 0^\circ$)



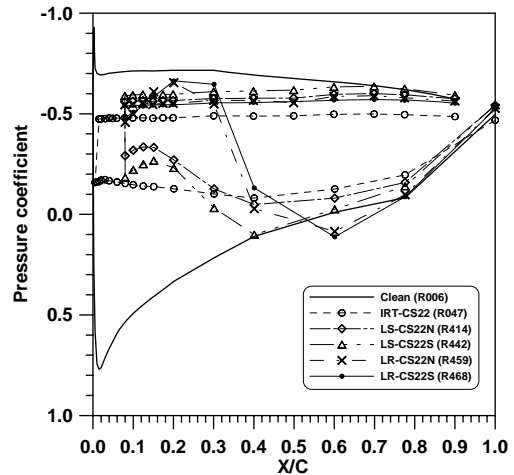
(c) C_p vs x/c ($\alpha = 4^\circ$)



(d) C_p vs x/c ($\alpha = 8^\circ$)

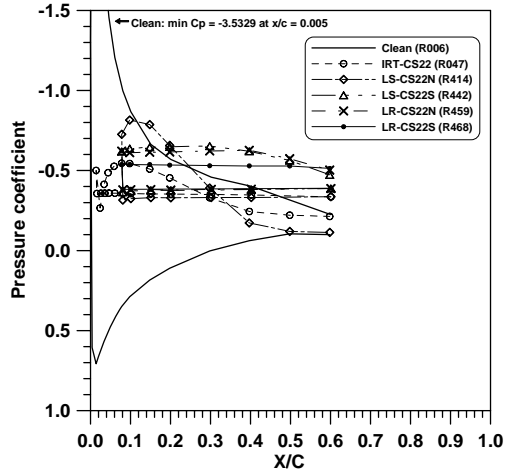


(e) C_p vs x/c ($\alpha = 12^\circ$)

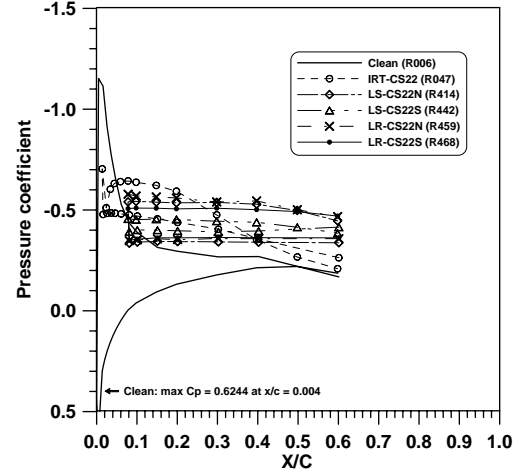


(f) C_p vs x/c ($\alpha = 16^\circ$)

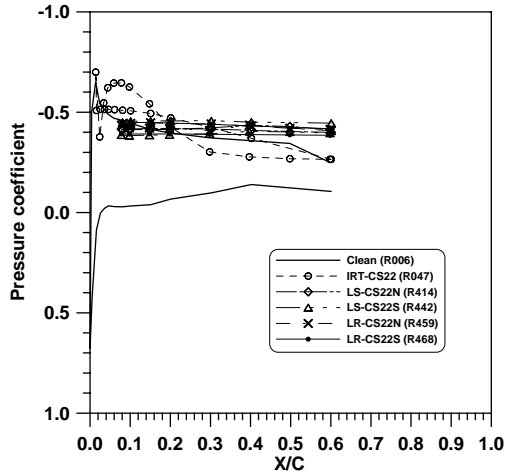
FIGURE 3-65. EFFECT OF IRT-CS22, LS-CS22N, LS-CS22S, LR-CS22N, AND LR-CS22S ICE SHAPES (ICING CONDITION 5) ON PRESSURE DISTRIBUTIONS AT 50% SEMISPAN; $Re = 1.8 \times 10^6$; $\delta_A = 0^\circ$



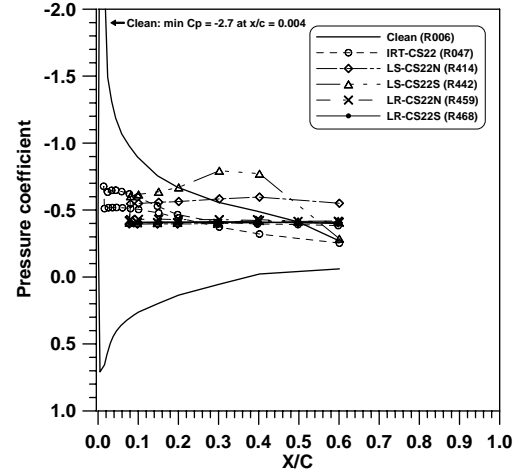
(a) C_p vs x/c ($\alpha = -4^\circ$)



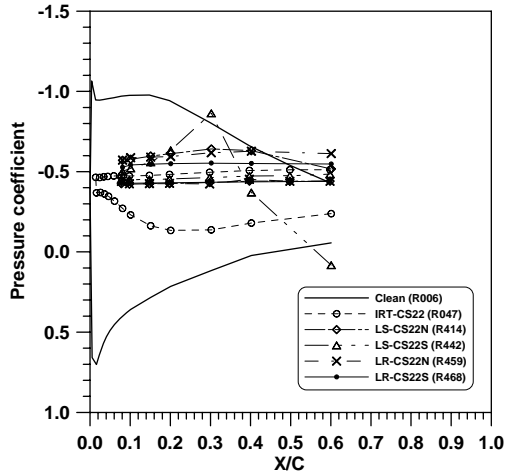
(b) C_p vs x/c ($\alpha = 0^\circ$)



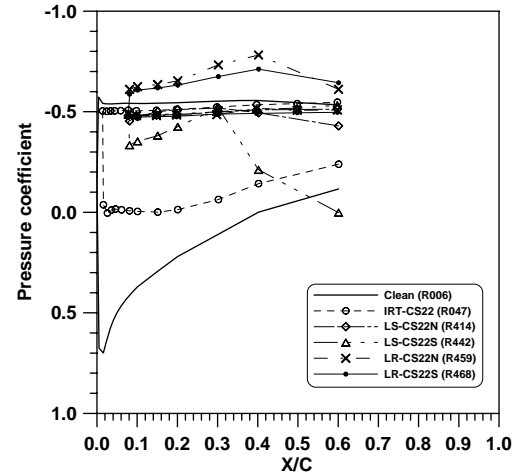
(c) C_p vs x/c ($\alpha = 4^\circ$)



(d) C_p vs x/c ($\alpha = 8^\circ$)

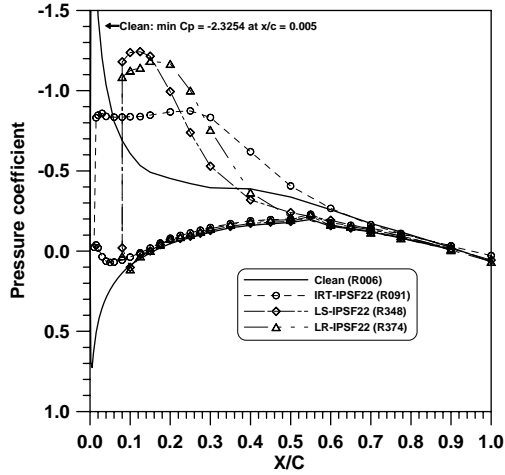


(e) C_p vs x/c ($\alpha = 12^\circ$)

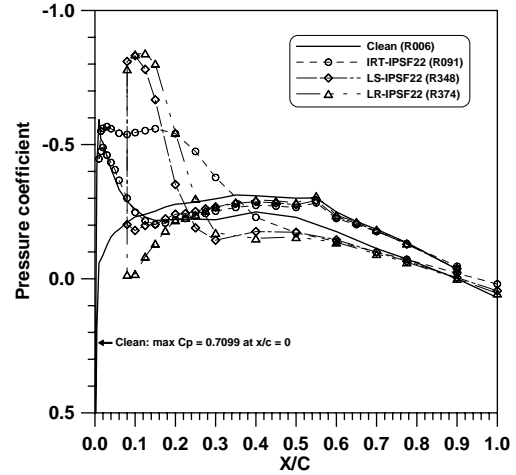


(f) C_p vs x/c ($\alpha = 16^\circ$)

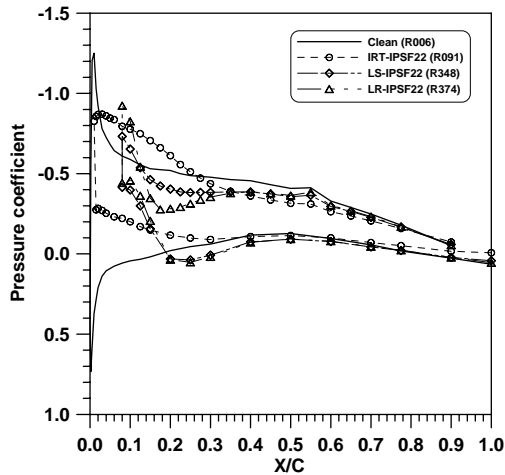
FIGURE 3-66. EFFECT OF IRT-CS22, LS-CS22N, LS-CS22S, LR-CS22N, AND LR-CS22S ICE SHAPES (ICING CONDITION 5) ON PRESSURE DISTRIBUTIONS AT 85% SEMISPAN; $Re = 1.8 \times 10^6$; $\delta_A = 0^\circ$



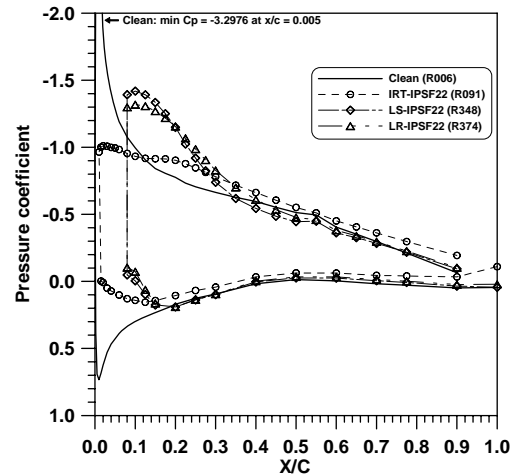
(a) C_p vs x/c ($\alpha = -4^\circ$)



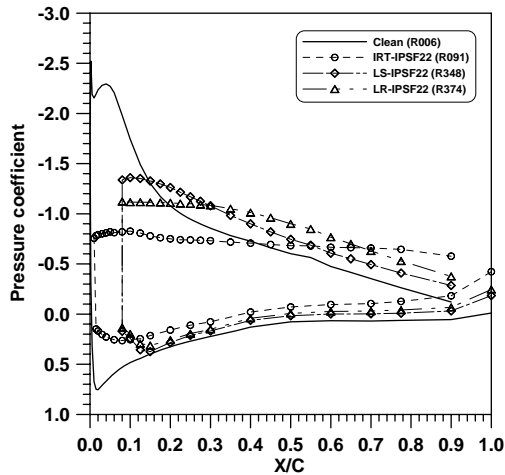
(b) C_p vs x/c ($\alpha = 0^\circ$)



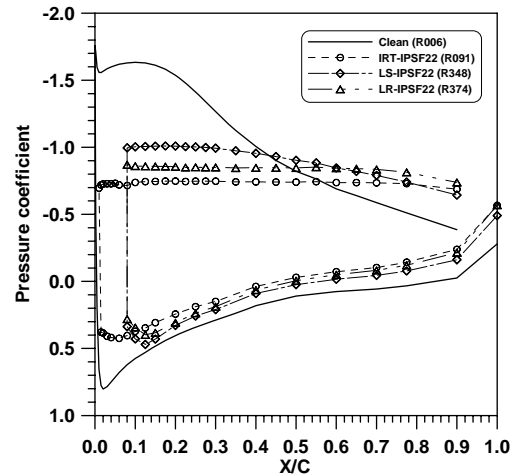
(c) C_p vs x/c ($\alpha = 4^\circ$)



(d) C_p vs x/c ($\alpha = 8^\circ$)



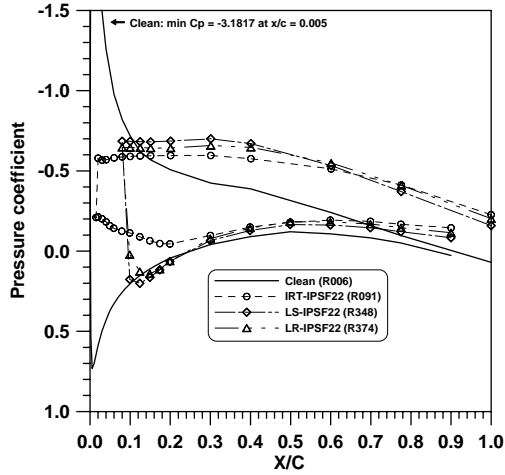
(e) C_p vs x/c ($\alpha = 12^\circ$)



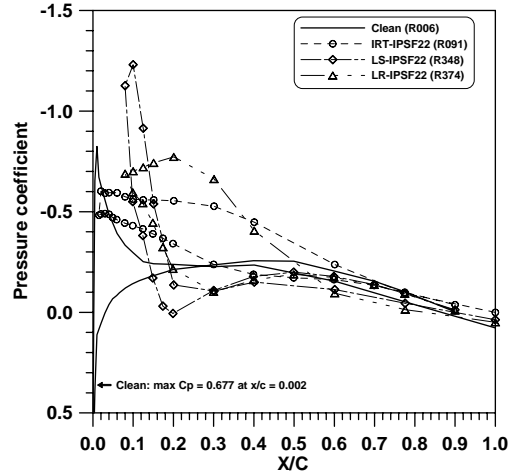
(f) C_p vs x/c ($\alpha = 16^\circ$)

FIGURE 3-67. EFFECT OF IRT-IPSF22, LS-IPSF22, AND LR-IPSF22 ICE SHAPES (ICING CONDITION 6) ON PRESSURE DISTRIBUTIONS AT 15% SEMISPAN;

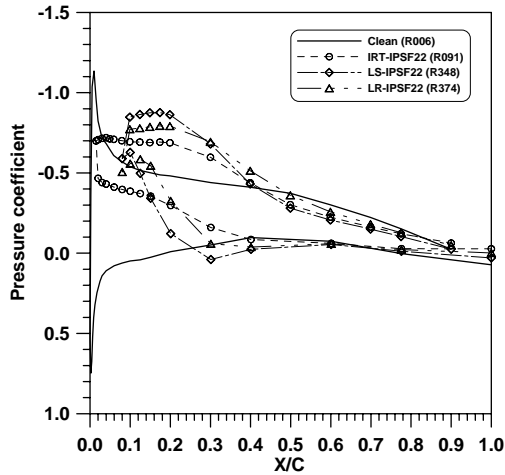
$$Re = 1.8 \times 10^6; \delta_A = 0^\circ$$



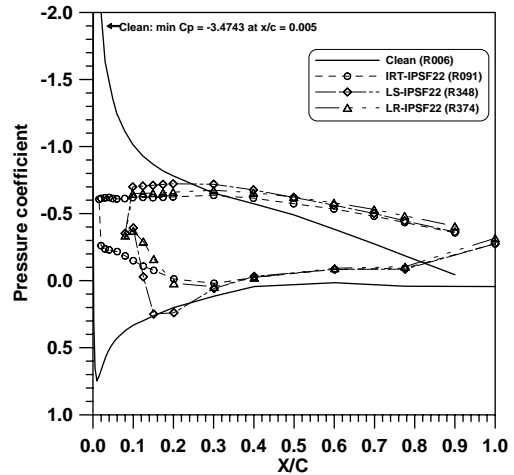
(a) C_p vs x/c ($\alpha = -4^\circ$)



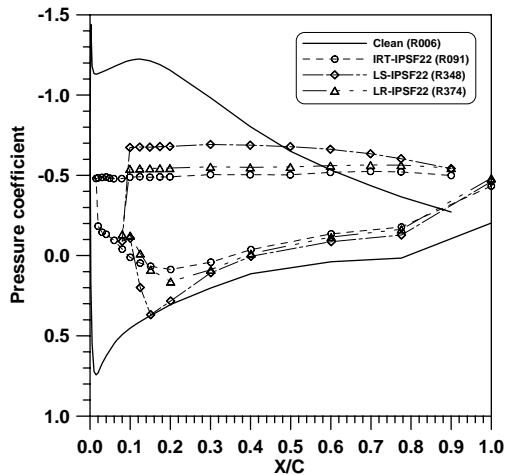
(b) C_p vs x/c ($\alpha = 0^\circ$)



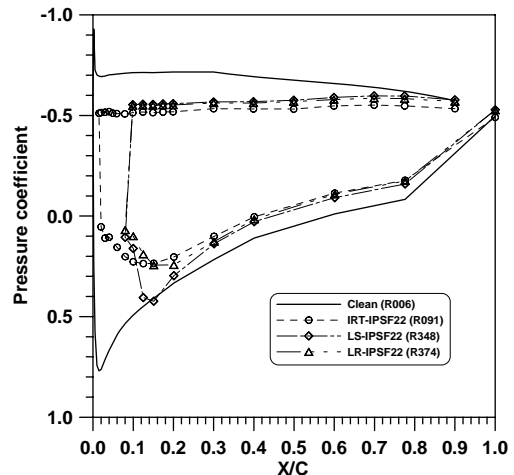
(c) C_p vs x/c ($\alpha = 4^\circ$)



(d) C_p vs x/c ($\alpha = 8^\circ$)



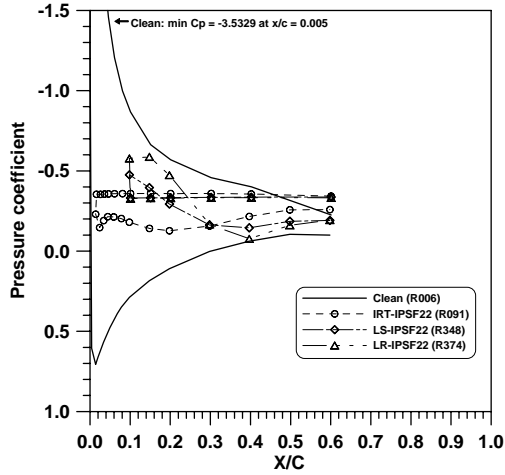
(e) C_p vs x/c ($\alpha = 12^\circ$)



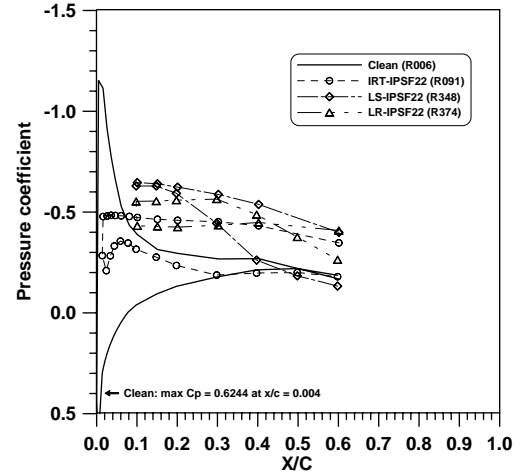
(f) C_p vs x/c ($\alpha = 16^\circ$)

FIGURE 3-68. EFFECT OF IRT-IPSF22, LS-IPSF22, AND LR-IPSF22 ICE SHAPES (ICING CONDITION 6) ON PRESSURE DISTRIBUTIONS AT 50% SEMISPAN;

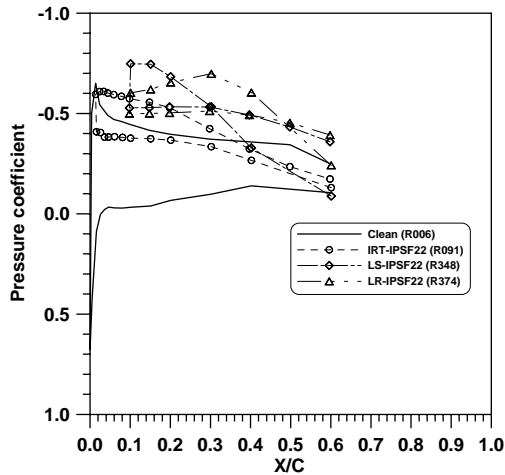
$$Re = 1.8 \times 10^6; \delta_A = 0^\circ$$



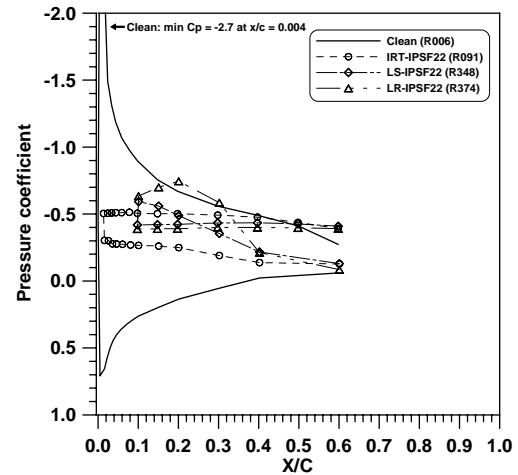
(a) C_p vs x/c ($\alpha = -4^\circ$)



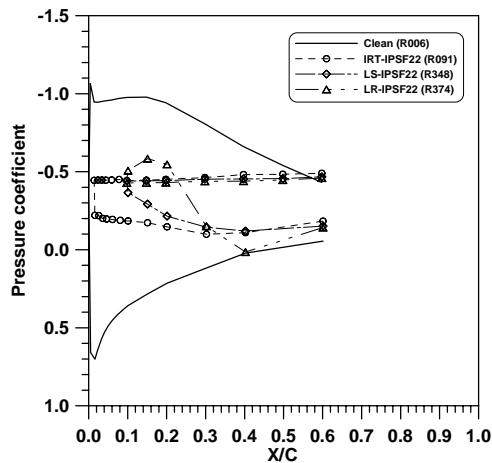
(b) C_p vs x/c ($\alpha = 0^\circ$)



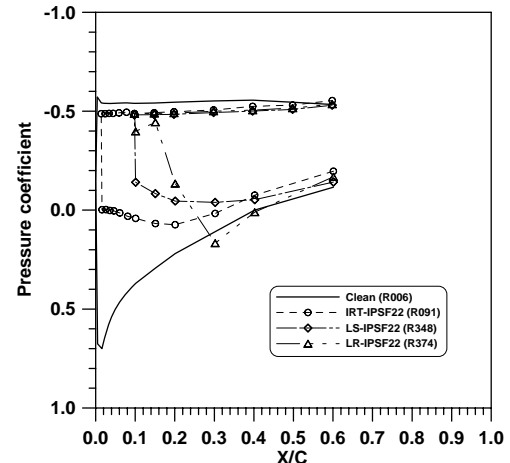
(c) C_p vs x/c ($\alpha = 4^\circ$)



(d) C_p vs x/c ($\alpha = 8^\circ$)



(e) C_p vs x/c ($\alpha = 12^\circ$)



(f) C_p vs x/c ($\alpha = 16^\circ$)

FIGURE 3-69. EFFECT OF IRT-IPSF22, LS-IPSF22, AND LR-IPSF22 ICE SHAPES (ICING CONDITION 6) ON PRESSURE DISTRIBUTIONS AT 85% SEMISPAN;

$$Re = 1.8 \times 10^6; \delta_A = 0^\circ$$

3.2.4.1 Icing Condition 1.

Lift, drag, and hinge-moment coefficients for this case are presented in figure 3-46. The results indicate the following:

- Lift coefficients for the IRT, smooth, and rough LEWICE ice shapes were in good overall agreement for α in the range of -7° to 7° , as shown in figure 3-46(a). All ice shapes resulted in a lower lift slope with respect to the clean wing. Over the stall region, the lift curves for the rough LEWICE ice shape (LR-CS10) and that of the IRT casting (IRT-CS10) were in good correlation. The smooth LEWICE ice shape (LS-CS10), however, resulted in higher $C_{L, \text{stall}}$ and α_{stall} . The reduction in $C_{L, \text{stall}}$ with respect to the clean wing for the IRT-CS10, LS-CS10, and LR-CS10 ice shapes was 38%, 18%, and 30% respectively. The change in α_{stall} with respect to the clean wing case was -24%, 5.8%, and -1.4% for ice shapes IRT-CS10, LS-CS10, and LR-CS10 respectively.
- All ice shapes caused a significant increase in C_D (e.g., 1100% to 1200% in $C_{D, \text{min}}$) with respect to the clean wing, as demonstrated in tables 3-1, 3-2, 3-4, 3-5, 3-7, and 3-8. Drag coefficients obtained with all three ice shapes were in good overall agreement. However, the drag due to LEWICE ice shapes was, in general, higher than the IRT ice shape casting, as shown in figure 3-46(c). For α greater than 10° , the smooth LEWICE ice shape produced higher drag compared to the rough LEWICE shape. This was the result of more extensive flow separation downstream of the smooth LEWICE ice horns. In general, the size and extent of flow separation downstream of large glaze ice shapes are affected by the roughness of the horn tip.
- Pitching-moment characteristics of clean and iced configurations are presented in figure 3-46(e). The results show that all three ice shapes produced pitching moments that were considerably higher or lower than the clean wing, depending on α . The trends in pitching moment with α for the ice shapes IRT-CS10, LS-CS10, and LR-CS10 were similar. As α was increased from -8° to α_{stall} , pitching moment was increased from negative (nose down) to positive (nose up) for all iced wing cases. This was mainly due to the leading-edge bubbles that resulted in a forward shift (ahead of the 25% MAC point) of the lift vector. When the bubble was on the lower surface (negative α), lift was negative, and the lift vector was ahead of the 25% MAC, resulting in negative C_M . Positive α had the opposite effect on lift and C_M . Past stall, C_M exhibited a downward trend as the load center moved aft of the 25% MAC point. This was due to massive flow separation over the wing, which resulted in a flat pressure distribution over the upper surface of the wing. Notable differences in the magnitude of the pitching moment of the IRT-CS10 ice shape compared to the LEWICE ice shapes were observed for α in the range of 6 to about 15° . These differences were, again, a function of the extent of the flow separation over each ice shape.
- Aileron hinge-moment coefficients for the IRT and LEWICE ice shapes are presented in figure 3-46(f). In all cases, the hinge moments due to the ice shapes were within the range defined by the minimum and maximum hinge moments of the clean wing. In general, the increase in hinge moments caused by the LEWICE ice shapes was greater

than the IRT ice shape for α in the range of -3° to 20° . Note that the $C_{H\alpha}$ in region A of the LEWICE ice shape curves was considerably higher than the IRT ice shape.

3.2.4.2 Icing Condition 2.

Lift, drag, and hinge-moment coefficients for this ice shape configuration are presented in figure 3-47. The results indicate the following:

- Lift coefficients for the IRT, smooth, and rough LEWICE ice shapes were in good overall agreement for α in the range of -7° to 12° , as shown in figure 3-47(a). The lift slope for all three ice shapes was the same as the clean wing. The reduction in $C_{L, \text{stall}}$ with respect to the clean wing for the IRT-IS10, LS-IS10, and LR-IS10 cases was 26.4%, 21.8% and 25.3% respectively. The reduction in α_{stall} with respect to the clean wing was 23%, 1.4%, and 1.4% for ice shapes IRT-IS10, LS-IS10, and LR-IS10 respectively.
- Drag coefficients for all three ice shapes were in good overall agreement for α in the range of 6° to 20° , as shown in figure 3-47(c). For α less than 6° , the IRT-IS10 ice shape resulted in higher drag than that obtained with the smooth and rough LEWICE ice shapes. The increase in $C_{D, \text{min}}$ for the iced wing with respect to the clean wing case was 683%, 500%, and 550% for the IRT-IS10, LS-IS10, and LR-IS10 ice shapes respectively.
- Pitching-moment coefficients for the IRT-IS10, LS-IS10, and LR-IS10 ice shapes are shown in figure 3-47(e). For α in the linear lift range, the results show that all ice shapes exhibited similar trends in C_M behavior. Specifically, a maximum C_M , of approximately 0.03 was attained at α of about 7° . However, beyond 7° AOA, the wing with the IRT-IS10 ice shape exhibited a drop followed by a small increase in C_M , indicating that the lift vector was moving back and forth. The LEWICE ice shapes resulted in a flat pitching-moment curve with positive C_M values for α in the range 7° to about 14° . After wing stall, all ice shapes manifested decreasing C_M (more negative) with α .
- Aileron hinge-moment coefficients for the IRT and LEWICE ice shapes are presented in figure 3-47(f). The ice shapes increased aileron hinge moments for α in the range of -6° to 13° . In all cases, however, the hinge moments due to the ice shapes were within the range defined by the minimum and maximum hinge moments of the clean wing. The increase in the iced wing hinge moment with respect to the clean wing for the LEWICE cases was greater than that obtained with the IRT ice shape for α in the range of 5° to 10° .

3.2.4.3 Icing Condition 3.

The IRT and LEWICE ice shapes were very similar in shape and size, as demonstrated in figure 2-35. Aerodynamic performance of the GLC-305 wing with the IRT and LEWICE rime ice shapes is presented in figure 3-48. The data presented indicate the following:

- Note that effects of higher Reynolds numbers representative of flight on the clean wing are not known. The lift coefficients for the clean and all iced wing cases were in good

overall agreement for α in the range of -8° to 12° , as shown in figure 3-48(a). The ice shapes tested resulted in 3.4% to 12.6% higher $C_{L,stall}$ and 7.2% to 14.5% higher α_{stall} with respect to the clean wing. The main reason for the observed increase in $C_{L,stall}$ and α_{stall} for the iced wing cases was the wing leading edge droop (see figure 2-35) feature of these three ice shapes. Note that the rough LEWICE shape resulted in the largest lift performance increment. This was probably due to delayed boundary layer separation caused by the grit roughness.

- The IRT and rough LEWICE ice shapes resulted in higher drag with respect to the clean wing for most of the α -range tested. The smooth LEWICE ice shape (LS-SC5) increased drag for α up to 10° , as shown in figure 3-48(c). At higher angles of attack, however, the drag of LS-SC5 was in most cases lower than that of the clean wing. The increase in the iced wing $C_{D,min}$ with respect to the clean wing case was 133%, 67%, and 117% for the IRT-SC5, LS-SC5, and LR-SC5 ice shapes respectively.
- From figure 3-48(e), it is observed that C_M was gradually increased with AOA prior to stall. But, as the IRT-SC5 and LR-SC5 configurations stalled, C_M decreased considerably and eventually became considerably more negative compared to the clean wing. As for LS-SC5 ice shape, its C_M distribution maintained more positive C_M than that of the clean case for angles of attack greater than 7° .
- Aileron hinge-moment coefficients for the IRT and LEWICE ice shapes were very similar to that of the clean wing for angles of attack greater than -4° , as shown in figure 3-48(f). Between α of -8° and -4° , the ice shapes resulted in lower aileron hinge-moment coefficient.

3.2.4.4 Icing Condition 4.

The IRT and LEWICE ice shape sections presented in figure 2-36 were in good overall agreement. Note that the cross section area of LEWICE ice shape at station A was larger than that of the IRT ice shape casting. Aerodynamic performance degradation due to the IRT and the LEWICE ice shapes is presented in figure 3-49. The experimental lift, drag and, hinge-moment coefficients presented indicate the following:

- The lift coefficients of the clean and iced wing cases were in good agreement over the linear lift range corresponding to angles of attack between -6° and 9° , as shown in figure 3-49(a). The reduction in the $C_{L,stall}$ with respect to the clean wing caused by the IRT, smooth LEWICE, and rough LEWICE ice shapes were 11.5%, 13.8%, and 17.2% respectively. The corresponding change in α_{stall} with respect to the clean wing was -8%, 6.5%, and -1%. Note that the rough LEWICE shape resulted in the largest lift reduction near stall, while the IRT casting caused the largest reduction in α_{stall} .
- The IRT and rough LEWICE ice shapes resulted in higher drag with respect to the clean wing throughout the α -range, as shown in figure 3-49(c). The increase in the iced wing $C_{D,min}$ with respect to that of the clean wing was 200%, 183%, and 233% for the IRT-CS2, LS-CS2, and LR-CS2 ice shapes respectively.

- Pitching moment trends for all three ice shapes were very similar. In general, the iced wing C_M was more negative or more positive than that of the clean wing throughout the α -range. The difference between the clean and the iced wing C_M ranged from -0.04 to 0.02.
- The aileron hinge moment behavior for the clean and IRT-CS2 cases were very similar for angles of attack in the range of -7° to 14° . The LEWICE ice shapes increased aileron hinge moments with respect to the clean case over region B of the C_H curve. For all ice shapes, the hinge-moment coefficients were within the range defined by the hinge moments of the clean wing.

3.2.4.5 Icing Condition 5.

The IRT and LEWICE ice shape sections presented in figure 2-37 exhibited large differences in horn shape, size, and overall section area. In addition, the IRT-CS22 ice shape had complex roughness and scallop features not present in the LEWICE ice shapes. Two sets of smooth and rough LEWICE ice shapes were tested for this icing condition as discussed in section 2.2.3.2. One was based on computations using sections normal (N) to the wing leading edge while the other was computed using streamwise (S) sections. The wing aerodynamic performance data for the IRT, the smooth, and rough LEWICE ice shapes presented in figure 3-50 indicate the following:

- The iced wing performance exhibited large reductions in lift, α_{stall} and in lift slope with respect to that of the clean wing. The largest degradation in lift was caused by the IRT-CS22 ice shape. The rough LEWICE ice shapes caused larger reductions in lift than their smooth counterparts. The rough LEWICE ice shape LR-CS22S obtained using streamwise wing sections and free-stream velocity resulted in larger lift degradation than that obtained with the rough LEWICE ice shape LR-CS22N, which was computed with the normal component of the free-stream velocity and airfoil sections normal to the wing leading edge. The difference in lift reduction due to the IRT-CS22 ice shape and that caused by the rough LEWICE ice shapes was considerable, particularly for angles of attack in the range of 0° to approximately 13° . The reduction in the $C_{L,\text{stall}}$ with respect to the clean wing caused by the IRT-CS22, LS-CS22N, LS-CS22S, LR-CS22N, and LR-CS22S ice shapes was 93.6%, 44%, 38%, 53%, and 61% respectively. The corresponding reduction in α_{stall} with respect to the clean wing was 56%, 2%, 3%, 17%, and 25%.
- All ice shapes tested caused very large drag increments, as shown in figure 3-50(c). The increase in the $C_{D,\text{min}}$ for the iced wing was 3533%, 2033%, 2367%, 2933%, and 3317% for the ice shapes IRT-CS22, LS-CS22N, LS-CS22S, LR-CS22N, and LR-CS22S respectively. The LEWICE ice shape that provided the best drag correlation with the IRT-CS22 ice shape was the LR-CS22S.
- Figure 3-50(e) shows pitching moment characteristics of the wing with all five CS22 ice shapes. Separated flow downstream of both upper and lower ice horns on the IRT-CS22 ice shape led to small changes in C_M compared to the clean case, despite the large differences in the wing pressure distributions obtained with the IRT-CS22 ice shape and

the clean wing. The four LEWICE ice shapes produced significantly more negative or more positive C_M than that of the clean wing. Also, the difference in $C_{M, \text{clean}} - C_{M, \text{LEWICE}}$ ranged from 0.07 at negative AOA to -0.085 at positive AOA. With increasing positive α , the separation bubbles behind the glaze ice horns shifted the load center upstream of the quarter-chord location and hence increased C_M . Conversely, beyond α_{stall} , separated flow over the upper surface and attached flow over the lower surface moved the center of pressure downstream and led to decreased C_M . It is worth noting that both LS-CS22N and LR-CS22S ice shapes had higher maximum C_M than their CS22S counterparts. Also, the break from positive to negative values in the C_M curve occurred at a higher α for the CS22N ice shapes.

- The aileron hinge moment behavior for the clean and iced wing cases exhibited large differences, as shown in figure 3-50(f). However, for all ice shapes, the hinge-moment coefficients were practically within the range defined by the minimum and maximum hinge moments of the clean wing. The LEWICE ice shape that provided the best C_H correlation with the IRT casting was the LS-CS22N.

3.2.4.6 Icing Condition 6.

The IRT and LEWICE ice shape sections presented in figure 2-38 demonstrated notable differences in size and shape. However, the horn angles and horn heights of the IRT ice shape castings and the LEWICE ice shapes were similar. Aerodynamic performance degradation due to the IRT and the LEWICE ice shapes is presented in figure 3-51. The experimental lift, drag and hinge-moment coefficients presented in these figures indicate the following:

- The lift coefficient for the iced wing exhibited lower lift and linear lift slope than that of the clean wing, as evident in figure 3-51(a). The reduction in the $C_{L, \text{stall}}$ of the iced wing with respect to the clean wing was 39%, 21% and 30% for the IRT, smooth LEWICE, and rough LEWICE ice shapes respectively. The corresponding change in α_{stall} with respect to the clean wing was -24%, 6%, and -9%. Note that the IRT-IPSF22 ice shape resulted in the largest reduction of $C_{L, \text{stall}}$ and α_{stall} with respect to the clean wing. The lift curves for the IRT and rough LEWICE ice shapes were in good agreement except near stall where the IRT shape caused approximately 1% to 8% more reduction in lift with respect to the clean wing.
- All ice shapes resulted in significant drag increments with respect to the clean wing drag, as shown in figure 3-51(c). The increase in $C_{D, \text{min}}$ of the iced wing with respect to the clean configuration was 1200%, 1000%, and 983% for the IRT-IPSF22, LS-IPSF22 and LR-IPSF22 ice shapes respectively. The trends in the IRT and LEWICE ice shapes drag curves were similar. However, the IRT ice shape caused higher drag at angles of attack in the range of -8° to 11° . For α greater than 11° , the LEWICE ice shapes resulted in higher drag.
- The trends in C_M for the IPSF22 ice shapes were quite similar to that obtained with the CS10 ice shapes. In general, the LS-IPSF22 and LR-IPSF22 cases produced similar pitching moment characteristics, as demonstrated in figure 3-51(e). The observed

differences in C_M between IRT and LEWICE ice shapes included more positive C_M for the LEWICE ice shapes for angles of attack between 6° and 18° and higher $dC_M/d\alpha$ after α of approximately 12° . The iced wing cases resulted in considerably more positive C_M than the clean wing for angles of attack in the range of 1° to 11° for the IRT-IPSF22 and 1° to 15° for the LEWICE ice shapes.

- The iced wing aileron hinge moment was within the range defined by the minimum and maximum hinge moments of the clean wing for all ice shape cases. For most angles of attack, the LEWICE ice shapes caused a larger increase (more negative or more positive) in hinge moments than that caused by the IRT ice shape.

3.2.4.7 Summary.

With the exception of icing condition 5, the rough LEWICE ice shapes caused similar loss in lift compared with the IRT ice shape castings. The difference in iced wing $C_{L,stall}$ (IRT $C_{L,stall}$ - rough LEWICE $C_{L,stall}$) obtained with the rough LEWICE and IRT ice shapes was -0.07, -0.01, -0.08, 0.05, -0.35, -0.28, and -0.08 for CS10, IS10, SC5, CS2, CS22N, CS22S, and IPSF22 respectively. In all but one case, the IRT ice shape castings resulted in higher reduction in $C_{L,stall}$ compared to that obtained with the rough LEWICE ice shapes. Again, with the exception of icing condition 5, the observed differences in $C_{L,stall}$ reduction between the IRT and LEWICE ice shapes were in the range of 1% to 9% with respect to the clean wing $C_{L,stall}$ which was equal to 0.87. In addition, the behavior of the lift curves obtained with the IRT and LEWICE ice shapes was very similar.

In general, the increment in wing drag caused by the LEWICE and IRT ice shapes was in good correlation. The difference in iced wing $C_{D,min}$ (rough LEWICE $C_{D,min}$ - IRT $C_{D,min}$) for the rough LEWICE and IRT cases was 0.004, -0.008, -0.001, 0.002, -0.036, -0.013, and -0.013 for CS10, IS10, SC5, CS2, CS22N, CS22S, and IPSF22 respectively.

With the exception of icing condition 5, the trends in aileron hinge moments obtained with the rough LEWICE and IRT ice shapes were in good agreement. For icing conditions 2 and 3, the IRT and LEWICE C_H magnitudes were in good correlation throughout the α -range. For icing conditions 1, 4, and 6, the LEWICE ice shapes resulted in larger hinge moments over regions A and B of the C_H curve compared with the IRT ice shapes. For icing condition 5, the behavior of C_H for the rough LEWICE and IRT ice shapes was considerably different. This was mainly due to higher suction over the wing upper surface caused by the rough LEWICE ice shapes.

In view of the differences in the geometric features of the large glaze IRT and LEWICE ice shapes tested, the LEWICE ice shapes provided a good engineering approximation to the aerodynamic effects of the IRT ice shapes for five out of the six cases tested.

3.2.4.8 Pressure Distributions—Clean and All Iced Configurations.

Pressure distributions for the clean wing and all 20 ice shape configurations tested are presented in figures 3-52 to 3-69 for α in the range of -4° to 16° and for spanwise locations corresponding to 15% semispan (near wing root), 50% semispan, and 85% semispan (near wing tip). The

pressure data provided insight into the change in wing load distribution with α and the stalling behavior of the clean and iced wing. In the discussion below, reference is made to three angles of attack, namely the wing geometric angle of attack, the local geometric angle of attack, and the effective angle of attack. These angles are defined as follows:

- Geometric angle of attack (α): this is the wing angle of attack as set on the wind tunnel turntable and is the α used in all force and moment plots.
- Local geometric angle of attack (α_{local}): this is the geometric angle of attack at a given spanwise station, which can be determined from α and the local geometric twist.
- Effective angle of attack (α_e): this angle of attack is the sum of α_{local} and the local upwash or downwash angle. Upwash or downwash is caused by the wing tip vortex and depends on wing lift.

For negative α , the wing upper surface was at a higher pressure than the lower surface. Due to wing twist, which was 0° at the root and -4° at the tip, the α_{local} varied from root to tip. Thus, at negative α , the wing root was at a lower α_{local} than the wing tip. In other words, the α_{local} increased from root to tip. At positive α , the wing tip was at a lower α_{local} than the wing root. However, for positive α , the wing experienced upwash, which increased as the α was increased. Thus, for positive lift, the wing upwash was higher near the wing tip than near the wing root.

The term suction used in the discussion of the clean and iced wing pressures refers to a region of flow where the static pressure is lower than in the free stream. Suction is associated with negative pressure coefficients and is usually observed in regions of the wing where the combination of wing curvature and α accelerates the flow to speeds higher than the free stream.

In most cases, the pressure data presented in figures 3-52 to 3-69 indicated that the addition of ice shapes resulted in a dramatic change in the pressure distribution mainly due to a combination of leading-edge separation bubbles and extensive flow separation over the wing. Flow separation is a function of ice shape and α . The length of the separated region increased as α , or the height of the ice shape horn, were increased. The large changes in surface pressures downstream of the ice shapes were responsible for the observed behavior of the iced wing force and moment coefficients.

Separated flows contain vortex structures, bubbles, and free shear layers that have a significant impact on the flow field. Vortex structures may be fixed in location as in the case of cavity flows and large stationary bubbles, or they can convect with the flow and interact with other vortices, free shear layers, or wall-bounded flows. Vortices can also stretch, depending on external forces (normal and shear forces) imposed on the vortex. The shape and strength of vortices in close proximity to the airfoil surface can produce considerable changes in surface pressures and, therefore, in aerodynamic loads.

The flow over iced wings, particularly for cases involving glaze ice shapes with large horns, features large regions of flow separation downstream of the ice shapes, which are typically referred to as leading-edge bubbles or long bubbles. These bubbles are regions of viscous flow

bound by the inviscid flow streamlines. The streamlines detach from the wing surface upstream of the bubble and reattach downstream of the bubble. If reattachment takes place over the wing surface, then the bubble is closed. The location of the reattachment point is a function of α and horn size. As α is increased, the bubble becomes progressively longer and eventually massive flow separation takes place once the bubble reaches the wing TE. In some cases, a long bubble can combine with separated flow initiated at the TE, and massive flow separation can occur before the bubble reaches the wing TE.

For swept wings, LE separation bubbles may include a combination of LE flow separation and LE vortex flow. When sweep is incorporated in a wing, a conical vortex lying on the wing surface can occur, as discussed in reference 18. This LE vortex results from both the LE separation bubble and the spanwise pressure gradient due to sweep. The vortex cross section grows nearly perpendicular to the wing LE (conical vortex) in the spanwise direction. The growth of vortex diameter as the wing tip is approached is the result of a combination of vortex flow with the thick boundary layer transported by the spanwise flow from the inboard sections. With increased α , the vortex becomes stronger near the inboard sections but diffuses near the outboard sections. Near the wing tip, the diffused conical LE vortex can combine with the wing tip vortex, and complex flow separation patterns are often observed. LE vortices were observed with both the clean and iced wing configurations tested as α was increased.

In general, pressure distributions for wing flows with LE bubbles exhibit a considerable reduction in LE suction and a rounding of the LE pressure distribution. As the α is increased, the bubble becomes longer in the streamwise direction and the suction over the bubble is typically reduced. This led to a flat pressure distribution over the wing surface. In general, LE bubbles shift the load towards the LE. However, as the bubble becomes longer and massive flow separation takes place, the wing load shifts in the downstream direction. Massive flow separation is an unsteady phenomenon that involves convection of vortices, which cause significant changes to the load distribution over the wing and, thus, to wing pitching moments. Flow separation near the outboard portion of the iced wings could also cause large changes in the load over aileron controls, and in some cases, it could reduce or even eliminate the control effectiveness. Flow separation over the aileron is also responsible for control force reversal and potential large changes in control stick forces. Thus, bubble formation, growth, and bursting can cause large changes in the wing pitching moments and in aileron hinge moments.

Another control issue regarding rolling moments is that ice accretions on the left and right wings are not typically symmetric. As a result of the ice asymmetry, flow separation in the spanwise direction could be different between the two sides of the wing, thus leading to considerable rolling moments.

In reviewing the pressures distributions of the clean and iced wing configurations presented in figures 3-52 to 3-69, the following trends and features in the pressure data should be examined:

- Location of the area centroid of the chordwise pressure distribution with respect to the 25% MAC point of the wing. This determines pitching-moment behavior.

- Change in pressure distribution in the spanwise direction. This affects spanwise load distribution and provides insight into spanwise flow separation. The spanwise load distribution also affects wing rolling moment.
- The growth of separation bubbles with α . Sudden changes in bubble features are undesirable because they cause sudden changes in wing loads.
- The shape of the pressure distribution over the upper and lower control surface. This is responsible for the observed behavior of control hinge moments.

3.2.4.9 Clean Wing (Figures 3-52 to 3-54).

- $\alpha = -4^\circ$: High suction was observed over the lower surface of the wing. Suction increased with spanwise distance and reached a maximum suction C_p of -3.53 at the 85% semispan station. The pressure data indicated that the flow was attached.
- $\alpha = 0^\circ$: The flow remained attached. Due to the wing geometric twist, the average α was negative, resulting in negative lift. In all cases, the lower surface of the wing experienced suction that was lower near the root and higher near the tip.
- $\alpha = 4^\circ$: For this α , α_{local} was 4° at the root and 0° at the tip. The pressure over the wing upper surface was lower than over the lower surface, resulting in positive lift. Upper surface suction was higher near the wing root than near the wing tip. The flow remained attached.
- $\alpha = 8^\circ$: High suction was observed over the wing upper surface at all spanwise stations. The suction C_p increased from -3.3 at 15% semispan to -3.5 at 50% semispan, and then it decreased to -2.7 at 85% semispan. The pressure data indicated that flow separation was not present over the wing for this α .
- $\alpha = 12^\circ$: LE separation bubbles are evident for this near stall α . The extent of the separation bubbles increased from root to tip, while the suction over the bubble decreased.
- $\alpha = 16^\circ$: A large LE separation bubble was observed near the wing root. The flat C_p curves corresponding to the wing upper surface at the 50% and 85% semispan stations are indicative of massive flow separation. The pressure data presented for α of 12° and 16° show that flow separation (wing stall) was initiated at the tip of the wing and progressed toward the root.

3.2.4.10 Iced Wing.

Pressure distributions for the iced wing with the IRT castings and the simulated smooth and rough LEWICE ice shapes are discussed below. The experimental pressure distributions for the iced configurations tested exhibited leading-edge bubbles over the upper, lower, and in many cases, over both surfaces of the wing. As the α was increased, the bubble(s) grew longer in the

downstream direction and eventually burst into massive flow separation as the streamlines failed to reattach to the wing surface.

3.2.4.10.1 Icing Condition 1—Ice shapes: IRT-CS10, LS-CS10, LR-CS10 (Figures 3-52 to 3-54).

- $\alpha = -4^\circ$: At 15% semispan, LE bubbles were evident over the wing lower surface for all ice shape cases. The suction over the bubble region was greater for the LEWICE ice shapes compared to the IRT ice shape casting. At the mid-semispan location, extensive flow separation was observed over the lower wing surface for the cases presented. The flow remained separated over the lower surface near the tip station, and the suction was reduced. An LE bubble was present over the lower surface for the LEWICE ice shapes.
- $\alpha = 0^\circ$: Flow separation in the form of LE bubbles was present over both wing surfaces for all ice shapes tested. Suction over the lower surface was higher than over the upper surface. In most cases, the LEWICE ice shapes resulted in higher suction over the lower surface. The bubble extent was less near the wing root than at the outboard stations. Near the wing tip, flow separation extended to the wing TE.
- $\alpha = 4^\circ$: For this angle of attack, suction was increased over the wing upper surface. The C_p on the lower surface varied from high negative near the LE, indicating the presence of separation bubbles to low negative and, in some cases, slightly positive near the TE. The extent of the upper surface bubbles decreased (separation was reduced) with spanwise distance from root to tip due to the negative wing twist, which lowered the α_{local} over the outboard sections.
- $\alpha = 8^\circ$: Long bubbles were observed over the inboard wing upper surface for all the ice shapes. The bubbles grew longer (chordwise) over the outboard sections of the wing and eventually, complete flow separation was observed near the wing tip. Suction over the bubbles for the LEWICE ice shapes was higher than obtained with the IRT ice shape casting. In most cases, the pressure distribution over the wing lower surface obtained with the LEWICE shapes exhibited bubble formation between 0% and approximately 50% chord.
- $\alpha = 12^\circ$: Large bubbles were observed at the 15% station, and complete flow separation was evident over the wing upper surface at the 50% and 85% semispan locations with all ice shapes tested. The IRT ice shape had lower suction over the two inboard stations than the LEWICE ice shapes. Bubbles were also present over the lower surface of the wing for the two LEWICE shapes.
- $\alpha = 16^\circ$: At this angle of attack, extensive flow separation was observed over the upper surface of the wing at all spanwise stations. The only exception was the smooth LEWICE ice shapes for which the flow over the inboard (15% semispan) station was partially attached.

3.2.4.10.2 Icing Condition 2—Ice Shapes: IRT-IS10, LS-IS10, LR-IS10 (Figures 3-55 to 3-57).

- $\alpha = -4^\circ$: At 15% semispan, LE bubbles were evident over the wing lower surface for all ice shape cases. In addition, at the mid-semispan location, the bubbles grew longer. Furthermore, reduced suction and extensive flow separation were observed over the wing lower surface near the tip station. Note that the LE bubbles of the IRT-IS10 and LR-IS10 cases were comparable at the 50% and 85% semispan stations, while the bubble of the LS-IS10 configuration produced higher suction.
- $\alpha = 0^\circ$: Flow separation in the form of LE bubbles was present over both wing surfaces for all ice shapes tested. Suction over the lower surface was higher than over the upper surface. The IRT and LEWICE ice shapes resulted in comparable suction over the lower surface. The bubble extent was less near the wing root than at the outboard stations. Near the wing tip, flow separation extended to the wing TE.
- $\alpha = 4^\circ$: For this angle of attack, suction was increased over the wing upper surface. The C_p on the lower surface varied from high negative near the LE, indicating the presence of separation bubbles, to low negative and, in some cases, slightly positive near the TE. Note that at the 15% semispan station, the suction on the wing upper surface, due to the IRT-IS10 ice shape, was lower than that produced by the LEWICE ice shapes. However, the difference in suction between the IRT and LEWICE ice shapes diminished with spanwise distance from root to tip.
- $\alpha = 8^\circ$: Long bubbles were observed over the inboard wing upper surface for all ice shapes. The bubbles grew longer (chordwise) over the outboard sections of the wing and eventually complete flow separation was observed near the wing tip. Suction over the bubbles for the LEWICE ice shapes was higher than that obtained with the IRT ice shape casting near the wing root. In most cases, the pressure distribution over the wing lower surface obtained with the LEWICE ice shapes exhibited bubble formation between 0% and approximately 50% chord.
- At the higher α of 12° and 16° , extensive flow separation was observed over the upper surface of the wing at all spanwise stations. The only exception was the flow at the 15% semispan station, which was partially attached for all ice shape configurations.

3.2.4.10.3 Icing Condition 3—Ice Shapes: IRT-SC5, LS-SC5, LR-SC5 (Figures 3-58 to 3-60).

- $\alpha = -4^\circ$: At 15% semispan, small LE bubbles were observed over the wing lower surface for all ice shape cases. The suction over the bubble region was comparable between the LEWICE and IRT ice shapes casting. The bubbles grew longer (chordwise) at the mid-semispan station. At the 85% semispan location, extensive flow separation was observed over the wing lower surface for all cases presented. An LE bubble was present over the lower surface for all ice shapes.
- $\alpha = 0^\circ$: Flow separation in the form of LE bubbles was present over both wing surfaces for all ice shapes tested. Suction over the lower surface was higher than over the upper

surface. The bubble extent was less near the wing root than at the outboard stations. Near the wing tip, flow separation extended to the wing trailing edge.

- For angles of attack of 4° and 8° , C_p distributions of all ice shape configurations were in good agreement with the clean case. At the two inboard locations, the minimum pressure near the LE for the iced wing was lower than the clean wing, indicating lower α_e . The reduction in α_e was due to the LE droop caused by the rime ice accretion.
- $\alpha = 12^\circ$: At the 15% semispan station, only the IRT-SC5 ice shape produced a LE bubble on the wing upper surface. At the same time, observe that suction was increased for both LEWICE ice shapes. As the flow progressed to the 50% semispan location, the C_p distributions exhibited a bubble near the LE for all three iced wing configurations, where the suction over the bubble for the LS-SC5 case was higher than the other two SC5 ice shapes. The LE bubbles grew in chordwise length from the 50% semispan station to the wing tip.
- $\alpha = 16^\circ$: At this angle of attack, all ice shapes maintained partial attached flow over the wing suction surface at the two inboard stations. However, extensive flow separation was observed over the upper surface of the wing at the 85% location.

3.2.4.10.4 Icing Condition 4—Ice Shapes: IRT-CS2, LS-CS2, LR-CS2 (Figures 3-61 to 3-63).

- $\alpha = -4^\circ$: At 15% semispan, LE bubbles were evident over the wing lower surface for all ice shape cases. From root to mid-semispan stations, the bubble region extent increased. Extensive flow separation was observed over the wing lower surface near the tip station for all cases presented.
- $\alpha = 0^\circ$: Flow separation in the form of LE bubbles was present over both wing surfaces for all ice shapes tested. Suction over the lower surface was higher than over the upper surface. Note that the bubble extent was less near the wing root than at the outboard stations. However, the LEWICE ice shapes produced separation bubbles of greater extent than the IRT ice shape.
- $\alpha = 4^\circ$: For this angle of attack, suction was increased over the wing upper surface. Separation bubbles were observed over the lower surface between 0% and approximately 20% chord. The extent of the upper surface bubbles decreased (separation was reduced) with spanwise distance from root to tip due to the negative wing twist, which lowered the α_{local} over the outboard sections. Moreover, suction over the LE bubbles of the LEWICE ice shapes was higher than the IRT-CS2 case at all spanwise stations.
- $\alpha = 8^\circ$: Once again, bubbles were observed over the inboard wing upper surface for all the ice shapes. The bubbles grew longer (chordwise) over the outboard sections of the wing. For the LEWICE ice shapes, suction over the bubbles was higher than obtained with the IRT ice shape casting at the 15% semispan station. However, at the mid-semispan and near tip stations, the smooth and rough LEWICE ice shapes had lower suction over the separation bubbles than the IRT-CS2 ice shape.

- $\alpha = 12^\circ$: Large LE bubbles were observed at the 15% semispan station, and complete flow separation was evident over the wing upper surface at the two outboard locations with all the ice shapes, except the IRT-CS2 ice shape for which the flow was partially attached near the wing tip.
- $\alpha = 16^\circ$: At this angle of attack, extensive flow separation was observed over the upper surface of the wing at all spanwise stations.

3.2.4.10.5 Icing Condition 5—Ice Shapes: IRT-CS22, LS-CS22N, LS-CS22S, LR-CS22N, and LR-CS22S (Figures 3-64 to 3-66).

- $\alpha = -4^\circ$: At 15% semispan, LE bubbles were evident over the wing lower surface for all ice shapes. Suction over the bubble region was greater for the LEWICE ice shapes compared to the IRT-CS22 case. Comparing the smooth and rough LEWICE ice shapes, it was observed that the addition of roughness to the ice horns produced bubbles with lower suction but of greater chordwise extent than obtained with the smooth LEWICE ice shape. At the mid-semispan location, extensive flow separation was observed over the wing lower surface for all cases, except the LS-CS22S and LR-CS22S ice shapes. The flow remained separated over the lower surface near the tip station.
- $\alpha = 0^\circ$: Flow separation in the form of LE bubbles was present over both wing surfaces for all ice shapes tested. Suction over the lower surface was higher than over the upper surface. In most cases, the LEWICE ice shapes resulted in higher suction over the lower surface. Near the wing tip, flow was completely separated.
- $\alpha = 4^\circ$: For this angle of attack, LE bubbles were present over both surfaces near the wing root. For the rough LEWICE ice shapes, suction over the bubbles was higher than their smooth counterparts. At the mid-semispan location, extensive flow separation was observed for the IRT and rough LEWICE ice shapes, while for the LS-CS22N and LS-CS22S cases, the flow was partially attached. An LE bubble was evident for the IRT-CS22 ice shape at the 85% semispan station. Flow remained separated near the wing tip for all LEWICE cases.
- $\alpha = 8^\circ$: Long bubbles were observed over the inboard wing upper surface for all LEWICE ice shapes, whereas flow downstream of the IRT-CS22 horns was completely separated over the wing upper surface. For the LEWICE cases, the LE separation bubbles failed to reattach over the wing sections at the 50% and 85% semispan stations, and complete flow separation was observed. For the wing with LEWICE ice shapes, the pressure distribution over the lower surface exhibited bubble formation between 0% and approximately 50% chord.
- $\alpha = 12^\circ$: Aft of IRT-CS22 upper ice horn, complete flow separation occurred. For all LEWICE ice shapes, large bubbles were observed at the 15% semispan station, and massive flow separation was evident over the wing upper surface at the 50% and 85% semispan locations. Note that the IRT ice shape had lower suction than the LEWICE ice shapes. Bubbles were also present over the lower surface of the wing for all ice shapes

from root to tip. Yet, only the LS-CS22S ice shape maintained a lower surface bubble near the wing tip.

- $\alpha = 16^\circ$: At this angle of attack, extensive flow separation was observed over the upper surface of the wing at all spanwise stations. Once again, all ice shapes produced an LE bubble over the wing pressure surface at the three spanwise stations, as shown in the figures.

3.2.4.10.6 Icing Condition 6—Ice Shapes: IRT-IPSF22, LS-IPSF22, LR-IPSF22 (Figures 3-67 to 3-69).

- $\alpha = -4^\circ$: At 15% semispan, LE bubbles were evident over the wing lower surface for all ice shape cases. The suction over the bubble region was greater for the LEWICE ice shapes compared to the IRT ice shape casting. At the mid-semispan location, bubbles of greater extent were observed over the wing lower surface for all cases presented. Over the lower surface, the flow was separated near the tip station for the IRT-IPSF22 configuration, whereas an LE bubble was present for the LEWICE ice shapes.
- $\alpha = 0^\circ$: Flow separation in the form of LE bubbles was present over both wing surfaces for all ice shapes tested. Suction over the lower surface was higher than that over the upper surface. In most cases, the LEWICE ice shapes resulted in higher suction over the lower surface. The bubble extent was less near the wing root than at the outboard stations. Near the wing tip, flow separation extended to the wing TE.
- $\alpha = 4^\circ$: For this angle of attack, suction was increased over the wing upper surface. The C_p on the lower surface varied from high negative near the LE, indicating the presence of separation bubbles, to low negative and, in some cases, slightly positive near the TE.
- $\alpha = 8^\circ$: Long bubbles were observed over the inboard wing upper surface for all ice shapes. The bubbles grew longer (chordwise) over the outboard sections of the wing, and eventually, complete flow separation was observed near the wing tip. Suction over the bubbles for the LEWICE ice shapes was higher than obtained with the IRT ice shape casting. Separation bubbles were also observed on the lower wing surface for all ice shapes. The lower surface bubble increased its chordwise length from root to tip.
- $\alpha = 12^\circ$: Large bubbles were observed at the 15% station, and complete flow separation was evident over the wing upper surface at the 50% and 85% semispan locations for all ice shapes tested. The IRT ice shape had lower suction over the two inboard stations than the LEWICE ice shapes. Bubbles were also present over the lower surface of the wing for all ice shapes.
- $\alpha = 16^\circ$: At this angle of attack, extensive flow separation was observed over the upper surface of the wing at all spanwise stations. The only exception was the smooth LEWICE ice shapes for which the flow over the inboard (15% semispan) station was partially attached. Once again, LE bubbles were observed for all ice shapes over the wing lower surface.

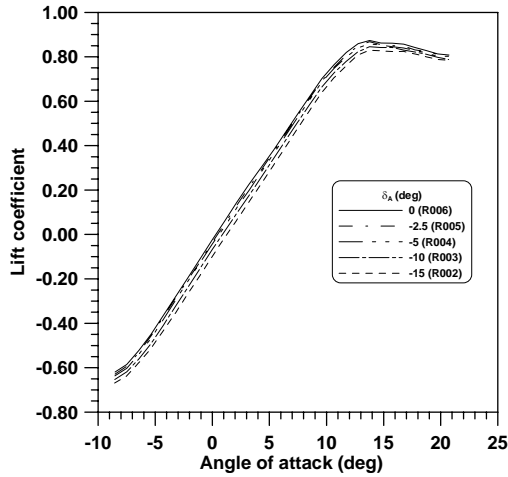
3.2.5 Effect of Aileron Deflection.

The effect of aileron deflection on the aerodynamic performance of the clean and iced wing is presented in figures 3-70 to 3-73 and in table 3-10. The main performance parameters presented include:

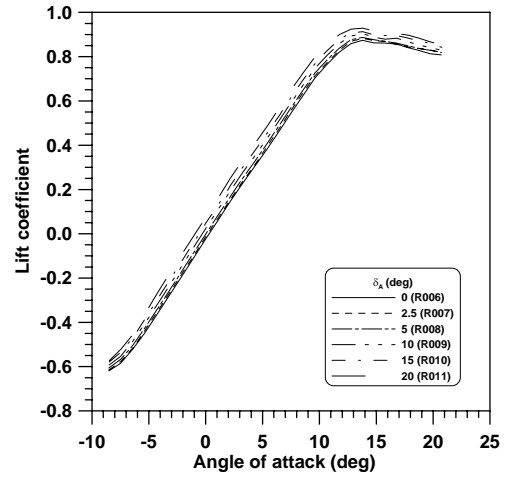
- C_L versus α for all aileron deflections (δ_A)
- C_H versus α for all δ_A
- C_L versus δ_A for selected α
- C_H versus δ_A for selected α

Another important parameter for assessing aileron performance is the change in rolling moment with δ_A and α . Rolling moment data were obtained during the experimental investigation at WSU.

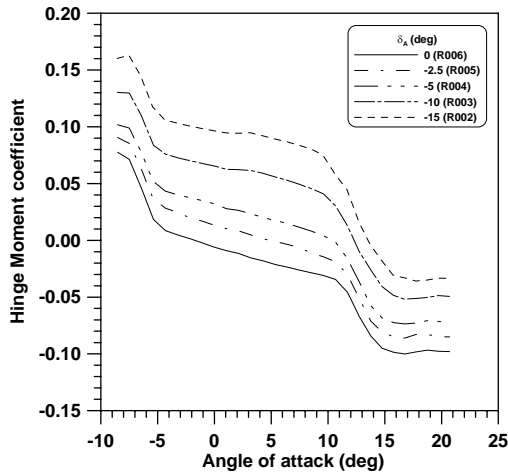
The experimental lift and hinge-moment data presented in figures 3-70 to 3-73 were obtained with a reflection plane wing model having a single aileron. Aircraft wings, however, have left and right ailerons that are not independent but are connected via cables to the control wheel. Thus, the control forces experienced by the pilot are due to the difference in the hinge moments generated by the left and right ailerons. To estimate the net aileron control force from the experimental data presented, the hinge moment for positive and negative aileron deflections must be combined. For example, using the results presented in figure 3-70(f) for the clean wing, α of 0° and δ_A of 5° , the difference between C_H for aileron deflection of -5° and C_H for aileron deflection of 5° provides the net aileron control force. This procedure assumes that the up and down aileron deflection angles are the same. However, in some aircraft, left and right aileron deflection angles are not the same, and in such a case, the actual deflections for each aileron have to be used to compute the control force. Another assumption made regarding the superimposition of the experimental results is that ice accretions for the left and right wings are symmetric. In general, the left and right wing ice shapes will not be exactly the same, and this could cause different separation patterns over the left and right sides of the wing and the ailerons.



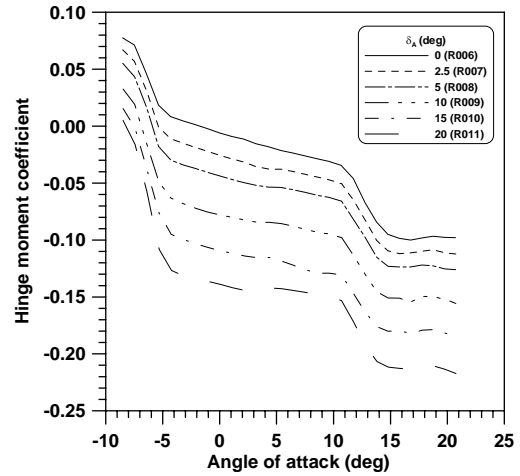
(a) Lift coefficient (negative δ_A)



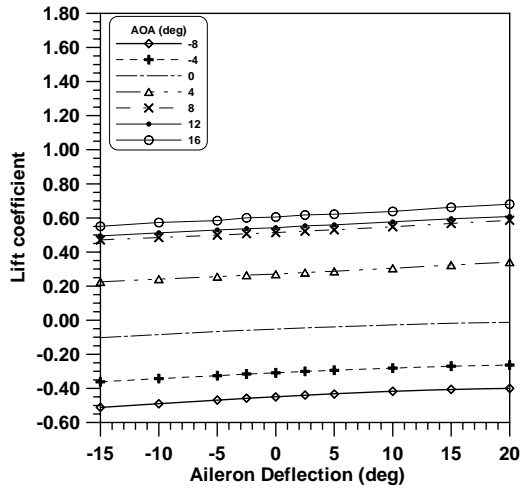
(b) Lift coefficient (positive δ_A)



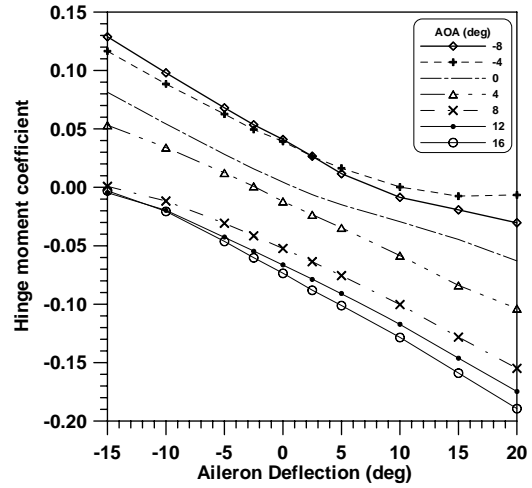
(c) Hinge-moment coefficient (negative δ_A)



(d) Hinge-moment coefficient (positive δ_A)

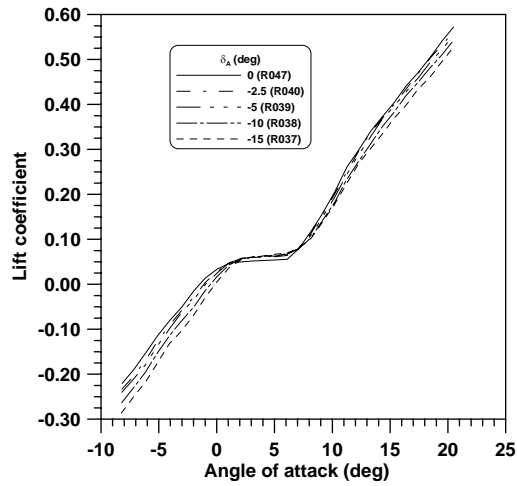


(e) Lift coefficient vs δ_A

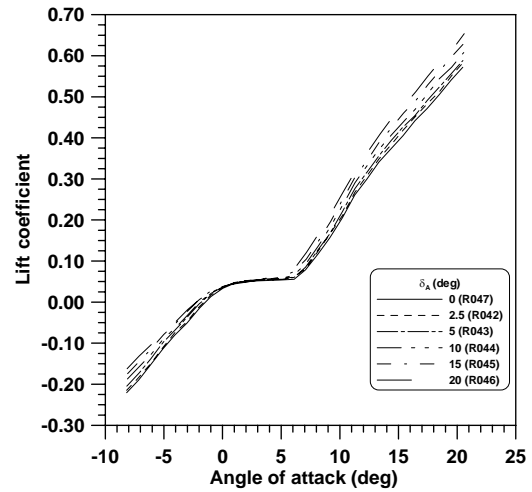


(f) Hinge-moment coefficient vs δ_A

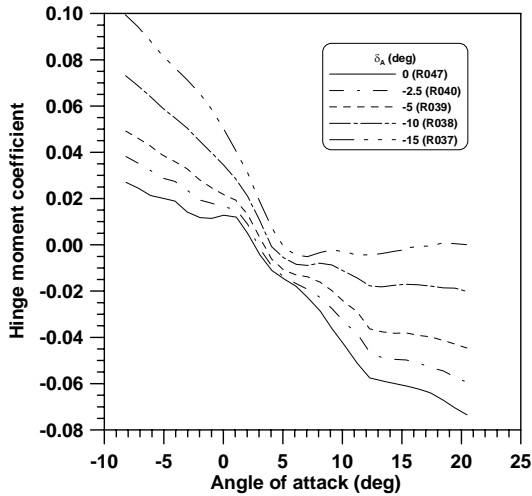
FIGURE 3-70. EFFECT OF AILERON DEFLECTION ON LIFT AND AILERON HINGE-MOMENT COEFFICIENTS; CLEAN CONFIGURATION; $Re = 1.8 \times 10^6$



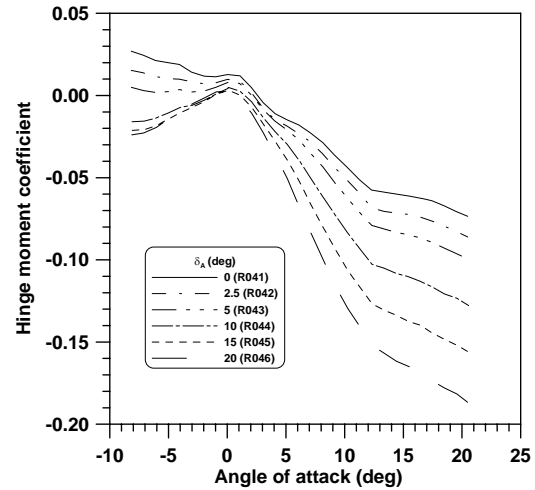
(a) Lift coefficient (negative δ_A)



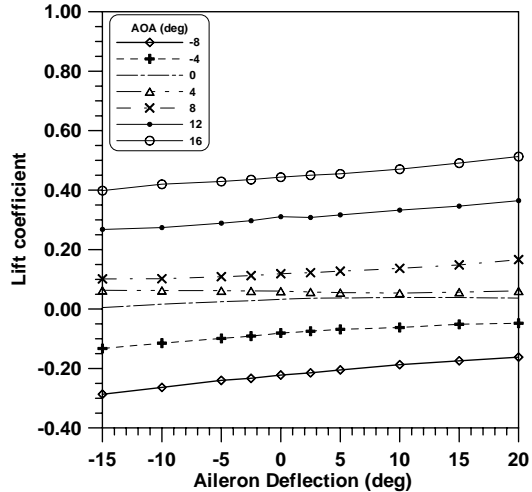
(b) Lift coefficient (positive δ_A)



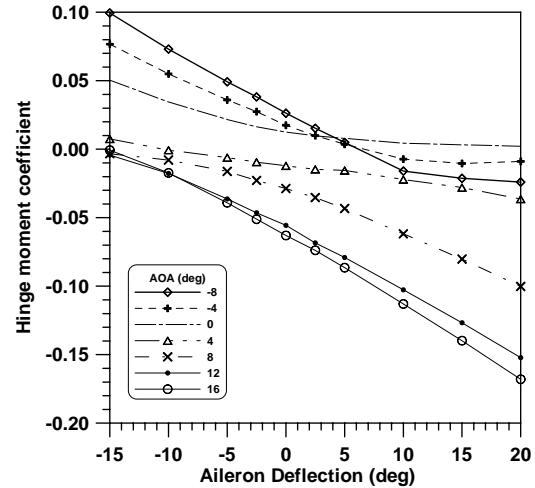
(c) Hinge-moment coefficient (negative δ_A)



(d) Hinge-moment coefficient (positive δ_A)

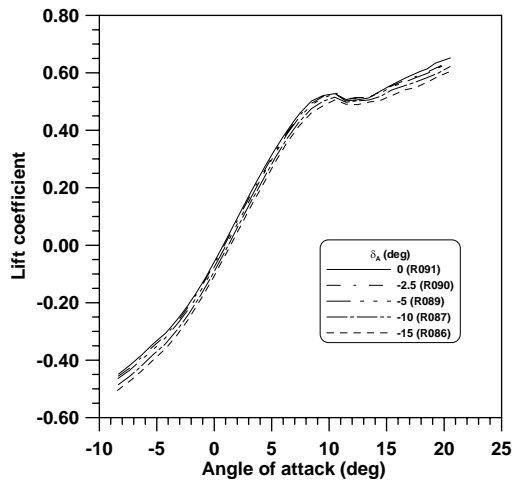


(e) Lift coefficient vs δ_A

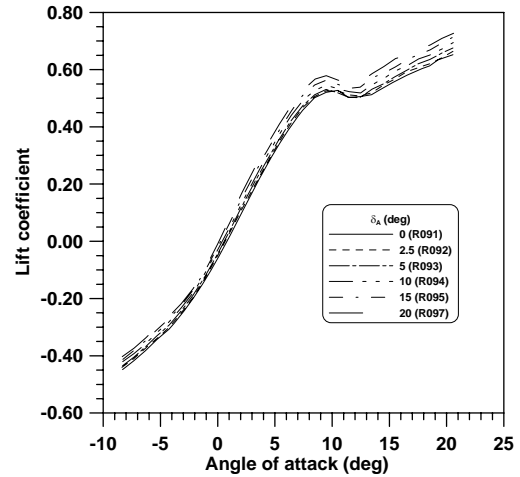


(f) Hinge-moment coefficient vs δ_A

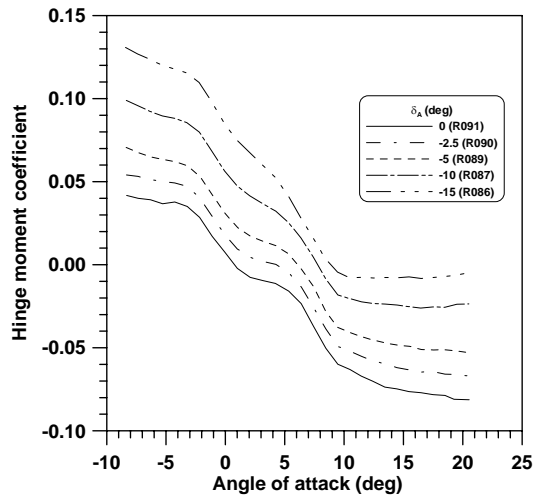
FIGURE 3-71. EFFECT OF AILERON DEFLECTION ON LIFT AND AILERON HINGE-MOMENT COEFFICIENTS; IRT-CS22 ICE SHAPE; $Re = 1.8 \times 10^6$



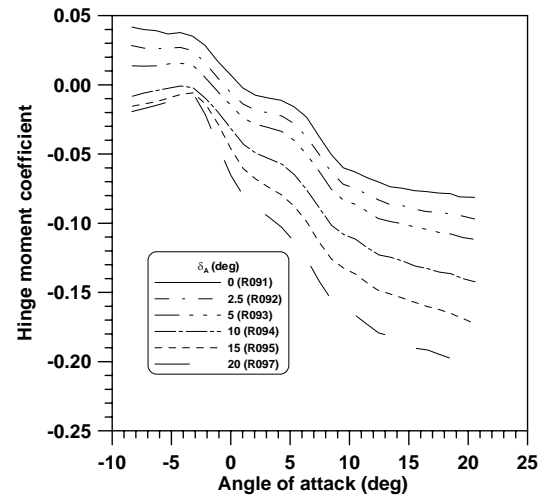
(a) Lift coefficient (negative δ_A)



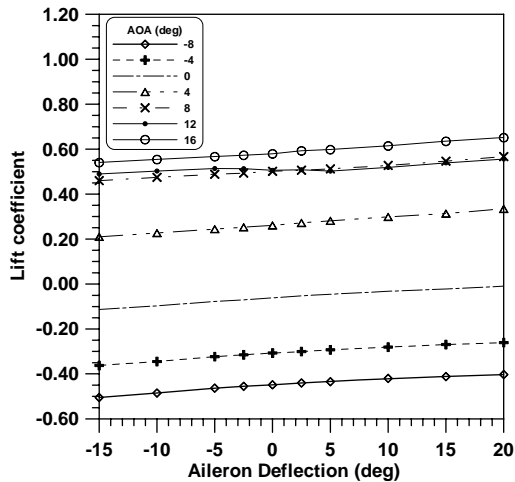
(b) Lift coefficient (positive δ_A)



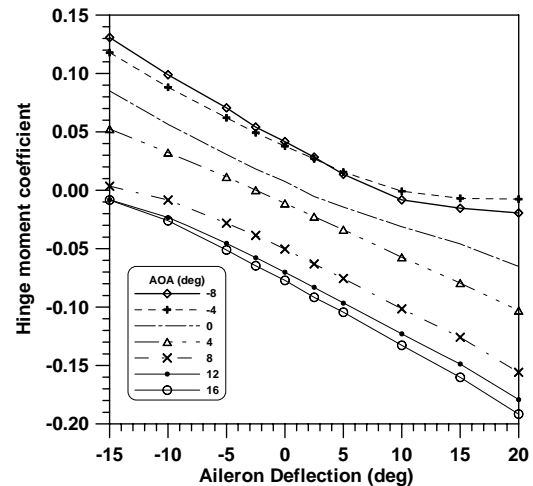
(c) Hinge-moment coefficient (negative δ_A)



(d) Hinge-moment coefficient (positive δ_A)

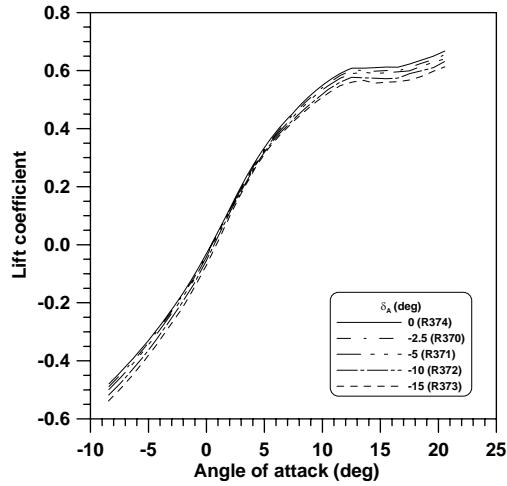


(e) Lift coefficient vs δ_A

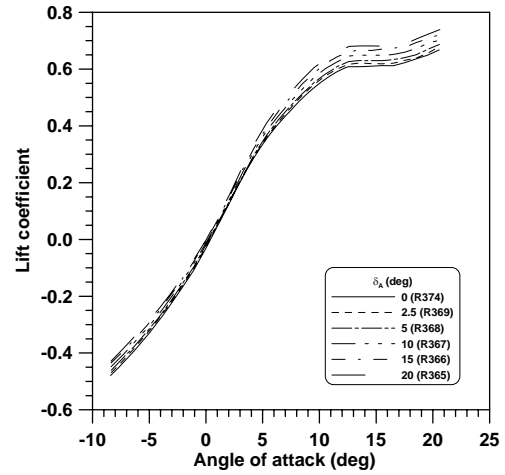


(f) Hinge-moment coefficient vs δ_A

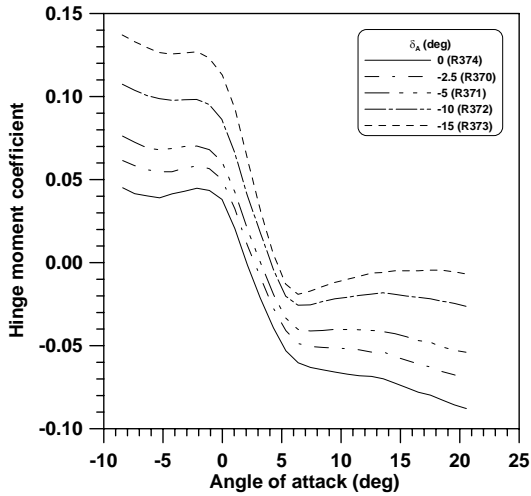
FIGURE 3-72. EFFECT OF AILERON DEFLECTION ON LIFT AND AILERON HINGE-MOMENT COEFFICIENTS; IRT-IPSF22 ICE SHAPE; $Re = 1.8 \times 10^6$



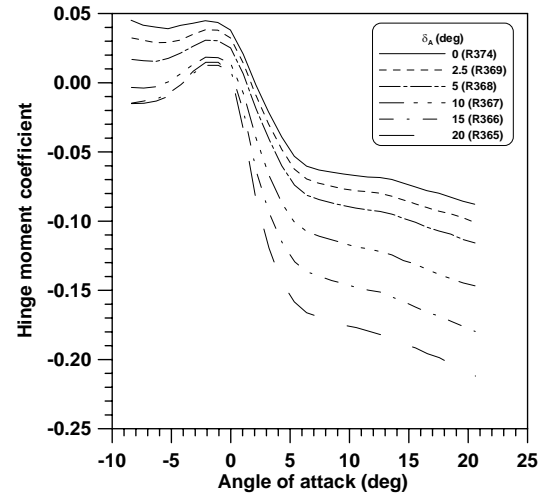
(a) Lift coefficient (negative δ_A)



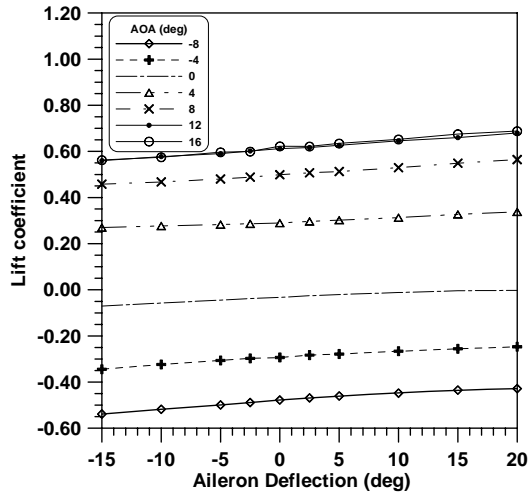
(b) Lift coefficient (positive δ_A)



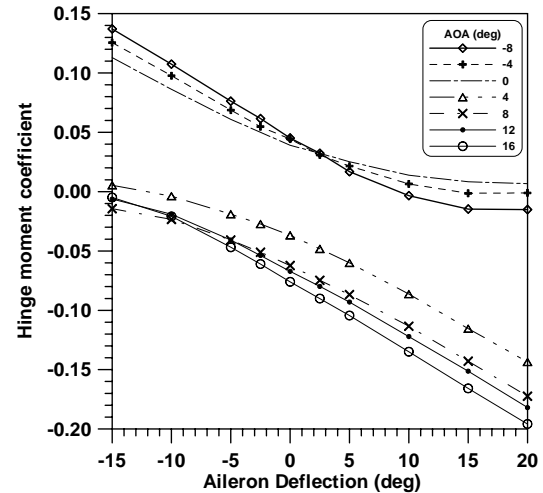
(c) Hinge-moment coefficient (negative δ_A)



(d) Hinge-moment coefficient (positive δ_A)



(e) Lift coefficient vs δ_A



(f) Hinge-moment coefficient vs δ_A

FIGURE 3-73. EFFECT OF AILERON DEFLECTION ON LIFT AND AILERON HINGE-MOMENT COEFFICIENTS; LR-IPSF22 ICE SHAPE; $Re = 1.8 \times 10^6$

TABLE 3-10. $C_{L, stall}$ OF ALL CONFIGURATIONS WITH
AILERON DEFLECTION; $Re_{MAC} = 1.8 \times 10^6$

δ_A Configuration	-15°	-10°	-5°	-2.5°	0°	2.5°	5°	10°	15°	20°
Clean	0.829	0.845	0.858	0.868	0.874	0.883	0.887	0.904	0.913	0.929
IRT-CS10	0.491	0.506	0.522	0.526	0.536	0.544	0.533	0.573	0.593	0.613
IRT-IS10	0.591	0.603	0.618	0.628	0.646	0.648	0.662	0.676	0.688	0.716
IRT-SC5	0.862	0.874	0.888	0.893	0.896	0.908	0.918	0.930	0.948	0.961
IRT-CS2	0.737	0.752	0.770	0.774	0.775	0.782	0.788	0.807	0.819	0.835
IRT-CS22	0.005	0.016	0.025	0.028	0.033	0.036	0.037	0.039	0.039	0.037
IRT-IPSF22	0.506	0.515	0.527	0.532	0.528	0.527	0.531	0.546	0.563	0.579
LS-CS10	0.669	0.679	0.692	0.705	0.710	0.719	0.723	0.744	0.760	0.772
LS-IS10	0.640	0.656	0.666	0.672	0.679	0.687	0.697	0.722	0.735	0.747
LS-SC5	0.900	0.915	0.927	0.933	0.939	0.952	0.965	0.980	0.984	1.000
LS-CS2	0.714	0.722	0.737	0.741	0.748	0.759	0.769	0.780	0.800	0.812
LS-CS22N	0.450	0.462	0.476	0.476	0.484	0.490	0.496	0.505	0.512	0.520
LS-CS22S	0.495	0.507	0.516	0.517	0.537	0.542	0.548	0.564	0.575	0.601
LS-IPSF22	0.635	0.648	0.660	0.667	0.676	0.683	0.697	0.713	0.737	0.746
LR-CS10	0.564	0.584	0.597	0.607	0.613	0.624	0.635	0.647	0.669	0.683
LR-IS10	0.589	0.605	0.627	0.636	0.644	0.651	0.661	0.678	0.694	0.711
LR-SC5	0.921	0.939	0.955	0.962	0.980	0.982	0.994	1.012	1.027	1.044
LR-CS2	0.677	0.691	0.703	0.709	0.717	0.730	0.736	0.754	0.770	0.783
LR-CS22N	0.406	0.405	0.409	0.406	0.407	0.412	0.413	0.416	0.424	0.427
LR-CS22S	0.352	0.351	0.349	0.346	0.342	0.344	0.343	0.352	0.351	0.356
LR-IPSF22	0.566	0.577	0.590	0.602	0.612	0.617	0.626	0.646	0.659	0.680

3.2.5.1 General Comments Regarding Aileron Controls.

Ailerons are designed to meet aircraft roll performance criteria in terms of roll rate (typically 10 to 15 degrees per second) and attitude. In addition, the ailerons should be able to provide sufficient roll control to handle special aircraft situations such as an engine-out case or steady heading sideslip. Aileron forces should remain within the capabilities of the pilot as defined by the certification requirements [11], which state that the maximum permissible aileron control force is 50 lb with two hands on the control wheel and 25 lb for a single hand on the control wheel (autopilot settings vary with design but often a 20 lb limit is used).

The change in aileron hinge moments with δ_A and α has a direct impact on aileron control forces. The slope of C_H with δ_A , C_{H, δ_A} , also known as the control heaviness parameter, is of primary importance in evaluating control surface behavior and control forces. In general, aileron designs have negative C_{H, δ_A} so that the aileron has the tendency to return to its undeflected position. The hinge-moment slope, $C_{H, \alpha}$, also known as the control floating parameter, affects the change in the control force resulting from the response of the aircraft to the control movement. When the ailerons are deflected and wing roll is initiated, the local α of the upward and downward moving wings is changed (typically by a couple of degrees for small deflection), and the control force required to maintain a steady maneuver is either greater or less than the control force required to

initiate the maneuver, depending on the sign and magnitude of $C_{H,\alpha}$. Control surface designers usually aim at small positive or negative values for $C_{H,\alpha}$ to avoid large differences in control forces during maneuver [18 and 19]. The effect of $C_{H,\alpha}$ on control forces is of secondary importance, particularly for small aileron deflection and roll rates that cause small changes in α . For large deflections, however, which can produce large roll rates and therefore a large change in α , $C_{H,\alpha}$ could have a notable effect on control forces.

Once the clean wing aileron design requirements have been satisfied, the effect of ice shapes on aileron performance should be assessed for unwanted changes in control behavior. In general, the presence of ice on the wing leading edge can result in early flow separation over the wing and control surfaces, and the iced wing lift with δ_A could change with respect to the clean wing. It is important that the lift of the iced wing exhibits the expected behavior with positive and negative aileron deflections, although some loss in aileron effectiveness is expected.

The effect of ice shapes on aileron hinge moments (i.e., control forces) and on the overall behavior of the hinge-moment curve should be evaluated. With iced wings, the growth in hinge moment with α (region B as defined in figures 3-26(a) and 3-26(b)) takes place at a lower α with respect to the clean wing, as shown in figures 3-26(c) and 3-26(d). For such a case, a large amplitude roll maneuver could change the α sufficiently to place the aileron on the down moving side of the wing in the steep region of the hinge-moment curve. This could cause a considerable increase in control force. If, in addition to the increase in control force, the aileron effectiveness is reduced because of flow separation over the ailerons caused by the ice shape, then a situation could develop where recovery may be difficult.

In assessing aileron performance for iced wings, the magnitude of C_H and the slope of C_H with respect to α and δ_A should be considered. Ideally, the magnitude of C_H should be balanced; small enough to avoid excessively high forces, yet large enough to avoid very small forces. The actual permissible values of C_H will be a function of the aerodynamic and mechanical design of the control, as well as certification requirements. Any change in the slope of C_H with α or δ_A should also be small and gradual.

3.2.5.2 Clean Wing.

For a reflection place model, positive aileron deflections increase wing lift and reduce the α_{stall} , while negative deflections have the opposite effect. Note that large positive aileron deflections at high angles of attack should be evaluated carefully since they increase the angle of attack over the outboard portion of the wing and can result in early tip stall.

For the clean wing tested, the aileron remained effective for all α and aileron deflections, i.e., positive aileron deflection (TE down) increased wing lift, while negative deflection resulted in lift reduction, as expected. In addition, as the aileron deflection was increased, the lift increment (for aileron TE down) or decrement (for aileron TE up) increased, as shown in figures 3-70(a) and 3-70(b).

The aileron hinge moments presented in figures 3-70(c) and 3-70(d) exhibited gradual change with α for all aileron deflections tested. The slope, $C_{H,\alpha}$, for all three regions A, B, and C (as

defined in figure 3-26) of the C_H curve were negative, indicating that the hinge moment became less positive or more negative as α was increased from -8° to 20° . On a number of cases, a change in the sign of C_H was observed in the hinge-moment data. Consider, for example, the case in figure 3-70(c), corresponding to δ_A of -15° (TE up). For this case, a change in α from 10° to 16° resulted in a change in aileron hinge moments from 0.07 to approximately -0.03. The change in sign of C_H occurred near wing stall, corresponding to α of approximately 13.5° . For α between 10° and 13.5° and for δ_A of -15° , the hinge moment was positive, indicating that the aileron trailing edge had the tendency to return to its undeflected position. However, at α greater than 13.5° , the aileron had the tendency to maintain its deflected position due to extensive flow separation over the upper surface of the aileron. Flow conditions which force a control surface to maintain its deflection status result in control force reversal. However, with aileron controls, such a condition over one of the ailerons may not be a problem if the other aileron (the one deflected TE down in this case) remains effective. Considering the 15° aileron deflection case in figure 3-70(d), it is observed that for α of 13.5° , the hinge moment for the TE down aileron was approximately -0.18, i.e., the TE down aileron had a strong tendency to return to its neutral position. Thus, the combined hinge moment and, therefore, the net control force due to both ailerons maintained the correct behavior (i.e., the controls had the tendency to return to the neutral position).

The change in C_L with δ_A depicted in figure 3-70(e) was practically linear for α in the range of -8° to 16° . The change in lift as δ_A was increased from -15° to 20° , while maintaining a constant α , was in the range of 0.1 to 0.2, depending on α . The higher lift increments were obtained for α in the linear lift range where the flow over the control surface was mostly attached.

The change in control hinge moment with δ_A is demonstrated in figure 3-70(f). The aileron C_H was a function of the prevailing flow conditions over the aileron. Consider the line in figure 3-70(f) corresponding to α of 0° . At this α , the flow was attached on both surfaces of the wing for all aileron deflections. The results show that for negative δ_A (aileron TE up), C_H was positive, that is the aileron had the tendency to return to its undeflected position. For positive aileron deflections (TE down), C_H is negative, which once again indicates that the aileron had the tendency to return to the neutral position. The linear behavior of the curve shows that as δ_A was increased, the moment and, therefore, the control force were increased in a linear fashion. Note that for a full-span wing, the net aileron control force can be obtained from the results presented in figure 3-70(f) by computing the change in C_H , corresponding to the same positive and negative aileron angular deflections. For example, at α of 0° , the change in the magnitude of C_H corresponding to aileron deflections of $\pm 5^\circ$, was approximately 0.075; C_H for TE up aileron was 0.032, while C_H for TE down aileron was -0.043.

Now consider the C_H versus δ_A curve corresponding to α of -8° . At this α , the upper surface of the wing was the pressure side, while the lower surface was the suction side. For negative aileron deflections, the hinge moment was positive as the aileron upper surface experienced higher pressure than the lower surface. For small positive aileron deflections, the pressure over the aileron upper surface remained higher than over lower surface, which now had lower suction, and the hinge moment remained positive. As the aileron approached maximum positive deflection, the pressure over the upper surface did not change significantly but the suction over

the lower surface was considerably reduced. Thus, the magnitude of the positive hinge moment was reduced. The reason for the nonlinearity in C_H versus δ_A curve was mild flow separation over the aileron lower surface.

The results presented in figure 3-70(f) demonstrate approximately linear change in C_H with δ_A for α corresponding to the linear lift range. For these α , the change in aileron hinge moment was approximately 0.21 as δ_A was increased from -15° to 15° . At high negative or positive α , the change in hinge moment with aileron deflection was not linear. This is demonstrated in figure 3.70(f) for α of 16° , 12° , and -8° .

3.2.5.3 IRT-CS22 Ice Shape.

The effects of the 22.5-min glaze ice accretion with the large scallop features on the aerodynamic performance of the swept wing for all aileron deflections tested is presented in figure 3-71. The experimental results obtained indicate the following:

- Lift increase or decrease with δ_A was as expected for most α as demonstrated in figures 3-71(a) and 3-71(b). For α -range of 1° to 6° , however, negative aileron deflections increased lift while positive deflections had practically no effect on lift. This was mainly due to massive flow separation over the wing and control surfaces caused by the large size (2- to 3-in.) ice horns.
- The maximum positive C_H was 0.1 and occurred for δ_A of -15° and α of -8° as shown in figure 3-71(c). The maximum negative hinge-moment coefficient was -0.19 at α of 20° and δ_A of 20° as evident from figure 3-71(d). Corresponding maximum and minimum values for the clean wing were 0.165 and -0.22. Thus, the iced wing hinge moments were within the maximum and minimum limits of the clean wing hinge moments. It is important, however, to point out that for some aircraft, the maximum hinge moment for the clean wing are typically not reached either due to the aircraft natural angle of attack limits or due to an artificial stall barrier. In such a case, the iced wing hinge moments should be compared to the actual clean wing hinge moment limits.
- A change in the sign of C_H was observed for all negative aileron deflections and for α -range of 2° to 5° , as shown in figure 3-71(c). For positive aileron deflections in the range of 0° to 5° , the change in the sign of C_H occurred between α of 1° and 3° , as demonstrated in figure 3-71(d). For larger positive aileron deflections, the sign of C_H was reversed twice near α of 0° . As discussed previously, for the clean wing case, a sign change in C_H indicates that the aileron has the tendency to maintain its deflected position. To determine the net aileron control hinge moment and its direction for the combined left and right aileron system, the C_H for both positive and negative aileron deflections should be examined.
- As demonstrated in figure 3-71(e), the change in wing lift with δ_A for constant α was practically linear for all α presented. The lines had a small positive slope for most α .

However, for α -range of 0° to 4° , the slope was nearly zero and, in some cases, slightly negative, indicating that the aileron was not effective in changing lift.

- The behavior of C_H with δ_A was notably nonlinear for all α presented in figure 3-71(f). Given an α and assuming attached flow, C_H will be positive for negative aileron deflections (TE up) since the aileron will tend to move to its undeflected position. For positive aileron deflections, the sign of C_H will eventually become negative. For fixed positive aileron deflection, the pressure over the aileron lower surface and the suction over the upper surface should increase as the α is increased from -8° to 0° (note that such a change in α with fixed δ_A is not practical under flight conditions). The C_H should become progressively more negative and the hinge-moment curves will move further apart. This was not the case with the IRT-CS22 ice shape, as shown in figure 3-71(f) for α -range of -8° to 0° . The intersection in the hinge-moment curves corresponding to these α near δ_A of 5° is indicative of extensive flow separation over the control surface.

3.2.5.4 IRT-IPSF22 and LR-IPSF22 Ice Shapes.

Aerodynamic performance with aileron deflection for the 22.5-min glaze ice shape casting IRT-IPSF22 and the corresponding rough LEWICE ice shape LR-IPSF22 are presented in figures 3-72 and 3-73 respectively. These ice accretions were representative of ice protection system failure cases for the wing model tested. The results presented in figures 3-72 and 3-73 indicate the following:

- Increase or decrease in lift with δ_A was as expected for all aileron deflections and α , as demonstrated in figures 3-72(a), 3-72(b), 3-73(a), and 3-73(b).
- The maximum positive C_H for both ice shapes was approximately 0.14 and occurred for δ_A of -15° and α of -8° , while the maximum negative C_H was -0.2 at α of 20° and δ_A of 20° , as shown in figures 3-72(c), 3-72(d), 3-73(c), and 3-73(d). Once again, the iced wing hinge moments were within the maximum and minimum hinge-moment bounds of the clean wing.
- The change in lift with δ_A for the IRT-IPSF22 and LR-IPSF22 ice shapes was practically linear for all α as shown in figures 3-72(e) and 3-73(e). For all cases presented in these figures, the C_L versus δ_A curves had a small positive slope indicating a monotonic increase in lift with aileron deflection.
- For most of the cases presented in figures 3-72(f) and 3-73(f), the change in the hinge-moment coefficient with aileron deflection exhibited nonlinear behavior mainly due to flow separation over the aileron.

3.2.6 Effect of Large Scallop Features.

In general, ice accretions on swept wings can be classified as complete scallops, incomplete scallops, and no-scallop, as discussed in references 2, 4, 20, and 21. Schematics of these three types of ice accretions are provided in figure 3-74.

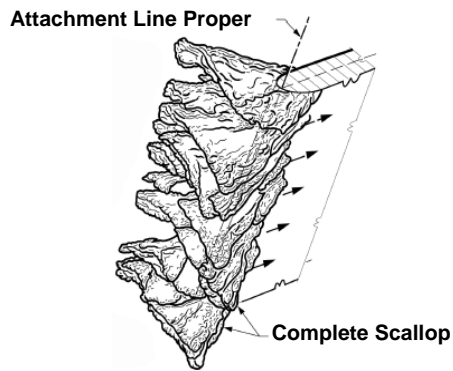
Complete scallops are glaze ice accretions that appear only on swept wings and are characterized by the presence of scallop tips extending from the attachment line. The scallop tips have a particular shape, height, and spacing. Incomplete scallops are glaze ice shapes that also appear only on swept wings and where scallops tips form beginning at some distance from the attachment line. No-scallops are ice accretions where scallop tips are not present.

Scallop tips are made of glaze ice feathers, which develop from roughness elements that form during the ice accretion process as shown in figure 3-75(a). The feathers have a preferred direction of growth that is perpendicular to the external streamlines, as shown in figures 3-75(b) and 3-75(c). Ice feathers join along the preferred direction to form ridges, with incipient scallop tips formed by the feathers at the end of each ridge. As the ridges grow, they form scallop tips. As the ice accretion grows, the scallop tips merge with adjacent scallop tips by joining at the top. This increases both the size of the scallop tips and the gap between them. Detailed descriptions and experimental data for scallop ice accretions can be found in references 2, 4, 20, and 21.

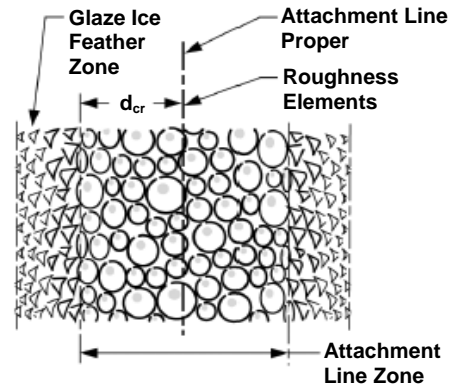
The type of ice accretion that will form on a swept wing depends on the airfoil geometry, sweep angle, flow, and tunnel conditions. Icing conditions that lead to scalloped ice features can produce ice shapes with complex surface characteristics such as the IRT-CS10 and IRT-CS22 cases shown in figure 2-33.

Ice shapes with large scallop formations contain gaps between scallops, as demonstrated in figure 2-33(b) for the IRT-CS22 case. Aerodynamicists have debated over the years the effects of scallop features on aerodynamic performance. This is of practical interest because state-of-the-art ice accretion codes are not able to produce scalloped ice shapes. Simulated ice shapes for swept wings developed with the use of ice accretion codes or other empirical means have solid horns, as shown in figure 2-34. If the scallop-gap features in the ice horns have a significant impact on aerodynamic performance, then methods should be explored for incorporating their effects in simulated ice shapes.

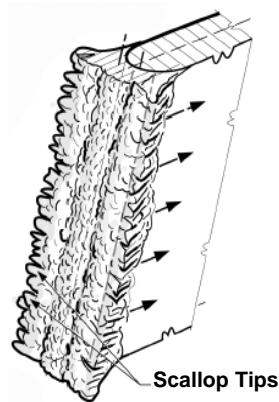
To investigate the effect of scalloped ice shapes on aerodynamic performance, a limited study was conducted with the IRT-CS22 ice shape. In this study, the gaps between scallops were progressively filled with a modeling compound to produce an ice shape with solid horns, as shown in figure 3-76. To reduce the aerodynamic loads on the modeling compound, the experimental study with the baseline and modified IRT-CS22 ice shapes was conducted at a lower airspeed for which the Reynolds number based on MAC was 1.0 million. Experimental results from these tests are presented in figure 3-77. The first set of tests was conducted with the middle 25-in segment of the IRT-CS22 ice shape filled with the modeling compound (case 1, R516 in figure 3-77). Next, the gaps in the 18-in tip segment were filled (case 2, R517 in figure 3-77), and finally, the gaps in all three ice segments were filled (case 3, R518 in figure 3-77). Each time a new set of force, moment, and pressure data was obtained.



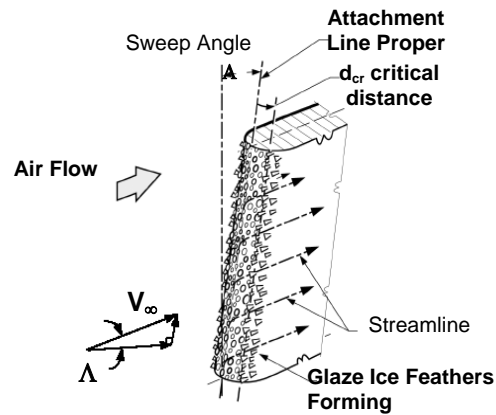
(a) Complete scallop



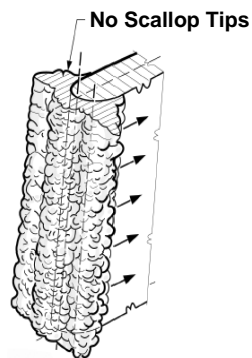
(a) Attachment line zone, glaze ice feathers zone and critical distance (view from direction normal to leading edge)



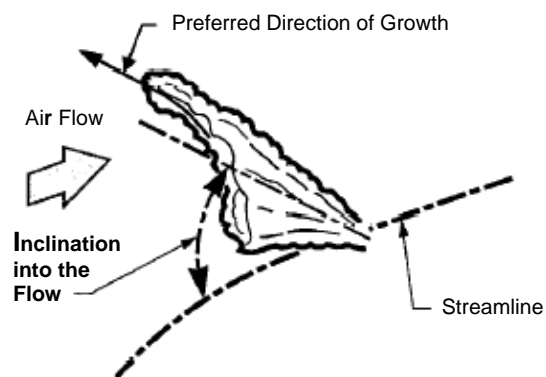
(b) Incomplete scallop



(b) Attachment line zone, glaze ice feathers zone and critical distance (overall view)



(c) No scallops



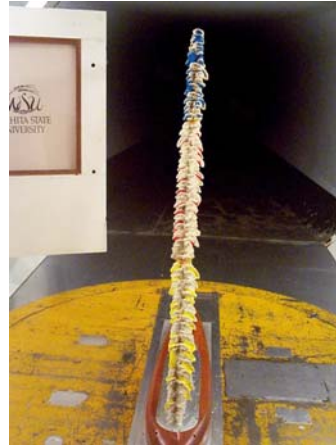
(c) Feather detail

FIGURE 3-74. ICE ACCRETION ON A SWEEP WING AT GLAZE ICE CONDITIONS [21]

FIGURE 3-75. DEVELOPMENT OF ROUGHNESS ELEMENTS AND ICE FEATHERS DURING ICE ACCRETION ON A SWEEP WING [20 AND 21]



(a) Filling in the tip segment



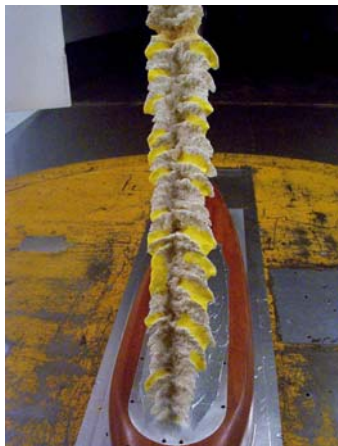
(d) Filling in all segments – Front View



(b) Filling in the middle and tip segments



(e) Filling in all segments – Side View (Pressure)

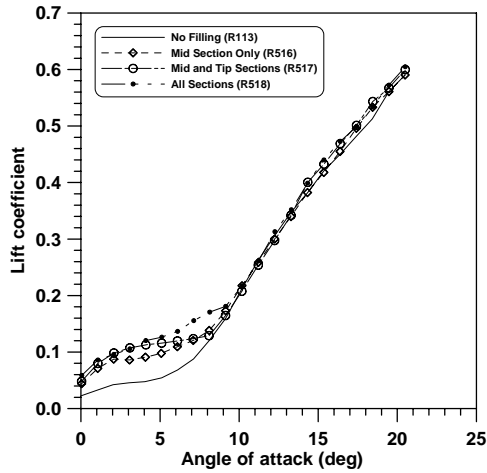


(c) Filling in the root segment

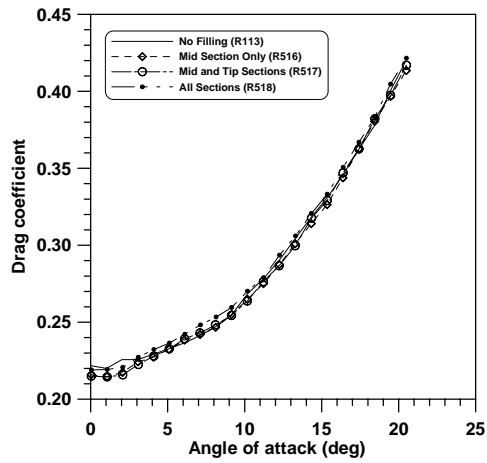


(f) Filling in all segments – Side View (Suction)

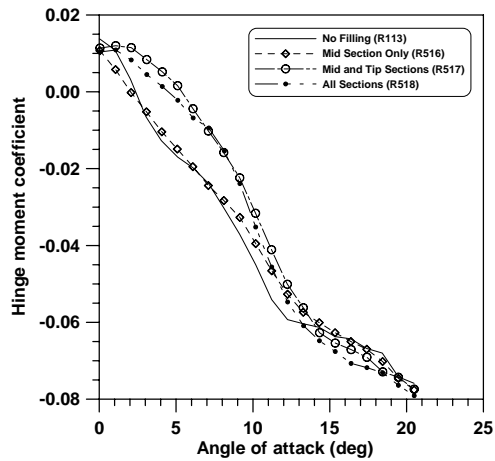
FIGURE 3-76. ICING RESEARCH TUNNEL CS22 ICE SHAPE FILLED WITH MODELING COMPOUND



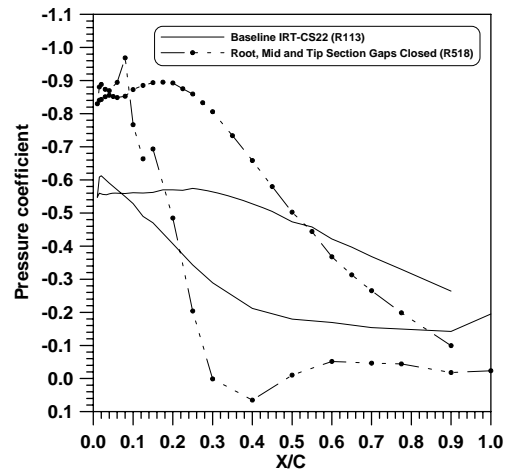
(a) Lift coefficient



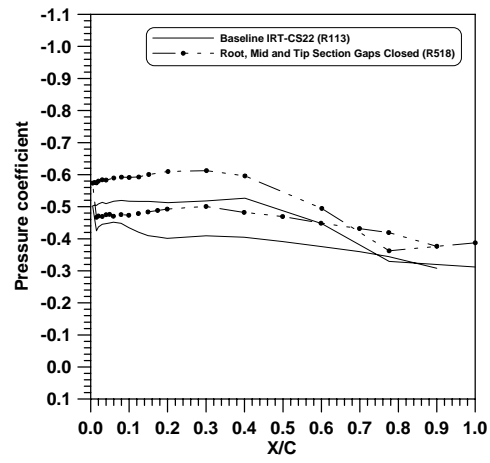
(b) Drag coefficient



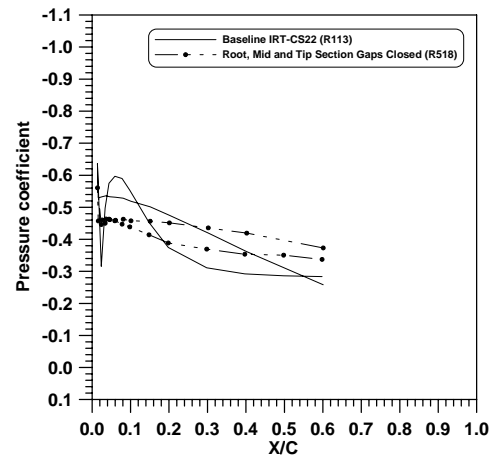
(c) Hinge-moment coefficient



(d) C_p vs. x/c , 15%-semispan, $\alpha = 5^\circ$



(e) C_p vs. x/c , 50%-semispan, $\alpha = 5^\circ$



(f) C_p vs. x/c , 85%-semispan, $\alpha = 5^\circ$

FIGURE 3-77. EFFECT OF SCALLOP FEATURES ON AERODYNAMIC PERFORMANCE; IRT-CS22 ICE SHAPE WITH AND WITHOUT MODELING COMPOUND; $Re = 1.8 \times 10^6$; $\delta_A = 0^\circ$

Lift, drag, hinge-moment, and pressure coefficients for the baseline IRT-CS22 ice shape (R113 in figure 3-77) and for the three cases where the gaps between scallops were partially or completely filled with modeling compound are compared in figure 3-77. The results presented in this figure show a progressive increase in C_L for α -range of -2° to 9° as more gaps in the ice horns were filled with the modeling compound. The maximum gain in C_L was obtained for case 3 and ranged from 0.022 to 0.073 with respect to that of the baseline IRT-CS22 case. The change in C_D with respect to the baseline ice shape was small but measurable for all three cases tested. For case 1, the change in the C_H with respect to the baseline IRT-CS22 ice shape was small. However, for cases 2 and 3, the hinge moments were less negative (i.e., the aileron trailing edge had less of a tendency to move up).

The exact mechanism for the observed aerodynamic effects caused by the gaps between the ice scallops is not known. However, the pressure data at 15%, 50%, and 85% semispan stations for case 3 (R518) presented in figure 3-77 for α of 5° offer some clues. The pressure distributions for the case where all the gaps between scallops were filled with the modeling compound exhibited increased suction on both the upper and lower wing surfaces with respect to the baseline IRT-CS22 ice shape.

For large glaze ice accretions, the region between the horns is typically a high-pressure region because the air flow slows down within the cavity formed by the horns. The regions downstream of the upper and lower horns are in general low-pressure regions with small or large separation bubbles. With scalloped ice shapes, the gaps between the scallops allow the high pressure between the horns to leak to the low-pressure region downstream of the horns, thus reducing the suction near the wing LE. This is clearly evident in the 15% and 50% semispan pressure distributions presented in figures 3-77(d) and 3-77(e). At the 80% semispan station, the IRT-CS22 ice shape with modeling compound produced lower suction peaks near the wing LE than the baseline ice shape. This was mainly due to flow separation that was more extensive for the case of the modified ice shape. Since C_L depends on the pressure difference between the upper and lower wing surfaces, as this difference was reduced due to flow leakage in the case of the baseline IRT-CS22 ice shape, the net lift was also decreased.

The observed lift increase with the modified IRT-CS22 ice shape (case 3, R518) in figure 3-77(a) can be explained by direct examination of the pressure distributions presented in figures 3-77(d) to 3-77(f). The pressure distributions show that, for the 15% semispan station, case 3 produced 72% more positive lift than the baseline case. At the 50% semispan station, case 3 resulted in 18% less negative lift than the baseline ice shape. At the 85% semispan location, both configurations resulted in about the same amount of negative lift. Thus, for case 3 where all gaps between the scallops were closed, the increase in suction over the wing resulted in a net increase in C_L with respect to the baseline ice shape.

In summary, the limited study conducted with the glaze IRT-CS22 scalloped ice shape showed that the scallop features and in particular the gaps between scallops can result in greater loss of lift than ice shapes with solid horns. It must be stressed, however, that these results should not be generalized until further studies are conducted with more scalloped type ice shapes. Furthermore, the results presented here may only be applicable to ice shapes with large scalloped features and for ice shapes with small scallops, the effects may not be as significant.

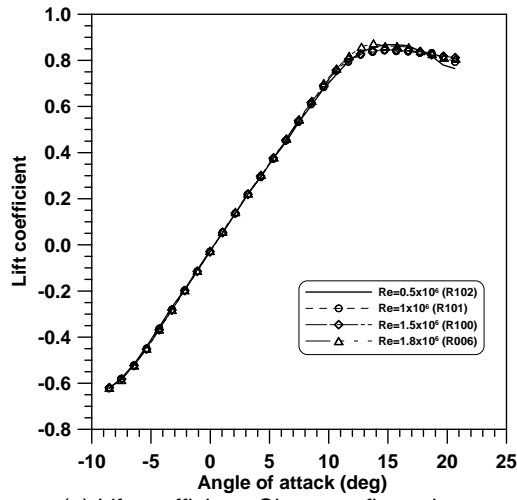
3.2.7 Reynolds Number Effects.

Reynolds number effects on the clean and selected iced wing configurations is presented in figure 3-78. Reynolds numbers included 0.5, 1.0, 1.5, and 1.8 million were computed based on the wing mean aerodynamic chord of 1.56 ft. Corresponding tunnel airspeeds were 42, 84, 128, and 152 mph.

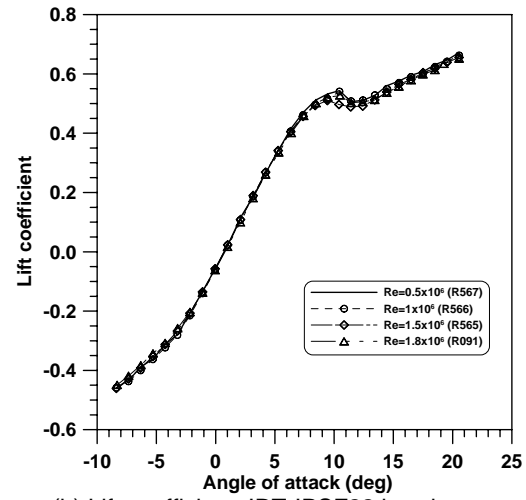
For the clean wing, experimental results for Reynolds numbers in the range of 0.5 to 1.8 million are presented in figure 3-78. For the low Reynolds number of 0.5 million, the $C_{L,stall}$ was approximately 0.87 and α_{stall} was approximately 16° . For higher Reynolds numbers of 1.0 and 1.5 million, both $C_{L,stall}$ and α_{stall} decreased and were approximately 0.84 and 15° respectively. However, as the Reynolds number was increased to 1.8 million, $C_{L,stall}$ increased to 0.87 while α_{stall} decreased to 13.8° .

Reynolds number effects on C_L of the IRT-IPSF22, LS-IPSF22, LR-IPSF22, IRT-SC5, and LR-SC5 configurations are presented in figures 3-78b to 3-78(f). In general, the Reynolds number effects on C_L of the IRT-IPSF22 ice shape was small, as demonstrated in figure 3-78(b). The effects of Reynolds number on the near stall lift performance of the LS-IPSF22 and LR-IPSF22 ice shapes were more pronounced than for the IRT-IPSF22 case, as demonstrated in figures 3-78(c) and 3-78(d). For the LR-IPSF22 configuration, as the Reynolds number was increased from 0.5 to 1.8 million, $C_{L,stall}$ decreased while α_{stall} remained approximately the same.

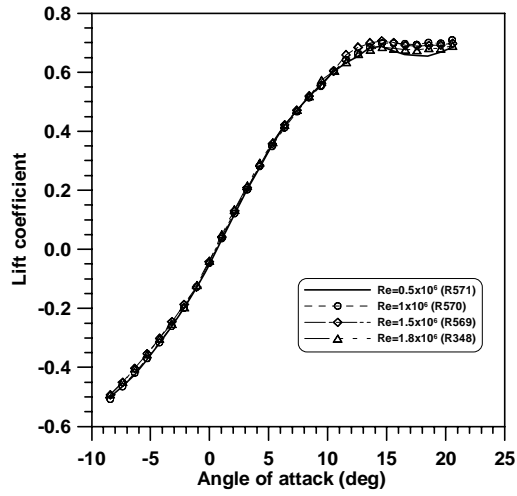
For the 5-min rime IRT-SC5 and LR-SC5 ice shapes, the effects of Reynolds number on C_L are demonstrated in figures 3-78(e) and 3-78(f) respectively. Most of the change in lift with Reynolds number was observed in the near-stall and poststall flow regimes. In general, $C_{L,stall}$ decreased as the Reynolds number was increased from 1.0 to 1.8 million. The behavior of C_L for the low Reynolds number case of 0.5 million was similar to that for the 1.5 million Reynolds number. The Reynolds number effects observed with the 5-min rime ice cases were mainly due to the change in the location of flow separation over the rough ice shapes. At low Reynolds numbers, roughness can enhance or reduce performance, depending on the value of Reynolds number, by changing the state of the viscous boundary layer. At flight Reynolds number, however, even small levels of roughness can result in considerable performance losses, as was demonstrated in reference 18. The Reynolds number range explored in this study was small and considerably lower than that experienced by full-scale wings at flight conditions. It is not known how much different flight test results would be.



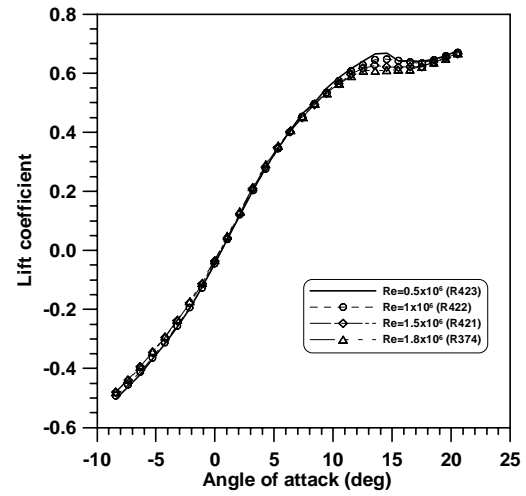
(a) Lift coefficient; Clean configuration



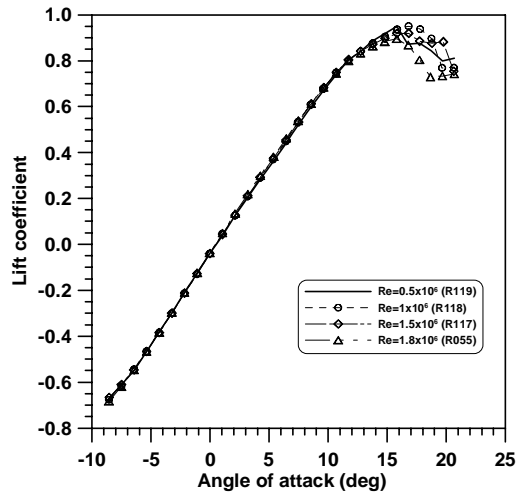
(b) Lift coefficient; IRT-IPSF22 ice shape



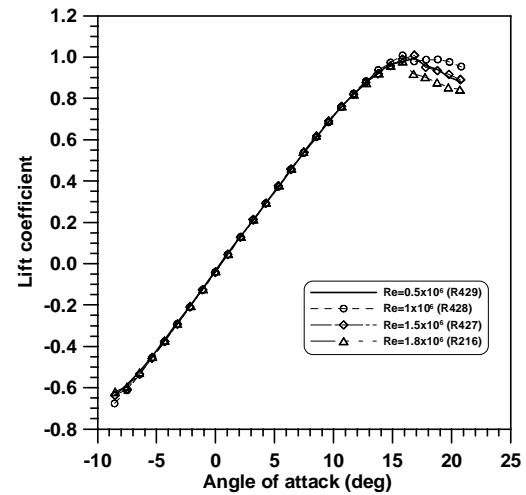
(c) Lift coefficient; LS-IPSF22 ice shape



(d) Lift coefficient; LR-IPSF22 ice shape



(e) Lift coefficient; IRT-SC5 ice shape



(f) Lift coefficient; LR-SC5 ice shape

FIGURE 3-78. REYNOLDS NUMBER EFFECT ON C_L ; CLEAN AND ICED WING; $\delta_A = 0^\circ$

4. CONCLUSIONS.

Wind tunnel tests were conducted to investigate the effect of 20 ice shapes on the aerodynamic performance of a swept finite wing model. The wing consisted of an 8.7% thick airfoil section, which remained constant from root to tip. The wing was tapered and had a leading-edge (LE) sweep of 28° , a trailing-edge sweep of 15.6° , aspect ratio of 6.8, and -4° geometric twist at the tip (washout). Tests were performed with the clean wing, six ice shapes castings obtained from ice accretion experiments at the NASA Glenn Icing Research Tunnel (IRT), and seven smooth and seven rough LEWICE ice shapes. The LEWICE ice shapes were obtained for the same icing conditions as those used in the IRT ice accretion tests. One LEWICE ice shape was defined for each icing condition using airfoils sections normal to the wing LE at five spanwise stations. For icing condition 5, an additional LEWICE ice shape was defined using streamwise airfoil sections, as discussed in section 2.2.3 of this report. Roughness effects for the LEWICE ice shapes were simulated with 36-size grit. Tests were performed with the clean and iced wing in the low-speed 7- x 10-ft wind tunnel at Wichita State University. A complete set of force and moment coefficients were obtained along with aileron hinge moments and pressure distributions for a range of test conditions. Test conditions included Reynolds number of 1.8 million based on the wing mean aerodynamic chord yielding test Reynolds numbers well below typical flight Reynolds numbers, angles of attack in the range of -8° to 20° , and aileron deflections of -15° , -10° , -5° , -2.5° , 0° , 2.5° , 5° , 10° , 15° , and 20° . From the results presented, the following conclusions are drawn.

4.1 PERFORMANCE OF CLEAN WING.

The clean wing $C_{L,stall}$ was 0.87 and occurred at α of 13.8° . The linear lift slope was 0.077 per degree or 4.41 per radian. Drag coefficient (C_D) varied from a minimum value of 0.0063 at α of 1° to 0.15 at α of 13.8° . The maximum lift to drag ratio for the swept wing was 27.5 at α of 3.2° . The hinge-moment coefficient (C_H) with the aileron in the neutral position varied from 0.079 at α of -8° to -0.02 at α of 0° , to -0.098 at α of 15.8° . The C_H increased gradually through the nonlinear portion of the lift curve and attained a maximum slope of -0.0195 per degree. The clean wing experienced a leading edge long bubble/vortex stall, which progressed from the center of the wing to the tip and then to the root as α was increased.

4.2 EFFECTS OF IRT ICE SHAPE CASTINGS.

The six IRT ice shape castings included 2-, 10- and 22.5-min glaze ice accretions with incomplete and complete scallop features and a 5-min rime ice shape. The glaze ice shapes resulted in 11% to 93.6% reduction in $C_{L,stall}$ and 8% to nearly 56.5% reduction in α_{stall} with respect to the clean wing. These ice shapes increased the clean wing $C_{D,min}$ by 200% to 3533%. In many cases, the behavior of the aileron C_H for the clean wing was considerably altered by the glaze ice accretions. However, in all cases, C_H of the iced wing remained within the maximum and minimum limits defined by the clean wing aileron C_H . The 5-min rime ice shape improved the wing $C_{L,stall}$ by approximately 3% and the α_{stall} by 14.5%. The iced wing $C_{D,min}$ was 133% greater than that of the clean wing. Aileron C_H for the 5-min rime case were similar to that of the clean wing.

For the IRT-CS22 ice shape with the large scallops, the results presented showed that the gaps between the scallops increased lift degradation. This was due to flow leakage from the near stagnation region between the ice shape horns to the low-pressure region downstream of the ice horns. This is a preliminary finding and requires further investigation before more general conclusions can be drawn regarding the effects of gaps in scalloped ice shapes.

4.3 DEFINITION OF LEWICE ICE SHAPES.

A methodology for defining three-dimensional simulated ice shapes for a swept finite wing using the two-dimensional LEWICE ice accretion code was presented.

4.4 EFFECTS OF SMOOTH LEWICE ICE SHAPES.

The glaze ice shapes resulted in 14% to 44% reduction in $C_{L,stall}$. The α_{stall} for the iced wing ranged from 13.4° to 14.8° . The iced wing $C_{D,min}$ was 183% to 2367% greater than that of the clean wing. In most cases, the aileron C_H for the wing with the glaze LEWICE ice shapes were more positive or more negative than that of the clean wing for α -range of -7° to $+13^\circ$. However, in all cases, the C_H of the iced wing remained within the maximum and minimum limits defined by the clean wing aileron C_H . The 5-min rime LEWICE ice shape improved $C_{L,stall}$ by approximately 8% and the clean wing α_{stall} was increased by 1° . The $C_{D,min}$ for this ice shape was 67% greater than that of the clean wing. Aileron C_H for the 5-min rime LEWICE ice shape were similar to that of the clean wing.

4.5 EFFECTS OF ROUGH LEWICE ICE SHAPES.

The rough glaze ice shapes resulted in 17% to 61% reduction in $C_{L,stall}$. The α_{stall} for the iced wing ranged from 12.6° to 13.7° . The iced wing $C_{D,min}$ was 233% to 3317% greater than that of the clean wing. In most cases, the aileron C_H for the wing with the rough glaze LEWICE ice shapes were more positive or more negative than those of clean wing for α -range of -7° to $+13^\circ$. However, in all cases, C_H of the iced wing remained within the maximum and minimum limits defined by the clean wing aileron C_H . The 5-min rime LEWICE ice shape improved the clean wing $C_{L,stall}$ by approximately 13% and increase α_{stall} by 2° . The $C_{D,min}$ for this ice shape was 117% greater than that of the clean wing. Aileron C_H for the 5-min rime LEWICE ice shape were in general similar to that of the clean wing.

4.6 ROUGH VERSUS SMOOTH LEWICE ICE SHAPES.

In general, the smooth and rough LEWICE ice shapes produced similar lift curves for all but two of the seven ice shapes tested. The two cases where considerable differences in lift behavior were observed were the CS22N and CS22S cases. With the exception of the 5-min rime ice shape, the addition of roughness resulted in lower lift coefficients at stall. The change in C_L (i.e., rough LEWICE $C_{L,stall}$ - smooth LEWICE $C_{L,stall}$) was as follows: -0.1, -0.03, +0.04, -0.03, -0.08, -0.2, and -0.08 for the CS10, IS10, SC5, CS2, CS22N, CS22S, and IPSF22 cases. With the exception of the CS22N and CS22S cases, the rough and smooth LEWICE ice shapes resulted in similar C_D and C_H .

The trends in aerodynamic performance losses observed with the smooth and rough LEWICE ice shapes tested were consistent with results from other experimental studies involving LEWICE ice shapes.

4.7 ICING RESEARCH TUNNEL VERSUS ROUGH LEWICE ICE SHAPES.

With the exception of icing condition 5 (22.5-min complete scallop case), the rough LEWICE ice shapes caused similar loss in lift compared with the IRT ice shape castings. The difference in iced wing $C_{L, \text{stall}}$ defined by ($\Delta C_{L, \text{stall}} = \text{IRT casting } C_{L, \text{stall}} - \text{rough LEWICE } C_{L, \text{stall}}$) was -0.07, -0.01, -0.08, +0.05, -0.35, -0.28, and -0.08 for CS10, IS10, SC5, CS2, CS22N, CS22S, and IPSF22 respectively.

In most cases, the wing drag increase caused by the LEWICE and IRT ice shapes was in good correlation. The difference in iced wing $C_{D, \text{min}}$ (i.e., Rough LEWICE $C_{D, \text{min}}$ - IRT ice shape $C_{D, \text{min}}$) was 0.004, -0.008, -0.001, +0.002, -0.036, -0.013, and -0.013 for CS10, IS10, SC5, CS2, CS22N, CS22S, and IPSF22 respectively.

With the exception of icing condition 5, the trends in aileron C_H obtained with the rough LEWICE and IRT ice shapes were in good agreement. For icing conditions 2 and 3, the IRT and LEWICE C_H magnitudes were in good correlation throughout the α -range. For icing conditions 1, 4, and 6, the LEWICE ice shapes resulted in larger C_H over regions A and B of the C_H curve compared with the IRT ice shapes.

In summary, the IRT and the rough LEWICE ice shapes produced similar aerodynamic effects for five out of the six icing conditions tested. This is an important finding considering the observed differences between the actual and the simulated ice shapes. It must be stressed, however, that considerable more experimental work is needed with a range of ice accretions to determine the generality of this finding.

4.8 AILERON PERFORMANCE.

For the clean wing and, for practically, all iced wing cases presented, the aileron remained effective in increasing and decreasing lift with aileron deflection. The ice shapes caused considerable changes to the C_H of the clean wing. However, in all cases, the iced wing C_H remained within the maximum and minimum limits of the clean wing C_H .

4.9 REYNOLDS NUMBER EFFECTS.

In general, for the low Reynolds number (Re) range of 0.5 to 1.8 million used in this study, the effects of Re on iced wing lift performance were small. The only notable Re effect was in the behavior of $C_{L, \text{stall}}$ for the 5-min rime ice shapes. For these ice shapes, lift near stall decreased as Re was increased from 1.0 to 1.8 million.

5. REFERENCES.

1. Lynch, F.T. and Khodadoust, A., "Effects of Ice Accretions on Aircraft Aerodynamics," *Progress in Aerospace Sciences*, Vol. 37, Issue 8, November 2001, pp. 669-767.
2. Vargas, M. and Reshotko, E., "Physical Mechanisms of Glaze Ice Scallop Formations on Swept Wings," NASA TM-1998-206616, AIAA Paper 98-0491, January 1998.
3. Vargas, M., "Ice Accretion on Swept Wings at Glaze Ice Conditions," Ph.D. Thesis, Case Western Reserve University, Cleveland, Ohio, May 1998.
4. Vargas, M. and Reshotko, E., "Parametric Experimental Study of the Formation of Glaze Ice Shapes on Swept Wings," NASA TM-1999-208900, AIAA Paper 99-0094, January 1999.
5. Wright, W.B., "User Manual for the NASA Glenn Ice Accretion Code LEWICE (Version 2.0)," NASA CR-1999-209409, September 1999.
6. Potapczuk, M., Papadakis, M. and Vargas, M., "LEWICE Modeling of Swept Wing Ice Accretions," AIAA-2003-0730, January 2003.
7. "Multi-Hole Probe Information Packet," Edition 1.5, Aeroprobe Corporation, October 2001.
8. Vargas, M., Papadakis, M., Potapczuk, M., Addy, H., Sheldon, D., and Giriunas, J., "Ice Accretions on a Swept GLC-305 Airfoil," NASA TM-2002-211557, SAE Paper 2002-01-1519, General Aviation Technology Conference and Exhibition, Wichita, KS, April 2002.
9. Personal communication between Dr. James T. Riley, Dr. Dave N. Anderson, and Mr. Harold E. Addy. Mr. Addy provided the reference icing condition. Dr. Anderson did the scaling from the reference condition.
10. Addy, H., "Ice Accretions and Icing Effects for Modern Airfoils," DOT/FAA/AR-99/89, NASA TP-2000-210031, April 2000.
11. Codes of Federal Regulations, Aeronautics and Space, Part 1 to 59.
12. Johnson, B.L., "Three-Dimensional/Reflection Plane Force Data Acquisition and Boundary Corrections for the Walter H. Beech Memorial 7-x-10-foot Low Speed Wing Tunnel," AR96-2, NIAR, Wichita State University, April 1996.
13. Shapiro, A.H., *"The Dynamics and Thermodynamics of Compressible Fluid Flow – Volume I,"* John Wiley and Sons, 1953.
14. Anderson, J.D., *"Fundamentals of Aerodynamics,"* McGraw-Hill Book Company, 1984.

15. Drela, M., "XFOIL 6.6 User Primer," MIT Aero and Astro Engineering, March 1996.
16. McCormick, B.W., "*Aerodynamics Aeronautics and Flight Mechanics*," 2nd edition, John Wiley and Sons, 1995.
17. Addy, H.E., Potapczuk, M. and Sheldon, D.W., "Modern Airfoil Ice Accretions," *AIAA Paper* 92-0647, January 1992.
18. Hoerner, I.S.F. and Borst, H.V., "Fluid Dynamic – Lift," Hoerner Fluid Dynamics, P. O. Box 342, Brick Town, NJ, 1975.
19. Torenbeek, E., "Synthesis of Subsonic Airplane Design," Delft University Press, 1982.
20. Vargas, M. and Reshotko, E., "LWC and Temperature Effects of Ice Accretion Formation on Swept Wings at Glaze Ice Conditions," *AIAA Paper* 2000-0483, January 2000.
21. Vargas, M., Giriunas, J.A. and Ratvasky, T.P., "Ice Accretion Formations on a NACA 0012 Swept Wing Tip in Natural Icing Conditions," *AIAA Paper* 2002-0244, January 2002.
22. Papadakis, M. Yeong, H.W., Chandrasekharan, V.R., Hinson, M. and Ratvasky, T.P., "Effects of Roughness on the Aerodynamic Performance of a Business Jet Tail," *AIAA Paper* 2002-0242, January 2002.
23. Dorsch, R.G. and Brun, R.J., "A Method for Determining Cloud-Droplet Impingement on Swept Wings," NACA TN 2931, April 1953.

APPENDIX A—RUN LOG FOR ICING TEST AT NASA GLENN ICING RESEARCH TUNNEL

Run Number	Description	AOA (deg.)	V (mph)	T _{total} (°F)	LWC (g/m ³)	MVD (μm)	τ (min)
071701.01_LE_1_T	Complete Scallop Condition	4	250.00	25.0	0.68	20.0	10.0
071701.02_LE_1_T	Complete Scallop Condition	4	250.00	25.0	0.68	20.0	10.0
071701.03_LE_2_T	Incomplete Scallop Condition	4	150.00	25.0	0.65	20.0	10.0
071701.04_LE_3_T	Run based on Scaled Condition 2 for run in 2D table	6	201.30	11.7	0.51	14.5	5.0
071701.05_LE_2_T	SLD Condition A	4	172.60	25.0	0.60	70.0	10.0
071701.06_LE_2_T	Incomplete Scallop Condition	4	150.00	25.0	0.65	20.0	10.0
071801.01_LE_1_T	SLD Condition C	4	172.62	25.0	1.00	175.0	22.5
071801.02_LE_1_T	22.5 minutes failed ice protection App C	4	150.00	27.0	0.46	20.0	22.5
071801.03_LE_2_T	Complete Scallop Condition Long ice accretion time	4	250.00	25.0	0.68	20.0	22.5
071801.04_LE_3_T	SLD Condition D	4	172.62	30.0	1.00	175.0	15.0
071801.05_LE_3_T	Complete Scallop Condition Short ice accretion time	4	250.00	25.0	0.68	20.0	2.0
071901.01_LE_1_M	SLD Condition B	4	172.60	25.0	1.00	175.0	22.5
071901.01_LE_1_B	22.5 minutes failed ice protection App C	4	150.00	27.0	0.46	20.0	22.5
071901.02_LE_1_M	Complete Scallop Condition Long ice accretion time	4	250.00	25.0	0.68	20.0	22.5
071901.02_LE_1_B	Incomplete Scallop Condition	4	150.00	25.0	0.65	20.0	10.0
071901.03_LE_2_M	Complete Scallop Condition	4	250.00	25.0	0.68	20.0	10.0
071901.03_LE_2_B	Run based on Scaled Condition 2 for run in 2D table	6	201.30	11.7	0.51	14.5	5.0
071901.04_LE_2_M	Run based on Scaled Condition 2 for run in 2D table	6	201.30	11.7	0.51	14.5	5.0
071901.04_LE_2_B	Complete Scallop Condition Short ice accretion time	4	250.00	25.0	0.68	20.0	2.0
071901.05_LE_3_M	Complete Scallop Condition Long ice accretion time	4	250.00	25.0	0.68	20.0	22.5
071901.05_LE_3_B	Substitute condition to avoid losing the ice accretion	4	225.00	25.0	0.68	20.0	22.5

APPENDIX B—RUN LOG FOR AERODYNAMIC INVESTIGATION AT
WICHITA STATE UNIVERSITY

Date	Run No.	δ_A (deg)	Configuration Name	Comments
25-Apr-02	1	0	Clean	
	2	-15	Clean	
	3	-10	Clean	
	4	-5	Clean	
	5	-2.5	Clean	
	6	0	Clean	
	7	2.5	Clean	
	8	5	Clean	
	9	10	Clean	
	10	15	Clean	
	11	20	Clean	
26-Apr-02	13	20	IRT-CS10 (irt-ice1)	Repeat R012
	14	15	IRT-CS10 (irt-ice1)	
	15	10	IRT-CS10 (irt-ice1)	
	16	5	IRT-CS10 (irt-ice1)	
	17	2.5	IRT-CS10 (irt-ice1)	
	18	0	IRT-CS10 (irt-ice1)	
	19	-2.5	IRT-CS10 (irt-ice1)	
	20	-5	IRT-CS10 (irt-ice1)	
	21	-10	IRT-CS10 (irt-ice1)	
	22	-15	IRT-CS10 (irt-ice1)	
	23	0	IRT-CS10 (irt-ice1)	
	24	0	Clean	
29-Apr-02	26	0	Clean	Gap opened
	27	0	Clean	Gap closed
	28	-2.5	IRT-IS10 (irt-ice2)	
	29	-5	IRT-IS10 (irt-ice2)	
	30	-10	IRT-IS10 (irt-ice2)	
	31	-15	IRT-IS10 (irt-ice2)	
	32	0	IRT-IS10 (irt-ice2)	
	33	2.5	IRT-IS10 (irt-ice2)	
	34	5	IRT-IS10 (irt-ice2)	Ice shape broke
30-Apr-02	36	0	Clean	Baseline repeat
	37	-15	IRT-CS22 (irt-ice5)	
	38	-10	IRT-CS22 (irt-ice5)	
	39	-5	IRT-CS22 (irt-ice5)	
	40	-2.5	IRT-CS22 (irt-ice5)	
	41	0	IRT-CS22 (irt-ice5)	
	42	2.5	IRT-CS22 (irt-ice5)	
	43	5	IRT-CS22 (irt-ice5)	

Date	Run No.	δ_A (deg)	Configuration Name	Comments
1-May-02	44	10	IRT-CS22 (irt-ice5)	
	45	15	IRT-CS22 (irt-ice5)	
	46	20	IRT-CS22 (irt-ice5)	
	47	0	IRT-CS22 (irt-ice5)	
	49	0	Clean	Baseline repeat
	50	0	IRT-SC5 (irt-ice3)	
	51	-15	IRT-SC5 (irt-ice3)	
	52	-10	IRT-SC5 (irt-ice3)	
	53	-5	IRT-SC5 (irt-ice3)	
	54	-2.5	IRT-SC5 (irt-ice3)	
	55	0	IRT-SC5 (irt-ice3)	
2-May-02	56	2.5	IRT-SC5 (irt-ice3)	Loose tape
	57	2.5	IRT-SC5 (irt-ice3)	Loose tape
	58	2.5	IRT-SC5 (irt-ice3)	Repeat R056 and R057
	59	5	IRT-SC5 (irt-ice3)	
	60	10	IRT-SC5 (irt-ice3)	
	61	15	IRT-SC5 (irt-ice3)	
	62	20	IRT-SC5 (irt-ice3)	
	64	0	Clean	Baseline repeat
	65	0	IRT-CS2 (irt-ice4)	
	66	-15	IRT-CS2 (irt-ice4)	
	67	-10	IRT-CS2 (irt-ice4)	
	68	-5	IRT-CS2 (irt-ice4)	
	69	-2.5	IRT-CS2 (irt-ice4)	
3-May-02	70	0	IRT-CS2 (irt-ice4)	
	71	2.5	IRT-CS2 (irt-ice4)	
	72	5	IRT-CS2 (irt-ice4)	
	73	10	IRT-CS2 (irt-ice4)	
	74	15	IRT-CS2 (irt-ice4)	
	75	20	IRT-CS2 (irt-ice4)	
	82	0	Clean	Baseline repeat
6-May-02	84	0	Clean	Baseline repeat
	85	0	IRT-IPSF22 (irt-ice6)	
	86	-15	IRT-IPSF22 (irt-ice6)	
	87	-10	IRT-IPSF22 (irt-ice6)	
	88	-5	IRT-IPSF22 (irt-ice6)	
	89	-5	IRT-IPSF22 (irt-ice6)	Repeat R088
	90	-2.5	IRT-IPSF22 (irt-ice6)	
	91	0	IRT-IPSF22 (irt-ice6)	
	92	2.5	IRT-IPSF22 (irt-ice6)	
	93	5	IRT-IPSF22 (irt-ice6)	Max out speed; $T_{\text{tunnel}} = 152^\circ\text{F}$
	94	10	IRT-IPSF22 (irt-ice6)	

Date	Run No.	δ_A (deg)	Configuration Name	Comments
7-May-02	95	15	IRT-IPSF22 (irt-ice6)	
	96	20	IRT-IPSF22 (irt-ice6)	Loose tape. Terminate run
	97	20	IRT-IPSF22 (irt-ice6)	Repeat R096
	99	0	Clean	Baseline repeat ($Re_{MAC} = 1.8 \times 10^6$)
	100	0	Clean	$Re_{MAC} = 1.5 \times 10^6$
	101	0	Clean	$Re_{MAC} = 1.0 \times 10^6$
	102	0	Clean	$Re_{MAC} = 0.5 \times 10^6$
	103	0	IRT-IS10 (irt-ice2)	Repeat R032
	104	2.5	IRT-IS10 (irt-ice2)	Repeat R033
	105	5	IRT-IS10 (irt-ice2)	Repeat R034
	106	10	IRT-IS10 (irt-ice2)	
	107	15	IRT-IS10 (irt-ice2)	
8-May-02	108	20	IRT-IS10 (irt-ice2)	
	109	-15	IRT-IS10 (irt-ice2)	
	110	0	IRT-IS10 (irt-ice2)	
	111	0	IRT-CS22 (irt-ice5)	$Re_{MAC} = 0.5 \times 10^6$
	112	0	IRT-CS22 (irt-ice5)	$Re_{MAC} = 1.5 \times 10^6$
	113	0	IRT-CS22 (irt-ice5)	$Re_{MAC} = 1.0 \times 10^6$
	114	0	IRT-CS22 (irt-ice5)	$Re_{MAC} = 1.8 \times 10^6$
	115	0	IRT-SC5 (irt-ice3)	$Re_{MAC} = 1.8 \times 10^6$ (tape loose)
	116	0	IRT-SC5 (irt-ice3)	$Re_{MAC} = 1.8 \times 10^6$; Repeat R115
	117	0	IRT-SC5 (irt-ice3)	$Re_{MAC} = 1.5 \times 10^6$
	118	0	IRT-SC5 (irt-ice3)	$Re_{MAC} = 1.0 \times 10^6$
	119	0	IRT-SC5 (irt-ice3)	$Re_{MAC} = 0.5 \times 10^6$
	121	0	Clean	Baseline repeat
9-May-02	135	0	Clean	Baseline repeat
	136	0	Clean	Baseline (using Model Constants Table 2).
10-May-02	149	0	Clean	Baseline repeat
13-May-02	151	0	Clean	Baseline repeat
14-May-02	167	0	LS-IS10 (ls-ice2)	
	168	-15	LS-IS10 (ls-ice2)	
	169	-10	LS-IS10 (ls-ice2)	
	170	-5	LS-IS10 (ls-ice2)	
	171	-2.5	LS-IS10 (ls-ice2)	
	172	0	LS-IS10 (ls-ice2)	
	173	2.5	LS-IS10 (ls-ice2)	
	174	5	LS-IS10 (ls-ice2)	
15-May-02	175	10	LS-IS10 (ls-ice2)	
	176	15	LS-IS10 (ls-ice2)	
	177	20	LS-IS10 (ls-ice2)	
	178	0	LS-IS10 (ls-ice2)	
	180	0	Clean	Baseline repeat
	181	0	LS-SC5 (ls-ice3)	

Date	Run No.	δ_A (deg)	Configuration Name	Comments
15-May-02	182	-15	LS-SC5 (ls-ice3)	
	183	-10	LS-SC5 (ls-ice3)	
	184	-5	LS-SC5 (ls-ice3)	
	185	-2.5	LS-SC5 (ls-ice3)	
	186	0	LS-SC5 (ls-ice3)	
	187	0	LS-SC5 (ls-ice3)	
16-May-02	188	2.5	LS-SC5 (ls-ice3)	
	189	5	LS-SC5 (ls-ice3)	
	190	10	LS-SC5 (ls-ice3)	
	191	15	LS-SC5 (ls-ice3)	
	192	20	LS-SC5 (ls-ice3)	
	193	0	LS-SC5 (ls-ice3)	
	195	0	Clean	Baseline repeat
	196	0	LR-IS10 (lr-ice2)	
	197	-15	LR-IS10 (lr-ice2)	
	198	0	LR-IS10 (lr-ice2)	Repeat of R196 (start at $\alpha = 0^\circ$), losing grit
	199	-10	LR-IS10 (lr-ice2)	
	200	-5	LR-IS10 (lr-ice2)	
17-May-02	201	0	LS-CS2 (ls-ice4)	
	202	-15	LS-CS2 (ls-ice4)	
	203	-10	LS-CS2 (ls-ice4)	
	204	-5	LS-CS2 (ls-ice4)	
	205	-2.5	LS-CS2 (ls-ice4)	
	206	0	LS-CS2 (ls-ice4)	
	207	2.5	LS-CS2 (ls-ice4)	
	208	5	LS-CS2 (ls-ice4)	
	209	10	LS-CS2 (ls-ice4)	
	210	15	LS-CS2 (ls-ice4)	
	211	20	LS-CS2 (ls-ice4)	
	213	0	LR-SC5 (lr-ice3)	
	214	-15	LR-SC5 (lr-ice3)	
	215	-10	LR-SC5 (lr-ice3)	
20-May-02	216	0	LR-SC5 (lr-ice3)	
	217	-5	LR-SC5 (lr-ice3)	
	218	-2.5	LR-SC5 (lr-ice3)	
	219	2.5	LR-SC5 (lr-ice3)	
	220	5	LR-SC5 (lr-ice3)	
	221	10	LR-SC5 (lr-ice3)	
	222	15	LR-SC5 (lr-ice3)	
	223	20	LR-SC5 (lr-ice3)	
	225	0	Clean	Baseline repeat
	226	0	LR-CS2 (lr-ice4)	Use static tare R1114

Date	Run No.	δ_A (deg)	Configuration Name	Comments
20-May-02	227	-15	LR-CS2 (lr-ice4)	
	228	-10	LR-CS2 (lr-ice4)	
	229	-5	LR-CS2 (lr-ice4)	
	230	-2.5	LR-CS2 (lr-ice4)	
	231	2.5	LR-CS2 (lr-ice4)	
21-May-02	232	0	LR-CS2 (lr-ice4)	
	233	2.5	LR-CS2 (lr-ice4)	
	234	5	LR-CS2 (lr-ice4)	
	235	10	LR-CS2 (lr-ice4)	
	236	15	LR-CS2 (lr-ice4)	
	237	20	LR-CS2 (lr-ice4)	
	239	0	Clean	Baseline repeat
22-May-02	240	0	LR-IS10 (lr-ice2)	Use static tare R1113
	241	-5	LR-IS10 (lr-ice2)	Repeat of R199
	242	-2.5	LR-IS10 (lr-ice2)	
	243	2.5	LR-IS10 (lr-ice2)	
	244	5	LR-IS10 (lr-ice2)	
	245	10	LR-IS10 (lr-ice2)	
	246	15	LR-IS10 (lr-ice2)	
	247	20	LR-IS10 (lr-ice2)	
24-May-02	264	0	Clean	Baseline repeat
28-May-02	276	0	Clean	Baseline repeat
29-May-02	291	0	Clean	Baseline repeat
30-May-02	299	0	Clean	Baseline repeat
31-May-02	314	0	Clean	Baseline repeat
	315	-15	Clean (fixed transition)	2 layers of aluminum strips at 2%c
	316	-5	Clean (fixed transition)	2 layers of aluminum strips at 2%c
	317	0	Clean (fixed transition)	2 layers of aluminum strips at 2%c
	318	5	Clean (fixed transition)	2 layers of aluminum strips at 2%c
	319	15	Clean (fixed transition)	2 layers of aluminum strips at 2%c
3-Jun-02	325	0	Clean	Baseline repeat
	328	0	LS-CS10 (ls-ice1)	
	329	-15	LS-CS10 (ls-ice1)	
	330	-10	LS-CS10 (ls-ice1)	
	331	-5	LS-CS10 (ls-ice1)	
	332	-2.5	LS-CS10 (ls-ice1)	
	333	2.5	LS-CS10 (ls-ice1)	
4-Jun-02	334	0	LS-CS10 (ls-ice1)	
	335	5	LS-CS10 (ls-ice1)	
	336	10	LS-CS10 (ls-ice1)	
	337	15	LS-CS10 (ls-ice1)	
	338	20	LS-CS10 (ls-ice1)	

Date	Run No.	δ_A (deg)	Configuration Name	Comments
4 June-02	339	0	LS-IPSF22 (ls-ice6)	
	340	-15	LS-IPSF22 (ls-ice6)	
	341	-10	LS-IPSF22 (ls-ice6)	
	342	-5	LS-IPSF22 (ls-ice6)	
	343	-2.5	LS-IPSF22 (ls-ice6)	
	344	2.5	LS-IPSF22 (ls-ice6)	
	345	5	LS-IPSF22 (ls-ice6)	
	346	10	LS-IPSF22 (ls-ice6)	
	347	15	LS-IPSF22 (ls-ice6)	
5-Jun-02	348	0	LS-IPSF22 (ls-ice6)	
	349	15	LS-IPSF22 (ls-ice6)	Repeat R347
	350	20	LS-IPSF22 (ls-ice6)	
	351	10	LS-IPSF22 (ls-ice6)	Repeat R346
	352	0	LR-CS10 (lr-ice1)	Use Static Tare R1116
	353	-15	LR-CS10 (lr-ice1)	
	354	-10	LR-CS10 (lr-ice1)	
	355	-5	LR-CS10 (lr-ice1)	
	356	-2.5	LR-CS10 (lr-ice1)	
	357	2.5	LR-CS10 (lr-ice1)	
	358	5	LR-CS10 (lr-ice1)	
	359	10	LR-CS10 (lr-ice1)	
	360	15	LR-CS10 (lr-ice1)	
	361	20	LR-CS10 (lr-ice1)	Aileron binding. Terminate run
	362	20	LR-CS10 (lr-ice1)	Repeat R361
	363	0	LR-CS10 (lr-ice1)	
6-Jun-02	364	0	LR-IPSF22 (lr-ice6)	
	365	20	LR-IPSF22 (lr-ice6)	
	366	15	LR-IPSF22 (lr-ice6)	
	367	10	LR-IPSF22 (lr-ice6)	
	368	5	LR-IPSF22 (lr-ice6)	
	369	2.5	LR-IPSF22 (lr-ice6)	
	370	-2.5	LR-IPSF22 (lr-ice6)	
	371	-5	LR-IPSF22 (lr-ice6)	
	372	-10	LR-IPSF22 (lr-ice6)	
	373	-15	LR-IPSF22 (lr-ice6)	
	374	0	LR-IPSF22 (lr-ice6)	
	376	0	Clean	Baseline repeat
10-Jun-02	390	0	Clean	Baseline repeat
11-Jun-02	396	0	Clean	Baseline repeat (automation wrong)
	397	0	Clean	Baseline repeat
	399	0	IRT-CS22 (irt-ice5)	
	400	0	IRT-IS10 (irt-ice2)	

Date	Run No.	δ_A (deg)	Configuration Name	Comments
12-Jun-02	402	0	Clean	Baseline repeat
	403	0	LS-CS22N (ls-ice5n)	
	404	20	LS-CS22N (ls-ice5n)	
	405	15	LS-CS22N (ls-ice5n)	
	406	10	LS-CS22N (ls-ice5n)	
	407	5	LS-CS22N (ls-ice5n)	Horn on pressure side split, due to heat. Was glued back and reinforced with screws.
	408	5	LS-CS22N (ls-ice5n)	Repeat of R407
	409	2.5	LS-CS22N (ls-ice5n)	
	410	-2.5	LS-CS22N (ls-ice5n)	
	411	-5	LS-CS22N (ls-ice5n)	
	412	-10	LS-CS22N (ls-ice5n)	
13-Jun-02	413	-15	LS-CS22N (ls-ice5n)	
	414	0	LS-CS22N (ls-ice5n)	
	417	0	LS-CS22N (ls-ice5n)	$Re_{MAC} = 0.5 \times 10^6$
	418	0	LS-CS22N (ls-ice5n)	$Re_{MAC} = 1.0 \times 10^6$
	419	0	LS-CS22N (ls-ice5n)	$Re_{MAC} = 1.5 \times 10^6$
	420	0	LR-IPSF22 (lr-ice6)	Repeat R364 and R374
	421	0	LR-IPSF22 (lr-ice6)	$Re_{MAC} = 1.5 \times 10^6$
	422	0	LR-IPSF22 (lr-ice6)	$Re_{MAC} = 1.0 \times 10^6$
	423	0	LR-IPSF22 (lr-ice6)	$Re_{MAC} = 0.5 \times 10^6$
	424	0	LR-IS10 (lr-ice2)	Repeat R196 and R240
	425	0	LR-SC5 (lr-ice3)	Repeat R213 and R216
14-Jun-02	426	0	LR-SC5 (lr-ice3)	Re-installed ice shape. Repeat R425
	427	0	LR-SC5 (lr-ice3)	$Re_{MAC} = 1.5 \times 10^6$
	428	0	LR-SC5 (lr-ice3)	$Re_{MAC} = 1.0 \times 10^6$
	429	0	LR-SC5 (lr-ice3)	$Re_{MAC} = 0.5 \times 10^6$
	430	0	LS-CS22S (ls-ice5s)	
	431	0	LS-CS22S (ls-ice5s)	
	432	20	LS-CS22S (ls-ice5s)	
	433	15	LS-CS22S (ls-ice5s)	
	434	10	LS-CS22S (ls-ice5s)	
	435	5	LS-CS22S (ls-ice5s)	
	436	2.5	LS-CS22S (ls-ice5s)	
	437	-2.5	LS-CS22S (ls-ice5s)	
	438	-5	LS-CS22S (ls-ice5s)	
	439	-10	LS-CS22S (ls-ice5s)	Aileron binding. Terminate run
17-Jun-02	440	-10	LS-CS22S (ls-ice5s)	Repeat R439
	441	-15	LS-CS22S (ls-ice5s)	
	442	0	LS-CS22S (ls-ice5s)	
	444	0	Clean	Baseline repeat
	445	0	LR-CS22N (lr-ice5n)	

Date	Run No.	δ_A (deg)	Configuration Name	Comments
17-Jun-02	446	20	LR-CS22N (lr-ice5n)	
	447	15	LR-CS22N (lr-ice5n)	
	448	10	LR-CS22N (lr-ice5n)	
	449	5	LR-CS22N (lr-ice5n)	
	450	2.5	LR-CS22N (lr-ice5n)	
	451	-2.5	LR-CS22N (lr-ice5n)	Loose tape. Terminate run
18-Jun-02	455	-2.5	LR-CS22N (lr-ice5n)	Repeat R451
	456	-5	LR-CS22N (lr-ice5n)	
	457	-10	LR-CS22N (lr-ice5n)	
	458	-15	LR-CS22N (lr-ice5n)	
	459	0	LR-CS22N (lr-ice5n)	
	460	0	LR-CS22S (lr-ice5s)	
	461	20	LR-CS22S (lr-ice5s)	
	462	15	LR-CS22S (lr-ice5s)	
	463	10	LR-CS22S (lr-ice5s)	
	464	5	LR-CS22S (lr-ice5s)	Loose tape. Terminate run
	465	0	LR-CS22S (lr-ice5s)	Repeat R460, loose tape
	466	0	LR-CS22S (lr-ice5s)	Repeat R460, loose tape
	467	0	LR-CS22S (lr-ice5s)	Repeat R460, loose tape
19-Jun-02	468	0	LR-CS22S (lr-ice5s)	Repeat R460
	469	5	LR-CS22S (lr-ice5s)	Repeat R464
	470	2.5	LR-CS22S (lr-ice5s)	
	471	-2.5	LR-CS22S (lr-ice5s)	Sandpaper started to peel off at about 17°, but data looks good.
	472	-5	LR-CS22S (lr-ice5s)	
	473	-10	LR-CS22S (lr-ice5s)	
	474	-15	LR-CS22S (lr-ice5s)	Lost sandpaper
	475	-15	LR-CS22S (lr-ice5s)	Repeat R474
	476	0	LR-CS22S (lr-ice5s)	$Re_{MAC} = 1.5 \times 10^6$
	477	0	LR-CS22S (lr-ice5s)	$Re_{MAC} = 1.0 \times 10^6$
	478	0	LR-CS22S (lr-ice5s)	$Re_{MAC} = 0.5 \times 10^6$
	480	15	Clean	Repeat R010
	481	0	LR-CS22N (lr-ice5n)	Repeat R445
	482	0	LR-CS22N (lr-ice5n)	$Re_{MAC} = 0.5 \times 10^6$
20-Jun-02	483	0	LR-CS22N (lr-ice5n)	$Re_{MAC} = 1.0 \times 10^6$
	484	0	LR-CS22N (lr-ice5n)	$Re_{MAC} = 1.5 \times 10^6$
	485	0	LR-CS10 (lr-ice1)	Repeat R352
	486	0	LR-CS10 (lr-ice1)	$Re_{MAC} = 1.5 \times 10^6$
	487	0	LR-CS10 (lr-ice1)	$Re_{MAC} = 1.0 \times 10^6$
	488	0	LR-CS10 (lr-ice1)	$Re_{MAC} = 0.5 \times 10^6$
21-Jun-02	501	0	Clean	Baseline repeat
25-Jun-02	521	0	Clean	Flow-viz, $Re_{MAC} = 1.5 \times 10^6$
	522	0	IRT-CS10 (irt-ice1)	Flow-viz, $Re_{MAC} = 1.5 \times 10^6$

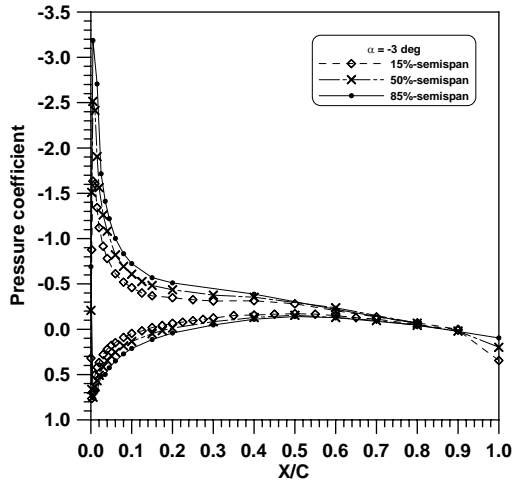
Date	Run No.	δ_A (deg)	Configuration Name	Comments
25-Jun-02	523	0	IRT-IPSF22 (irt-ice6)	Flow-viz, $Re_{MAC} = 1.5 \times 10^6$
	524	0	IRT-IS10 (irt-ice2)	Flow-viz, $Re_{MAC} = 1.5 \times 10^6$
	525	0	IRT-SC5 (irt-ice3)	Flow-viz, $Re_{MAC} = 1.5 \times 10^6$
	526	0	IRT-CS2 (irt-ice4)	Flow-viz, $Re_{MAC} = 1.5 \times 10^6$
26-Jun-02	527	0	LR-IS10 (lr-ice2)	Flow-viz, $Re_{MAC} = 1.5 \times 10^6$
	528	0	LR-SC5 (lr-ice3)	Flow-viz, $Re_{MAC} = 1.5 \times 10^6$
	529	0	LR-CS2 (lr-ice4)	Flow-viz, $Re_{MAC} = 1.5 \times 10^6$
	530	0	LR-CS10 (lr-ice1)	Flow-viz, $Re_{MAC} = 1.5 \times 10^6$
	531	0	LR-IPSF22 (lr-ice6)	Flow-viz, $Re_{MAC} = 1.5 \times 10^6$
	532	0	LR-CS22S (lr-ice5s)	Flow-viz, $Re_{MAC} = 1.5 \times 10^6$
	533	0	LR-CS22N (lr-ice5n)	Flow-viz, $Re_{MAC} = 1.5 \times 10^6$
	534	0	IRT-CS22 (irt-ice5)	Repeat R520, $Re_{MAC} = 1.0 \times 10^6$
	536	0	Clean	Repeat R521, $Re_{MAC} = 1.5 \times 10^6$
27-Jun-02	537	20	Clean	Flow-viz, $Re_{MAC} = 1.5 \times 10^6$
	538	-15	Clean	Flow-viz, $Re_{MAC} = 1.5 \times 10^6$
27-Jun-02	539	0	Clean	Take data with yarn tufts on model, $Re_{MAC} = 1.5 \times 10^6$
	541	0	Clean	Baseline repeat
	548	0	LR-IPSF22 (lr-ice6)	Added 24-grit to tip of horns of ice shape
	549	15	LR-IPSF22 (lr-ice6)	Added 24-grit to tip of horns of ice shape
	550	-15	LR-IPSF22 (lr-ice6)	Added 24-grit to tip of horns of ice shape
1-Jul-02	564	0	IRT-IPSF22 (irt-ice6)	$Re_{MAC} = 1.8 \times 10^6$
	565	0	IRT-IPSF22 (irt-ice6)	$Re_{MAC} = 1.5 \times 10^6$
	566	0	IRT-IPSF22 (irt-ice6)	$Re_{MAC} = 1.0 \times 10^6$
	567	0	IRT-IPSF22 (irt-ice6)	$Re_{MAC} = 0.5 \times 10^6$
	568	0	LS-IPSF22 (ls-ice6)	$Re_{MAC} = 1.8 \times 10^6$
1-Jul-02	569	0	LS-IPSF22 (ls-ice6)	$Re_{MAC} = 1.5 \times 10^6$
	570	0	LS-IPSF22 (ls-ice6)	$Re_{MAC} = 1.0 \times 10^6$
	571	0	LS-IPSF22 (ls-ice6)	$Re_{MAC} = 0.5 \times 10^6$
	573	0	Clean	Baseline repeat
2-Jul-02	582	0	LS-CS22S (ls-ice5s)	Flow-viz, $Re_{MAC} = 1.5 \times 10^6$, one of the VCR was not recording
	583	0	LS-CS22S (ls-ice5s)	Flow-viz, $Re_{MAC} = 1.5 \times 10^6$, Repeat R582
	584	0	LS-IPSF22 (ls-ice6)	Flow-viz, $Re_{MAC} = 1.5 \times 10^6$
3-Jul-02	587	0	IRT-CS22 (irt-ice5)	Flow-viz, $Re_{MAC} = 1.5 \times 10^6$
5-Jul-02	595	0	Clean	Baseline repeat
	596	0	Clean	Checking flow angularity probe installation, $q = 15$ psf
	597	0	Clean	7-hole flow angularity probes
	598	20	Clean	7-hole flow angularity probes
	599	-15	Clean	7-hole flow angularity probes
	603	0	Clean	Gap opened
	604	0	IRT-CS22 (irt-ice5)	Gap opened

APPENDIX C—PRESSURE DATA FROM ICING TESTS

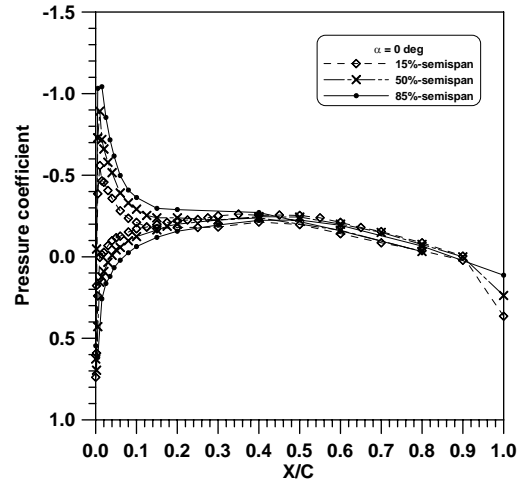
Surface pressures at 15%, 50%, and 85% semispan locations were obtained prior to the ice accretion tests. At velocity of approximately 150 mph, with the wing in normal position (refer to section 2.1.3), pressures were measured at angles of attack of -3° , -2.5° , -2° , -1.5° , -1° , -0.5° , 0° , 0.5° , 1° , 1.5° , 2° , 4° , 6° , 8° , 10° , 11° , 12° , 13° , 14° , and 14.5° . Pressure coefficient (C_p) distributions of selected α are presented in figure C-1.

Pressure measurements were performed with the icing research tunnel (IRT) electronically scanned pressure (ESP) system. Six 32-port (± 5 psid) ESP modules were available in the IRT, providing a total of 192 pressure channels. One port in each module was used for a check pressure; thus 31 channels per module were available for test data, or a total of 186 ports. The ESP system applied a three-point pressure calibration to all port transducers. This on-line three-point calibration ensured that measurement errors were not greater than $\pm 0.1\%$ of full-scale. The standard calibration interval was every 400 cycles (approximately 15 minutes).

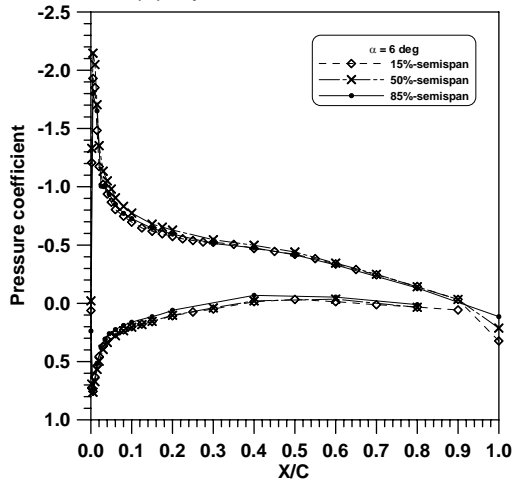
The experimental pressure data were used to validate C_p distributions from LEWICE analyses and wind tunnel tests at Wichita State University.



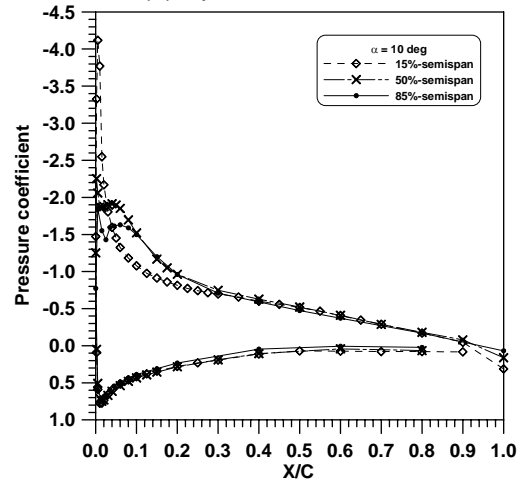
(a) C_p vs. x/c , $\alpha = -3^\circ$



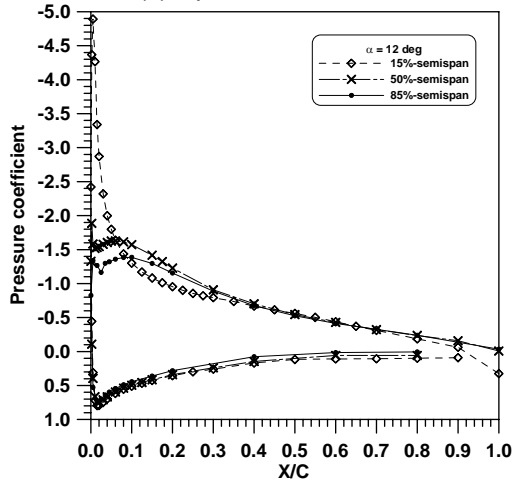
(b) C_p vs. x/c , $\alpha = 0^\circ$



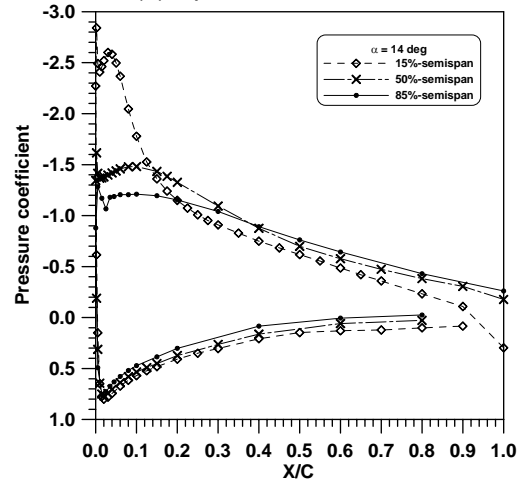
(c) C_p vs. x/c , $\alpha = 6^\circ$



(d) C_p vs. x/c , $\alpha = 10^\circ$



(e) C_p vs. x/c , $\alpha = 12^\circ$



(f) C_p vs. x/c , $\alpha = 14^\circ$

FIGURE C-1. PRESSURE DISTRIBUTIONS OF CLEAN CONFIGURATION FROM IRT; WING IN NORMAL POSITION; $V_\infty = 150$ mph

APPENDIX D—FLOW ANGULARITY STUDIES

Two, seven-hole flow angularity probes were installed on the clean wing at two stations corresponding to approximately 16% and 80% semispan. Seven-hole probes can measure the three components of velocity, the total pressure, and the static pressure at a point in the flow. The flow probe provides results with high accuracy for angles as high as 75° . The data from the seven-hole probes were used to estimate the local angle of attack of the wing due to geometric twist of the wing, presence of the streamlined body, and vortices at the wing tip. Angle of attack sweeps were conducted for three aileron deflections (-15° , 0° , and 20°) and at Reynolds number of 1.8 million based on wing mean aerodynamic chord. Pressures measured from the seven-hole probes were recorded. Installation of the seven-hole flow probes is shown in figures 2-52 to 2-55.

In order for the probes to provide accurate downwash angle measurements, they were attached onto the wing leading edge and aligned to the free-stream flow direction. Note that this line of direction is not concurrent to the wing chordwise direction, and therefore, a set of brackets was specifically made to accommodate the installation.

Effects of flow probes on the wing lift and drag coefficients are demonstrated in figures D-1 and D-2. It is observed that the flow probes improved lift performance of the wing; i.e., lift coefficient (C_L) was increased throughout the α -range and as a result $C_{L,stall}$ was increased as well. This is because the flow probes generated vortices that re-energized the boundary layer, which delayed transition and flow separation; hence, improved $C_{L,stall}$. From figure D-1, it is observed that the offsets between the C_L values obtained with and without the flow probes, amongst all three aileron deflections of -15° , 0° , and 20° , were very similar, and that higher lift curves were produced with higher δ_A . It is of interest to draw attention to the fact that the lift curve generated with the flow probes at δ_A of -15° behaved very much like that from without the probes at δ_A of 0° .

The same vortices that re-energized the boundary layer also inadvertently increased drag coefficient (C_D), as shown in figure D-2. In general, the increment in drag contributed by the probes was only accountable when the wing was experiencing a positive α . Consider the case of drag coefficients generated by the wing with the flow probes installed at δ_A of 20° , its C_D values were the highest amongst all three aileron deflection configurations, with and without the probes, yet only at the range of positive α from 2° onwards. In contrary, its C_D values from α of -4° to -8° were the lowest amongst all configurations tested.

Downwash (or upwash) angle as a function of geometric angle of attack is depicted in figures D-3 and D-4. Results from figure D-3 were collected from the probe at 16% semispan location, whereas those from figure D-4 were collected from the one at 80% semispan. In both cases, the most negative aileron deflection ($\delta_A = -15^\circ$) configuration generated the largest amount of downwash angles for the positive α -sweep. Under the same argument, the test configuration of the most positive aileron deflection ($\delta_A = 20^\circ$) generated the largest upwash angles (negative downwash angles) during the negative α -sweep. Note that the downwash angle curve in figure D-4 obtained near the tip of the semispan behaved less linearly than the one

observed towards the wing root, as shown in figure D-3. Also, the slope of the downwash angle with respect to the angle of attack observed at the near-tip section is smaller than that of the near-root section.

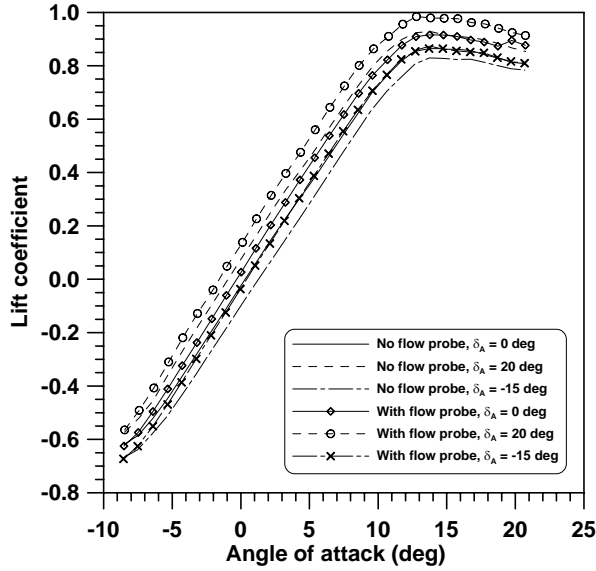


FIGURE D-1. EFFECTS OF FLOW PROBES ON CL; $Re = 1.8 \times 10^6$

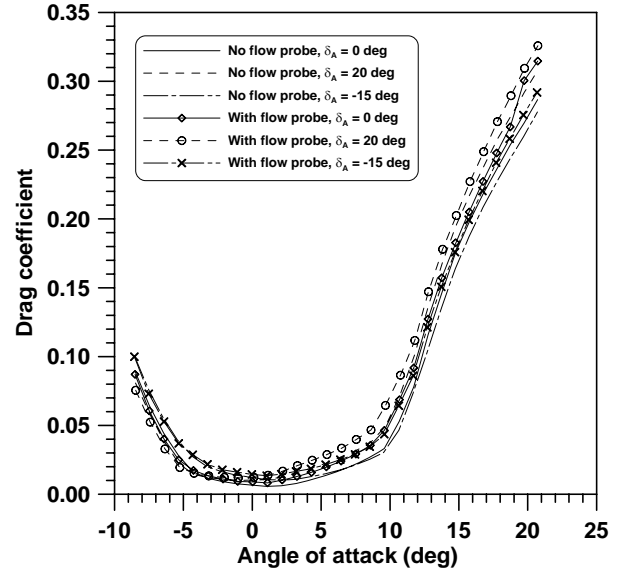


FIGURE D-2. EFFECTS OF FLOW PROBES ON CD; $Re = 1.8 \times 10^6$

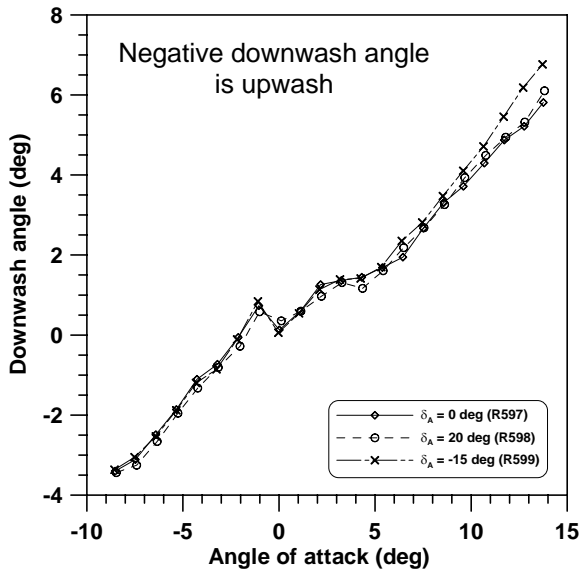


FIGURE D-3. RELATIONSHIP OF DOWNWASH ANGLE WITH GEOMETRIC ANGLE OF ATTACK; 16% SEMISPAN; $Re = 1.8 \times 10^6$

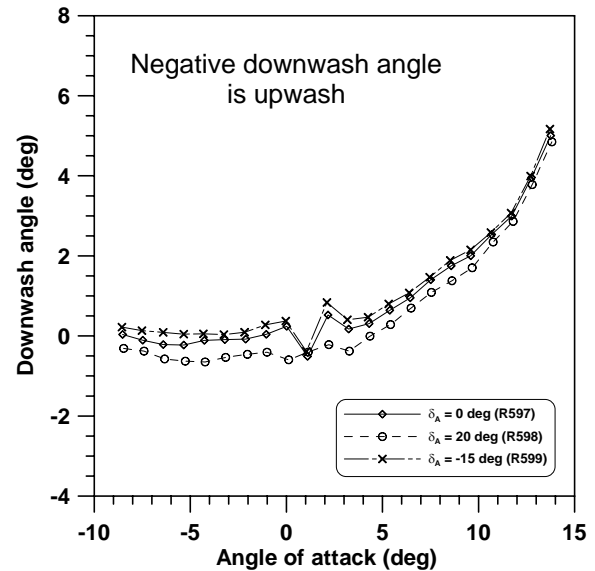


FIGURE D-4. RELATIONSHIP OF DOWNWASH ANGLE WITH GEOMETRIC ANGLE OF ATTACK; 80% SEMISPAN; $Re = 1.8 \times 10^6$

APPENDIX E—SIMULATED FROST USING SANDPAPER

As per Federal Aviation Administration request, a total of eight configurations of frost simulation using 2-grit sandpaper (times four coverage) were identified and investigated to study the effects of frost on aerodynamic performance of a swept wing. The use of sandpaper in simulating ice shape roughness aligns with current procedures used by airframers during aircraft icing certification*.

Sandpaper tested were 40 grit and 150 grit. With mean aerodynamic chord (MAC) of 1.25 ft, 40-grit provided normalized roughness (k/MAC) of 1×10^{-3} , where the 150-grit sandpaper provided k/MAC of 2×10^{-4} . Figure E-1 shows the four different frost simulation coverage using 40-grit sandpaper. The first configuration (figure E-1(a)) simulated frost coverage on the whole wing. From figures E-1(b) and E-1(c), the second and third configurations were to simulate frost coverage on the aft 87.5% and 35% of the wing, respectively. In addition, the fourth coverage (figure E-1(d)) was to simulate failed deicing fluid condition. All sandpaper coverage were applied on the wing upper surface only.

Figure E-2 demonstrates the effects of simulated frost on C_L , C_D , C_M , and C_H of the wing using 40-grit sandpaper, whereas the simulated frost effect using 150-grit roughness was shown in figure E-3.

* Papadakis, M., Yeong, H.W., Chadrsekharan, V.R., Hinston, M., and Ratvasky, T.P., "Effects of Roughness on the Aerodynamic Performance of a Business Jet Tail," AIAA Paper 2002-0242, January 2002.



FR1-40 (configuration 5)



FR2-40 (configuration 6)

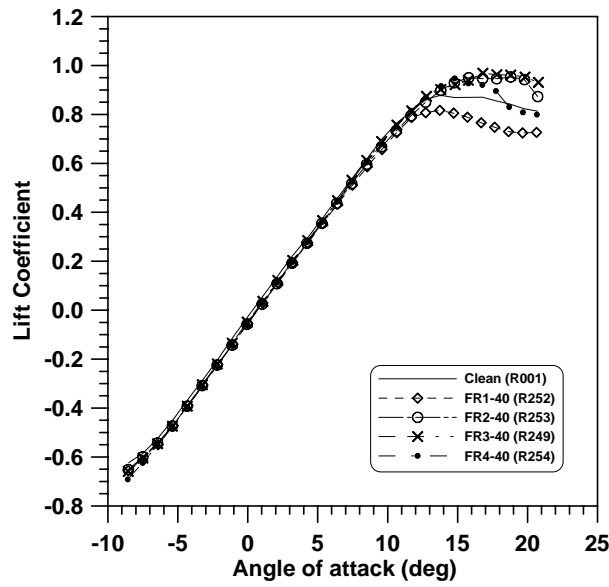


FR3-40 (configuration 7)

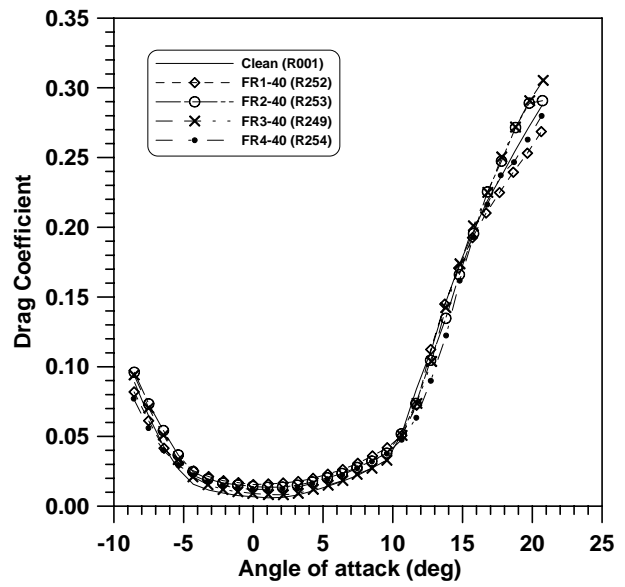


FR4-40 (configuration 8)

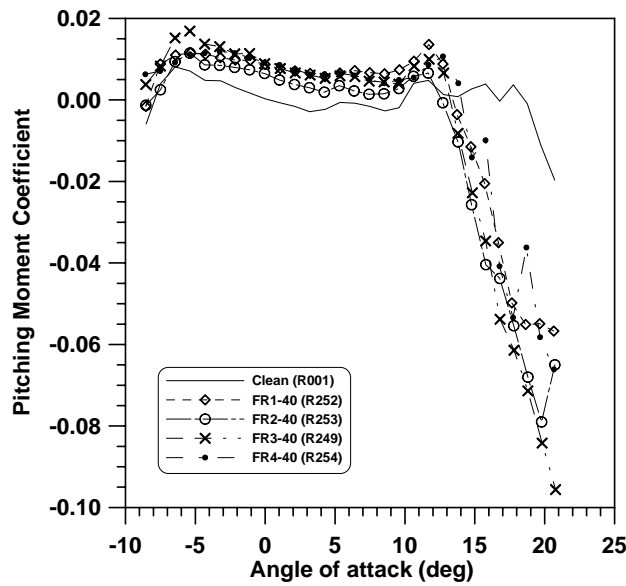
FIGURE E-1. GLC-305 MODEL WITH 40-GRIT ($K/MAC = 1 \times 10^{-3}$) SANDPAPER, SIMULATING FROST FORMATION



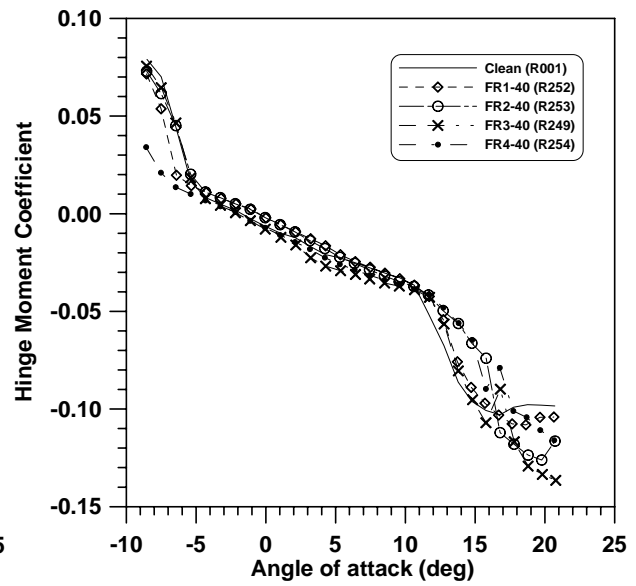
(a) Lift coefficient



(b) Drag coefficient

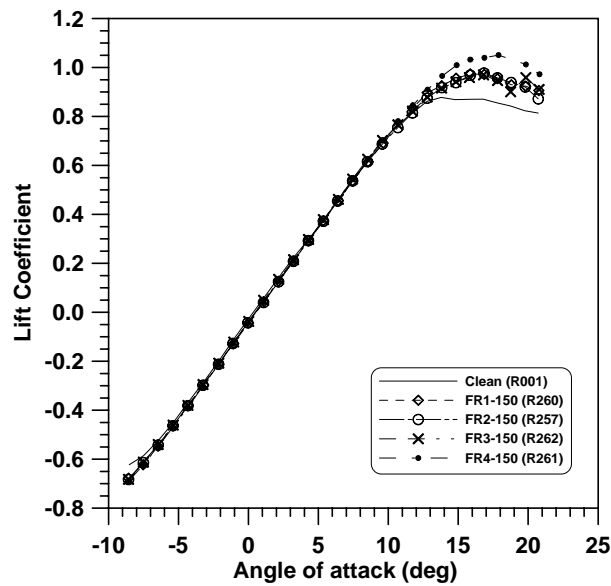


(c) Pitching-moment coefficient

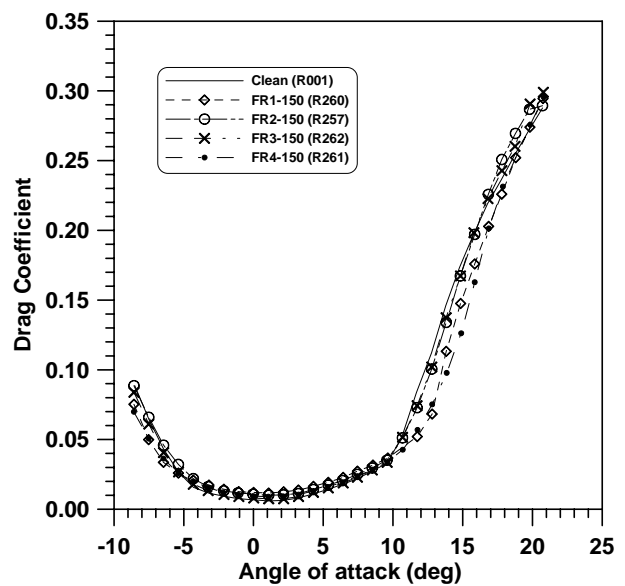


(d) Hinge-moment coefficient

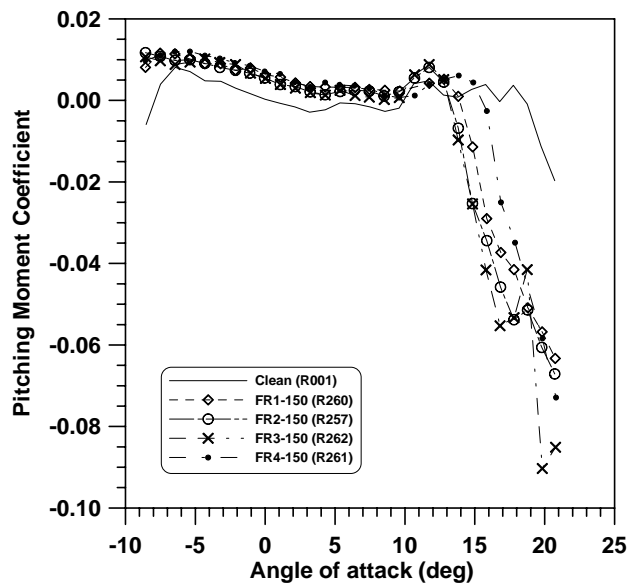
FIGURE E-2. EFFECT OF FROST ON AERODYNAMIC PERFORMANCE; 40-GRIT SANDPAPER; $Re = 1.8 \times 10^6$; $\delta_A = 0^\circ$



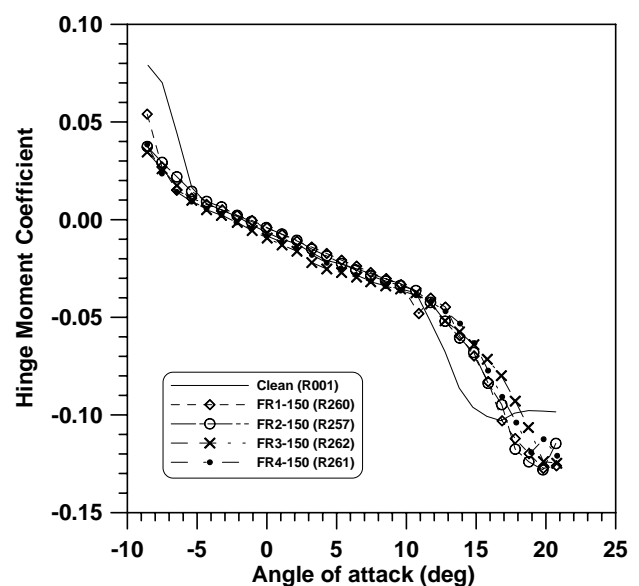
(a) Lift coefficient



(b) Drag coefficient



(c) Pitching-moment coefficient



(d) Hinge-moment coefficient

FIGURE E-3. EFFECT OF FROST ON AERODYNAMIC PERFORMANCE; 150-GRIT SANDPAPER; $Re = 1.8 \times 10^6$; $\delta_A = 0^\circ$

APPENDIX F—EFFECT OF AILERON DEFLECTION (SUPPLEMENTARY)

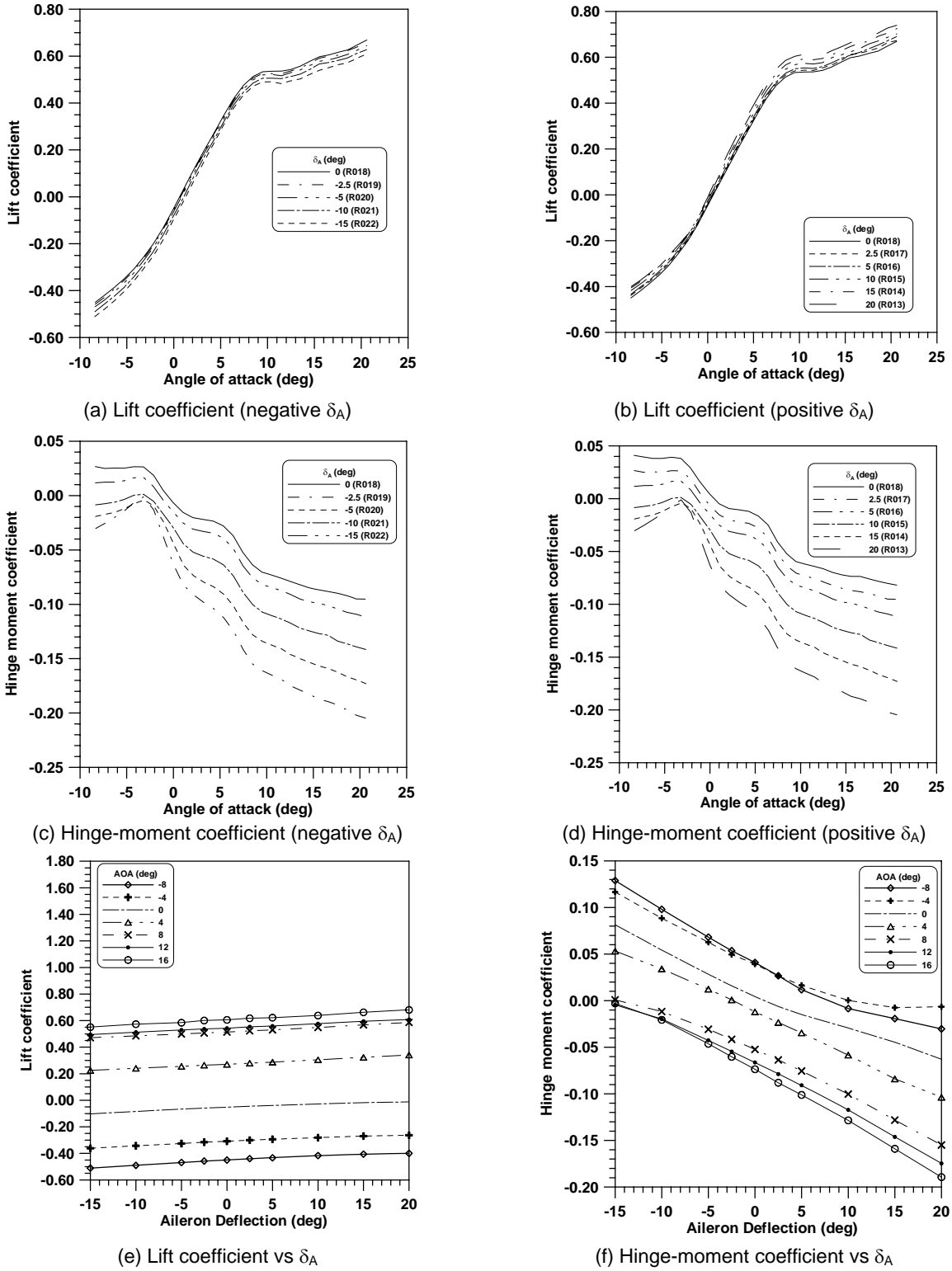
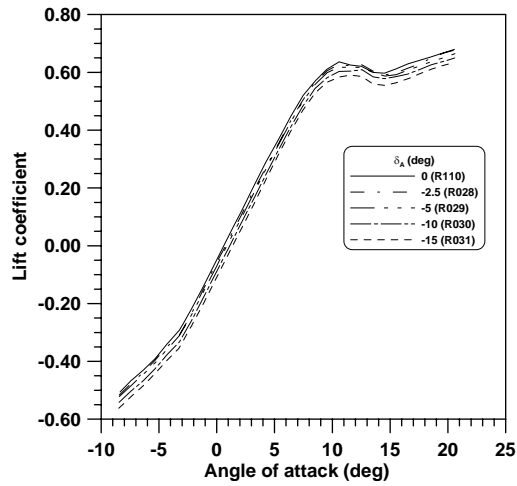
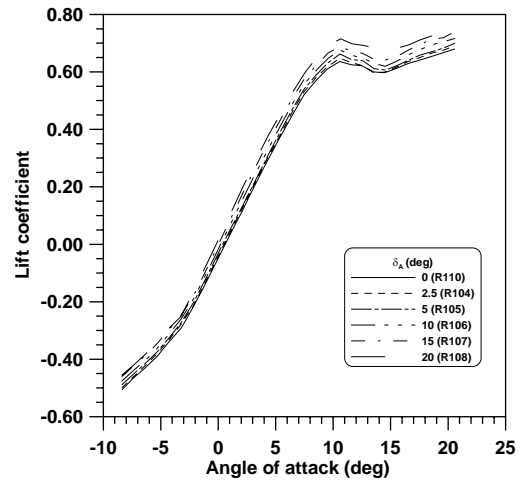


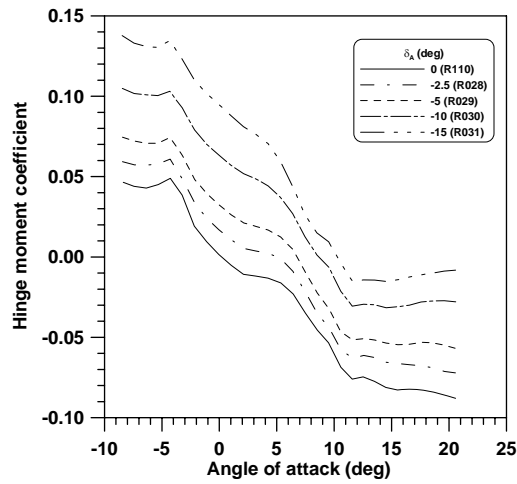
FIGURE F-1. EFFECT OF AILERON DEFLECTION ON LIFT AND HINGE-MOMENT COEFFICIENTS; IRT-CS10 (ICING CONDITION 1); $Re = 1.8 \times 10^6$



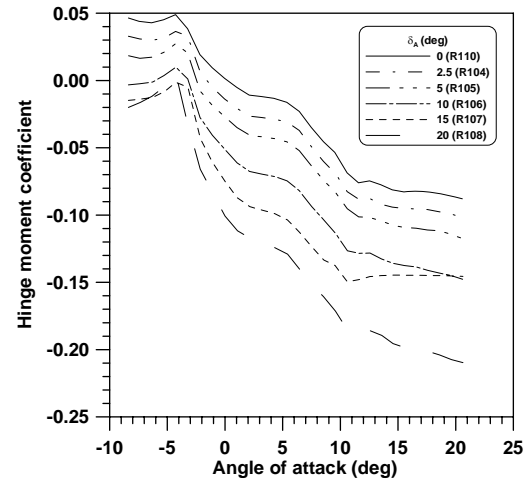
(a) Lift coefficient (negative δ_A)



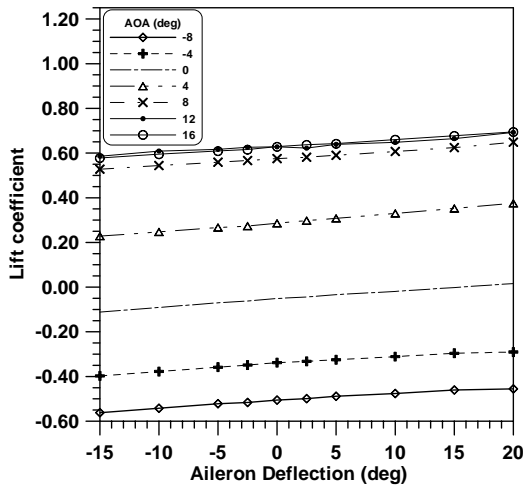
(b) Lift coefficient (positive δ_A)



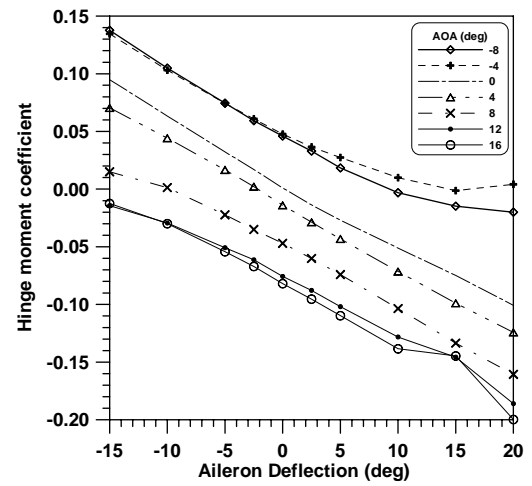
(c) Hinge-moment coefficient (negative δ_A)



(d) Hinge-moment coefficient (positive δ_A)

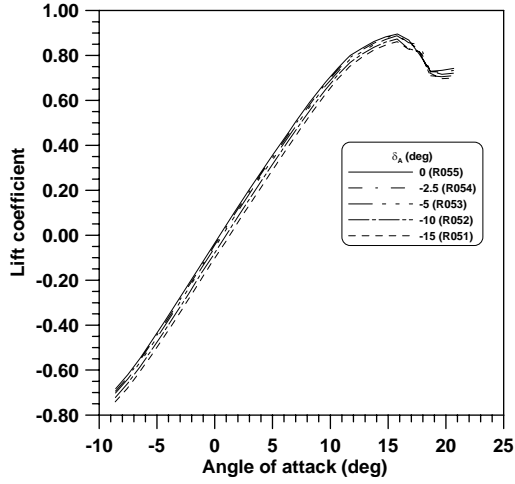


(e) Lift coefficient vs δ_A

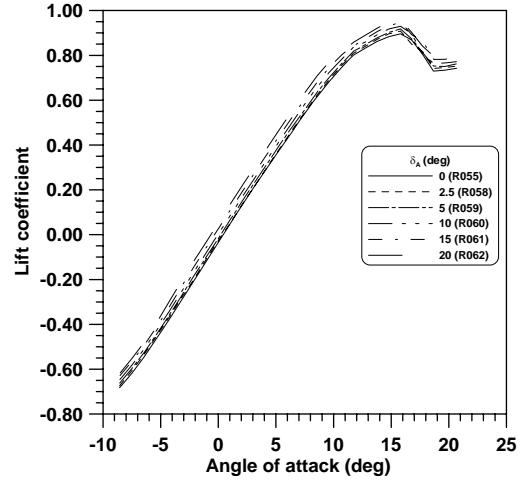


(f) Hinge-moment coefficient vs δ_A

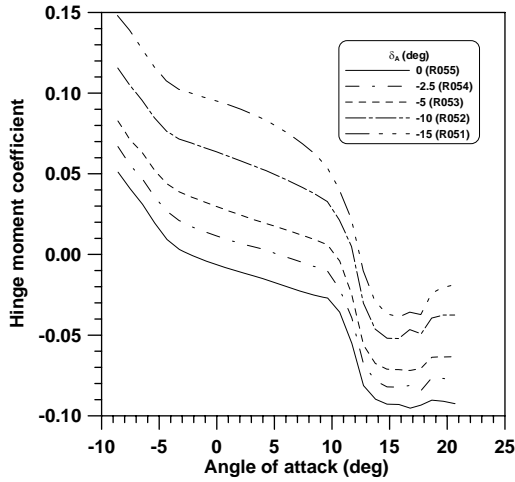
FIGURE F-2. EFFECT OF AILERON DEFLECTION ON LIFT AND HINGE-MOMENT COEFFICIENTS; IRT-IS10 (ICING CONDITION 2); $Re = 1.8 \times 10^6$



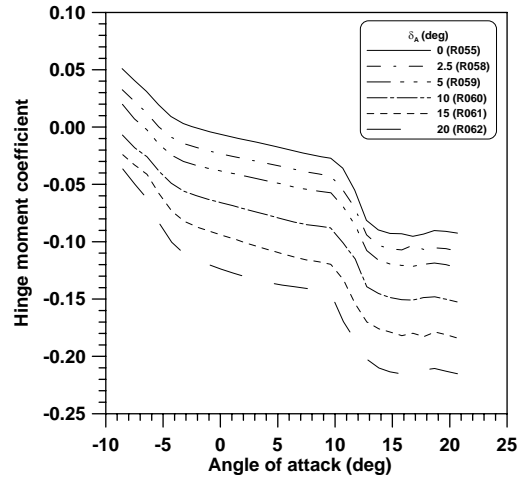
(a) Lift coefficient (negative δ_A)



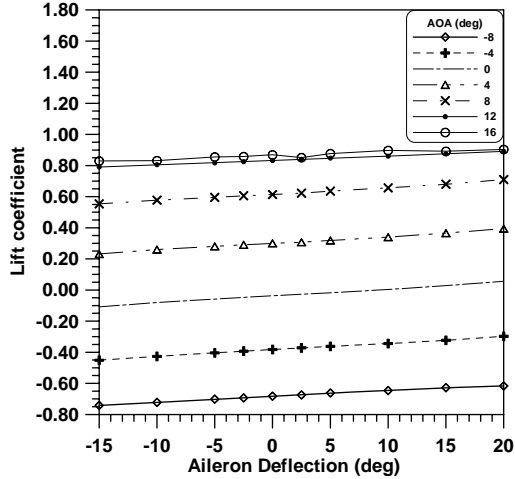
(b) Lift coefficient (positive δ_A)



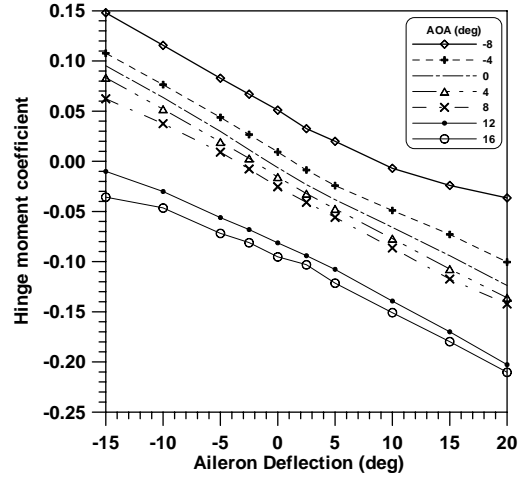
(c) Hinge-moment coefficient (negative δ_A)



(d) Hinge-moment coefficient (positive δ_A)

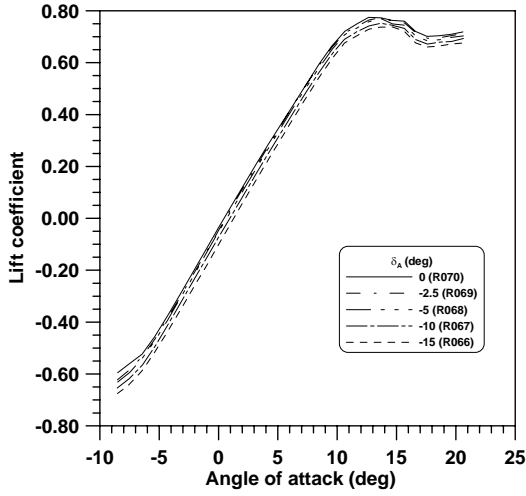


(e) Lift coefficient vs δ_A

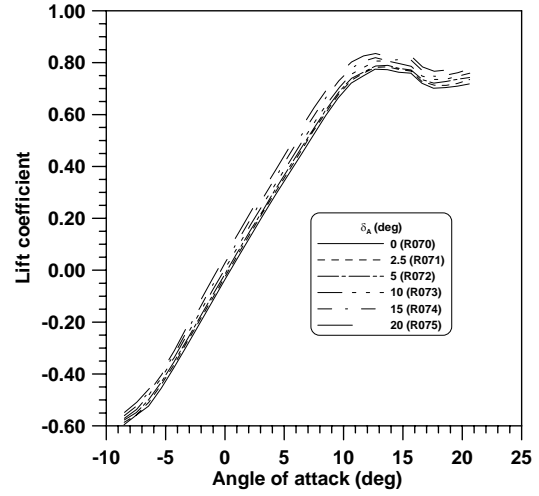


(f) Hinge-moment coefficient vs δ_A

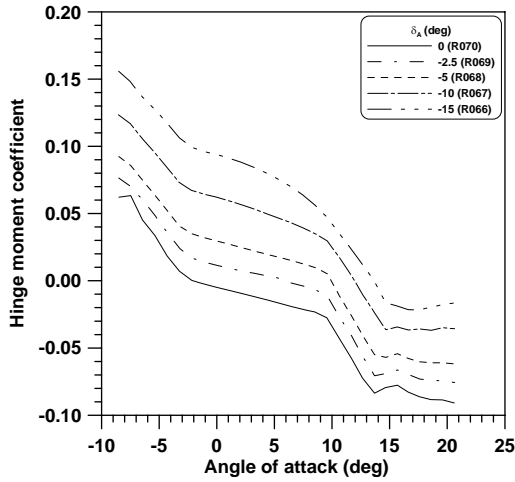
FIGURE F-3. EFFECT OF AILERON DEFLECTION ON LIFT AND HINGE-MOMENT COEFFICIENTS; IRT-SC5 (ICING CONDITION 3); $Re = 1.8 \times 10^6$



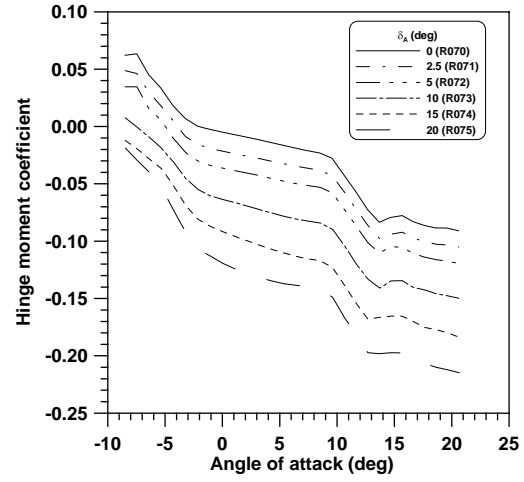
(a) Lift coefficient (negative δ_A)



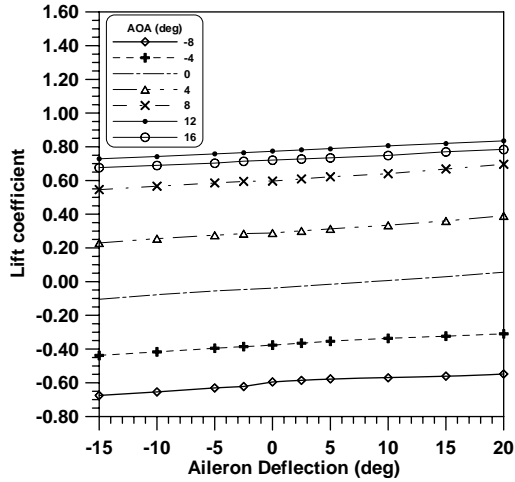
(b) Lift coefficient (positive δ_A)



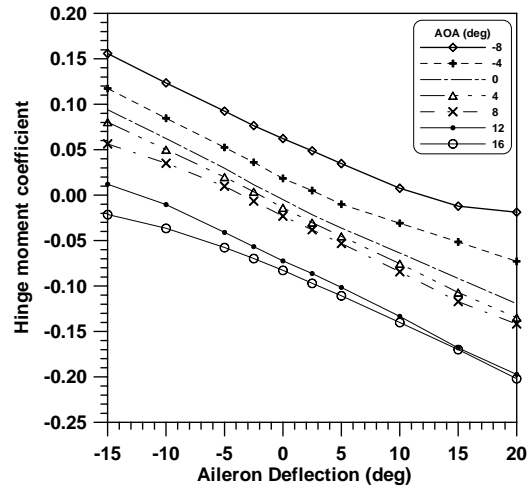
(c) Hinge-moment coefficient (negative δ_A)



(d) Hinge-moment coefficient (positive δ_A)

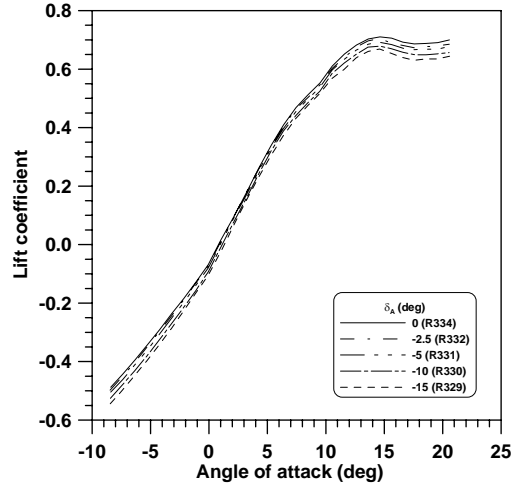


(e) Lift coefficient vs δ_A

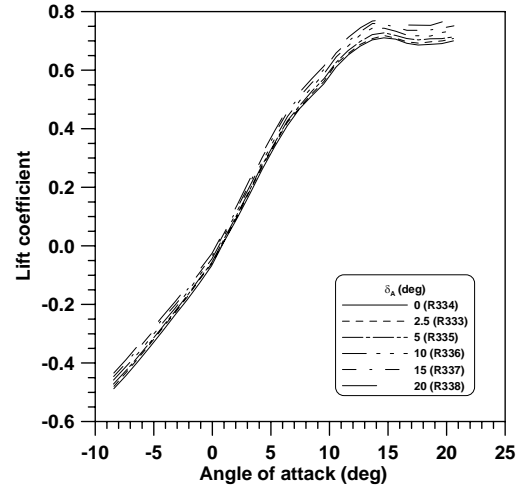


(f) Hinge-moment coefficient vs δ_A

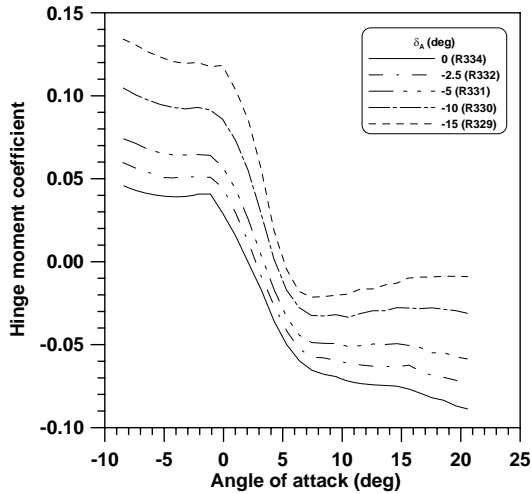
FIGURE F-4. EFFECT OF AILERON DEFLECTION ON LIFT AND HINGE-MOMENT COEFFICIENTS; IRT-CS2 (ICING CONDITION 4); $Re = 1.8 \times 10^6$



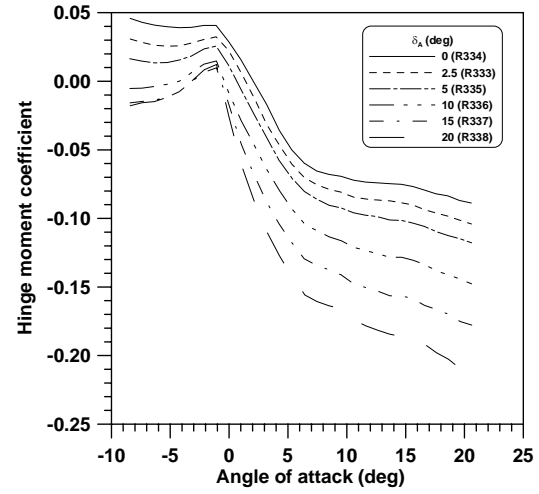
(a) Lift coefficient (negative δ_A)



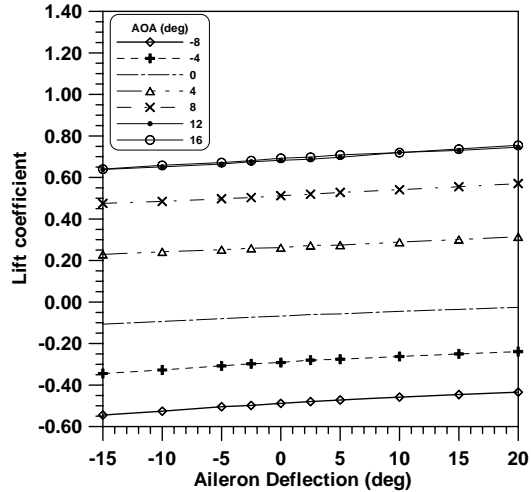
(b) Lift coefficient (positive δ_A)



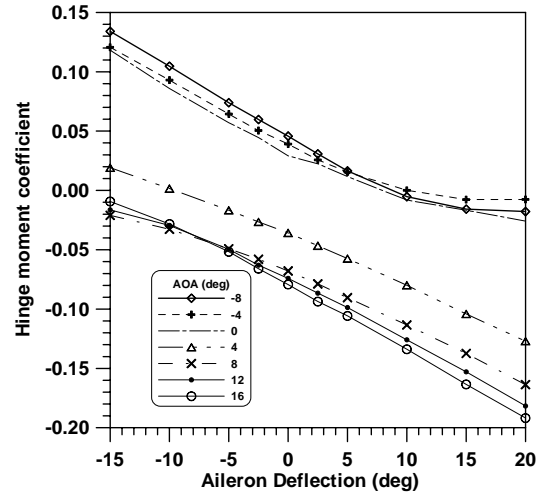
(c) Hinge-moment coefficient (negative δ_A)



(d) Hinge-moment coefficient (positive δ_A)

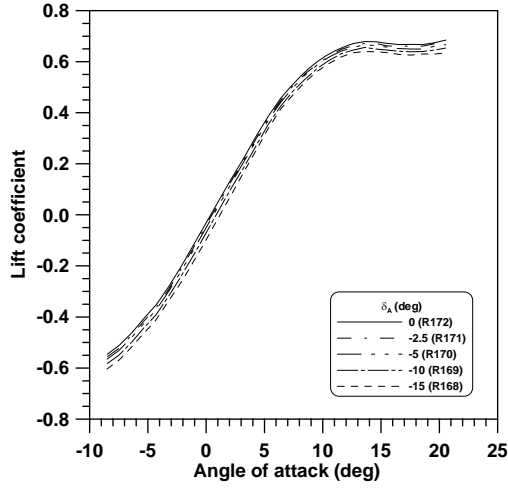


(e) Lift coefficient vs δ_A

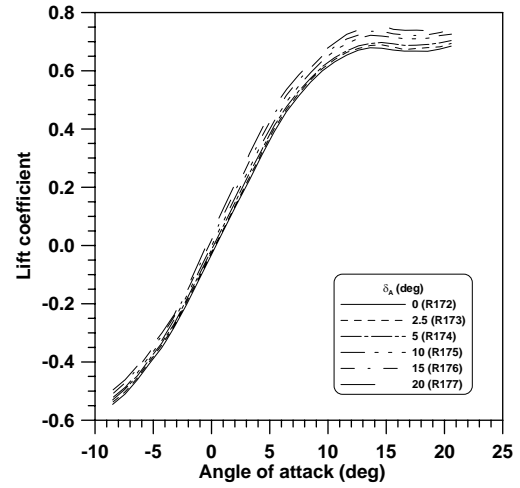


(f) Hinge-moment coefficient vs δ_A

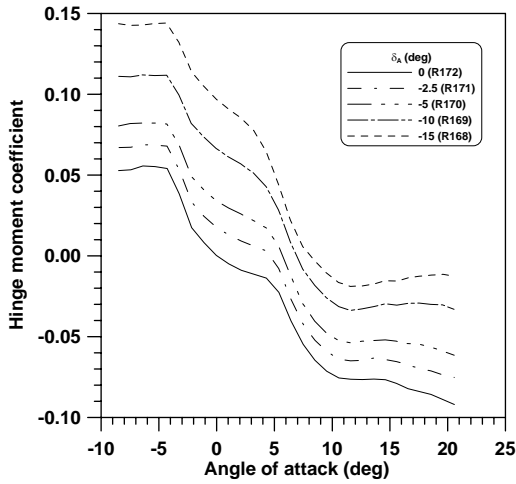
FIGURE F-5. EFFECT OF AILERON DEFLECTION ON LIFT AND HINGE-MOMENT COEFFICIENTS; LS-CS10 (ICING CONDITION 1); $Re = 1.8 \times 10^6$



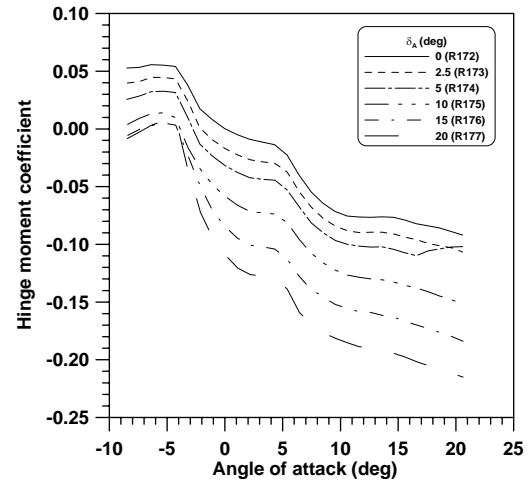
(a) Lift coefficient (negative δ_A)



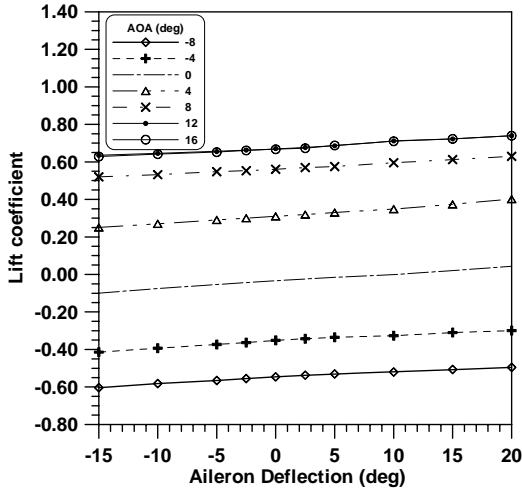
(a) Lift coefficient (positive δ_A)



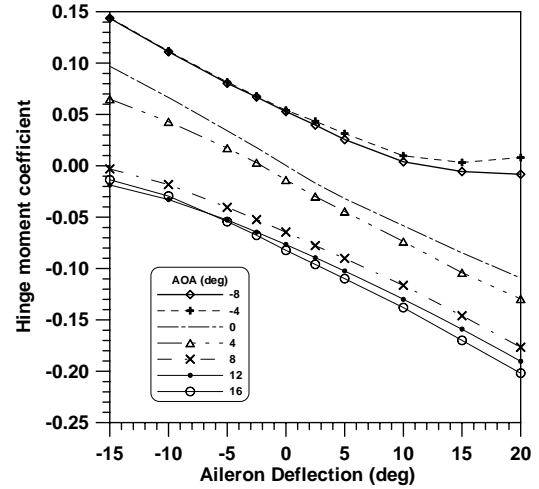
(c) Hinge-moment coefficient (negative δ_A)



(d) Hinge-moment coefficient (positive δ_A)

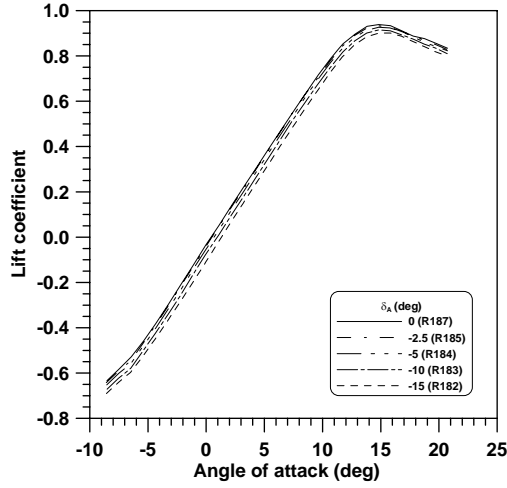


(e) Lift coefficient vs δ_A

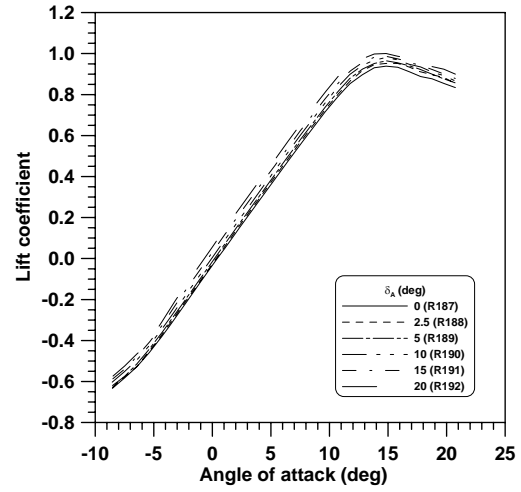


(f) Hinge-moment coefficient vs δ_A

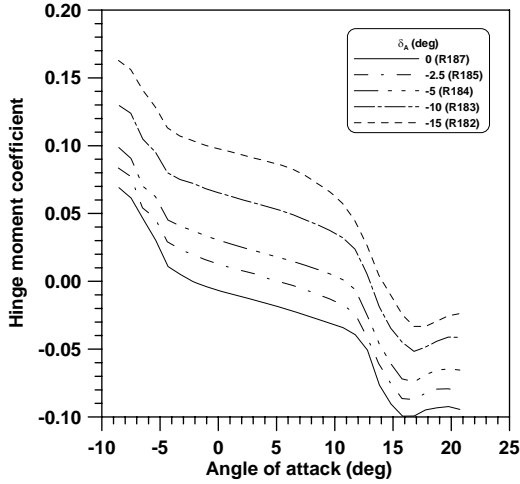
FIGURE F-6. EFFECT OF AILERON DEFLECTION ON LIFT AND HINGE-MOMENT COEFFICIENTS; LS-IS10 (ICING CONDITION 2); $Re = 1.8 \times 10^6$



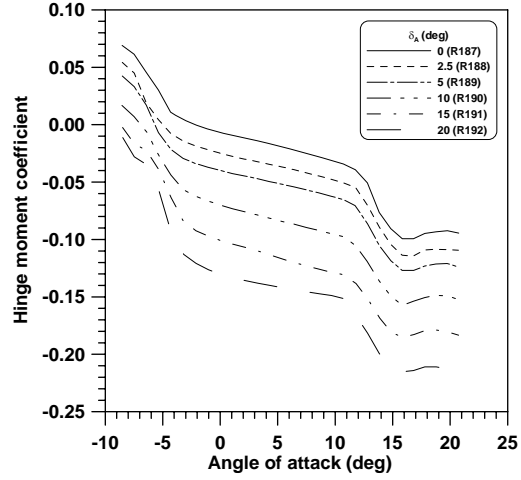
(a) Lift coefficient (negative δ_A)



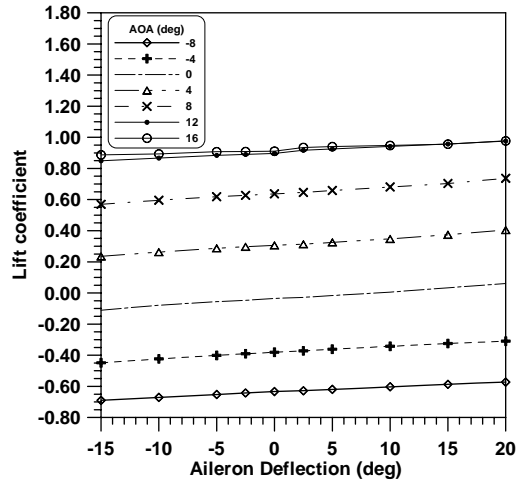
(b) Lift coefficient (positive δ_A)



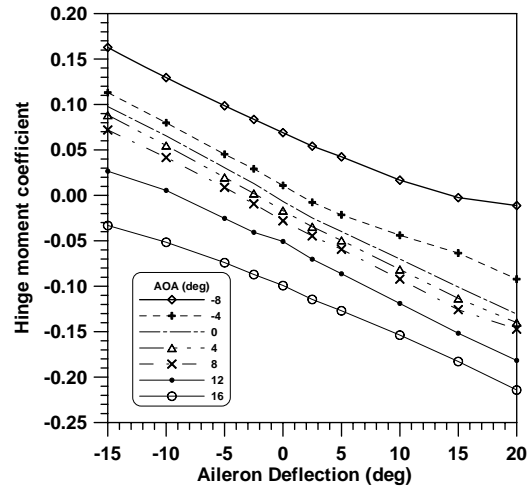
(c) Hinge-moment coefficient (negative δ_A)



(d) Hinge-moment coefficient (positive δ_A)

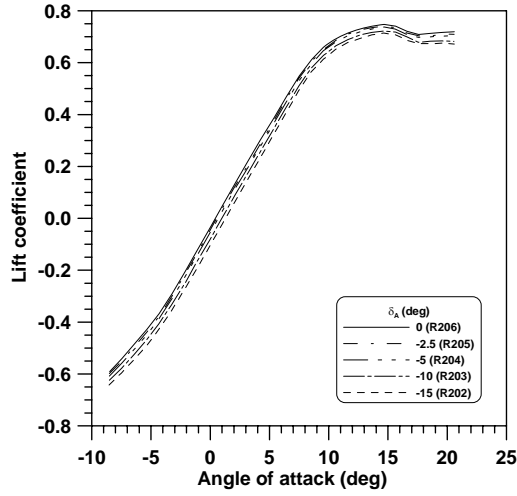


(e) Lift coefficient vs δ_A

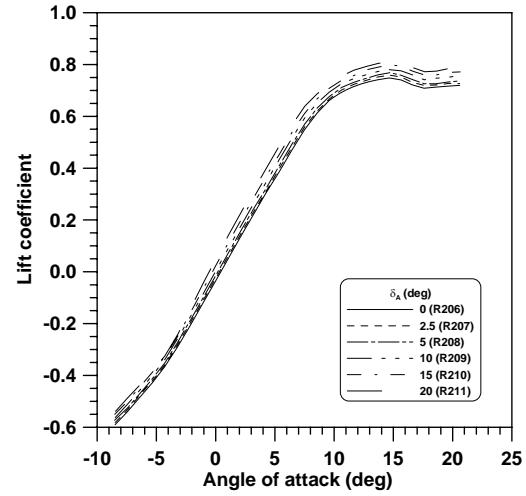


(f) Hinge-moment coefficient vs δ_A

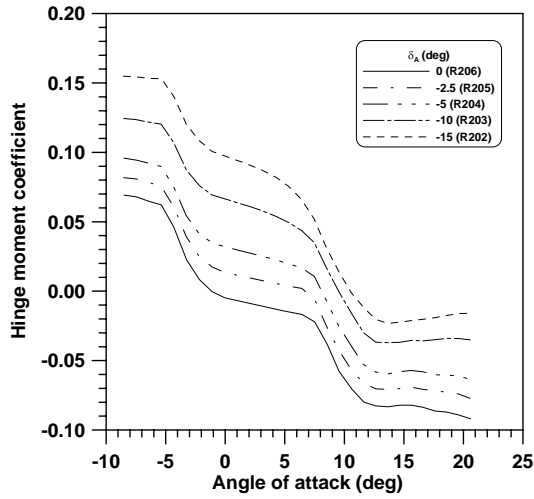
FIGURE F-7. EFFECT OF AILERON DEFLECTION ON LIFT AND HINGE-MOMENT COEFFICIENTS; LS-SC5 (ICING CONDITION 3); $Re = 1.8 \times 10^6$



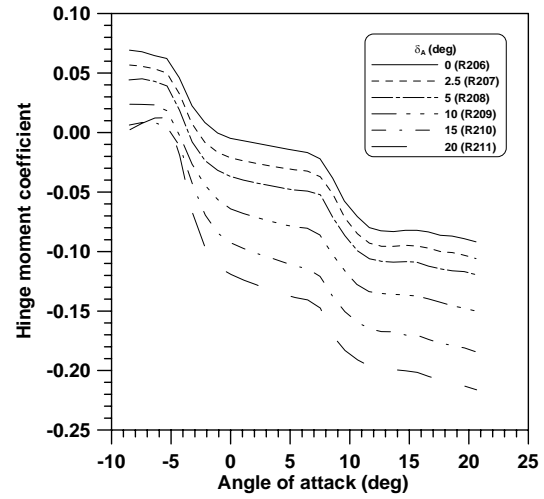
(a) Lift coefficient (negative δ_A)



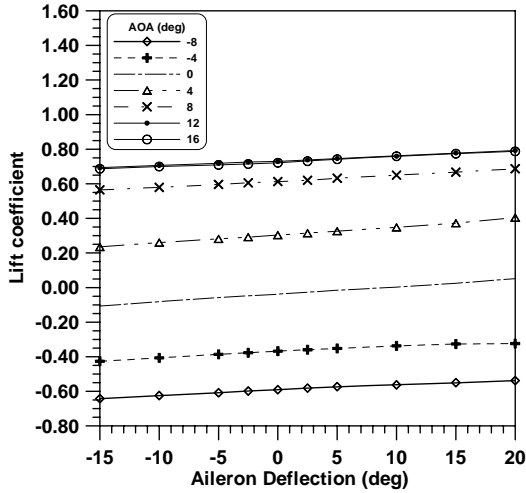
(b) Lift coefficient (positive δ_A)



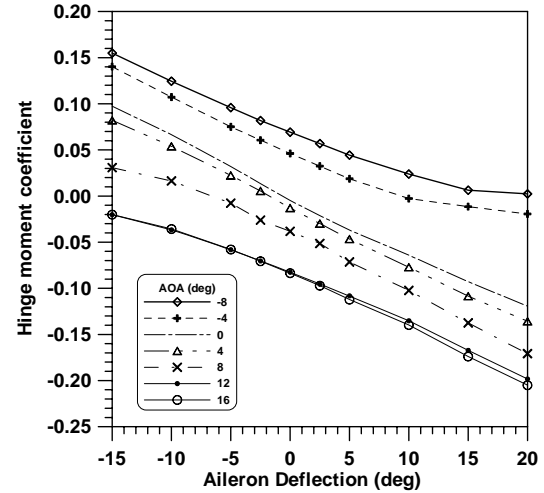
(c) Hinge-moment coefficient (negative δ_A)



(d) Hinge-moment coefficient (positive δ_A)

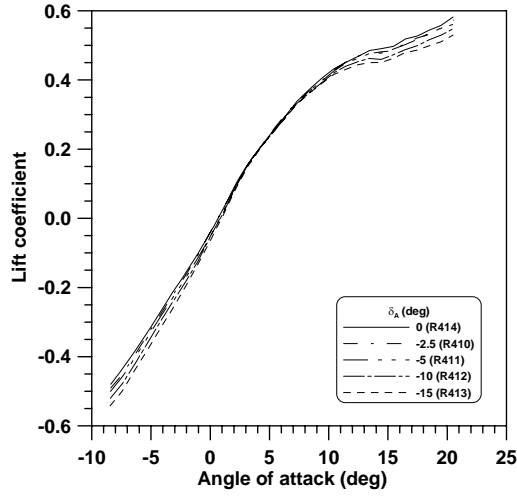


(e) Lift coefficient vs δ_A

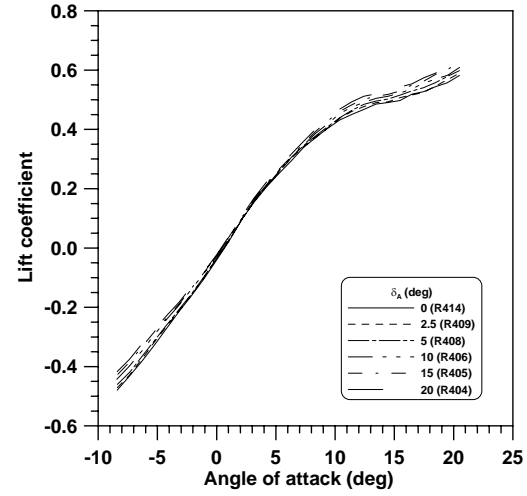


(f) Hinge-moment coefficient vs δ_A

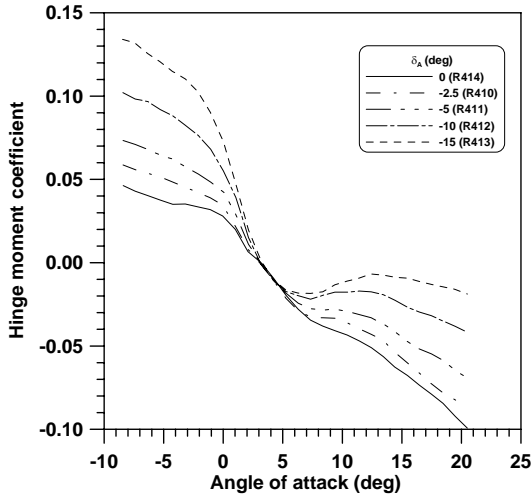
FIGURE F-8. EFFECT OF AILERON DEFLECTION ON LIFT AND HINGE-MOMENT COEFFICIENTS; LS-CS2 (ICING CONDITION 4); $Re = 1.8 \times 10^6$



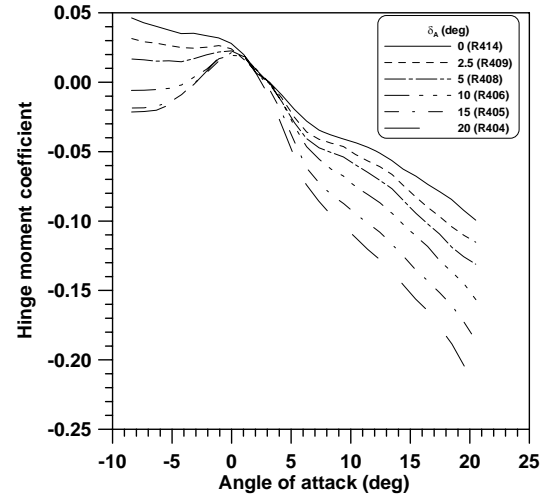
(a) Lift coefficient (negative δ_A)



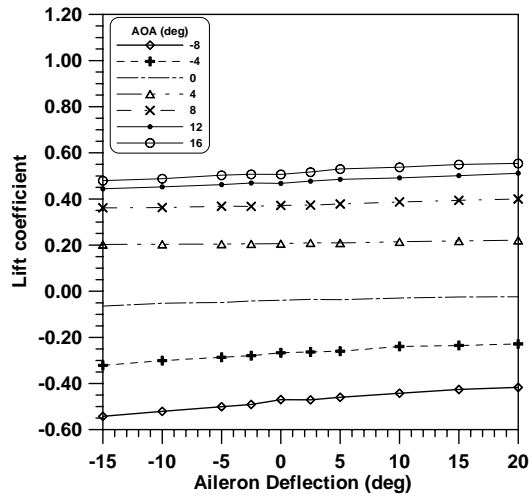
(b) Lift coefficient (positive δ_A)



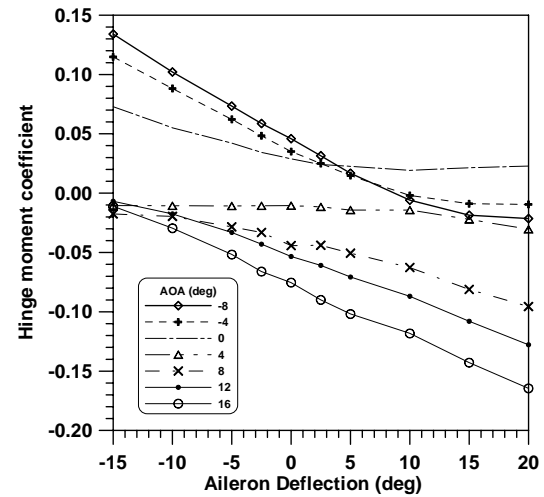
(c) Hinge-moment coefficient (negative δ_A)



(d) Hinge-moment coefficient (positive δ_A)

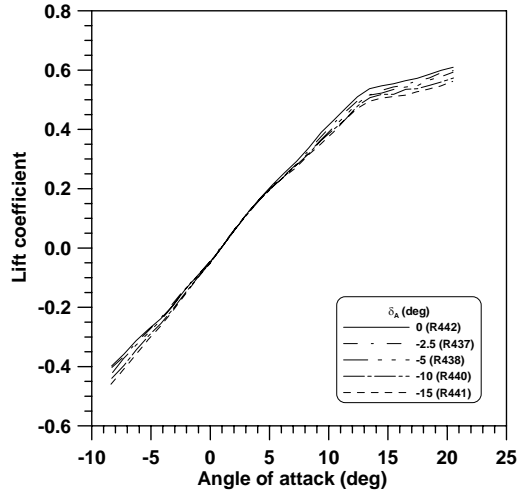


(e) Lift coefficient vs δ_A

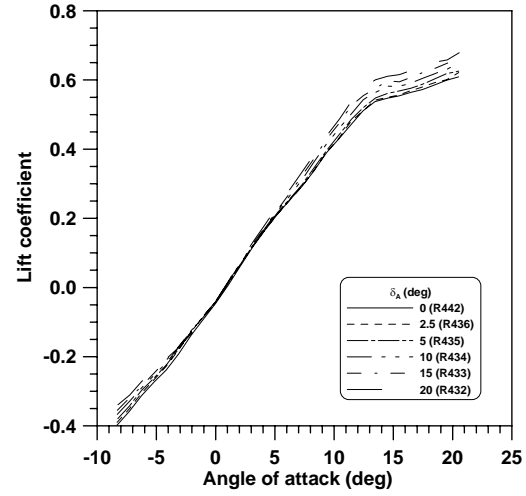


(f) Hinge-moment coefficient vs δ_A

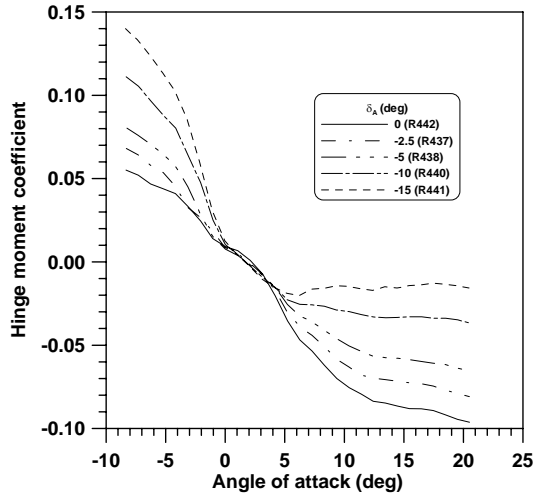
FIGURE F-9. EFFECT OF AILERON DEFLECTION ON LIFT AND HINGE-MOMENT COEFFICIENTS; LS-CS22N (ICING CONDITION 5); $Re = 1.8 \times 10^6$



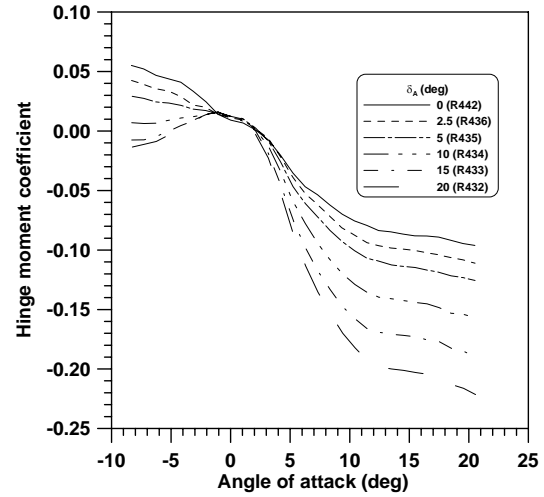
(a) Lift coefficient (negative δ_A)



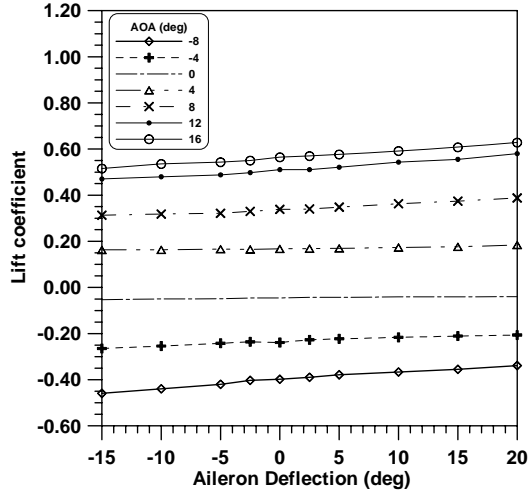
(b) Lift coefficient (positive δ_A)



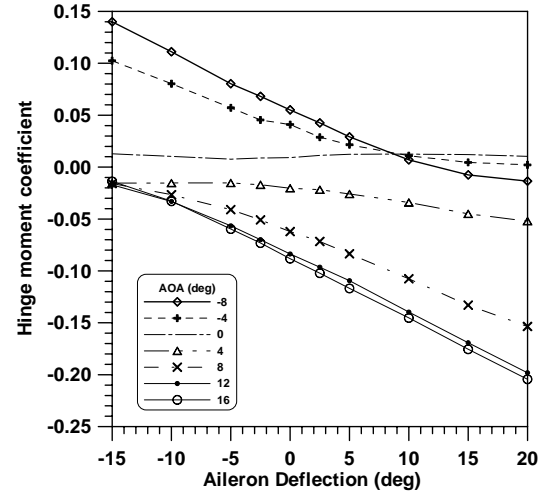
(c) Hinge-moment coefficient (negative δ_A)



(d) Hinge-moment coefficient (positive δ_A)

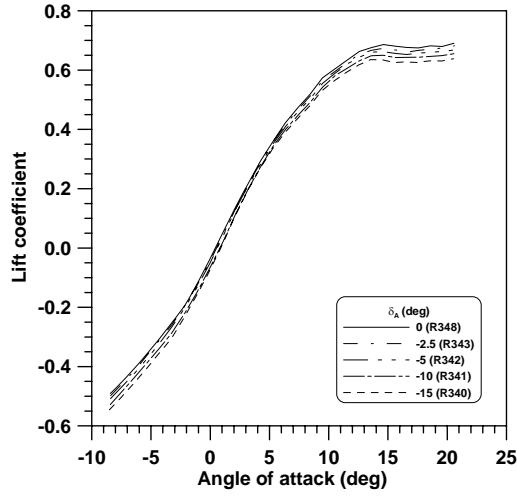


(e) Lift coefficient vs δ_A

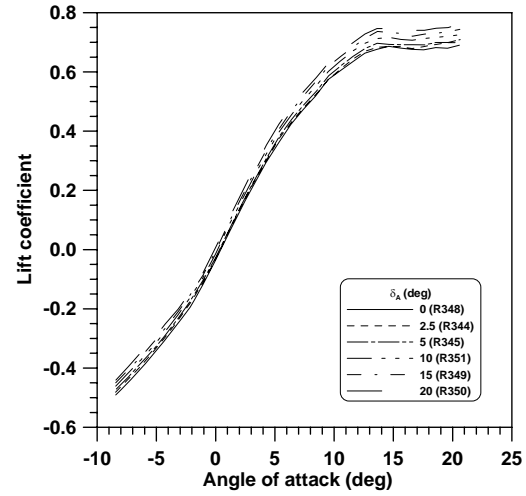


(f) Hinge-moment coefficient vs δ_A

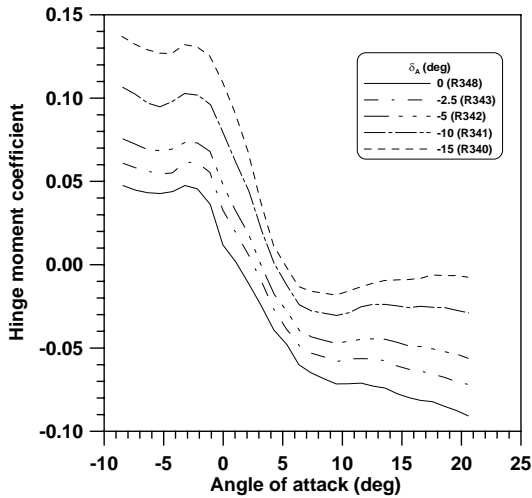
FIGURE F-10. EFFECT OF AILERON DEFLECTION ON LIFT AND HINGE-MOMENT COEFFICIENTS; LS-CS22S (ICING CONDITION 5); $Re = 1.8 \times 10^6$



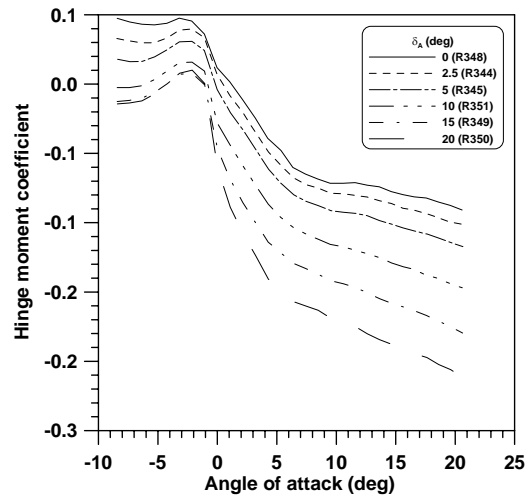
(a) Lift coefficient (negative δ_A)



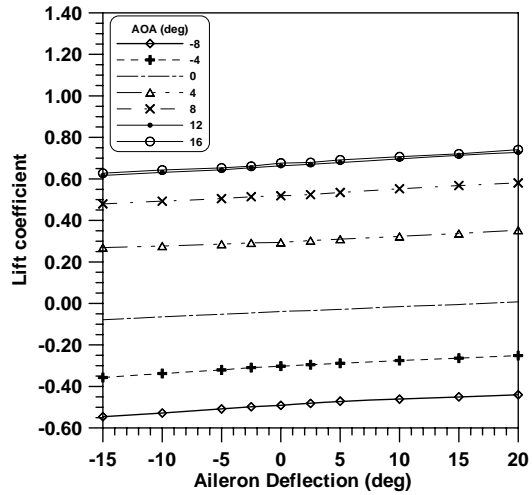
(b) Lift coefficient (positive δ_A)



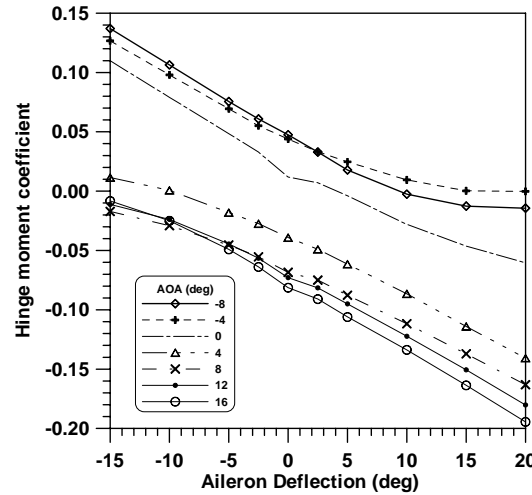
(c) Hinge-moment coefficient (negative δ_A)



(d) Hinge-moment coefficient (positive δ_A)

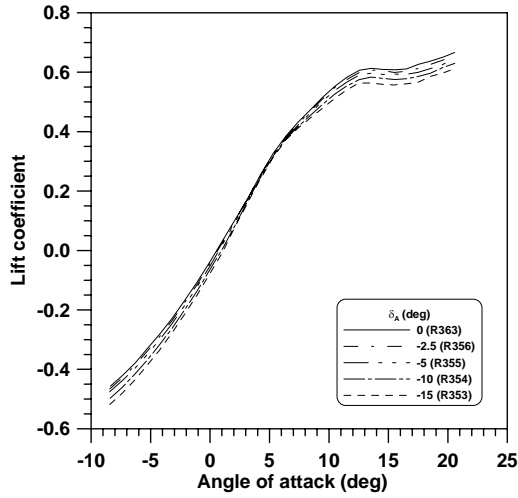


(e) Lift coefficient vs δ_A

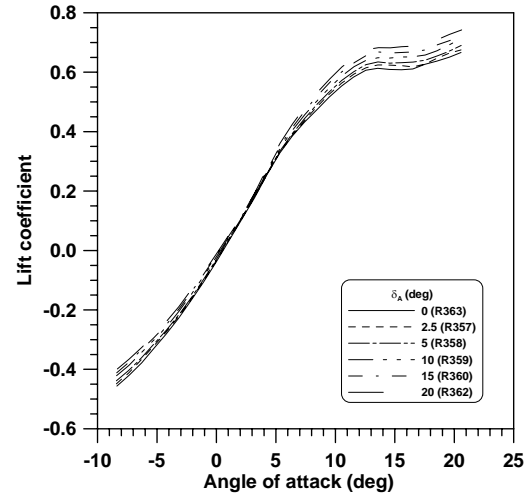


(f) Hinge-moment coefficient vs δ_A

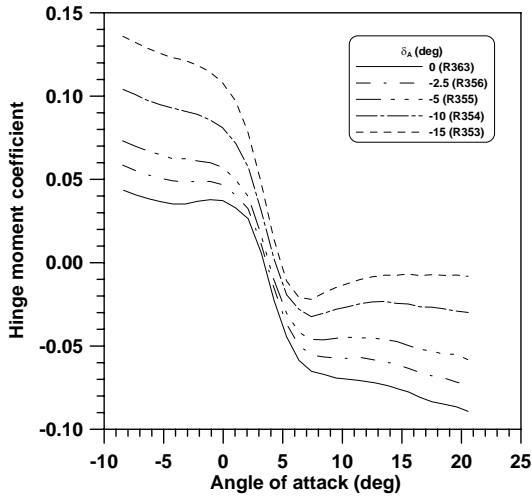
FIGURE F-11. EFFECT OF AILERON DEFLECTION ON LIFT AND HINGE-MOMENT COEFFICIENTS; LS-IPSF22 (ICING CONDITION 6); $Re = 1.8 \times 10^6$



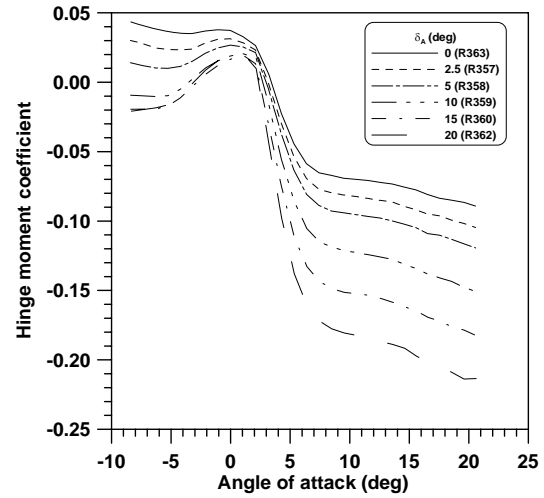
(a) Lift coefficient (negative δ_A)



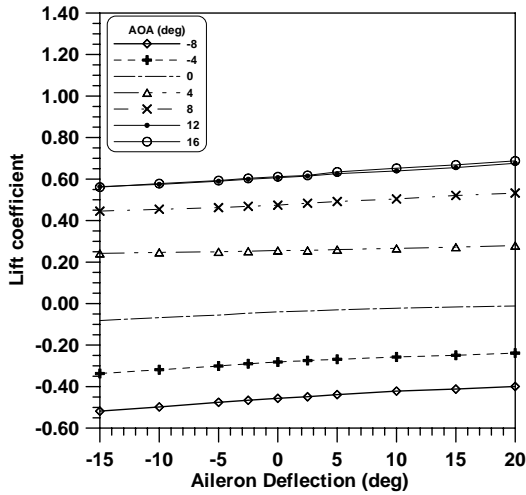
(b) Lift coefficient (positive δ_A)



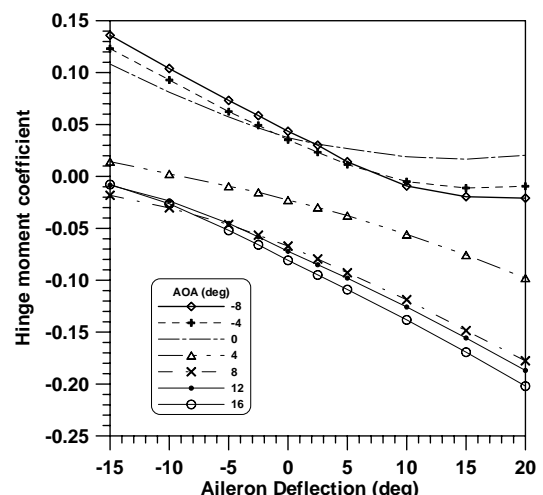
(c) Hinge-moment coefficient (negative δ_A)



(d) Hinge-moment coefficient (positive δ_A)

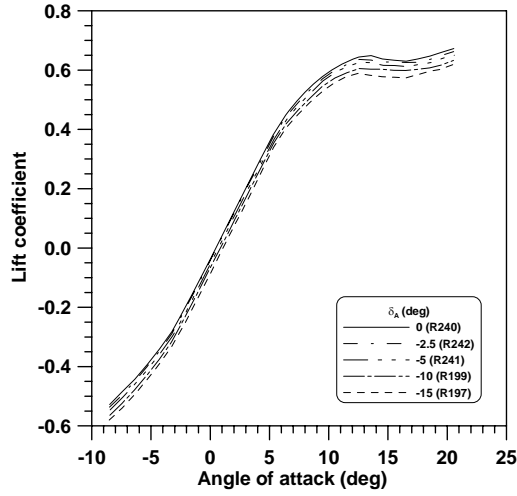


(e) Lift coefficient vs δ_A

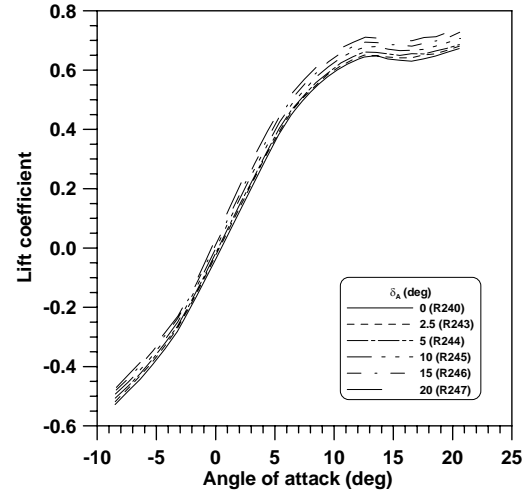


(f) Hinge-moment coefficient vs δ_A

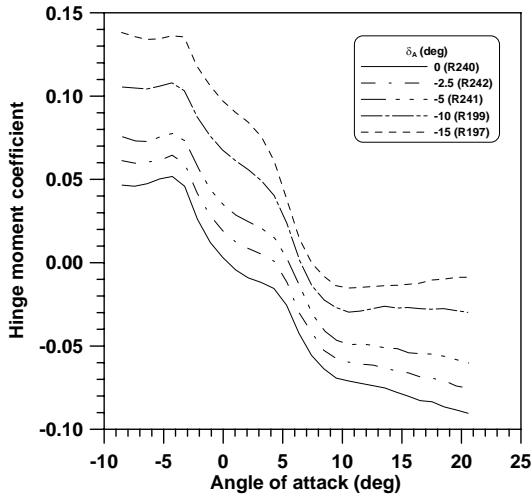
FIGURE F-12. EFFECT OF AILERON DEFLECTION ON LIFT AND HINGE-MOMENT COEFFICIENTS; LR-CS10 (ICING CONDITION 1); $Re = 1.8 \times 10^6$



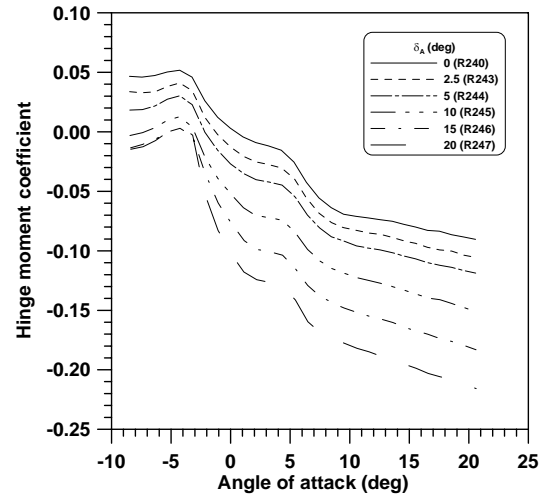
(a) Lift coefficient (negative δ_A)



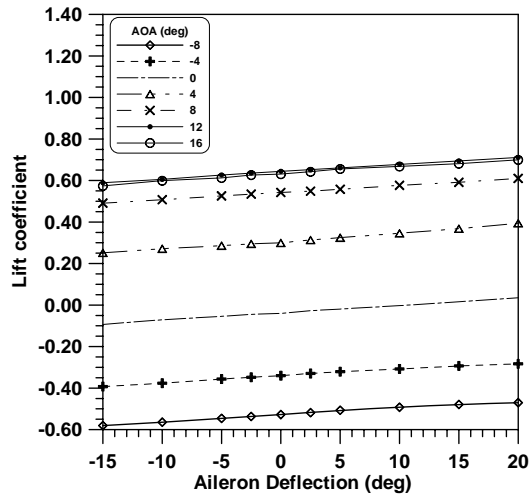
(b) Lift coefficient (positive δ_A)



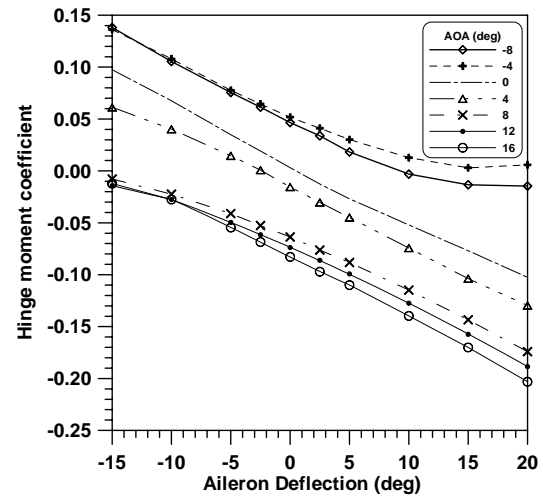
(c) Hinge-moment coefficient (negative δ_A)



(d) Hinge-moment coefficient (positive δ_A)

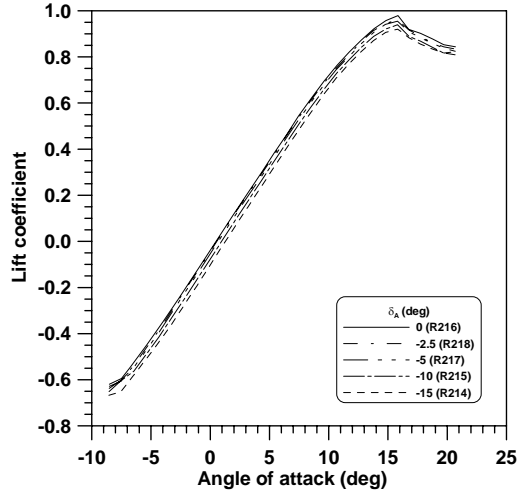


(e) Lift coefficient vs δ_A

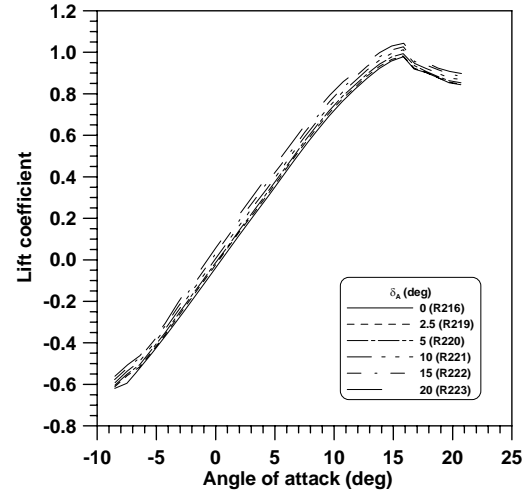


(f) Hinge-moment coefficient vs δ_A

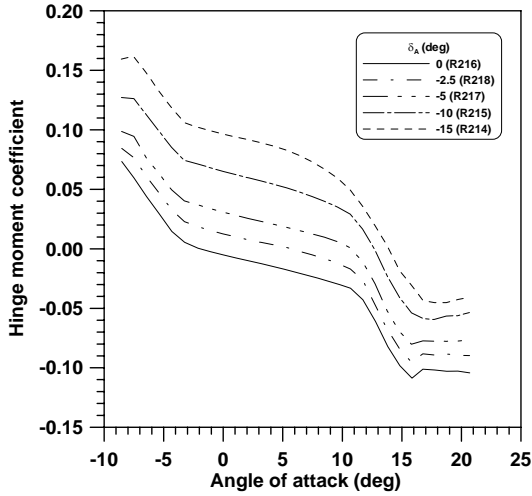
FIGURE F-13. EFFECT OF AILERON DEFLECTION ON LIFT AND HINGE-MOMENT COEFFICIENTS; LR-IS10 (ICING CONDITION 2); $Re = 1.8 \times 10^6$



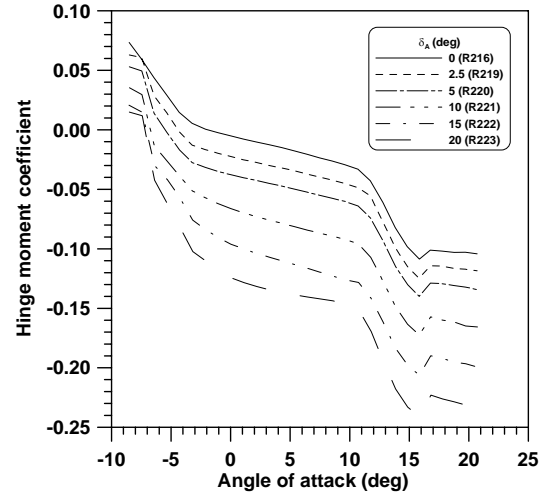
(a) Lift coefficient (negative δ_A)



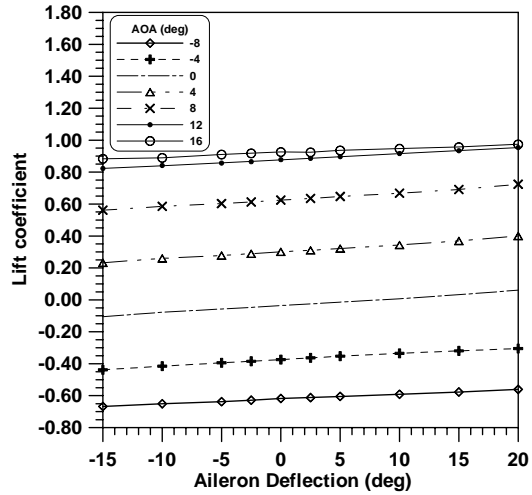
(b) Lift coefficient (positive δ_A)



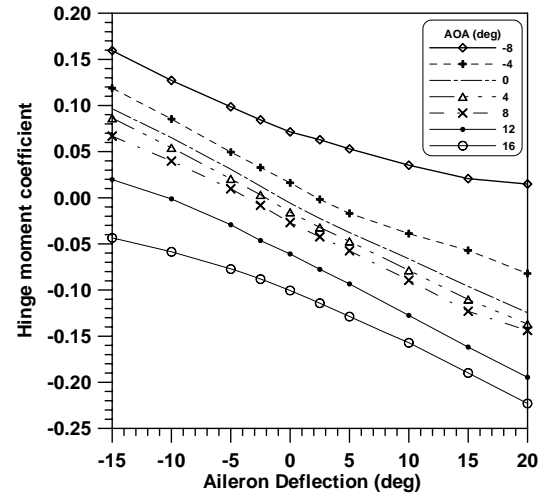
(c) Hinge-moment coefficient (negative δ_A)



(d) Hinge-moment coefficient (positive δ_A)

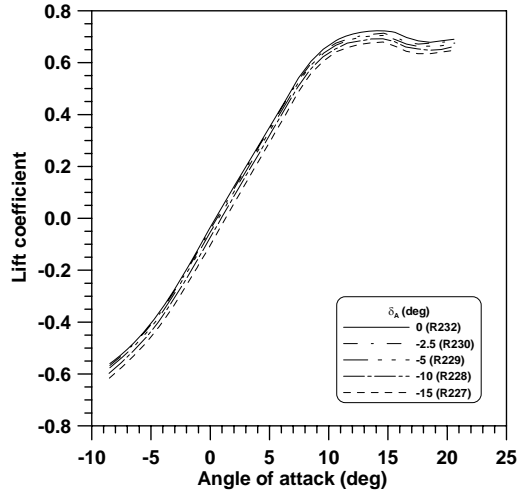


(e) Lift coefficient vs δ_A

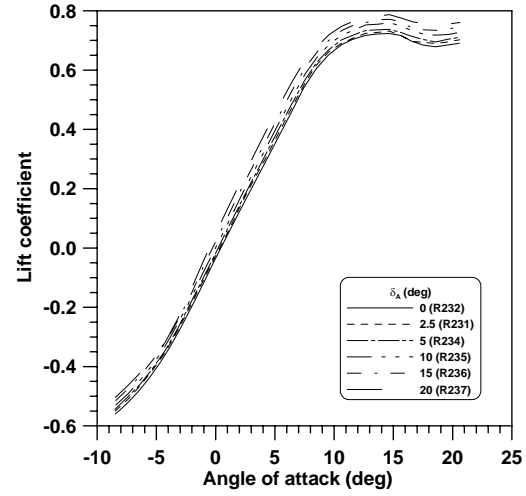


(f) Hinge-moment coefficient vs δ_A

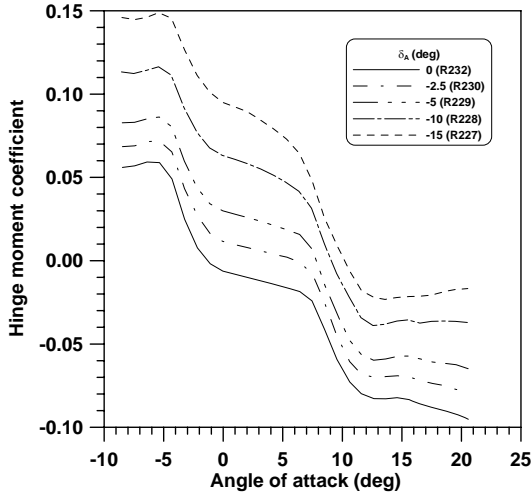
FIGURE F-14. EFFECT OF AILERON DEFLECTION ON LIFT AND HINGE-MOMENT COEFFICIENTS; LR-SC5 (ICING CONDITION 3); $Re = 1.8 \times 10^6$



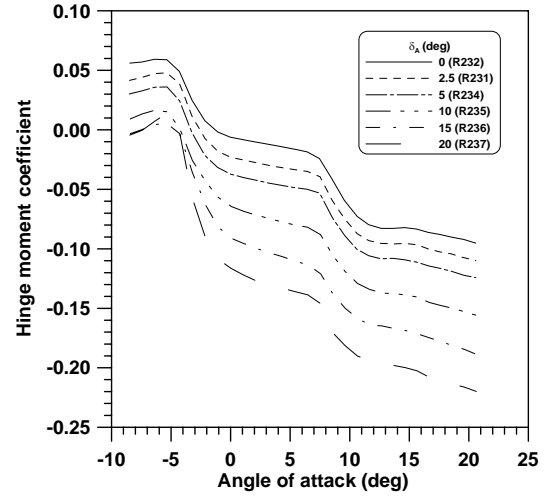
(a) Lift coefficient (negative δ_A)



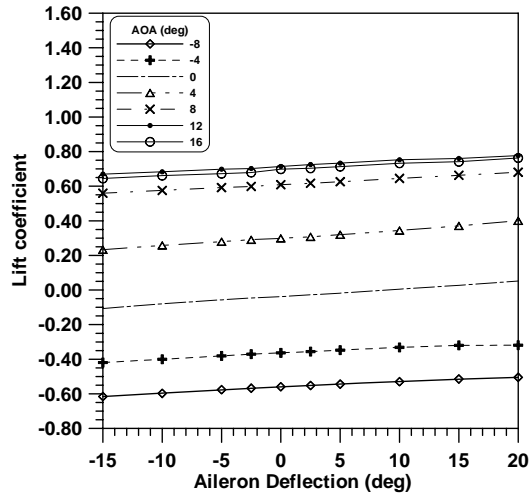
(b) Lift coefficient (positive δ_A)



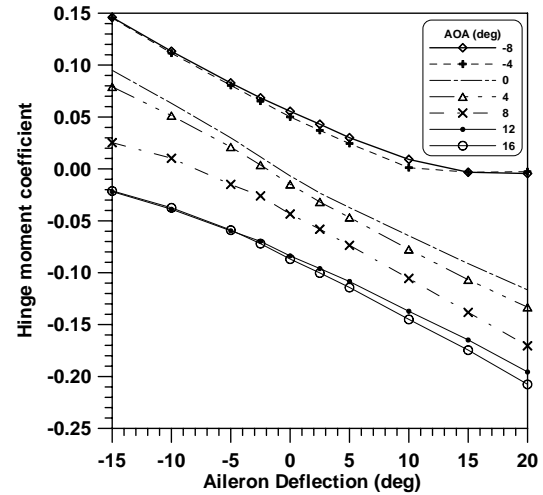
(c) Hinge-moment coefficient (negative δ_A)



(d) Hinge-moment coefficient (positive δ_A)

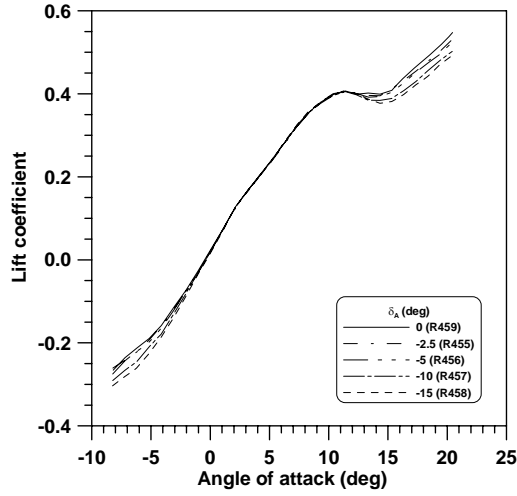


(e) Lift coefficient vs δ_A

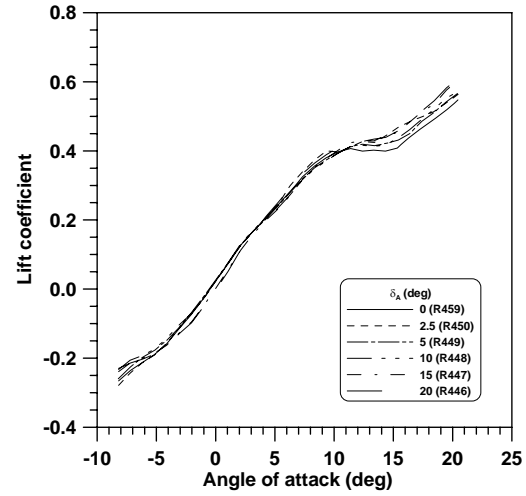


(f) Hinge-moment coefficient vs δ_A

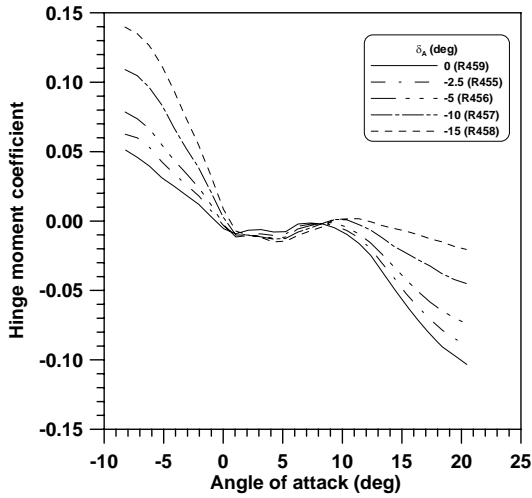
FIGURE F-15. EFFECT OF AILERON DEFLECTION ON LIFT AND HINGE-MOMENT COEFFICIENTS; LR-CS2 (ICING CONDITION 4); $Re = 1.8 \times 10^6$



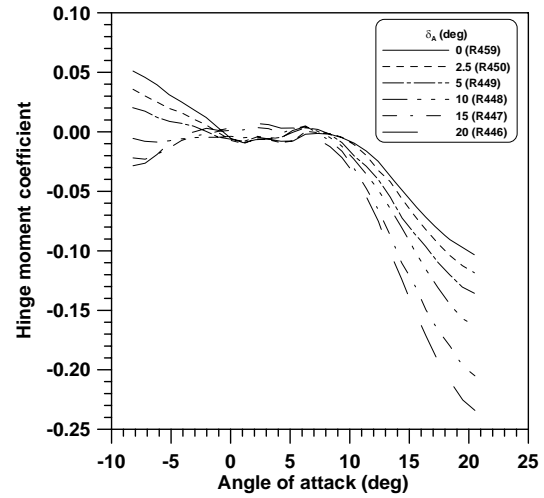
(a) Lift coefficient (negative δ_A)



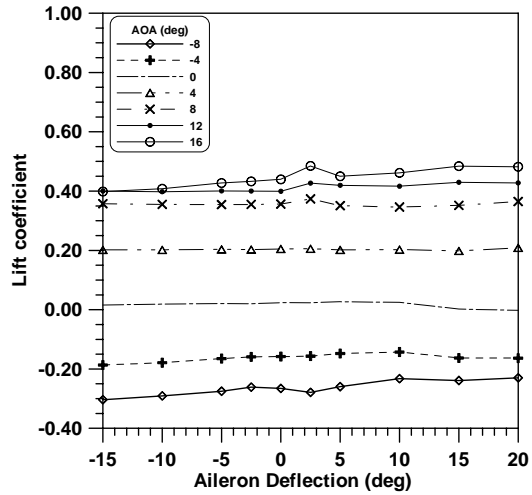
(b) Lift coefficient (positive δ_A)



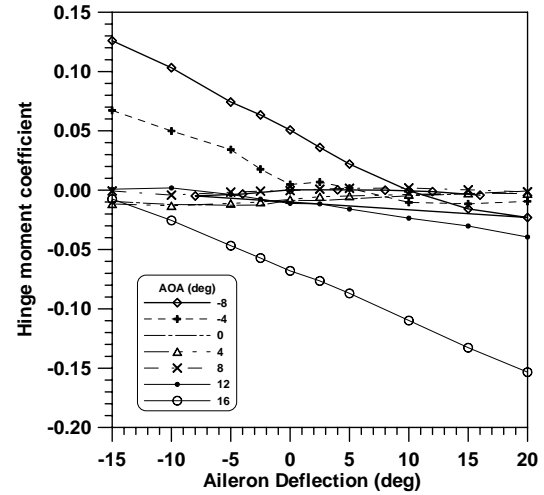
(c) Hinge-moment coefficient (negative δ_A)



(d) Hinge-moment coefficient (positive δ_A)

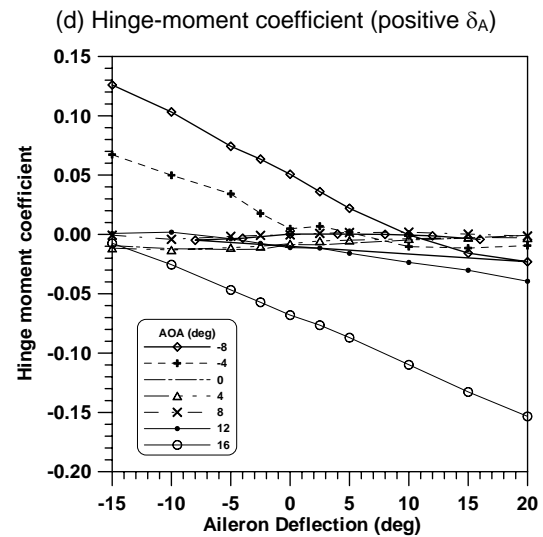
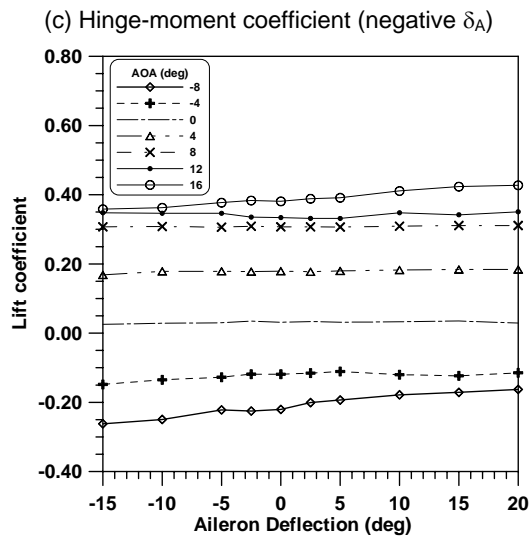
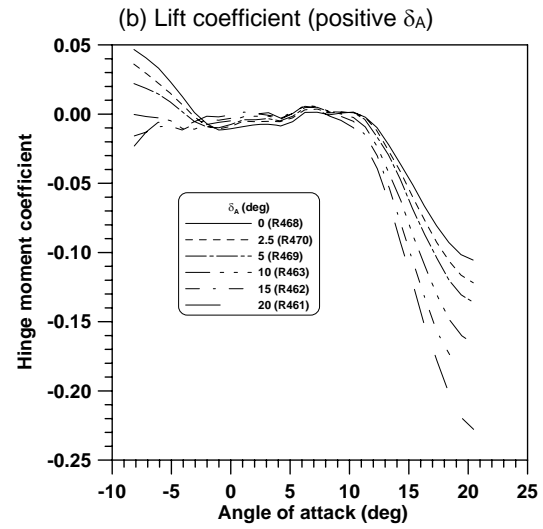
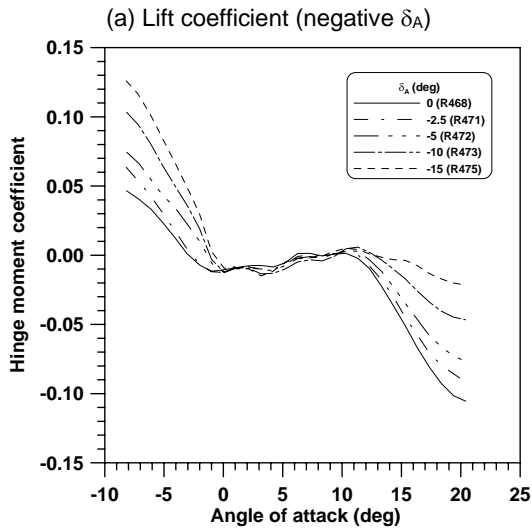
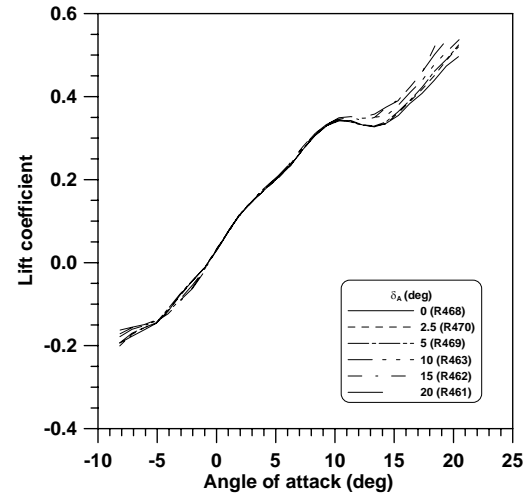
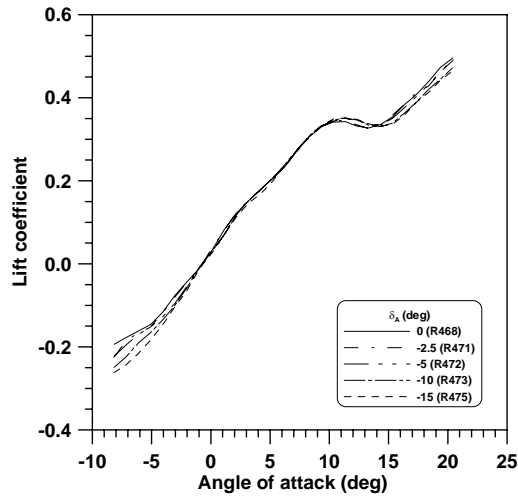


(e) Lift coefficient vs δ_A



(f) Hinge-moment coefficient vs δ_A

FIGURE F-16. EFFECT OF AILERON DEFLECTION ON LIFT AND HINGE-MOMENT COEFFICIENTS; LR-CS22N (ICING CONDITION 5); $Re = 1.8 \times 10^6$



(e) Lift coefficient vs δ_A

(f) Hinge-moment coefficient vs δ_A

FIGURE F-17. EFFECT OF AILERON DEFLECTION ON LIFT AND HINGE-MOMENT COEFFICIENTS; LR-CS22S (ICING CONDITION 5); $Re = 1.8 \times 10^6$

APPENDIX G—COMPUTATION OF LEWICE ICE SHAPE PROFILES

The ice accretion code used in this study is LEWICE v2.0 [G-1], developed by NASA Glenn Research Center. LEWICE is commonly used in the industry to determine ice shape profiles, water droplet impingement patterns, water or ice mass flux, and chordwise extent of ice growth on the body of interest. Due to the physical modeling and computational methods employed in the software, LEWICE executes very rapidly and thus can be used to perform extensive analysis as long as the assumptions inherent in the software are not violated. This software uses the clean body geometry along with the aerodynamic and meteorological conditions to compute an ice shape. The output of the software is a 2-dimensional (2D) ice shape profile that can be calculated for several locations along the span of the wing. The approach taken in this work was to calculate ice shapes at five locations along the span of the 3-dimensional (3D) wing and then construct a full 3D ice shape by lofting between sections. The five locations selected for the ice shape computations were 0% (wing root), 15%, 50%, 85%, and 100% (wing tip) semispan.

In order to use the 2D calculation for construction of the ice shape, adjustments were made to account for the 3D flow effects and how these effects impact the droplet trajectory, heat transfer, and ice growth calculations. From the work of Dorsch and Brun [G-2], the calculation of droplet impingement on a swept wing can be performed by taking a cross-section normal to the leading edge and adjusting the velocity by use of the following expression:

$$V_n = V_\infty \cos \Lambda \quad (G-1)$$

where V_n is the velocity in the plane normal to wing leading edge.

In addition to this velocity adjustment, α was modified to match the pressure profile at the leading-edge region as determined from a 3D Navier-Stokes calculation of pressures over the entire wing surface.

The 3D Navier-Stokes computations were performed at Wichita State University with the clean wing. In the computations, the NASA Glenn Icing Research Tunnel (IRT) walls were included to simulate the tunnel wall effects on the wing flow field. The α used in the analysis were 4° and 6° , to match the geometric angles of attack in the icing tests. Analysis pressures for streamwise sections at 15%, 50%, and 85% semispan were compared with experimental pressures distributions obtained in the IRT facility. Good correlation between experiment and analysis was demonstrated. From the computed flow fields, pressure distributions were obtained for the four wing sections normal to the wing leading edge (at 15%, 50%, and 85% semispan, and wing tip) and for the streamwise section at the wing root.

The two adjustments described above allow the velocity and pressure profile of the 2D calculation to be similar to those of the actual 3D flow. An alternative method to matching the pressure profile is to change the angle of attack in the 2D calculations so that the lift of the airfoil is equal to the lift of the wing at the cross section of interest or to simply adjust the angle of attack geometrically. These approaches were not attempted for this investigation; rather, the former method was employed throughout the study.

The exception to this approach was the calculation of the ice shape at the root of the wing. In that location, a section cut perpendicular to the leading edge would intersect the floor of the tunnel. In addition, the airflow in that region was affected by the presence of the tunnel floor. Flow visualization suggests that the flow was parallel to the tunnel walls. As such, the LEWICE calculation for the root section was performed using the geometry corresponding to a cross-sectional cut parallel to the tunnel walls.

The temperature input for the LEWICE software was also adjusted to approximate the conditions present on the actual wing model. LEWICE requires the static temperature of the free stream as input. Since the input velocity was reduced, as indicated in equation G-1, the resulting total temperature profile for the airfoil would be reduced by an amount approximately equal to

$$\frac{V_{\infty}^2 - V_n^2}{2C_p} \quad (\text{G-2})$$

where C_p is the specific heat of air.

Thus, the input free-stream static temperature was modified such that the free-stream total temperature matched that of the 3D flow. The expression used to make this adjustment is provided in equation G-3.

$$T_{s,n} = T_{s,f} + \frac{V_{\infty}^2}{2C_p} \sin^2 \Lambda \quad (\text{G-3})$$

where $T_{s,n}$ and $T_{s,f}$ are the static temperature in the plane normal to wing leading edge and free-stream plane, respectively.

In summary, the aerodynamic and icing conditions input for LEWICE analyses to generate the seven LEWICE ice shapes are documented in table G-1.

REFERENCES

- G-1. Wright, W.B., "User Manual for the NASA Glen Ice Accretion Code LEWICE (Version 2.0)," NASA CR-1999-2094009, September 1999.
- G-2. Dorsch, R.G. and Brun, R.J., "A Method for Determining Cloud-Droplet Impingement on Swept Wings," NACA TN 2931, April 1953.

TABLE G-1. FLOW AND ICING CONDITIONS INPUT FOR LEWICE ICE SHAPES

Ice Shape	LWC (g/m ³)	MVD (μm)	τ (min)	RH (%)	P _{static} (N/m ²)	T _{static} (K)	Spanwise Section	C (m)	V (m/s)	α (deg)
LS-CS10	0.68	20.0	10.0	100	100000	263	Root	0.640	111.76	4.0
							15%	0.572	98.678	2.8
							50%	0.440	98.678	2.2
							85%	0.308	98.678	0.6
							Tip	0.257	98.678	0.6
LS-IS10	0.65	20.0	10.0	100	100000	263	Root	0.640	67.056	4.0
							15%	0.572	59.207	2.8
							50%	0.440	59.207	2.2
							85%	0.308	59.207	0.6
							Tip	0.257	59.207	0.6
LS-SC5	0.51	14.5	5.0	100	100000	263	Root	0.640	89.989	4.0
							15%	0.572	79.456	2.8
							50%	0.440	79.456	2.2
							85%	0.308	79.456	0.6
							Tip	0.257	79.456	0.6
LS-CS2	0.68	20.0	2.0	100	100000	263	Root	0.640	111.76	4.0
							15%	0.572	98.678	2.8
							50%	0.440	98.678	2.2
							85%	0.308	98.678	0.6
							Tip	0.257	98.678	0.6
LS-CS22N	0.68	20.0	22.5	100	100000	263	Root	0.640	111.76	4.0
							15%	0.572	98.678	2.8
							50%	0.440	98.678	2.2
							85%	0.308	98.678	0.6
							Tip	0.257	98.678	0.6
LS-CS22S	0.68	20.0	22.5	100	100000	263	Root	0.640	111.76	4.0
							15%	0.580	111.76	2.8
							50%	0.448	111.76	2.2
							85%	0.314	111.76	0.6
							Tip	0.257	111.76	0.6
LS-IPSF22	0.46	20.0	22.5	100	100000	263	Root	0.640	67.056	4.0
							15%	0.572	59.207	2.8
							50%	0.440	59.207	2.2
							85%	0.308	59.207	0.6
							Tip	0.257	59.207	0.6

APPENDIX H—COMPARISON OF TWO- AND THREE-DIMENSIONAL WING ICE SHAPE TRACES AND LIFT DATA

H.1 COMPARISON OF TWO- AND THREE-DIMENSIONAL ICE SHAPES.

The icing conditions for ice shape IRT-SC5, listed in tables 2-1 and 2-2 of this report, were obtained by scaling the conditions used in an ice accretion test conducted with a two-dimensional (2D) 36-inch chord GLC-305 airfoil [H-1].

The scale conditions were determined using the Ruff method [H-2] for sea level testing with constant velocity. This method was developed for scaling 2D models to permit simulating a larger model by testing a smaller model, or to permit testing at one set of test conditions to simulate conditions that were not attainable in the facility being used. For either simulation, the objective is to produce a scaled ice shape that simulates the reference shape; in fact, when normalized by the model chord, the two shapes should match in overall size and in locations and size of individual features. The Ruff method matches scale and reference values of those nondimensional similarity parameters that have been demonstrated to have the strongest influence on the ice accretion quantity and shape. The dimensionless similarity parameters include the modified inertia parameter, K_0 , which relates to the droplet trajectories; the accumulation parameter, A_c , which is a measure of the quantity of ice that can potentially accrete on the model; and the freezing fraction, n_0 , which is the proportion of water impinging at stagnation that actually freezes. Another energy parameter that can be used is the water energy transfer parameter, ϕ . This parameter has units of temperature and collects all the terms in the energy balance that relate to energy carried to the surface by water drops. For rime ice, it is convenient and acceptable to set the scale velocity equal to the reference, although other methods of finding scale velocity have been shown to give better results for glaze ice. The five equations formed by matching the scale and reference values of the three nondimensional similarity parameters, plus the water energy parameter and the velocity can be solved to find the scale test conditions.

The method outlined in the previous paragraph has only been validated to scale 2D (straight wing) models. There have been no studies of 2D to three-dimensional (3D) (swept wing) scaling, and a crucial question is how valid are the 2D parameters, some of which apply only to the stagnation line, might be for swept wings. However, scaling between two geometrically similar swept wing models of different size was studied by ONERA [H-3 and H-4] by applying most of the same similarity parameters that Ruff later used. Although direct comparisons of scale and reference ice shapes were not possible, photographs suggested that quantities and features of the reference accretions were simulated well by the scale tests. These results provided some encouragement that the Ruff method might be valid for 2D to 3D scaling. To test this possibility in a very limited way, the present study included rime tests with a 2D model as a reference and compared those ice shapes with ones from a 3D model at scaled conditions.

The strategy was to apply the Ruff scaling calculations outlined above using rime tests with a 36-in chord, 2D GLC-305 model as the reference. The scale model was to have the same airfoil form as the reference but with a chord of 17.4 inches. Rime ice, even for swept wings, has a fairly simple shape, lacking the 3D scallops of swept wing glaze. Therefore, the assumption was that rime ice accretions would be no different whether on a 17.4-in chord 2D airfoil or on a 3D

airfoil with a mean aerodynamic chord (MAC) of 17.4 inches, at least at the MAC. The leading edge radius for the GLC-305 airfoils was taken to be $0.0134c$, where c is the chord. The reference conditions and resulting scale conditions are shown in the following table:

	c (in)	V (mph)	α (deg)	T_{total} (°F)	MVD (μm)	LWC (g/m^3)	Time (minutes)	β_0 (%)	$\beta_0 A_c$
Reference	36.0	201.3	6	11.7	20.0	0.40	16.7	66.3	1.065
Scaled	17.4	201.3	6	11.7	12.8	0.58	5.6	66.3	1.065

The relative thickness of ice accreted at the leading edge is proportional to the product of three parameters: the collection efficiency at stagnation, β_0 , the accumulation parameter, A_c , and the stagnation freezing fraction, n_0 . Thus, for rime ice (n_0 of 1), the product $\beta_0 A_c$ gives a measure of the relative size of the ice accretions. Note that for proper scaling, this product must match between scale and reference. Other similarity parameters are not important for rime scaling.

Some adjustments to the calculated scale conditions were necessary. First, because the scale drop size determined by the Ruff method was smaller than the minimum value for which the icing research tunnel (IRT) cloud was calibrated (14.5 μm), the minimum median volumetric diameter (MVD) for the IRT had to be substituted. For a straight wing, this increase in drop size would result in a stagnation collection efficiency about 6% higher than the reference. For the swept wing, the assumption was made that the change would have the same proportional effect as that for the straight wing. Thus, the second adjustment was to reduce the spray time from 5.6 to 5 minutes to compensate for the increased collection efficiency. Then the revised scale conditions were:

	c (in)	V (mph)	α (deg)	T_{total} (°F)	MVD (μm)	LWC (g/m^3)	Time (minutes)	β_0 (%)	$\beta_0 A_c$
Reference	36.0	201.3	6	11.7	20.0	0.40	16.7	66.3	1.065
Scaled	17.4	201.3	6	11.7	14.5	0.58	5.0	70.2	1.003

Although the scaling calculations were made using a chord of 17.4 inches, the icing tests were actually performed with a swept GLC-305 airfoil with a MAC of 18.72 inches. Both the collection efficiency and accumulation parameter are dependent on chord. The local chord at which icing traces were made also varied with spanwise location; therefore, the scale test conditions shown above were valid only for one location. In addition to the change in MAC, the liquid water content (LWC) actually tested was not the value desired due to an error in the IRT calibration discovered after the completion of tests. Thus, while the spray bar conditions were set to give an LWC of $0.58 \text{ g}/\text{m}^3$, as recommended from the scale calculations, the actual value is believed to have been $0.51 \text{ g}/\text{m}^3$.

Figure H-1 compares a trace of the ice shape obtained from the icing tests with the 2D GLC-305 with three traces of the ice shape obtained from the 3D swept wing icing tests at the NASA Glenn IRT facility. The traces of the 3D ice shape were obtained at wing stations A, B, and C, as shown in figure 2-5 of this report. The ice traces at stations A and B were taken normal to the

swept wing leading edge, while the trace at station C was taken in the streamwise direction. As discussed in the main body of this report, the swept wing had a GLC-305 airfoil section that was in the streamwise direction. Thus, sections taken normal to the leading edge of the swept wing were slightly thicker than the streamwise GLC-305 section and had a chord length that was approximately 99% of the streamwise airfoil chord length. The airfoil and ice traces presented in figure H-1 have been normalized with the normal or streamwise chord of each airfoil section. These nondimensional tracings show good agreement between the 2D trace and that of cut A of the swept wing, but the relative quantity of ice for cuts B and C are far less than that for the 2D trace. The following table shows the relevant similarity parameters for the conditions actually tested at the MAC and at each of the tracing locations:

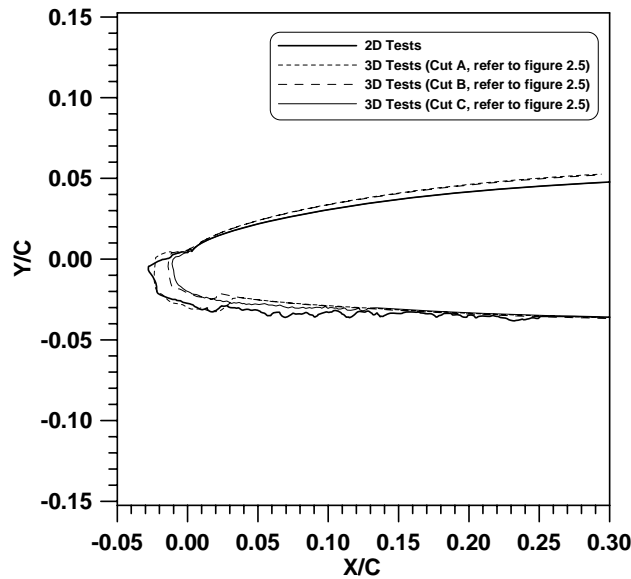


FIGURE H-1. COMPARISON OF THE ICE SHAPES FOR THE 2D AND 3D MODELS

	c (in)	V (mph)	α (deg)	T_{total} (°F)	MVD (μm)	LWC (g/m^3)	Time (minutes)	β_0 (%)	$\beta_0 A_c$
Reference	36.00	201.3	6	11.7	20.0	0.40	16.7	66.3	1.065
Scaled (MAC)	18.72	201.3	6	11.7	14.5	0.51	5.0	68.9	0.811
Scaled (Cut A)	13.80	201.3	6	11.7	14.5	0.51	5.0	74.1	1.182
Scaled (Cut B)	19.30	201.3	6	11.7	14.5	0.51	5.0	68.3	0.781
Scaled (Cut C)	25.10	201.3	6	11.7	14.5	0.51	5.0	63.2	0.555

Note that the scale value of $\beta_0 A_c$ is only close to the reference at cut A, where the scale and reference are within 11%. The parameter A_c is directly proportional to LWC, and the uncertainty in the LWC calibration for the IRT is generally quoted as $\pm 10\%$, so these numbers are reasonably close. The good agreement of the ice tracings for the 2D and 3D at cut A is, therefore, consistent with the $\beta_0 A_c$ value there, and this result shows that for this rime case, at least, it is possible to scale effectively from 2D to 3D. The much smaller scale shapes at cuts B and C are predicted by the significantly lower $\beta_0 A_c$ values at those locations.

Although the results for nearly matched $\beta_0 A_c$ were encouraging, the tests were very limited in scope, including only rime ice at one set of reference conditions. For glaze ice, the scallop formation on swept wings of large sweep angles makes a direct comparison with 2D ice shapes impossible. However, additional tests for glaze ice at several freezing fractions are encouraged to determine if useful similarities in 2D and 3D shapes can be identified. For future tests, it should also be recognized that the matching of reference and scale similarity parameters applies only at one swept wing spanwise location.

H.2 COMPARISON OF 2D AND 3D CLEAN AND ICED WING AERODYNAMIC PERFORMANCE.

In this section, the aerodynamic lift performance of the clean and iced GLC-305 2D wing model presented in reference H-1 is compared with the lift performance of the clean and iced GLC-305 3D wing presented in the main body of this report. The 2D and 3D iced wing configurations considered below are the ones presented in figure H-1. The aerodynamic performance comparisons will be limited to linear lift slope and maximum lift coefficient.

In comparing the aerodynamic performance of the two wing models, the following differences in model geometry and flow-field behavior should be considered:

- Model size and geometric features. The 2D model was a straight infinite span planar wing with a chord of 36 inches. The 3D model was a finite span swept wing with geometric twist and taper, and with a MAC of 18.72 inches.
- The lift data for the 2D model were obtained at Reynolds numbers in the range of 3 to 7.5 million compared to the 1.8 million Reynolds number used in the 3D wing tests.
- The flow field about a finite swept wing is three-dimensional and is, therefore, inherently different from 2D flow about an infinite straight wing. Three-dimensional effects include spanwise flow, leading edge and wing tip vortices, downwash effects, and complex separation patterns at high angles of attack as the wing approaches stall. As a result, the stall behavior of the 2D infinite span wing will in general be different from that of the finite span wing with the same airfoil section.
- Aerodynamic performance of finite swept wings depends on aspect ratio (AR), taper ratio (λ), sweep angle (Λ), Reynolds number (Re), wing twist, and potential fuselage/wing interaction effects. Note that the 3D wing was tested with a fuselage like body, as shown in figure 2-18 of this report.

From experimental work and classical aerodynamic theory, a number of simple equations have been developed for relating the lift slope of a straight finite wing to that of a 2D wing with the same airfoil section. For planar untapered swept wings, basic swept wing theory can be applied to correct the lift slope of straight wings for the effects of wing sweep as discussed in reference H-5. Sweep corrections account for the fact that, for swept wings only the velocity component normal to the wing leading edge is responsible for wing lift and surface pressures. The velocity component tangential to the wing leading edge is important only for the

determination of the frictional stresses on the surface. Corrections for sweep effects depend to some extent on the method used to convert a straight wing into a swept wing. In general, sweep is introduced by rotating or by shearing a straight wing. If rotation is applied to sweep the wing (bent-back or yawed wing), then the airfoil section of the unswept wing is the same as the airfoil section normal to the leading edge of the swept wing. A sheared wing is obtained by shearing backward (or forward) every section of the unswept airfoil, leaving its shape and lateral position unchanged. The swept finite GLC-305 wing was obtained by applying the shear method. Thus, the airfoil section of the straight 2D wing and the streamwise section of the swept wing were the same. However, the airfoil section normal to the swept wing leading edge was slightly thicker than that of the standard GLC 305 profile. Note that the simple sweep theory requires the use of the lift data for the airfoil section normal to the wing leading edge. A 2D viscous flow analysis was conducted with the XFOIL code [H-6] to assess the difference in lift performance between the GLC-305 airfoil and the thicker airfoil section normal to the wing leading edge. The results showed that the airfoil normal to the wing leading edge had a slightly higher maximum lift coefficient but in general the lift performance of both airfoils was very similar over the linear lift range. Thus, it was decided to use the baseline GLC-305 lift data in all calculations presented below.

Experimental lift curves for the 2D and 3D clean wing are compared in figure H-2. The main differences between the 2D and 3D wing lift curves include the following:

- Considerably higher lift slope for the 2D wing (i.e., higher lift at a given angle of attack).
- Angle of zero lift is negative for the 2D wing but slightly positive for the 3D wing.
- Maximum lift is considerably greater for the 2D wing.
- Stall behavior for the 2D and 3D wings is considerably different. A gradual stall is observed to take place for the 3D wing compared to a sharp stall for the 2D wing.

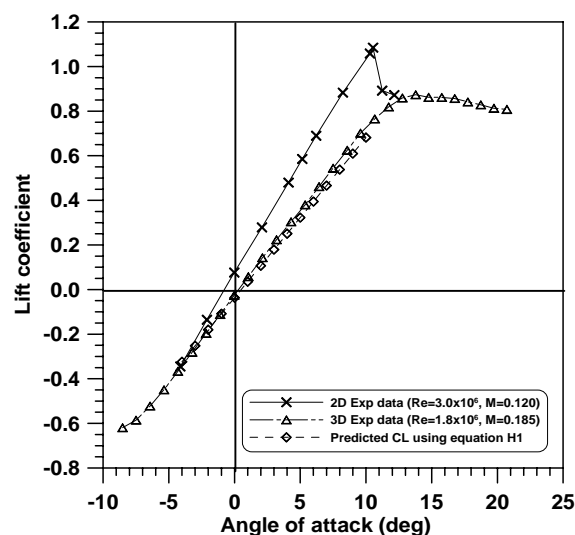


FIGURE H-2. COMPARISON OF LIFT CURVES FOR THE CLEAN 2D AND 3D WINGS

In the following, the lift characteristics of the clean and iced GLC-305 finite wing will be estimated from the lift properties of the clean and iced 2D wing using simple equations developed for swept wings. It should be emphasized that stall behavior cannot be predicted by these simple schemes.

The method used to estimate the finite swept wing lift data from that of the 2D wing was as follows:

- Apply standard sweep, aspect ratio, and compressibility corrections to estimate the 3D wing lift slope.
- Estimate effective twist angle for the 3D wing and use this value to correct the 3D wing geometric angle of attack.
- Estimate the effect of Reynolds number on lift slope using experimental data and a 2D viscous analysis panel code.
- Apply a simple formula to estimate maximum lift for the 3D wing from that of the 2D wing.

Due to downwash and geometric twist effects, the lift curve slope of the 3D swept wing was reduced compared to that of the 2D wing model. Knowing the 2D lift slope (a_0) and the angle of attack for zero lift ($\alpha_{L=0}$), one can predict the lift curve of a finite swept wing from equation H-1 [H-7] which takes sweep angle and aspect ratio into consideration. Note that all lift slopes in equation H-1 are per radian. From reference 24, the 2D slopes (a_0) of the clean and iced wing were 0.0973 and 0.0977 per degree, respectively. Corresponding lift slope values per radian were 5.574 and 5.598. From equation H-1, the lift slopes (CL_α) of the clean and iced finite swept wings were calculated to be 4.114 and 4.127 per radian or 0.0718 and 0.072 per degree, respectively.

$$CL_\alpha = \frac{a_0 \cdot AR}{\left(\frac{a_0}{\pi}\right) + \sqrt{\left(\frac{AR}{\cos \Lambda_{1/2}}\right)^2 + \left(\frac{a_0}{\pi}\right)^2 - (AR \cdot M_\infty)^2}} \quad (H-1)$$

where $AR = 6.8$, $\Lambda_{1/2} = 22^\circ$ and $M_\infty = 0.185$ for the swept finite wing tested.

Typically, planar wings with infinite and finite span and identical airfoil sections have the same angle of zero lift ($\alpha_{L=0}$). The GLC-305 swept wing model, however, had a washout of 4° at the wing tip, which reduced the effective angle of attack of the 3D wing, thus $(\alpha_{L=0})_{3D}$ and $(\alpha_{L=0})_{2D}$ were not the same. For a finite wing with washout, $(\alpha_{L=0})_{3D}$ should be the difference of $(\alpha_{L=0})_{2D}$ and θ_{eff} , where θ_{eff} is the effective angle of twist of the whole wing. Note that at zero lift, the downwash angle generated by a finite wing is practically zero, thus only wing geometric twist causes the 2D and 3D geometric angles of attack to differ. To estimate the effective twist angle of the finite swept wing, the spanwise lift distribution of the 3D wing must be considered. Using

the spanwise lift distribution, the spanwise location, where the wing local lift times the span of the wing is approximately equal to the total lift of the wing (integral under the curve), is determined. From the limited surface pressure data obtained with the 3D wing, an approximate spanwise lift distribution was computed and the data was used to determine the spanwise location corresponding to the effective twist angle. This location was close to the 50% semispan for the angles of attack presented in figure H-3. The geometric twist at the 50% semispan station (θ_{50}) was -1.14° . Thus, the effective twist of the wing at low angles of attack was -1.14° . Therefore, the difference between the 2D and 3D geometric angles of attack at zero lift was 1.14° (the 3D angle of attack was 1.14° higher than the 2D geometric angle of attack).

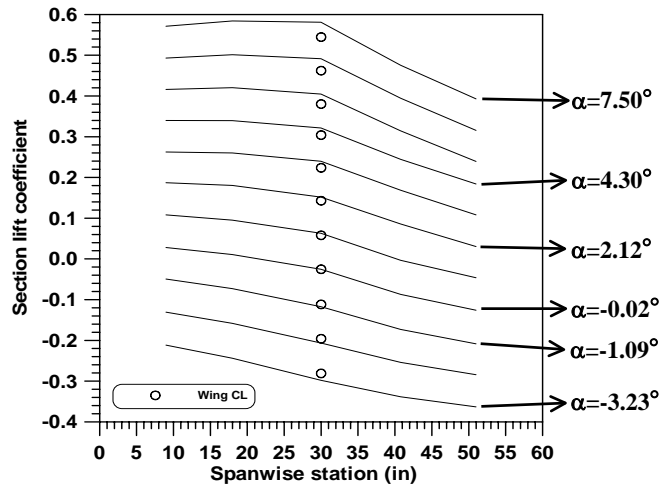


FIGURE H-3. SPANWISE LIFT DISTRIBUTIONS OF THE CLEAN SWEPT WING

The effect of Reynolds number on the lift behavior is demonstrated in figure H-4 using the experimental data of reference H-1 and computational data obtained with the XFOIL code [H-6]. Both the experimental and analysis data indicate a significant increase in maximum lift and angle of stall as expected. In addition, a small increase in lift slope is observed as Reynolds number is increased. Since the airfoil section for the 3D was constant from root to tip, the Re effects for the 3D wing should be similar to that observed with the 2D airfoil.

The experimental lift curves of the clean and iced wings are compared in figures H-2 and H-5 respectively. Each figure provides the 2D and 3D experimental lift curves and the linear part of the lift curve for the 3D wing (line with diamond symbols) that was computed from simple wing sweep theory. The results indicate that the estimated 3D wing slope is in good agreement with the experimental data of the 3D wing.

Next, an estimate of the maximum lift coefficient for the 3D wing is computed using simple wing sweep theory. According to Hoerner [H-5], CL_{max} for a swept wing can be predicted from the maximum lift coefficient ($Cl_{max,2D}$) of a 2D wing using equation H-2. Again, the formula provided is strictly applicable to planar wings and assumes that the airfoil section, in this case GLC-305, and the flow are normal to the wing leading edge.

$$CL_{max} = Cl_{max,2D} \cdot \cos^2 \Lambda_c / 4 \quad (H-2)$$

where $\Lambda_{c/4}$ is the quarter-chord sweep angle, which was 25° for the 3D GLC-305 swept wing. Experimental data presented in reference H-5 indicate that equation H-2 underestimates CL_{\max} for sweep angles greater than about 20° .

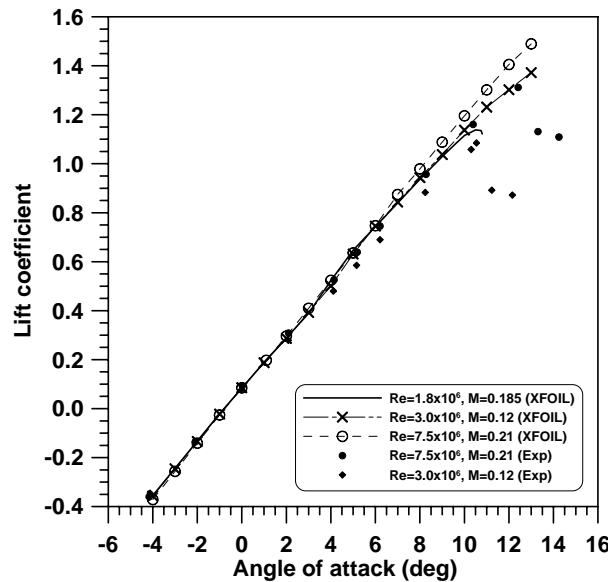


FIGURE H-4. EFFECT OF REYNOLDS NUMBER ON GLC-305 LIFT SLOPE

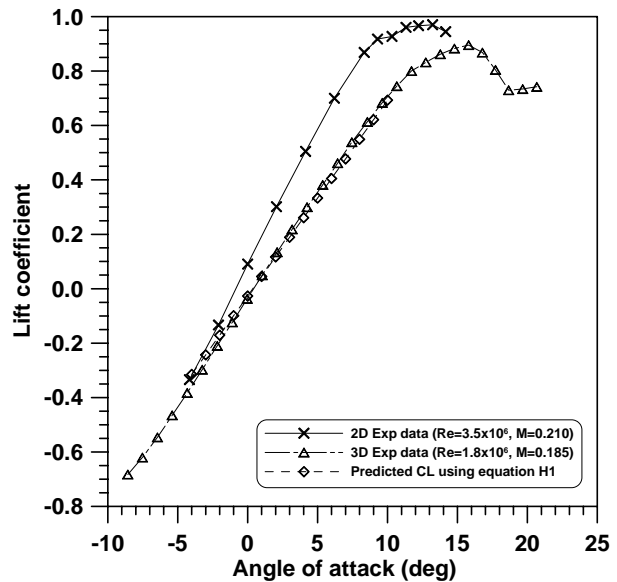


FIGURE H-5. COMPARISON OF LIFT CURVES FOR THE ICED 2D AND 3D WINGS

Lift slopes, maximum lift coefficients, and angles of stall for the 2D and 3D clean and iced wing models are summarized in table H-1. The stall angles provided in table H-1 were obtained from the experimental data. Due to spanwise flow, leading edge and tip vortex structures, washout, and downwash effects, the stall mechanism of finite swept wings is considerably different from that of straight 2D wings and in general the angle of stall for 3D wings is higher.

TABLE H-1. SUMMARY OF LIFT CURVE SLOPES AND CL_{\max}

			Clean Wing	Iced Wing
Lift curve slope (per degree)	2D Exp		0.0973	0.0977
	3D	Exp.	0.0765	0.0775
		Calc.*	0.0718	0.0720
CL_{\max}	2D Exp		1.0850	0.9702
	3D	Exp.	0.8738	0.8955
		Calc.*	0.8912	0.7969
α_{stall} (deg)	2D Exp		10.54	13.23
	3D Exp		13.78	15.80

* Estimates for 3D wing obtained from the 2D experimental data of reference H-1 and simple sweep wing theory.

H.3 RELATIONSHIP BETWEEN 2D AND 3D WING GEOMETRIC ANGLE OF ATTACK.

To estimate the effective angle of attack of the 3D wing, the geometric twist and downwash angle effects need to be estimated and the geometric angle of attack must be adjusted for these effects. These corrections will provide an equivalent geometric angle of attack for the 2D wing. Note that for the same lift, the geometric angle of attack of a finite wing is greater than that of an infinite span wing. According to Hoerner [H-5], the characteristic of pressure distributions in the vicinity of 50% semi-span of a swept wing is the same as that found in conventional infinite span straight wing sections. Therefore, by matching pressure distributions at 50% semispan of the clean 3D wing model to the coefficient pressure distributions of the clean 2D wing model, the relationship between the geometric angles of attack of the 2D and 3D wing models can be estimated. Note that this method assumes the Reynolds numbers of the 3D and 2D flows are the same, which is not the case here. However, as it was shown in figure H-4, the effect of Re over the linear portion of the lift curve was small. The results obtained by applying the pressure matching method are presented in figure H-6. By fitting a least-squares straight line to the data presented in figure H-2, the relationship between the 2D and 3D geometric angles of attack can be obtained. Note that the difference ($\alpha_{2D} - \alpha_{3D}$) provides an estimate of the average geometric twist and downwash angle at 50% semispan.

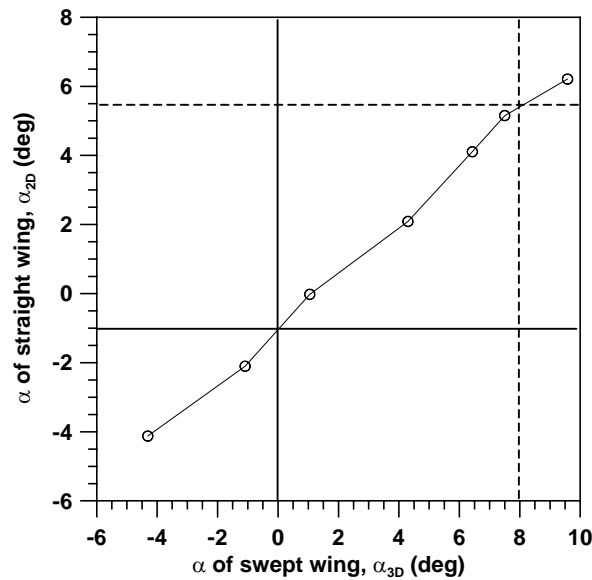


FIGURE H-6. RELATIONSHIP OF GEOMETRIC ANGLES OF ATTACK OF THE TWO-DIMENSIONAL AND THREE-DIMENSIONAL CLEAN WING MODELS

H.4 REFERENCES.

- H-1. Addy, H.E., Broeren, A.P., Zoeckler, J.G., and Lee, S., “A Wind Tunnel Study of Icing Effects on a Business Jet Airfoil,” AIAA Paper 2003-727, January 2003.
- H-2. Ruff, G.A., “Analysis and Verification of the Icing Scaling Equations,” AEDC-TR-85-30, Vol. 1 (Rev), March 1986.
- H-3. Armand, C., Charpin, F., Fasso, G., and LeClerc, G., “Techniques and Facilities Used at the ONERA Modane Centre for Icing Tests,” AGARD-AR-127, Appendix A6, November 1978.
- H-4. Charpin, F. and Fasso, G., “Icing Testing in the Large Modane Wind-Tunnel on Full-Scale and Reduced Scale Models,” NASA TM-75373, March 1979.
- H-5. Hoerner, I.S.F. and Borst, H.V., “Fluid Dynamic – Lift,” Hoerner Fluid Dynamics, P. O. Box 342, Brick Town, NJ, 1975.
- H-6. Drela, M., “XFOIL 6.6 User Primer,” MIT Aero and Astro Engineering, March 1996.
- H-7. McCormick, B. W., “*Aerodynamics Aeronautics and Flight Mechanics*,” 2nd edition, John Wiley and Sons, 1995.